# ADVANCED MATERIALS FOR NEXT-GENERATION LITHOGRAPHY: SELF-ASSEMBLING BLOCK COPOLYMERS AND INORGANIC NANOPARTICLE PHOTORESISTS

A Dissertation

Presented to the Faculty of the Graduate School

of Cornell University

In Partial Fulfillment of the Requirements for the Degree of

Doctor of Philosophy

by

Evan Lawrence Schwartz

January 2011

# ADVANCED MATERIALS FOR NEXT-GENERATION LITHOGRAPHY: SELF-ASSEMBLING BLOCK COPOLYMERS AND INORGANIC NANOPARTICLE PHOTORESISTS

Evan Lawrence Schwartz, Ph.D

Cornell University 2011

The constant demand for increased circuit density and higher resolution patterning calls for simultaneous advancements in materials chemistry. A variety of possible approaches for next-generation lithography are explored, centering on the use of directly patternable self-assembling block copolymers, along with hafnium oxide-based nanoparticle photoresists.

In one example of the first approach, a random copolymer brush layer of poly(styrene-*ran*-hydroxystyrene) was designed and synthesized to precisely tune the substrate/polymer surface energy for a lithographically patternable poly(α-methylstyrene-*block*-4-hydroxystyrene) (PαMS-*b*-PHOST) block copolymer. The surface was designed to avoid preferential wetting of either PαMS or PHOST domains to the substrate and orient the block copolymer domains vertically relative to the substrate. To neutralize the polymer/ vapor interface during solvent vapor processing, the film was exposed to a mixed solvent vapor of a defined polarity, creating vertical microdomains with long-range order.

In the latter approach, hafnium oxide nanoparticles were covalently coated with a photo-reactive ligand, which allowed neighboring nanoparticles to form a crosslinked network upon exposure to ultraviolet light. The basic science of this new class of resist material is discussed. These negative-tone resists have so far demonstrated sub-50 nm resolution using 193nm interference lithography, and plasma etch resistance over thirteen times greater than PHOST under standard silicon etching

conditions.

In a combination of the two approaches, the co-assembly of the inorganic nanoparticles with the PHOST phase of PαMS-*b*-PHOST is shown. TEM and SAXS studies indicated the expansion of the microdomain periodicity upon nanoparticle incorporation. These block copolymer nanocomposite films offer enhanced functionality and a larger process window for subsequent pattern transfer into semiconductor substrates.

In another example of co-assembly, phenolic molecular glass photoresists were blended with low molecular weight, triblock copolymer surfactants based on poly(ethylene oxide)(PEO). The miscibility of these blend components is shown to be a result of preferential hydrogen bonding between the hydroxyl groups attached to the molecular glass and the alkyl ether group of the PEO block, as shown by FTIR and DSC analysis. The blending resulted in an enhancement in segregation strength that led to the formation of sub-10nm self-assembled morphologies, as verified by SAXS. Options for the lithographic patterning of these blends are explored.

Lastly, a combined additive and subtractive patterning technique is demonstrated that allows the deposition of multiple block copolymer films, of different domain sizes and pitches, on the same layer of the substrate. The approach used a semifluorinated negative-tone photoresist which is designed to resist intermixing when spin coated on top of a block copolymer film.

## BIOGRAPHICAL SKETCH

Evan Lawrence Schwartz was born in Tampa, Florida on September 24, 1982 to Neil and Lea Schwartz. His childhood was spent in various locations around the United States, including Florida, Nebraska, Tennessee, New York, and Maryland. From an early age, his parents cultivated in him an interest in science and technology. A succession of several excellent science teachers brought this amorphous interest into clear focus, including Mr. Ken Folger at Harding Academy in Nashville, TN, and Mr. Barry Hopkins from Severna Park High School, in Severna Park, Maryland. Their mixture of professionalism and enthusiasm for their work convinced him that a career in the sciences would be exciting and rewarding.

After high school, Evan enrolled in James Madison University in Harrisonburg, VA as an undergraduate Biology major, aiming to become a medical doctor. However, this quickly changed after hearing one inspirational talk about the excitement of the nanosciences by Dr. Richard Roberds, the former Chair of the Integrated Science and Technology department. It was here that Evan met Professor David Lawrence, who was gracious enough to tutor Evan in the art of microfabrication. Under Dr. Lawrence's guidance, Evan completed a senior honors thesis on the design and microfabrication of "two-way" shape-memory alloy microactuators. This attraction to smart, multifunctional materials led him to the Materials Science and Engineering department at Cornell University in September of 2004, working in the research group of Professor Christopher Ober. After completing his M.S degree in the Fall of 2007, and his PhD degree in the Fall of 2010, Evan set out to begin his professional career at 3M's Display and Graphics Business Laboratory in St. Paul, MN.

To Neil and Lea, who made it all possible

To Anna, for her love and support

# ACKNOWLEDGMENTS

First and foremost, I would like thank my family, Neil, Lea, and Daniel for their constant support and encouragement. Without my parents' effort to find me the best schools and the best teachers growing up, I would certainly not be where I am today. Second, I would like to thank my thesis adviser Professor Christopher Ober, who was kind enough to accept me into his research group, and has been very patient and supportive through the early years of my life in research. In addition to his great ideas, his hard work and dedication to science has been truly inspirational to me. I am very grateful to have received financial support from the Semiconductor Research Corporation, Motorola, and SEMATECH. Professors Ulrich Wiesner and Dotsevi Sogah deserve special recognition for serving on my thesis committee and for their helpful suggestions towards the completion of my degree.

I would like to thank all my friends in the Ober group, past and present. In particular, I would like to thank Prof. Sitaraman Krishnan for being a great friend and mentor during my first couple years in the lab, as well as Dr. Shalin Jhaveri and Zhaoli Zhou, for being great friends and even greater listeners. I would also like to thank Dr. Katy Bosworth, Michelle Chavis, Dr. Jin Kyun Lee, Marie Krysak, and Dr. Markos Trikeriotis for their assistance in the lab and many helpful discussions. I have also had the privilege to work with brilliant undergraduate students during my time at Cornell, including Trevor Goff, Eric Sterling, Corissa Lee, Roy Lotz, Zhen Dai and Nathan Lee. Their contribution to my research effort is very much appreciated. For the majority of the technical work represented here I am indebted to John Grazul, Yuanming Zhang, Suntao Wang, Anthony Condo, John Hunt, Kit Umbach and Mick Thomas. I have truly enjoyed learning the technical aspects of scientific research from them. Last but not least, I would like to thank Anna Li, whose love and encouragement has made my final years of graduate school so much more enjoyable.

## TABLE OF CONTENTS

## LIST OF FIGURES

## LIST OF TABLES

# CHAPTER ONE:

## BLOCK COPOLYMER SELF-ASSEMBLY FOR SEMICONDUCTOR MICROFABRICATION[1]

[1]Portions of this chapter were adapted for use in the upcoming book chapter "Block Copolymer Nanostructured Thin Films for Advanced Patterning." Michelle Chavis, Evan Schwartz, Christopher K. Ober. Ed. Nikos Hadjichristidis, Wiley (2011).

### *1.1 Introduction*

Modern semiconductor devices contain billions of transistors in total areas that are often not much bigger than a quarter. Over thirty years of manufacturing expertise and research investment have enabled this development, but the march to higher circuit densities and smaller feature sizes is becoming increasingly difficult. The workhorse technology at the heart of circuit manufacture is called photolithography, which relies on high energy ultraviolet (UV) photons to transfer circuit information through a radiation-induced solubility change in a polymer film. The current state of the art process, known as 193nm immersion photolithography, can efficiently produce arbitrary device pattern geometries with critical dimension (CD) control below 40nm.[1] Other processing tricks, such as double patterning, can be used to extend this technology below 30nm, but it is widely known that improvements will be accompanied by rapidly increasing cost and difficulty.[2] To pattern device features below 22nm, the industry is investigating replacement technologies such as Extreme UV (EUV) lithography and nanoimprint lithography (NIL), but these techniques are also hampered by severe technical challenges that will require an indefinite amount of engineering refinements.[3,4] This interdisciplinary challenge has prompted an urgent call from the semiconductor community for alternative patterning approaches for electronic materials for the sub-22nm technology node. One of the potential solutions in this area employs the order manifest in natural systems, often called *self-assembly*. Self-assembly can be defined as a process in which disordered materials spontaneously organize into more ordered structures with atomic or molecular-level precision without human intervention.[5]

A class of soft matter known as block copolymers is one striking example of self-assembly that is being considered as a next-generation material for lithography. Similar to traditional polymeric photoresists used in photolithography, they can be

spin coated as a uniform thin film and can act as sacrificial templates for the creation of integrated circuit elements.[6] Unlike traditional resists, however, block copolymers form periodic patterns in the mesoscopic (10-100nm) regime without the use of an expensive lithographic toolset. While the idea of using a block copolymer as a functional material has been around since the late 1980's,[7] the use of self-assembled block copolymers as positive or negative lithographic etch resists began in 1995 at Princeton University.[8] Since these initial studies, the block copolymer community has demonstrated the potential of this material class to achieve pattern densities greater than $10^{11}$ features per square centimeter, and feature sizes less than 50 nm on a variety of different substrates such as Si, $Si_3N_4$ and Ge.[9] This review summarizes the theoretical and practical foundation for block copolymer lithography and discusses the challenges the field must overcome before it can meet the needs of the semiconductor community in the future.

### *1.2 Block Copolymer Self Assembly*

Block copolymers, herein abbreviated as BC's, are a class of macromolecules in which two or more chemically distinct polymer chains are covalently linked at their respective chain ends. Due to the very small mixing entropy for large chain polymers, each of the polymer “blocks” strive to pull apart from each other, but are restrained by the effect of the covalent bond which limits the maximum distance that the two polymer “blocks” can separate. The free energy of the system is minimized by the formation of a minimum interaction volume between the polymers, and a maximum in chain conformational entropy, which results in the formation of remarkable periodically repeating structures at mesoscopic (10-100 nm) length scales. This behavior has historically been referred to as “microphase separation” due to the formation of patterns that form in the molten and solid states.[10]

### *1.2.1 Block Copolymer Architectures*

The simplest and most studied architecture of block copolymers is that of the linear AB diblock, consisting of a long chain of A monomers covalently connected to a chain of B monomers. Coupling two of these AB diblocks together enables the formation of ABA triblocks, or $(AB)_n$ multiblocks. The incorporation of a third type of monomer enables the formation of ABC triblocks or other advanced architectures, resulting in a wide variety of exotic morphologies.[11] Additional complexity can be built into the polymer by changing the molecular topology, such as changing the block sequence (ACB instead of ABC), or by forming star-type architectures in which all three polymers are joined in the center.[12] Small changes in the synthetic strategy can lead to vastly different types of morphologies, as well as differences in material properties. For triblock copolymers, a plethora of new and exotic structures have been theoretically predicted and many of them have been observed experimentally, such as helical structures,[13] knitting-needle patterns,[14] core-shell morphologies,[15] Archimedean tiling patterns,[16] and double gyroid structures, which consist of two interpenetrating polymer networks.[17] Further discussion of block copolymer phase behavior is beyond the scope of this paper, but many excellent review articles exist on this topic.[18]

## *1.3 Physics of Microphase Separation*

In all types of block copolymer architectures, microphase separation depends on the chemical incompatibility of each of the polymer blocks with respect to each other. In this review, we will focus on the simplest case of the AB coil-type diblock copolymer, in which the incompatibility between the A and B blocks is the main driving force for microphase separation.

The free energy of mixing ($F_{mix}$) of a polymer solution is given by the Flory-Huggins equation for polymer solutions,

$$F_{mix} = kT[\frac{\phi}{N}\ln\phi + \ln(1-\phi) + \chi\phi(1-\phi)], \qquad \text{[Eq. 1.1]}$$

where N is equal to the molecular weight of the polymer in solution, and $\phi$ is equal to the volume fraction of the polymer relative to solvent. The first two terms in this equation are of an entropic origin, and always act to promote mixing, although this term is usually very small in the case of polymers. The last term is of an enthalpic origin, and can be positive (opposing mixing), zero (ideal mixing), or negative (promoting mixing) depending on the sign of the Flory-Huggins interaction parameter, $\chi$. This parameter refers to the free energy cost per monomer of contacts between A and B monomers, in units of the thermal energy (kT) and is inversely proportional to the temperature of the system. In other words, an increase in temperature will lead to a greater tendency for phase mixing in the polymer system. The $\chi$ parameter is used in most modern theories of polymer microphase separation to describe thermodynamic behavior at the molecular scale.

### *1.4 Periodic Array Formation*

Compositional fluctuation between the A and B microdomains lead to many different geometries that repeat periodically at the 10-100 nm length scale. Upon increasing the relative volume fraction of one block relative to the other, different microstructures including spheres, cylinders, bicontinuous networks, and lamellar sheets may form. Typical unit cells for each of these morphologies are shown in Figure 1.1. Increasing the volume fraction past the lamellar region will cause the phases to invert, i.e. the minority phase will become the majority phase. Changes in the interfacial curvature can be used to explain the changes in the morphology between the two connected blocks. In the simplest case, with equal amounts of each

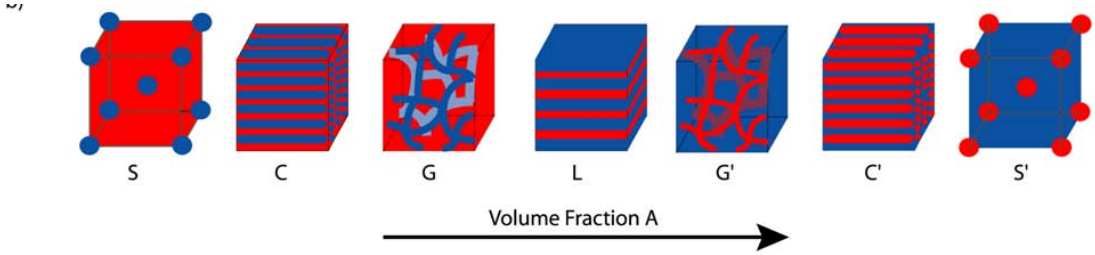


Figure 1.1 An illustration that shows the various morphologies present in diblock copolymers as the volume fraction of the A (blue) phase is increased.

block, the inter-material dividing surface (IMDS) will form into distinct layers with planar interfaces. If there is more than one block than the other, the IMDS will curve to minimize the repulsive interfacial contact between the A and B block, which also decreases the free energy of the system. Thus, by tailoring the relative amount of each block, the connectivity and dimensionality of the BC nanostructure can be precisely tuned. Spheres represent zero-dimensional points which stack on a face-centered cubic (FCC) or a hexagonally close packed (HCP) lattice. Cylinders represent one-dimensional lines which usually arrange in an HCP lattice. Lamellar morphologies represent two dimensional sheets, while bicontinuous network phases represent three dimensional "network" structures.

### *1.4.1 Block Copolymer Phase Diagrams*

Traditional thermodynamic arguments, such as phase diagrams, can be used to predict the behavior of the BC phase space. Self-consistent mean field theories can calculate the equilibrium morphology formed at different component volume fractions. These theories are based on the balance between the repulsive polymer-polymer interactions versus the elastic restoring force energy for a particular microphase structure, originating from the covalent bond connecting the two blocks. The structure with the lowest free energy sum will be the final equilibrium morphology. The results of these calculations can be conveniently plotted as a phase diagram, as shown in Figure 1.2. The ordinate axis plots the product $\chi N$ versus the block volume fraction, $f_A$. Here, N refers to the degree of polymerization, or number of monomer units in each polymer chain. The x-axis plots the volume fraction $f_A=N_A/N$, where $N_A$ is the number of A monomers per block. Block copolymer phase diagrams typically exhibit a local minimum at some product $\chi N$, theoretically predicted to be

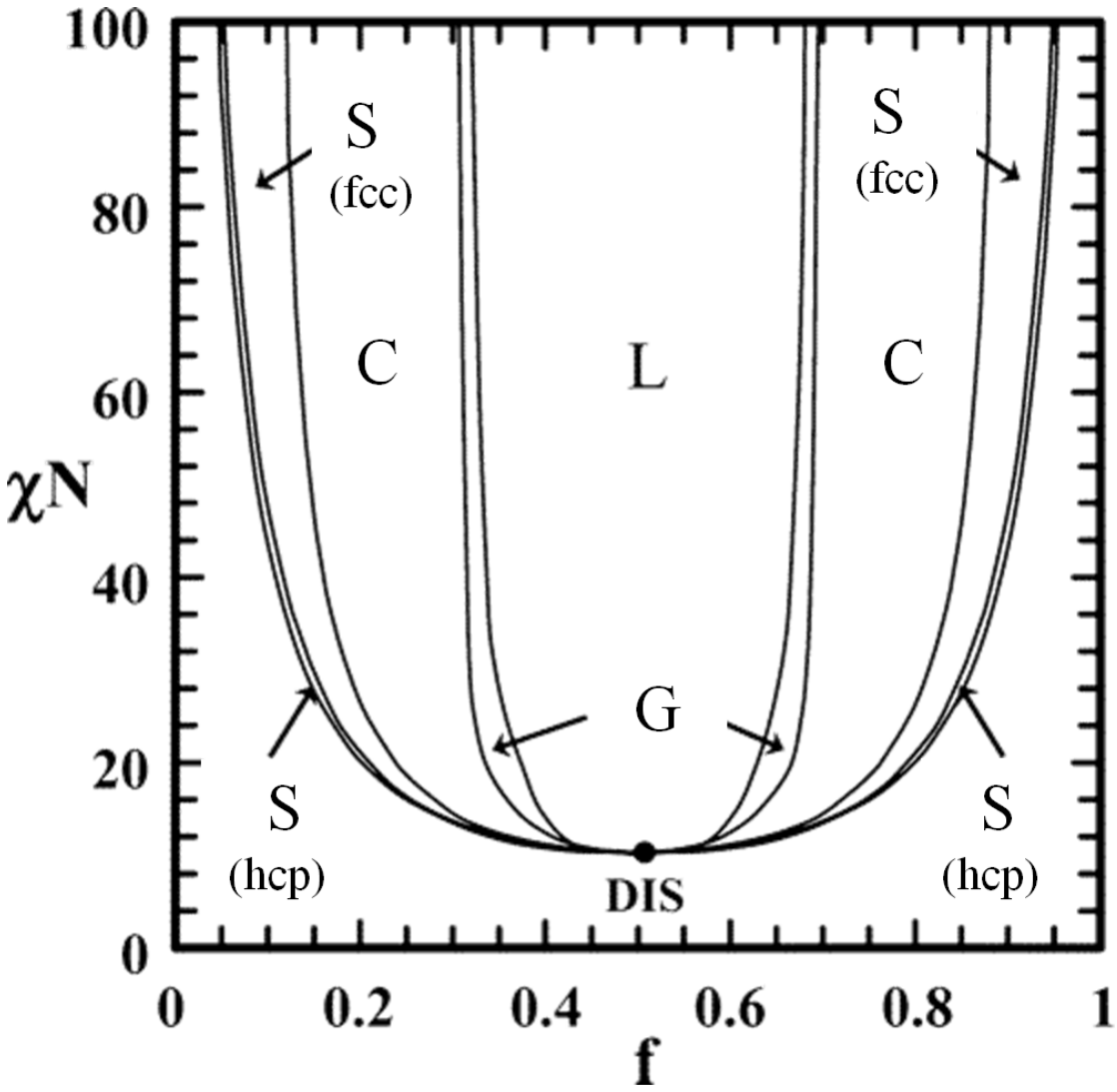


Figure 1.2. An illustration of a hypothetical phase diagram for block copolymers, with the volume fraction plotted as a function of the Flory-Huggins interaction parameter $\chi N$, with symbols corresponding to the morphologies shown in Figure 1.1 Adapted with permission from Ref. 20. Copyright 2006 American Chemical Society.

10.5 for typical block copolymers. This product sets a threshold molecular weight for microphase separation, and thus a minimum feature size, for a given BC. For example, a BC with a low $\chi$ value requires a high molecular weight (N) in order to microphase separate, while a BC with a high $\chi$ value only requires a low molecular weight in order to do the same. Due to the small difference in segregation strength between the polystyrene (PS) and polymethylmethacrylate (PMMA) blocks at room temperature ($\chi$~0.06),[19] PS-*b*-PMMA requires a relatively large molecular weight in order to microphase separate. Weaker segregation strength between the blocks also means that there is less driving force to remove energetically costly defects in the polymer structure, leading to BC microdomains with relatively poor long-range order.

### *1.4.2 Microdomain Critical Dimension Control*

With the development of well-controlled "living" polymerization techniques such as anionic[21] and atom-transfer radical polymerization (ATRP),[22] polymer chemists have learned to precisely control the morphology of the BC microdomains by varying the volume fraction of each of the blocks during the synthesis step. It is also possible to control the BC period spacing ($L_0$) by changing the total molecular weight (N) of the BC. In fact, a power law scaling model has emerged which can closely predict how the domain spacing will vary according the molecular weight of the block, which follows the form $L_0 \sim N^{\gamma}$. Theoreticians such as Semenov correctly predicted that the microdomain size ($L_0$) scales proportionally as the two-thirds power of the block's molecular weight ($\gamma$=2/3) for strongly segregating block copolymer pairs ($\chi N >> 10.5$).[23] This theoretical result has been proven experimentally using the PS-*b*-PMMA system.[24] For weakly segregating polymer pairs ( $\chi N \sim 10.5$), $\gamma$ =1/2.[25] There is also an intermediate segregation regime, where the value of $\alpha$ may vary from 0.8 to 0.83.[26]

### *1.5 Self-Assembled Pattern Formation*

The lithography community has taken an interest in BC's in part due to their ability to form nanoscopic features over large areas, simple process flow, and low cost. A typical process flow for block copolymer lithography is shown in Figure 1.3. Traditionally, PS-*b*-PMMA has been used as a model system for study in this area, due to its commercial availability and similarity to other common resist materials.[27] In this review we will use this polymer to illustrate several key concepts which will be discussed in subsequent chapters. For lithographic applications, typically the bulk BC is dissolved in a good solvent for both blocks and spin-coated as a thin film on a substrate of choice, usually a cleaned silicon wafer that has been pre-treated with a neutralization layer (Section 1.7). The wafer is then annealed in order to arrange the microdomains in either a parallel or perpendicular fashion, as required for the specific application (Section 1.8). Upon exposure to deep UV radiation, each one of its respective blocks act quite differently. The PS phase crosslinks, similar to a negative-tone photoresist in traditional photolithography (Section 1.9), while the PMMA phase is removable via wet or dry etching, similar to a positive-tone photoresist (Section 1.10). The mechanism of degradation is a chain scission process, in which the polymer breaks up into its constituent monomers in response to UV light.[28] In turn, the MMA monomers can be selectively removed by immersion in a selective solvent such as acetic acid. The crosslinking of the PS matrix phase adds mechanical strength to the template and avoids the collapse of the nanoporous structure on itself, since the creation of new surfaces is thermodynamically unfavorable. Furthermore, the high carbon content of the PS phase may act as an etch resist (Section 1.11) in order to carry out various semiconductor etching steps in the underlying substrate to create a

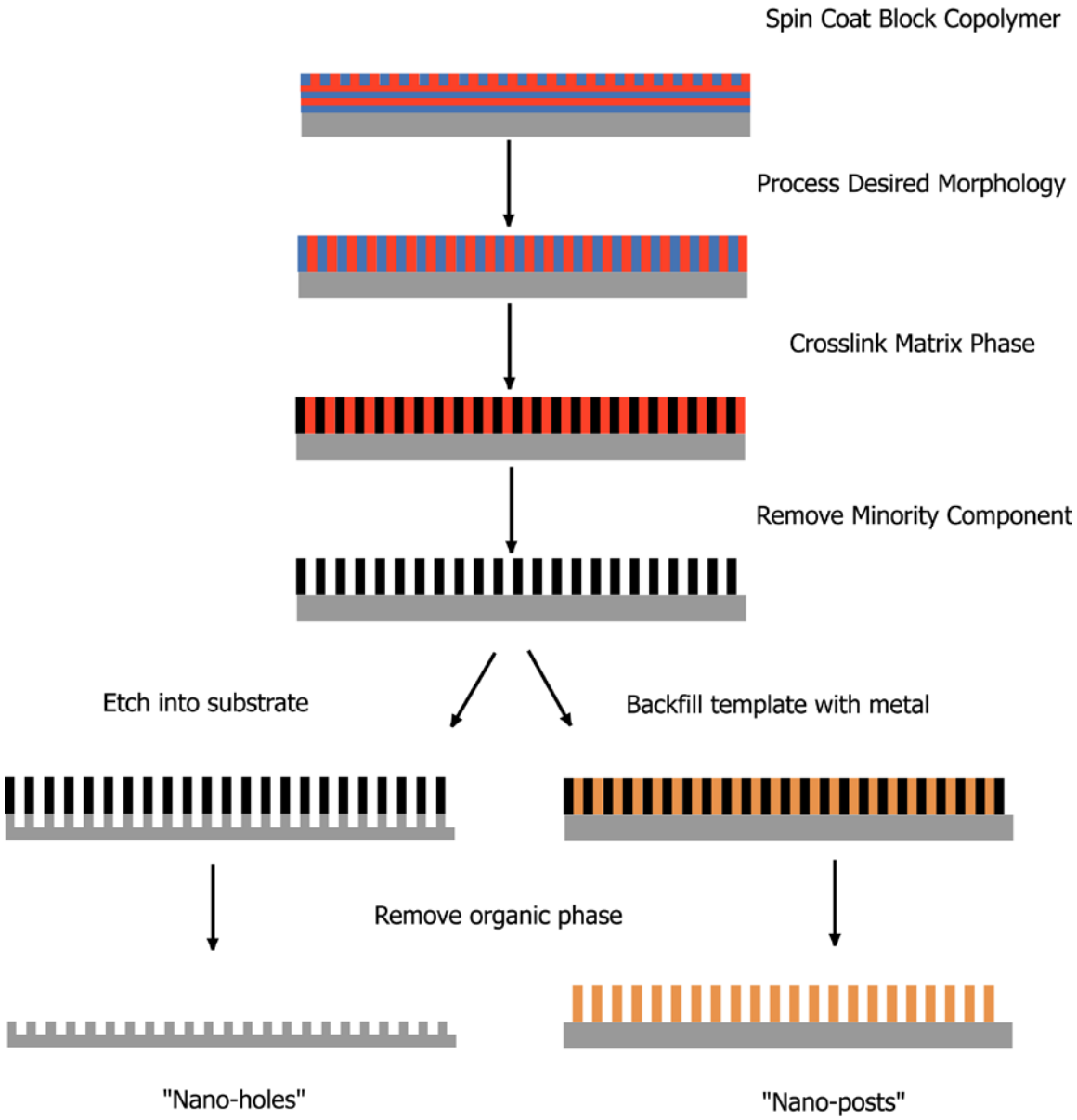


Figure 1.3. Illustration of two typical process schemes for block copolymer lithography

replica of the self-assembled nanoporous template (Section 1.14), as shown in the bottom left of Figure 1.3. In a less common approach, the nanopores may also be filled with metal via electro-deposition to form a negative image of the nanoporous replica, as shown in the bottom right of Figure 1.3. The example of PS-*b*-PMMA highlights many important principles in block copolymer lithography which will be discussed in more detail in subsequent sections.

### *1.5.1 Microdomain Geometry Requirements*

Most of the research in the field has focused on morphologies that are most useful for industrial applications. For example, contact holes can be patterned using perpendicularly oriented cylinders composed of the degradable block. This morphology is highly desired due to the ability of the cylinder to physically connect from the substrate to the surface of the film for subsequent plasma etching into a substrate. A single monolayer of spheres may also allow access to the substrate after the removal of the minority block. However, a spherical structure has an inherently lower aspect ratio compared to the cylindrical morphology, especially if the film thickness (cylinder length) is several times greater than $L_0$.

Considerable amounts of money in the semiconductor industry have been spent on circuit design software and fabrication processes that are based on a rectilinear geometry. However, typically BC nanostructures arrange on a hexagonally close packed (HCP) lattice. Scientists have learned how to force the local packing of the cylinders into square arrays using chemical nanopatterning of the substrate, (discussed in section 1.8.4)[29] and supramolecular hydrogen bonding interactions. In the latter approach, the authors created two separate block copolymers of poly(styrene-*block*-ethylene oxide) (PS-*b*-PEO) and poly(styrene-block-methyl methacrylate) (PS-*b*-PMMA). The PS blocks in both of the polymers were randomly copolymerized with

precise amounts of poly(4-hydroxystyrene) (PHOST) and poly(4-vinylpyridine)(P4VP), introducing hydroxy and pyridyl moieties, respectively, into the block copolymer. These units interacted with each other to alter the local packing of the block copolymer cylinders to form a square array, as shown in Figure 1.4.[30] Supramolecular interactions may also be used for other applications within block copolymer lithography, as discussed in Section 1.6.4.

### *1.6 Line Edge Roughness and CD Control in Self-Assembled Systems*

One of the main advantages of self-assembling materials such as block copolymers is their potential to improve problems in the dimensional control of patterned lines. Following exposure to UV light, the performance of the radiation-sensitive resists in traditional photolithography depends on the diffusion of small photoactive compounds (PACs) through a resist film, kinetically driven by a brief thermal bake. Small variations in the exposure dose or temperature during this post-exposure bake (PEB) step can lead to large deviations in the final patterned structures. The primary manifestation of these deviations is in the sidewall roughness of the patterned line edge and width, both of which directly impact device performance. Line edge roughness (LER) is defined as the three-sigma deviation of the real patterned line from the ideal line edge. Similarly, line width roughness (LWR) is defined as the three-sigma deviation of the line width. High frequency LWR leads to non-uniform dopant concentration profiles and affects interconnect wire resistance. Low frequency LWR leads to variations of transistor gate length over the active region of the device. This variation leads to fluctuations in the speed of the transistors, which can snowball into global interconnect timing issues.[31] In order to meet the requirements of the semiconductor community, the International Technology Roadmap

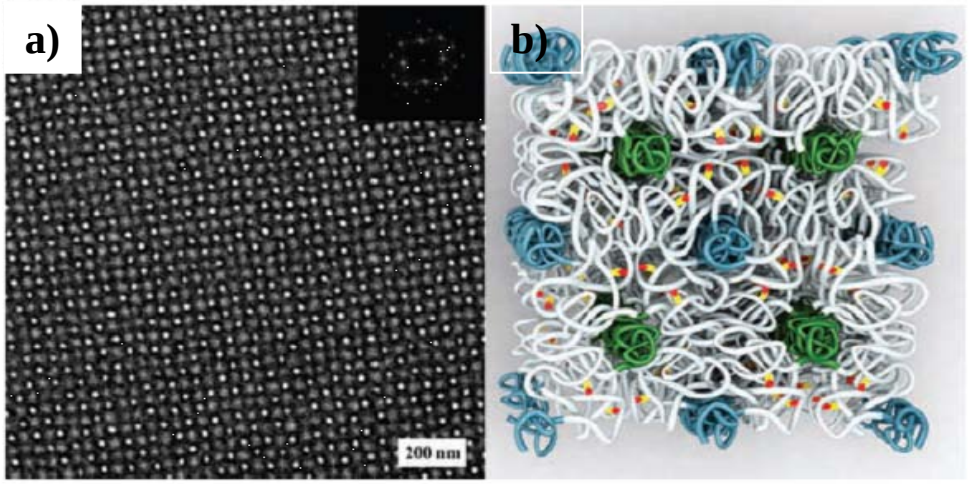


Figure 1.4.a)TEM image showing a square packing array of cylinders stemming from supramolecular hydrogen bonding interactions b) shows a cartoon of the proposed unit cell of the corresponding block copolymer blend. Reprinted with permission from from Ref. 30, Copyright AAAS.

for Semiconductors (ITRS) has defined the target of achieving 2.1 nm low-frequency LER by 2012.[32] Currently, there are no chemically amplified resists that can meet this standard, so it is hoped that self-assembly can provide some insight into a possible solution for this problem, especially since the LER/LWR tolerances will only get tighter as feature sizes decrease below 15nm.

### *1.6.1 Thermodynamic Considerations*

Relevant to any discussion of LER in self-assembled materials is the Flory Huggins interaction parameter, $\chi$. $\chi$ defines the minimum possible interfacial width between the block pairs, which is crucial for sharp definition in the nanoporous template and the possible reduction of LER and LWR. This width ($\Delta$) is given by, [33-35]

$$\Delta_{\infty} = \frac{2a}{\sqrt{6\chi}} \qquad \text{[Eq. 1.2]}$$

$$\Delta = \Delta_{\infty}(1 + \ln 2(\frac{1}{\chi N_A} + \frac{1}{\chi N_B})), \qquad \text{[Eq. 1.3]}$$

where $\Delta$ is the interfacial width in the limit of infinitely large molecular weight polymers, and *a* is a statistical monomer segment length. For PS-*b*-PMMA at 200 °C, Equation 1.3 gives $\Delta$=3 nm, while experimentally measured values of $\Delta$ are on the order of 5 nm.[36,37] Therefore, in a system which measures domain spacings of 20 nm, 25% of the polymer consists of interface, which will translate into sidewall roughness and LER after PMMA removal. In response, other research groups have investigated different block copolymer pairs with a higher segregation strengths, such as poly(styrene-*block*-ethylene oxide) (PS-*b*-PEO)($\chi$~0.08),[38,39] poly(styrene-*block*-2-vinyl pyridine)($\chi$~0.18),[40] or poly(styrene-*block*-dimethylsiloxane)( $\chi$~0.26).[41]

### *1.6.2 Triblock Copolymers with Enhanced χ*

There are ways to use the compositional tunability of triblock copolymers in conjunction with techniques to boost the χ parameter of the system. Tirumala and coworkers have shown that it is possible to boost χ by blending in small amounts of hydrogen bonding additives into a low molecular weight, nonionic triblock copolymer surfactant. The surfactant, poly(ethyleneoxide-block-propylene oxide-ethylene oxide)(PEO-*b*-PPO-*b*-PEO) typically does not have a large enough χ parameter by itself for microphase separation ($\chi$=0.08).[42] However, with the addition of the H-bonding component, microphase separation maximizes the number of hydrogen bonds between the additive and the PEO block. As a result very low molecular weight (~12,000 g/mol) the authors reported cylindrical phases with dimensions of 15nm and below.[43]

To combine the best features of both PS-*b*-PEO (long-range order) and PS-*b*-PMMA (high χ, processability), the triblock copolymer PS-*b*-PEO-*b*-PMMA has been synthesized and studied. [44] In this report, zero defects were found over 4 $\mu m^2$ square areas for low molecular weight (13,500 g/mol) triblock copolymers, forming cylinder domain spacings of about 22 nm. However, in these lower molecular weight systems they found the complete removal of the minority block difficult due to the miscibility of the PEO and PMMA blocks that make up the minority phase cylinder. The authors found that as the length of the PMMA block increased, its miscibility with PEO decreased, leading to phase separation between the PEO and PMMA. A core-shell type structure resulted, with PEO confined to the center core of the cylinder and PMMA forming the outer shell. Only then did complete photodegradation of the PMMA occur in this system, as a ring surrounding the remaining PEO cylinder.

### *1.6.3 Polydispersity Effects on CD Control*

As in all polymer syntheses, however, there is a distribution of polymer chain lengths, which also affects self-assembly. It has been shown theoretically that the polydispersity (PDI) of a block copolymer system has a direct relation to the perfection of the self-assembled pattern, since a distribution in the volume fraction of each component leads to a difference in interfacial curvature from one microdomain to the next.[33] Lynd et al. has confirmed this theory by investigating different PDI's in a poly(ethylene-*alt*-propylene-block-lactide) (PEP-b-PLA) system. The authors have shown that a large increase in the polydispersity not only leads to changes in the domain curvature and morphology, but also can change the segregation strength of the system, weakening the effective potential holding the microdomains to regular arrangements on a lattice.[45,46] It is unclear, however, if increased PDI will relate directly to increased LER in block copolymer systems. More important may be the morphology of the self-assembled pattern. Published cross-sectional line profiles of vertical lamellae and parallel cylinders provide a hint that lamellar line structures seem to have far smoother line profiles compared to the 'scalloped' line shape produced from cylindrical structures, although this remains to be quantified with actual LER measurements.[47]

### *1.6.4 Hierarchical Nanopore Formation*

Block copolymer self assembly can create a wide range of microdomain sizes that do not depend entirely on the $\chi N$ term. It is possible to bypass the thermodynamic restrictions of the $\chi$ parameter to achieve smaller size domains through a few processing tricks. For example, blended PMMA homopolymers, with a molecular weight less than the corresponding PMMA block in a PS-*b*-PMMA system have been shown to segregate to the center of the PMMA microdomain. The

homopolymer could then be selectively dissolved in order to create a pore much smaller (6-8 nm) than that produced by removing the entire PMMA block.[48] This has also been demonstrated using PS-*b*-PEO block copolymers to create sub-5nm pores.[49] PS-*b*-PMMA films with high levels of crosslinking induced by ozone exposure have also been shown to produce 3 nm nanopores inside the PMMA block originating from a large volume contraction in the PS matrix, which pulled the attached PMMA microdomain outward along with it.[50]

Supramolecular interactions within specific BC domains could also be used for nanopore formation. Ikkala and coworkers showed that a variety of different alkylphenol molecules could selectively coordinate through hydrogen bonding to a P4VP block in a PS-*b*-P4VP block copolymer. The resulting comb-coil supramolecule formed a zoo of exotic morphologies in the melt such as lamellar-*within*-lamellar and cylindrical-*within*-lamellar microstructures. Perhaps most relevant to lithography, the alkylphenol component could be selectively removed with a polar alcohol to form sub-5-nm nanopores within the bulk polymer.[51,52] Sidorenko and coworkers focused on a PS-*b*-P4VP thin film blended with 2-(4-hydroxybenzeneazo)benzoic acid (HABA) as a supramolecular assembling unit which coordinates to the P4VP block. After solvent annealing, the hydrogen bonding of the HABA block segregated to the center of the P4VP and was extracted with ethanol to create thin films with 8 nm diameter nanopores with a period of 23nm.[53]

### *1.7 Control of Microdomain Orientation*

Lithographic application of block copolymers requires their use in the form of a thin film, typically applied to a substrate by spin-coating from a dilute solution of organic solvent. The phase behavior of BC thin films are typically far richer and more complex than in bulk due to the many different surface-polymer and polymer-polymer

interactions that need to be controlled in order to obtain reproducible block copolymer morphologies. These factors that determine these various morphologies and orientations have become the subject of intense study in the BC research community.[54]

### *1.7.1 Surface Energy Effects*

A two-dimensional template for pattern transfer typically requires a continuous layer of periodic microdomains on a surface. By controlling the spin speed and concentration of the spin coating solvent, it is possible to vary the film thickness of the polymer film. Typically, the expected domain spacing and morphology of the BC in the thin film can be predicted by examining its bulk structure using transmission electron microscopy (TEM) or small angle x-ray scattering (SAXS). In other words, a diblock copolymer that shows only lamellae in bulk will typically also form lamellae when spin coated as a thin film. However, the fast evaporation resulting from the spin coating process leaves the microdomains in a non-equilibrium state, and the surface energy of the substrate plays a large role in the orientation of the lamellae. If one of the blocks preferentially wets the substrate (less interfacial energy difference between the polymer and the substrate), the free energy of the system is minimized by arranging that block along the substrate and the other block at the air interface. The alternative vertical orientation of the lamellae would result in the termination of the lamellae at both substrate and air interfaces, which would lead to an unfavorable increase in the free energy of the system and does not occur. Instead, an integer multiple of $L_0$ results in the parallel stacking of the lamellar sheets, which have no in-plane surface features and are thus unsuitable for lithography.

### *1.7.2 Island and Hole Formation*

If the film thickness does not match with integer values of $L_0$, the film will

form with two distinct thicknesses, as a result of incomplete layer formation. In other words, terraces of height $L_O$ will form on top of a foundation film of height $nL_O$, with n as an integer. Also called "islands and holes," they have been found in cylinders, spheres, and lamellae.[55] There is a high energy cost for the formation of islands and holes due to the resulting increase in contact area between the polymer film and air. Because of this high energy cost, the polymer surface tension usually avoids the formation of a discrete terrace step, usually forming a graded interface in which the film thickness changes over the span of several microdomains. At these transitions, where the local film thickness differs from integer multiples of the lattice constant, differences in the size, or even morphology of the microdomains compared to the bulk may result. For example, cylinder-forming diblocks have been shown to form spheres at the interface between two block copolymer layers.[56]

In practice, islands and holes can be very difficult to avoid. Small surface features on a wafer such as particles of dust can cause the polymer solution to wick up the particle of dust and cause changes in local film thickness, while the rest of the surface maintains an optimal thickness. Also, due to the inverse temperature dependence of the $\chi$ parameter, films of a commensurate thickness after annealing at one temperature may lead to islands and holes at another temperature. It is crucial to avoid island and hole formation for block copolymer lithography, since variations in film thickness lead to trouble later in the pattern transfer step. For example, they may cause a variation in the amount of time required in order to etch through a layer.

### *1.7.3 Sub-Monolayer Hybrid Morphologies*

When the thickness of the film (t) is less than that needed to form a complete layer of microdomains ($t < L_0$), the physics of BC film formation becomes even more complicated. In this regime, despite strong surface interactions, there is an entropic

penalty for the microdomains to compress in order to lay parallel to the substrate. As a result, the polymer chains will prefer to orient perpendicular to the substrate. Other hybrid morphologies have also been found in this instance, such as hexagonally perforated lamellar, half-lamellar, and half-cylinders, due to the competition between strong surface forces, slow kinetics, and the thermodynamic driving force to arrange in layers commensurate with the height $L_o$.[57] Due to all the complications of block copolymer morphology that can occur over three dimensions in a thin film, a combination of microscopy techniques and quantitative x-ray scattering data is usually necessary to solve the structure of the microdomains.[58]

### *1.7.4 Improving Aspect Ratio Using Vertical Orientation Control*

As discussed previously, vertically oriented cylinders are preferred for many applications in lithography. If neither block in the block copolymer is preferentially attracted to the substrate, the microdomains will tend to orient vertically to maximize the total conformational entropy of the polymer chains. Mansky and coworkers have found that it is possible to force this vertical orientation to occur by controlling the interfacial interactions between the block copolymer and the substrate. Using PS-*b*-PMMA, they demonstrated that a random copolymer brush with a precisely tuned composition of PS and PMMA acted as a surface modification layer that effectively neutralized the interaction of the BC with the substrate.[59,60] The random copolymer layer was anchored to the substrate by a terminal –OH group on the polymer chain which underwent a condensation reaction with the silanol groups on the $SiO_x$ wafer during a brief thermal anneal. Rather than using an end-functionalized random copolymer, another research group has used a PS-*ran*-PMMA random copolymer integrated with a small percentage of hydroxyl-containing poly(2-hydroxyethylmethacrylate) (PHEMA) groups along the polymer backbone. Similarly,

the –OH groups were used to bind to the substrate and achieve the same neutralization effect.[61,62] Then, the block copolymers were spin coated on top of this brush layer and thermally annealed to achieve vertically-oriented microdomains. This technique, in conjunction with thermal annealing, has been used to produce up to 230 nm of vertically oriented cylinders.[61]

In conjunction with altering the block copolymer surface, changing polymer-polymer interactions has also been shown to enhance the vertical orientations of cylinders in thick block copolymer films. Working with a PS-rich asymmetric PS-*b*-PMMA block copolymer, Jeong et al. has shown that adding up to 33% of PMMA homopolymer (relative to the total amount of PMMA in the system) with a molecular weight that is 50% greater than the PMMA block molecular weight led to vertical orientations over a wide range of film thicknesses up to 300 nm.[63] The PMMA homopolymer localized into the PMMA minority phase, causing the homopolymer to stretch along the long axis of the cylinder throughout the depth of the film. Kitano and coworkers have proven the generality of this phenomenon by synthesizing a PMMA-rich PS-*b*-PMMA block copolymer, and blended in PS homopolymer to achieve the same effect.[64] Simple blending approaches such as these may become very useful for future nanolithography.

### *1.8 Techniques to Improve Long-Range Order*

The ultimate application for block copolymers in semiconductor microfabrication involves their use in patterning simple circuit elements at high resolutions not capable using current lithography techniques. Examples might include field effect transistor (FET) gate structures from vertical lamellar line/space patterns and contact hole arrays from vertical cylinders.[65] A great deal of control is required over the lateral order of the microdomains in order to achieve perfect registration. The

ability to minimize defects in the pattern is crucial in order to make future semiconductor applications a reality.

### *1.8.1 Thermal Annealing*

In order to remove the energetically costly defects in the film microstructure produced during spin coating, polymer chains need mobility in order to reach an equilibrium condition. Increasing the temperature of the film sufficiently above the glass transition temperature ($T_g$) of both blocks and below the order-disorder transition temperature (ODT, $\chi N<10.5$) leads to increased polymer mobility and an increase in the grain size of the microdomains. A general rule of thumb is that reasonable mobility of the polymer film occurs at temperatures about 60 °C above $T_g$ [$(T-T_g) > 60°C$]. Higher annealing temperatures lead to an increase in polymer diffusivity and faster pattern formation, but the upper limit is the decomposition temperature of the polymer ($T_{dec}$), at which the polymer may spontaneously undergo crosslinking, chain scission, or both. Kramer and coworkers have found that the best way to induce large grain sizes of PS-*b*-P4VP block copolymer is to increase the temperature of the film above the order-disorder transition temperature ($T_{ODT}$) where the polymer blocks mix together and remove defects, and then slowly cool the film to below $T_{ODT}$ , where the now more strongly immiscible blocks are allowed to microphase separate to form very sharp interfaces between the blocks.[66] For PS-*b*-PMMA, Black and coworkers have found a very narrow processing window between $T_{ODT}$ and $T_{dec}$, meaning that it is very difficult to use this two-step thermal anneal process in order to improve microdomain ordering.[67]

Several other groups have also experienced success in achieving long-range order by thermally annealing different block copolymers. Using time-lapse atomic force microscopy (AFM) Harrison et al. showed that at a fixed temperature above the

polymer's $T_g$, the size of the grains in cylinder-forming PS-*b*-PI [PI=poly(isoprene)] increased with a $(time)^{1/4}$ dependency, which did not lead to defect-free patterns within a reasonable amount of time.[68,69] The group found similar behavior for a sphere-forming system.[70] Harrison and coworkers have also contributed to the understanding of the mobility of block copolymers with strong "pinning" interactions with supporting oxide substrates, such as blocks with highly polar majority diene components. They found that removing the substrate pinning effect using a buffer layer of PS brushes acted to increase the correlation length in these systems significantly during the thermal annealing step.[71] With the use of chemical surface patterns (Section 1.8.4) Welander et al. has shown that using a very high temperature thermal anneal (~250 °C) can reduce the amount of time required for defect-free self-assembly from many hours to minutes, which is similar to post-exposure bake times for a typical photoresist.[72]

### *1.8.2 Solvent Annealing*

There are other ways to gain polymer mobility without using heat. Infusion of a polymer film with solvent vapor also acts to increase polymer mobility. The solvent vapor molecules effectively act as a plasticizer, which decreases the polymer's $T_g$ and allows high mobility to occur even at room temperature. Furthermore, the solvent evaporation front from a thin film is highly directional, usually in the direction normal to the substrate. Thus, as the solvent evaporates from the top of the film towards the bottom, domains tend to orient in the same direction, inducing alignment of anisotropic microdomains normal to the direction of solvent evaporation, as illustrated in Figure 1.5. Kim and Libera have shown that the evaporation rate of the solvent-infused film has a strong bearing on the orientation of BC cylinders in a PS-*b*-PB-*b*-PS triblock copolymer [PB=poly(butadiene)].[73] Very slow solvent evaporation rates (0.2

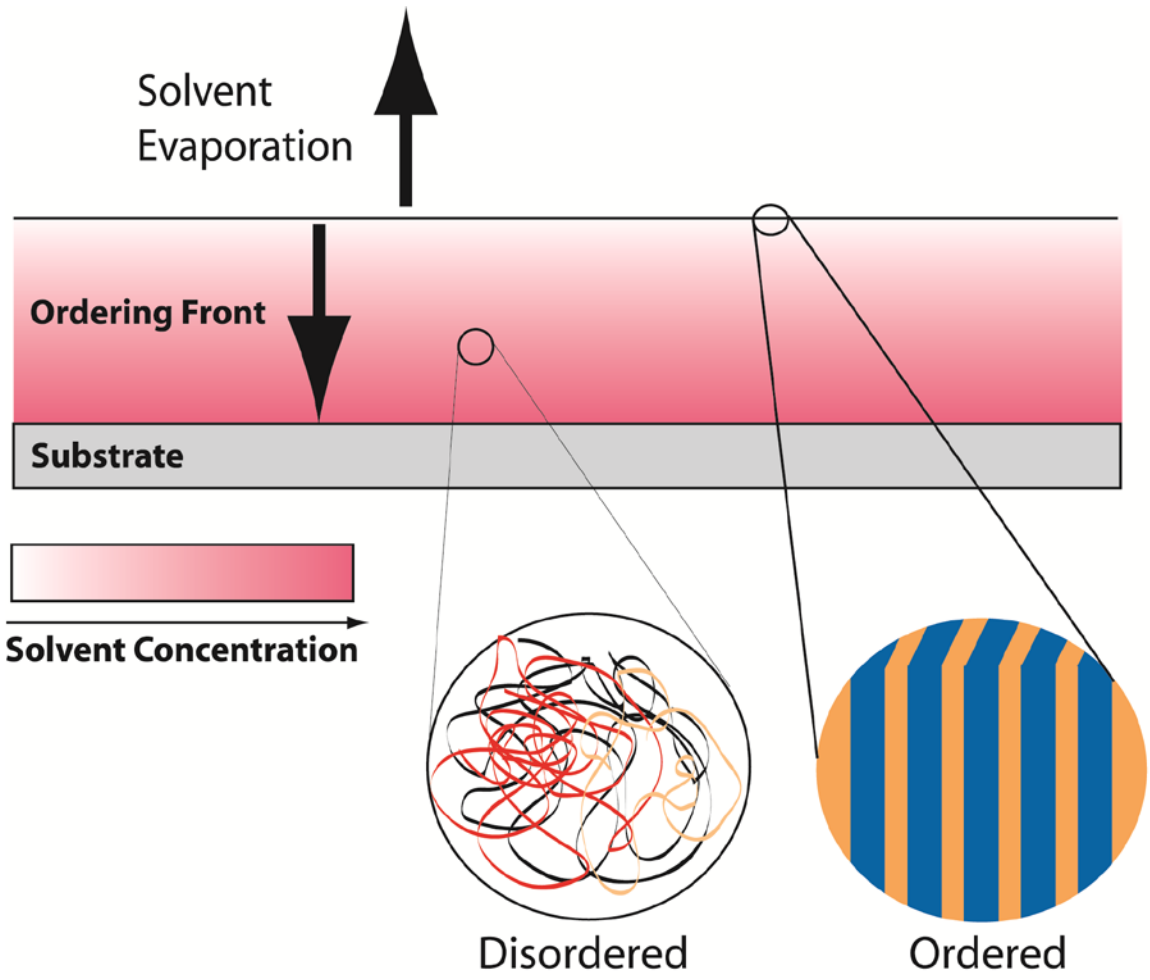


Figure 1.5. An illustration of the evaporation of solvent vapor from a polymer film, resulting in an ordering front moving from the top surface of the film down towards the substrate. Adapted from Ref. 74.

nL/sec) induced in-plane formation of cylinders, intermediate evaporation (5 nL/sec) produced vertical orientation of cylinders, while fast evaporation (200 nL/sec) resulted in a vertical microphase separated structure with poor long range order.

Strongly segregating block pairs such as PS-*b*-PEO are capable of extremely low defect densities after exposure to solvent vapor. In one example, 5 $\mu m^2$ single grains of vertically oriented cylinders have been achieved by exposing PS-*b*-PEO to an atmosphere of benzene and water for two days.[74] Solvent annealing techniques may significantly reduce the turnaround time for well-ordered BC domains. In specific, the industry would prefer the ability to process one wafer per minute.[75] Recently, in the effort to reduce the amount of time required to achieve well-ordered microdomains, well-ordered PS-*b*-PEO films were formed immediately from spin coating in a solvent-vapor saturated spin coating chamber of toluene and water. [76] Other variables, such as pressure, or different types of vapor-based solvents such as supercritical $CO_2$ have not yet been fully explored.[77]

### *1.8.3 Topography-Assisted Self-Assembly*

As discussed earlier, the substrate surface supporting the block copolymer film has a very large effect on the orientation and ordering of the microdomain pattern. BC microdomain arrays can also be templated by topographic surface patterns. The surface patterns can induce an epitaxial growth of the microdomain "grains" from the bottom to the top of the film. The first example of this principle occurring in the literature came from Fasolka and coworkers, who used a corrugated silicon surface to demonstrate the formation of vertically-oriented lamellae of PS-*b*-PnBMA, where PnBMA stands for poly(n-butyl methacrylate).[78] The corrugation, originating from the faceting transformation of a slightly misoriented Si(113) surface, acted to modulate the film thickness periodically across the substrate. With the film thickness greater than

$L_o/2$, the lamellae oriented parallel to the film surface, as seen from a lack of features in a top-view AFM micrograph. When the film thickness became less than $L_o/2$, lamellar PnBMA columns oriented perpendicular to the substrate, as discussed in Section 1.7.

Topographic surface relief patterns can also improve the long-range order of BC microdomain ordering. In a simple experiment, Segalman and coworkers confined films of PS-*b*-P2VP in microfabricated silica trenches many times larger than the domain period of the block copolymer. The BC was spin coated over these trenches, and thermally annealed at 180 °C for 72 hours. Inside the trench, they found the BC was able to form single crystals of up to 4.5 μm in width in both the trenches and the mesas.[79] In both the trenches and mesas, it was discovered that the single grain of spheres grew epitaxially from the boundary edges towards the center of the patterned feature. If the mesa areas were larger than 5 μm, areas of disorder would appear in the center of the mesa.

Since this initial work, the process of using top-down topographic pre-patterns to physically constrain block copolymers, also known as templated self-assembly (TSA) has expanded dramatically.[80] Ross and coworkers have published studies that quantified the effect of TSA on BC ordering. They have found that if the trench width does not match up perfectly to an ideal integer multiple of the period of the block copolymer, the periodicity of the microdomains will compress or expand to fit the trench to minimize the free energy of pattern formation.[81] However, the number of rows of block copolymer domains (N) that fit inside the trench width (W) transitions from N to (N+1) when $W \approx (N+0.5)*d$, where d is the equilibrium period spacing of the polymer.[82] They also quantified the increase in positional accuracy of sphere-forming PS-*b*-PFS block copolymers confined in trenches via correlation length measurements, finding that the edge roughness of the patterned trenches and inherent

fluctuations in the size of the microdomains both contribute to ~3nm of positional error in the microdomains.[83] The authors noted that this positional error is within the tolerance for bit-patterned media.[84]

### *1.8.4. Chemically Nanopatterned Surfaces*

Heterogeneous chemical surface patterns can also act as guides for the formation of well-ordered BC microdomain arrays. In an early work by Rockford and coworkers, alternating stripes of gold and $SiO_x$ were produced by grazing incidence thermal evaporation of gold on a miscut silicon wafer surface. By spin coating lamellar PS-*b*-PMMA over the top of these patterns and thermally annealing, they found that vertically oriented microdomains, with the corrugated substrate acting as a guide for perfect long-range order and the alternating chemical surface patterns used for vertical orientations of the block copolymer.[85] They also found that matching the period of the surface patterns with the block copolymer periodicity was important to produce low defect density films. For thick films, a mismatch between these two dimensions of greater than ±10% caused a loss in orientational control of the microdomains.[86] Recently, this technique was revisited when a miscut sapphire crystal surface with a grazing incidence of gold evaporation was used to orient 4 $cm^2$ sized grains of PS-*b*-PEO, as shown in Figure 1.6.[87]

The Nealey group from the University of Wisconsin has focused on using lithographically-defined chemical patterns to direct the self-assembly of PS-*b*-PMMA. In the first paper from the Nealey group in this area, they patterned a photoresist using extreme ultraviolet interferometric lithography (EUV-IL) and transferred the resist pattern into an underlying hydrophobic self-assembled monolayer (SAM). The resulting substrate featured nanopatterned stripes of nonpolar/polar regions which could be used as a strong surface field to attract the PS and PMMA domains,

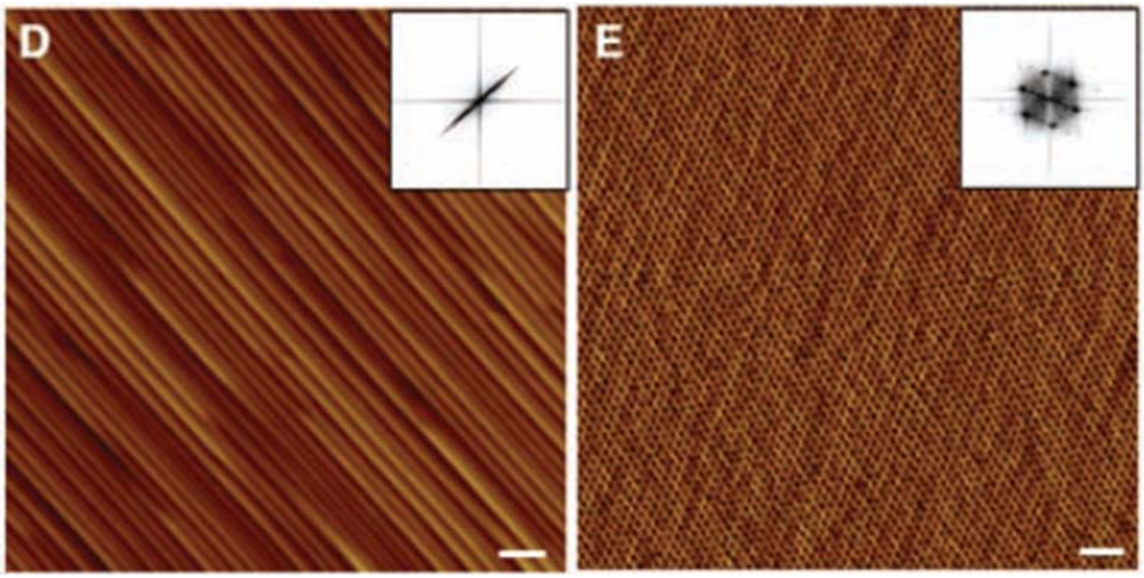


Figure 1.6. AFM images showing how a miscut sapphire surface (D) acts as a guide for benzene vapor-annealed PS-*b*-PEO block copolymer domains in (E). Reprinted from Ref. 87 with permission from AAAS.

respectively, of a lamellar PS-*b*-PMMA polymer over micron sized areas.[88] Since then the Nealey group has moved towards the use of traditional UV lithography for patterning purposes. Stoykovich and coworkers have shown that vertical lamellae can be directed around the sharp bend and jog structures typical of a microelectronic circuit.[89] In the case of sharp bends, the block copolymer pattern required the addition of PMMA homopolymer into the BC, which preferentially segregated to areas of high pattern curvature to alleviate the bending stress of the PMMA domain. However, in this work, the block copolymer merely replicates the underlying lithographically defined surface pattern, thereby gaining no advantage in terms of resolution.

#### *1.8.4.1 Density Multiplication using Chemical Surface Patterns*

Recently, the concept of "density multiplication" has been introduced into this sub-family of block copolymer orientation control. In this approach, lithographically-defined chemical surface patterns with wavelengths over twice that of the block copolymer period were used for templating. After printing these "sparse" patterns, consisting of alternating stripes of neutral and a PMMA-selective negative-tone resist, a lamellar PS-*b*-PMMA block copolymer was spin coated on top and used to subdivide the lithographically defined patterns, essentially doubling, tripling, or quadrupling the frequency of the patterns.[90] The patterns were placed on a regular lattice such that every other PMMA lamellae encounters the chemical pattern, as shown in Figure 1.7. Due to the strong interactions between the blocks and the sparse chemical surface pattern, the block copolymer was able to correct the defects in the original lithographically-defined surface while still doubling the frequency of the original pattern. Frequency doubling and "pattern-rectification" of cylindrical PS-*b*-PMMA oriented normal to the surface was used to create well-ordered hexagonal arrays of holes for bit-patterned media applications.[91] The ordering of spherical PS-*b*-

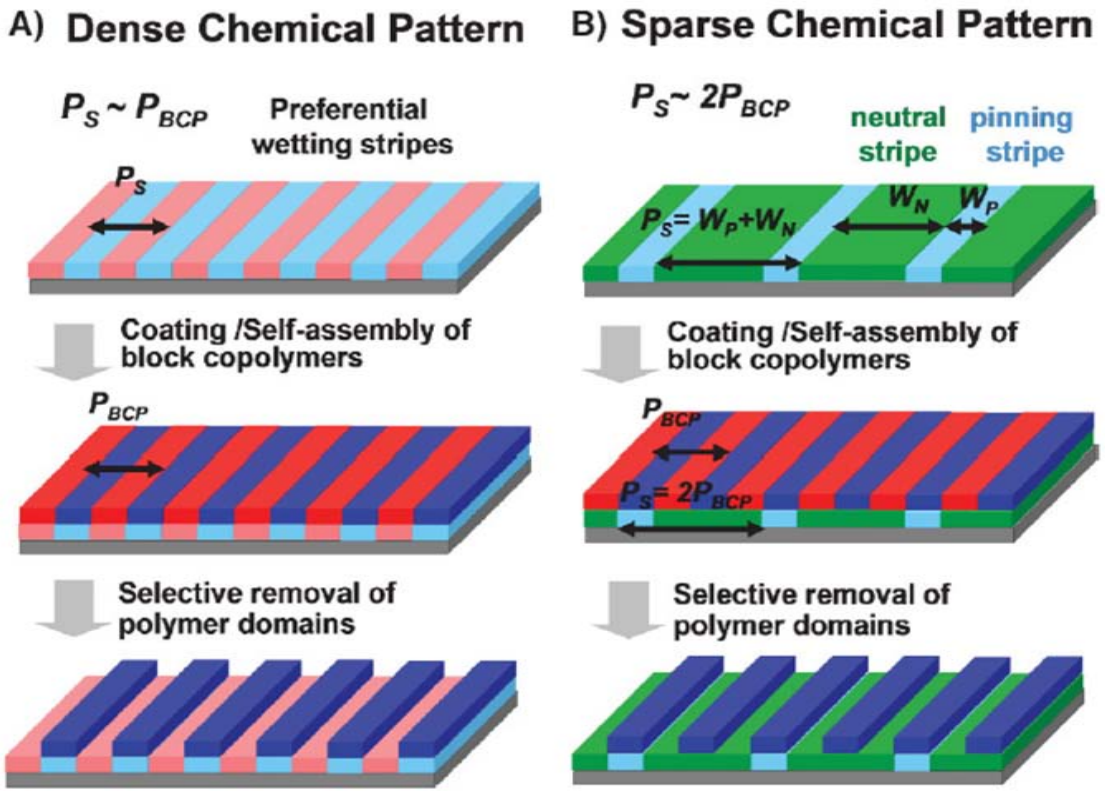


Figure 1.7. Illustration defining two different approaches for chemical surface patterning, employing dense (a) and sparse (b) chemical patterns to template block copolymers. Reprinted with permission from Ref. 90. Copyright Wiley-VCH Verlag GmbH & Co. KGaA.

PDMS has also been aided by a density multiplication technique, further proving the generality of this approach.[92]

### *1.9 Crosslinking the Self-Assembled Matrix*

After the block copolymer has achieved the desired level of lateral order, the self-assembled matrix must be photo-physically fixed before the minority phase is removed in order to avoid pattern collapse. In this case, the dramatic difference in the photo-speed of the PS crosslinking (25 J/cm$^2$) versus the PMMA degradation (3.4 J/cm$^2$) is one of the main drawbacks of using PS-*b*-PMMA for lithographic applications. Other material options have been explored as well.

#### *1.9.1 Thermal Curing Approach*

In Hawker's research group, then at IBM, the PS block was randomly polymerized with a vinylbenzocyclobutene (BCB) block, which was designed to crosslink efficiently with the PS block via a simple thermal curing step.[93,94] The BCB block undergoes a ring-opening mechanism and forms ring structures with other neighboring BCB molecules by heating to temperatures between 180 and 250 °C. This high temperature crosslinking step was performed after the annealing of the block copolymer at 170 °C to improve long-range order, but before the removal of the PMMA domain. Therefore, the PS-*ran*-BCB block could be covalently stabilized without the use of a high UV exposure dose, which improves the manufacturability of this system.

#### *1.9.2 Chemical Amplified Block Copolymer Lithography (CABL)*

Several research groups have realized the benefit of incorporating chemically amplified resist technology into block copolymer lithography. Chemical amplification

refers to the use of photoacid generating molecules in resist films, which produce acid when exposed to UV light and depend on a brief post-exposure bake in order to initiate a cascade of chemical reactions that spread homogenously through the film.[95] In the case of a positive-tone resist, the initial acid species is used to deprotect an acid-labile protecting group, which makes the exposed region more soluble in a developer solvent. In the case of a negative-tone resist, the acid catalyzes a condensation reaction between a crosslinking resin and a hydroxy or carboxy-containing resist species.[96]

Ober and coworkers have synthesized a block copolymer containing a negative-tone photoresist, poly(4-hydroxystyrene), as the majority phase for high quantum-yield UV crosslinking reactions with blended photoactive compounds.[97,98] The directly patternable block copolymer, poly(α-methylstyrene-*block*-4-hydroxystyrene) (PαMS-*b*-PHOST), can also be made into a nanoporous system through removal of the minority PαMS domain via a thermal depolymerization mechanism.[99] By exposing the spin-coated film to solvent vapor to orient the microdomains and then crosslinking using photolithography, this system affords the precise placement of well-ordered self-assembled structures. [100] In addition, Bosworth et al. demonstrated the ability to create multiple morphologies on the same resist layer by photo-physically fixing one solvent annealed area of the film and changing the other with a selective solvent.[101] The use of UV light could play a major in block copolymer lithographic applications that require precise placement of the self-assembled templates anywhere on a wafer.

### *1.10 Selective Domain Removal using Dry Etch Techniques*

Often block copolymers containing chemically distinct blocks can be treated in a reactive ion etching process that is selective towards one of the blocks. The vulnerable block is quickly converted to volatile products upon exposure to high-

energy ion plasmas. In an RIE process, the ions are accelerated towards the surface of the sample and can produce a much more anisotropic etch profile compared to a wet chemical etch. On impact with the surface of the wafer, the highly energetic ions can chemically react with the polymer film, and can also transfer their kinetic energy to physically remove material via a sputtering mechanism.

When it comes to RIE, not all polymers are created equal. In a now famous work, it was found that the etch rate of polymers in an RIE process depends critically on the carbon and oxygen content in a polymer. [104] The so called 'Ohnishi parameter' quantifies the etch rate ($R_{etch}$), as given by

$$R_{etch} \propto \frac{N}{N_c - N_o} \ , \qquad \text{[Eq. 1.4]}$$

where N is equal to the total number of atoms in a monomer unit, $N_c$ the number of carbon atoms in the monomer, and $N_o$ the number of oxygen atoms in the monomer. Several groups have taken advantage of this relation in order to selectively etch polymers containing a high percentage of oxygen molecules, such as methacrylates relative to styrenes.[105]

One of the most elegant examples of the use of dry etch techniques for nanolithography comes from one of the first journal articles about block copolymer lithography, introduced by Park and coworkers from Princeton University in 1997.[9] In this pioneering work, a monolayer of poly(styrene-*block*-butadiene) (PS-*b*-PB) was used to create positive tone “holes” and negative tone “nanopillars” on a silicon nitride substrate depending on the processing technique used to process the PB block.

In the first approach, diene containing blocks such as PB can be degraded upon exposure to ozone gas. The highly reactive ozone molecules attack carbon-carbon double bonds, cutting the linkages and converting the polymer into butadiene monomer, which can easily be dispersed in water. The resulting nanostructure consisted of a periodic array of $1.3 \times 10^{11}$ holes per square centimeter in a PS matrix

which could then be used as an etch mask for an underlying silicon nitride substrate.

The second approach demonstrated the ability to switch the durability of the PB block under RIE conditions. In the inverse process, the reactive double bonds in PB can be stained with a heavy metal vapor of osmium tetroxide, dramatically increasing the polymer's $CF_4/O_2$ etch resistance relative to the PS matrix (~2:1 etch ratio of PS: osmium-stained PB). This enabled the creation of Si nanopillars, which foresaw later applications of BC's for patterning high-density magnetic media.

### *1.11 Improving Etch Resistance*

Research in the block copolymer community has also focused on the incorporation of inorganic content into block copolymer structures to increase the etch resistance of the matrix phase and enable deeper etch into the substrate, leading to higher aspect ratios. The three methods that have been used in the literature are a) direct polymerization of an inorganic-containing monomer into a block copolymer architecture, b) growing inorganic nanoparticles into an already existing block copolymer using a "nanoreactor" scheme, or c) blending inorganic molecules in solution with the block copolymer.

#### *1.11.1 Polymerization of Monomers Containing Inorganics*

In the first approach, block copolymers are synthesized with an inorganic-containing monomer, often containing iron or silicon. Lammertink and coworkers have specialized in the synthesis of block copolymers incorporating poly(ferrocenyldimethylsilane) (PFS), an organo-metallic polymer consisting of alternating dimethylsilane and ferrocene units, using ring-opening anionic polymerization.[106-110] By creating BC's such as PI-*b*-PFS, with a minority phase PFS, they have showed the ability to form thin BC films exhibiting organo-metallic "dots"

packed in regular arrays. They used $O_2$ RIE plasma to accomplish this, in which the iron in the PFS is much more stable to the plasma than the carbon in the BC. In fact, the PFS phase forms an etch barrier on exposure to oxygen plasma due to the creation of an oxide layer at the surface of the polymer, as determined by Auger electron spectroscopy (AES). These results are coincident with other studies on the oxygen plasma removal of thin polymer films. After the formation of the oxide layer, the etch rate is determined by the competition between the oxide growth and oxide removal by ion sputtering, leading to a 40:1 PI:PFS etch selectivity towards the PI block, as determined by the respective homopolymer etch rates. Thus, the inorganic dots can act as conformal masks for high-aspect ratio etching into semiconductors such as silicon or gallium arsenide.[109]

### *1.11.2 Block Copolymers as Inorganic Nanoreactors*

In the second approach, block copolymers are used as 'nanoreactors' for the synthesis of inorganic components within one of the phases. In one example, the ability of poly(2-vinyl pyridine)(P2VP) to complex with metal clusters or nanoparticles was exploited to produce inorganic clusters. Haupt and coworkers dissolved PS-*b*-P2VP and a gold salt in a selective solvent to form micelles in solution, which were then dip coated onto a gallium arsenide substrate. The gold salt was selectively solubilized into the P2VP core, which acted as a nanoreactor for the formation of gold clusters upon exposure to oxygen plasma. Hydrogen plasma was then used to remove the organic content, resulting in an array of gold dots on the substrate.[111]

### *1.11.3 Selective Blending of Inorganic Macromolecules*

The third approach is based on blending inorganic macromolecules into one

block of the BC. Through this simple approach, a highly stable template can form with an extremely high etch resistance within one of its phases. Silicon-containing polymers are good candidates for these 'one-step lithography' applications using BC's, due also to their ability to form etch barriers upon exposure to oxygen plasma. In one example of this approach, Freer and coworkers have blended PS-*b*-PEO with methyl silsesquioxane (MSSQ), which is a partially condensed copolymer of methyl trimethoxysilane and tetraethoxy silane.[112] The MSSQ blended selectively into the PEO phase, and the authors generated cylindrical and spherical morphologies by changing the BC:MSSQ ratio or by changing the PEO block length. Solvent annealing followed by crosslinking the MSSQ phase through a high-temperature bake step allowed for the formation of highly stable, perpendicularly oriented cylinder nano-templates that could be used for patterning applications, as shown in Figure 1.8. In a separate paper using the same principle, vertical lamellae with a 20-nm half-pitch were used to pattern lines into silicon using a low-power $CF_4$ plasma etch.[113] Through a simple blending approach with amphiphilic block copolymers, high-aspect ratio nanostructures with good etch resistance were easily prepared.

### *1.12 Pattern Transfer and Applications*

Once a nanoporous template is created on the wafer, it can be used as a stencil to scribe patterns into an underlying functional substrate. Typically, an RIE with fluorinated gases such as $SF_6$, $CF_4$ are used to etch into silicon. There have been a few applications demonstrating the industrial feasibility of using BC's to make high-performance functional devices.

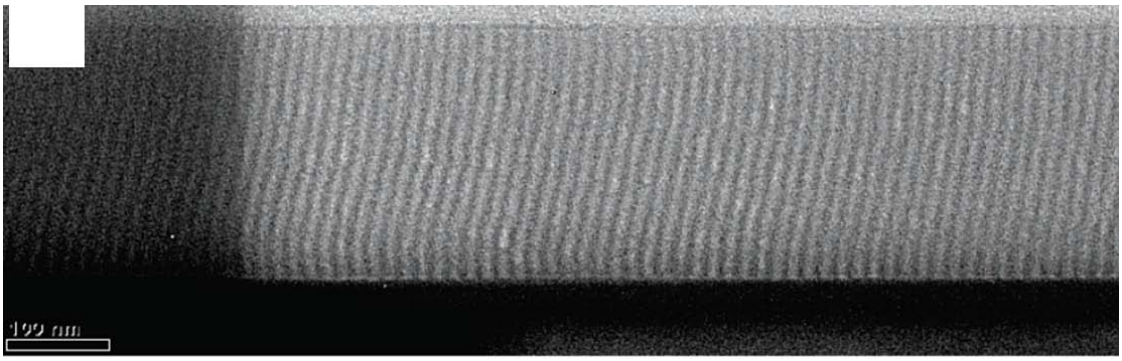


Figure 1.8. A PS-*b*-PEO film loaded with an organosilicate polymer and solvent annealed formed vertically oriented domains throughout the depth of the film. Reprinted with permission from Ref. 112. Copyright 2005 American Chemical Society.

### *1.12.1 MOS Capacitors*

Black and Guarini have demonstrated the use of PS-*b*-PMMA to increase the charge storage capacity of a metal oxide semiconductor (MOS) capacitor, as shown in Figure 1.9. The overall idea was to increase the device surface area using the block copolymer as an etch mask to form the electrode topography.[65] After processing PS-*b*-PMMA in the usual way to leave a crosslinked PS matrix with a hexagonal array of holes, an $SF_6$ etch was used to create etch pits in the underlying silicon. These etch pits were later covered with aluminum as a gate electrode followed by thermally grown silicon dioxide to form the dielectric layer. They found that the increase in surface area gained by the BC template improved the capacitance by 30%, although doubling the etch depth would have improved device capacitance by up to 115%, based on theoretical calculations.

### *1.12.2 Bit-Patterned Media*

Several research groups have investigated the possibility of using block copolymer microdomains as templates for high-density bit patterned media.[114] This application requires perfect registration of the block copolymer microdomains, which translates into addressable locations for the read/write head of a magnetic hard drive. The cost to produce one fab-size 8” wafer with tolerable defect densities would be very high, assuming the use of an e-beam patterned sparse chemical surface pattern. However, the rewards would be great. For example, using a PS-*b*-PMMA block copolymer with a 20nm domain spacing would create magnetic domain densities of greater than 1 terabit per square inch.[91]

### *1.12.3 IBM's Airgap Insulation Approach*

In reality, the difficulty in achieving perfect registration of the block copolymer

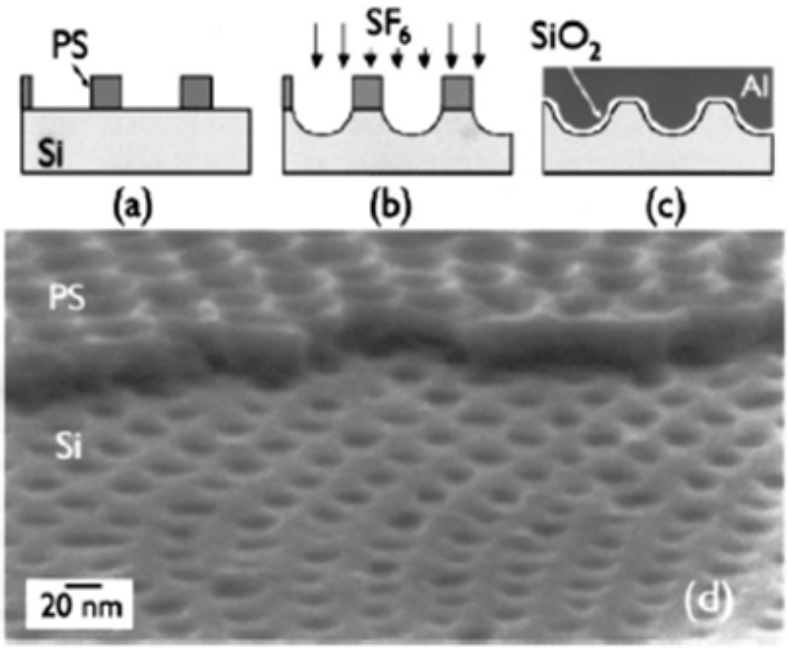


Figure 1.9. Process flow for BC-based MOS capacitor. a) Polymer template formation on silicon surface. b) RIE pattern transfer of PS template into Si, followed by removal of PS matrix. c) Al electrode deposition followed by $SiO_2$ growth. d) SEM image at 70° tilt. Reprinted with permission from Ref. 65. Copyright 2001, American Institute of Physics.

domains over large areas has limited the industrial use of nanoporous block copolymers to applications that depend more on pore size uniformity rather than long-range lateral ordering. IBM's recent “Airgap” technology is one example of this approach, in which PS-*b*-PMMA is used to create a nanoporous membrane that can be used to create vacuum insulation as a low-k dielectric in between current-carrying wires. In this case, the polymer does not need to be perfectly ordered, the pores just need to traverse the entire film thickness. They have shown that the Airgap process enables the electrical signals on the chip to travel 35 percent faster and reduces the power load by 15 percent compared to similar chips processed using conventional techniques.[115] Other devices have also been demonstrated, such as nanocrystal flash memory devices, where the dimensions, density and uniformity of the nanocrystals are defined by the polymer self assembly.[116]

### *1.13 Outlook and Future Perspectives*

The field of block copolymer lithography has accelerated dramatically in the past ten years, and shows no signs of slowing as the industry moves towards sub-20 nm feature sizes. At this size scale, companies will become more and more interested in low-cost methods that do not require heavy investments in material and labor-intensive processes.[118]

The challenges facing directed self-assembly for insertion into sub-22nm node technology were discussed in a recent review by Daniel Herr of the Semiconductor Research Corporation.[75] Of the challenges mentioned in this article, perhaps the largest challenge and most fundamental weakness of block copolymers is their inability to print arbitrary lines anywhere on a wafer. However, research is on track to remedy this weakness with increasing amounts of control over the positional placement of the block copolymer domains. Researchers are learning how to

maneuver block copolymer morphology into simple device geometries such as jogs, bends, and t-shaped junctions using lithographic pre-patterning techniques such as sparse chemical templates.[80, 89, 90]

Chemical nanopatterning approaches have been shown to produce isolated lines using self-assembly, as revealed in Figure 1.10.[119] The main drawback for the density multiplication approaches is that the fabrication of the chemically patterned underlayer adds dramatically to the cost of the process. However, it may be more industrially feasible to worry about the perfection of one "master" template and use it for the patterning of another polymer via a nanoimprint-type approach, as demonstrated by several research groups.[120,121] A thorough cost/benefit analysis for each type of technology must be performed by the semiconductor industry before insertion into a sub-22nm technology window.

Using photochemistry may be a more elegant solution to the problem of placing self-assembled patterns anywhere on a wafer. Work from the Ober group on a lithographically patternable block copolymer system, PαMS-*b*-PHOST, enables precise placement of the self-assembled patterns using traditional photolithography to crosslink the block copolymer in select areas of the wafer and may lead to the formation of an isolated small bundle of cylinders or lamellae via photochemical crosslinking.[98]

The ability to fabricate with multiple sizes and pitches within one resist layer may be possible using this system, similar to work shown by Bosworth et al.[101] While it has already been shown that solvent annealing using non-selective solvents can be used to enhance long-range order of this system,[100] it may also be possible to use selective solvents to swell individual microdomains to tailor the microdomain size, or if the swollen block is a majority component, the pitch of the block copolymer. Blended functional photoactive compounds in this system allows the swollen

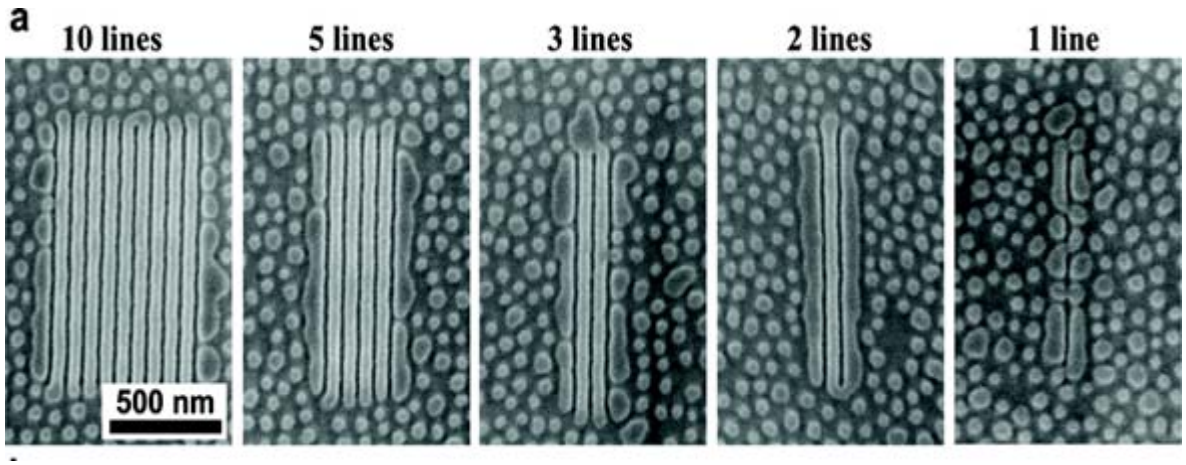


Figure 1.10. Directed assembly of the PS/PMMA ternary blend into isolated segment structures. (a) Top-down SEM images of isolated segment structures are shown for 10, 5, 3, 2, and 1 lines that have LS = 70 nm and are 1 μm in length. The number of lines represents the number of PMMA-preferential lines in the surface pattern and therefore the number of perpendicular PMMA domains that were assembled on the surface pattern. The isolated PMMA segment structures are dark gray or black and are sandwiched between light gray PS domains. Reprinted with permission from Ref. 119. Copyright 2007, American Chemical Society.

structures to be photo-physically fixed before moving on to the next size structure.

Other functionalities may also be possible for future generations of lithography, such as the incorporation of a conducting polymer domain, or a microdomain that could be "photophysically active." In one example of this approach, photo-active azobenzene pendant groups were attached to a PS-*b*-PEO block copolymer. With the help of a hexane solvent anneal for mobility and the cis-trans conformational switch of the azobenzene mesogens, the researchers were able to orient the parallel-oriented cylinders in the same direction of a linearly polarized light source [122] Perhaps such a focused light beam could also be used to guide block copolymers into arbitrary shapes and patterns?

Block copolymer processing techniques have advanced to the point that is possible to produce zero defects over large areas.[91] However, there is plenty of room for improvement of block copolymer orientation in the third dimension. We have yet to learn how to stack block copolymer layers on top of each other to create integrated gate and contact features, although this principle may have great impact on the device community. Difficulty arises when trying to spin coat one block copolymer over the top of another due to the two resist layers intermingling after exposure to the spin coating solvent of the upper layer. Recent work has been published in the area of organic electronics that may provide some insight into a solution for this problem, using the principle of orthogonal solvent systems.[123] In this work, highly chemically sensitive light-emitting organic materials were patterned into a crossbar architecture without any damage to the material, as proven by fluorescence microscopy. This technique of orthogonality requires the chemical synthesis of macromolecules that will not dissolve in typical organic solvents, such as water-soluble or fluorinated block copolymers, both of which have been demonstrated before.[124,125]

Outside the field of lithography, elegant solutions in the field of electronic

materials may emerge that does not require multiple spin coating steps to form multiple layers of patterned morphologies. For example, linear diblock copolymers may form complex 3-D structures such as the gyroid and double gyroid phase, which have been rigorously studied by the energy community for solar and fuel cell applications, but may also be interesting for the semiconductor industry for the heat dissipation of increasingly power-hungry microprocessors.[17] Triblock copolymers with star-shaped architectures have been demonstrated to form interconnected cylinders between lamellar phases, which could be built-in contact and gate structures if replaced by functional polymers.[12] One could envision using these complex 3-D architectures to create hetero-junctions between two metals, by selective removal of each phase followed by an electro-deposition, similar to work that has already been done by Aizawa and coworkers.[126] Whether or not these exciting technologies will become widely used in semiconductor manufacturing or used only for niche applications remains to be seen, but fundamental research in this area will undoubtedly continue in the years to come.

## REFERENCES


1. Rothschild, M.; Bloomstein, T. M.; Kunz, R. R.; Liberman, V.; Switkes, M.; Palmacci, S. T.; Sedlacek, J. H. C.; Hardy, D.; Grenville, A. *J. Vac. Sci. Tech. B* **2004**, *22*, 2877.
2. Mack, C. A. *Future Fab International* **2007**, *23*, 65.
3. Wu, B.; Kumar, A. *J. Vac. Sci. Tech. B* **2007**, *25*, 1743.
4. Schift, H. *J. Vac. Sci. Tech. B* **2008**, *26*, 458.
5. Whitesides, G. M.; Grzybowski, B. *Science (Washington, DC, United States)* **2002**, *295*, 2418-2421.
6. Wallraff, G. M.; Hinsberg, W. D. *Chemical Reviews (Washington, D. C.)* **1999**, *99*, 1801-1821.
7. Lee, J. S. H., A.; Nakahama, S. *Macromolecules* **1989**, *22*, 2602.
8. Mansky, P.; Chaikin, P.; Thomas, E. L. *Journal of Materials Science* **1995**, *30*, 1987-92.
9. Park, M.; Harrison, C.; Chaikin, P. M.; Register, R. A.; Adamson, D. H. *Science (Washington, D. C.)* **1997**, *276*, 1401-1404.
10. Bates, F. S.; Fredrickson, G. H. *Physics Today* **1999**, *52*, 32-38.
11. Chen, H.-Y.; Fredrickson, G. H. *Journal of Chemical Physics* **2002**, *116*, 1137-1146.
12. Hayashida, K.; Saito, N.; Arai, S.; Takano, A.; Tanaka, N.; Matsushita, Y. *Macromolecules* **2007**, *40*, 3695-3699.
13. Elbs, H.; Drummer, C.; Abetz, V.; Krausch, G. *Macromolecules* **2002**, *35*, 5570-5577.
14. Breiner, U.; Krappe, U.; Stadler, R. *Macromolecular Rapid Communications* **1996**, *17*, 567-575.
15. Guo, S.; Rzayev, J.; Bailey, T. S.; Zalusky, A. S.; Olayo-Valles, R.; Hillmyer,

M. A. *Chem. Mater.* **2006**, *18*, 1719-1721.

16. Hayashida, K.; Takano, A.; Arai, S.; Shinohara, Y.; Amemiya, Y.; Matsushita, Y. *Macromolecules* **2006**, *39*, 9402-9408.
17. Crossland, E. J. W.; Kamperman, M.; Nedelcu, M.; Ducati, C.; Wiesner, U.; Smilgies, D. M.; Toombes, G. E. S.; Hillmyer, M. A.; Ludwigs, S.; Steiner, U.; Snaith, H. J. *Nano Letters* **2009**, *9*, 2807-2812.
18. Abetz, V. S., P. F. W *Adv. Polym. Sci* **2005**, *189*, 125-212.
19. Bucholz, T. L.; Loo, Y. L. *Macromolecules* **2006**, *39*, 6075.
20. Cochran, E. W.; Garcia-Cervera, C. J.; Frederickson, G. H. *Macromolecules* **2006**, *39*, 2449-2451.
21. Hsieh, H. Q., R. *Anionic Polymerization: Principles and Practical Applications*; Marcel Dekker, Inc.: New York, NY, 1996.
22. Matyjaszewski, K.; Xia, J. *Chemical Reviews (Washington, D. C.)* **2001**, *101*, 2921-2990.
23. Hadjichristidis, N. P., M.; Iatrou, H. *Adv. Polym. Sci.* **2005**, *189*, 124.
24. Xu, T.; Kim, H. C.; DeRouchey, J.; Seney, C.; Levesque, C.; Martin, P.; Stafford, C. M.; Russell, T. P. *Polymer* **2001**, *42*, 9091-9095.
25. Matsen, M. W.; Bates, F. S. *Macromolecules* **1996**, *29*, 1091-8.
26. Sivaniah, E.; Matsubara, S.; Zhao, Y.; Hashimoto, T.; Fukunaga, K.; Kramer, E. J.; Mates, T. E. *Macromolecules* **2008**, *41*, 2584.
27. Thurn-Albrecht, T.; Steiner, R.; DeRouchey, J.; Stafford, C. M.; Huang, E.; Bal, M.; Tuominen, M.; Hawker, C. J.; Russell, T. P. *Advanced Materials (Weinheim, Germany)* **2000**, *12*, 787-790.
28. Guillet, J. *Polymer photophysics and photochemistry: an introduction to the study of photoprocesses in macromolecules*; Cambridge University Press: Cambridge, UK, 1985.

29. Park, S. M.; Craig, G. S. W.; La, Y.-H.; Solak, H. H.; Nealey, P. F. *Macromolecules* **2007**, *40*, 5084-5094.

30. Tang, C.; Lennon, E. M.; Frederickson, G. H.; Kramer, E. J.; Hawker, C. J. *Science* **2008**, *322*, 429.

31. International Technology Roadmap for Semiconductors (ITRS), 2007 Available at www.itrs.net.

32. Garner, M. C.; Herr, D.; Krautschik, C.; ITRS, 2007.

33. Broseta, D.; Fredrickson, G. H.; Helfand, E.; Leibler, L. *Macromolecules* **1990**, *23*, 132-9.

34. Helfand, E.; Sapse, A. M. *Journal of Chemical Physics* **1975**, *62*, 1327-31.

35. Helfand, E.; Tagami, Y. *Journal of Chemical Physics* **1972**, *56*, 3592-601.

36. Russell, T. P.; Hjelm, R. P., Jr.; Seeger, P. A. *Macromolecules* **1990**, *23*, 890-3.

37. Anastasiadis, S. H.; Russell, T. P.; Satija, S. K.; Majkrzak, C. F. *Physical Review Letters* **1989**, *62*, 1852-5.

38. Kim, S. H.; Misner, M. J.; Xu, T.; Kimura, M.; Russell, T. P. *Advanced Materials (Weinheim, Germany)* **2004**, *16*, 226-231.

39. Frielinghaus, H.; Hermsdorf, N.; Almdal, K.; Mortensen, K.; Messe, L.; Corvazier, L.; Fairclough, J. P. A.; Ryan, A. J.; Olmsted, P. D.; Hamley, I. W. *Europhys. Lett.* **2001**, *53*, 680.

40. Hammond, M. R.; Cochran, E.; Frederickson, G. H.; Kramer, E. J. *Macromolecules* **2005**, *38*, 6575.

41. Nose, T. *Polymer* **1995**, *36*, 2243.

42. Fairclough, J. P. A.; Yu, G.-E.; Mai, S.-M.; Crothers, M.; Mortensen, K.; Ryan, A. J.; Booth, C. *Phys. Chem. Chem. Phys.* **2000**, *2*, 1503-1507.

43. Tirumala, V. R. P., R. A.; Agarwal, S.; Testa, J. J.; Bhatnagar, G.; Romang, A. H.; Chandler, C.; Gorman, B.P.; Jones, R. L.; Lin, E. K.; Watkins, J. J. *Chem.*

*Mater.* **2007**, *19*, 5868-5874.

44. Bang, J.; Kim, S. H.; Drockenmuller, E.; Misner, M. J.; Russell, T. P.; Hawker, C. J. *Journal of the American Chemical Society* **2006**, *128*, 7622-7629.
45. Lynd, N. A.; Hillmyer, M. A. *Macromolecules* **2005**, *38*, 8803-8810.
46. Lynd, N. A.; Hillmyer, M. A. *Macromolecules* **2007**, *40*, 8050-8055.
47. Ruiz, R.; Sandstrom, R. L.; Black, C. T. *Advanced Materials (Weinheim, Germany)* **2007**, *19*, 587-591.
48. Jeong, U.; Kim, H.-C.; Rodriguez, R. L.; Tsai, I. Y.; Stafford, C. M.; Kim, J. K.; Hawker, C. J.; Russell, T. P. *Advanced Materials (Weinheim, Germany)* **2002**, *14*, 274-276.
49. Kim, S. H.; Misner, M. J.; Russell, T. P. *Adv. Mater.* **2004**, *16*, 2119.
50. Jeong, U.; Ryu, D. Y.; Kim, J. K.; Kim, D. H.; Russell, T. P.; Hawker, C. J. *Advanced Materials (Weinheim, Germany)* **2003**, *15*, 1247-1250.
51. Ikkala, O.; Ten Brinke, G. *Chem. Commun.* **2004**, *2004*, 2131-2137.
52. Ruokolainen, J.; Saariaho, M.; Ikkala, O.; Ten Brinke, G.; Thomas, E. L.; Torkkeli, M.; Serimaa, R. *Macromolecules* **1999**, *32*, 1152-1158.
53. Sidorenko, A.; Tokarev, I.; Minko, S.; Stamm, M. *JACS* **2003**, *125*, 12211-12216.
54. Fasolka, M. J.; Mayes, A. M. *Annual Review of Materials Research* **2001**, *31*, 323-355.
55. Segalman, R. A.; Schaefer, K. E.; Fredrickson, G. H.; Kramer, E. J.; Magonov, S. *Macromolecules* **2003**, *36*, 4498-4506.
56. Knoll, A.; Horvat, A.; Lyakhova, K. S.; Krausch, G.; Sevink, G. J. A.; Zvelindovsky, A. V.; Magerle, R. *Phys. Rev. Lett. J1 - PRL* **2002**, *89*, 035501.
57. Russell, T. P.; Menelle, A.; Anastasiadis, S. H.; Satija, S. K.; Majkrzak, C. F. *Macromolecules* **1991**, *24*, 6263-9.

58. Papadakis, C. M.; Busch, P.; Posselt, D.; Smilgies, D.-M. *Advances in Solid State Physics* **2004**, *44*, 327-338.

59. Mansky, P.; Liu, Y.; Huang, E.; Russell, T. P.; Hawker, C. *Science (Washington, D. C.)* **1997**, *275*, 1458-1460.

60. Huang, E.; Rockford, L.; Tussell, T. P.; Hawker, C. J. *Nature (London)* **1998**, *395*, 757-758.

61. Han, E.; Stuen, K. O.; Leolukman, M.; Liu, C.-C.; Nealey, P. F.; Gopalan, P. *Macromolecules* **2009**, *42*, 4896-4901.

62. In, I.; La, Y.-H.; Park, S. M.; Nealey, P. F.; Gopalan, P. *Langmuir* **2006**, *22*, 7855-7860.

63. Jeong, U.; Ryu, D. Y.; Kho, D. H.; Kim, J. K.; Goldbach, J. T.; Kim, D. H.; Russell, T. P. *Advanced Materials (Weinheim, Germany)* **2004**, *16*, 533-536.

64. Kitano, H.; Akasaka, S.; Inoue, T.; Chen, F.; Takenaka, M.; Hasegawa, H.; Yoshida, H.; Nagano, H. *Langmuir* **2007**, *23*, 6404-6410.

65. Black, C. T.; Guarini, K. W.; Milkove, K. R.; Baker, S. M.; Russell, T. P.; Tuominen, M. T. *Applied Physics Letters* **2001**, *79*, 409-411.

66. Hammond, M. R.; Cochran, E.; Fredrickson, G. H.; Kramer, E. J. *Macromolecules* **2005**, *38*, 6575-6585.

67. Black, C. T.; Ruiz, R.; Breyta, G.; Cheng, J. Y.; Colburn, M. E.; Guarini, K.; Kim, H.-C.; Zhang, Y. *IBM J. Res. Develop.* **2007**, *51*, 605-633.

68. Harrison, C.; Adamson, D. H.; Cheng, Z.; Sebastian, J. M.; Sethuraman, S.; Huse, D. A.; Register, R. A.; Chaikin, P. M. *Science (Washington, D. C.)* **2000**, *290*, 1558-1561.

69. Harrison, C.; Cheng, Z. D.; Sethuraman, S.; Huse, D. A.; Chaikin, P.; Vega, D. A.; Sebastian, J. M.; Register, R.; Adamson, D. H. *Phys. Rev. E* **2002**, *66*, 011706.

70. Harrison, C.; Angelescu, D. E.; Trawick, M.; Cheng, Z.; Huse, D. A.; Chaikin, P. M.; Vega, D. A.; Sebastian, J. M.; Register, R. A.; Adamson, D. H. *Europhysics Letters* **2004**, *67*, 800-806.

71. Harrison, C.; Chaikin, P. M.; Huse, D. A.; Register, R. A.; Adamson, D. H.; Daniel, A.; Huang, E.; Mansky, P.; Russell, T. P.; Hawker, C. J.; Egolf, D. A.; Melnikov, I. V.; Bodenschatz, E. *Macromolecules* **2000**, *33*, 857-865.

72. Welander, A.; Kang, H.; Stuen, K. O.; Solak, H. H.; Muller, M.; De Pablo, J. J.; Nealey, P. F. *Macromolecules* **2008**, *41*, 2759.

73. Kim, G.; Libera, M. *Macromolecules* **1998**, *31*, 2569-2577.

74. Kim, S. H.; Misner, M. J.; Xu, T.; Kimura, M.; Russell, T. P. *Advanced Materials (Weinheim, Germany)* **2004**, *16*, 226-231.

75. Herr, D. J. C. *Future Fab International* **2007**, *22*, 69-71.

76. Kim, S.; Briber, R. M.; Karim, A.; Jones, R. L.; Kim, H.-C. *Macromolecules* **2007**, *40*, 4102-4105.

77. RamachandraRao, V. G., Ravi; Watkins, James J.; Satija, S. *Polymeric Materials Science and Engineering* **2001**, *84*, 206.

78. Fasolka, M. J.; Harris, D. J.; Mayes, A. M.; Yoon, M.; Mochrie, S. G. J. *Phys. Rev. Lett. J1 - PRL* **1997**, *79*, 3018-3021.

79. Segalman, R. A.; Yokoyama, H.; Kramer, E. J. *Advanced Materials (Weinheim, Germany)* **2001**, *13*, 1152-1155.

80. Cheng, J. Y.; Ross, C. A.; Smith, H. I.; Thomas, E. L. *Adv. Mater.* **2006**, *18*, 2505-2521.

81. Cheng, J. Y.; Ross, C. A.; Thomas, E. L.; Smith, H. I.; Vancso, G. J. *Advanced Materials (Weinheim, Germany)* **2003**, *15*, 1599-1602.

82. Cheng, J. Y.; Mayes, A. M.; Ross, C. A. *Nature Materials* **2004**, *3*, 823-828.

83. Cheng, J. Y.; Zhang, F.; Smith, H. I.; Vancso, G. J.; Ross, C. A. *Adv. Mater.*

**2006**, *18*, 597-601.

84. Moritz, J.; Buda, L.; Dieny, B.; Nozieres, J. P.; van de Veerdonk, R. J. M.; Crawford, T. M.; Weller, D. *Appl. Phys. Lett.* **2004**, *84*, 1519.

85. Rockford, L.; Liu, Y.; Mansky, P.; Russell, T. P.; Yoon, M.; Mochrie, S. G. J. *Phys. Rev. Lett. J1 - PRL* **1999**, *82*, 2602-2605.

86. Rockford, L.; Mochrie, S. G. J.; Russell, T. P. *Macromolecules* **2001**, *34*, 1487-1492.

87. Park, S.; Lee, D. H.; Xu, J.; Kim, B.; Hong, S. W.; Jeong, U.; Xu, T.; Russell, T. P. *Science* **2009**, *323*, 1030-1033.

88. Kim, S. O.; Solak, H. H.; Stoykovich, M. P.; Ferrier, N. J.; de Pablo, J. J.; Nealey, P. F. *Nature (London, United Kingdom)* **2003**, *424*, 411-414.

89. Stoykovich, M. P.; Mueller, M.; Kim, S. O.; Solak, H. H.; Edwards, E. W.; de Pablo, J. J.; Nealey, P. F. *Science (Washington, DC, United States)* **2005**, *308*, 1442-1446.

90. Cheng, J. Y.; Rettner, C. T.; Sanders, D. P.; Kim, H.-C.; Hinsberg, W. D. *Adv. Mater.* **2008**, *20*, 3155-3158.

91. Ruiz, R.; Kang, H.; Detcheverry, F. A.; Dobisz, E. A.; Kercher, D. S.; Albrecht, T. R.; de Pablo, J. J.; Nealey, P. F. *Science* **2008**, *321*, 936.

92. Bita, I.; Yang, J. K. W.; Jung, Y. S.; Ross, C. A.; Thomas, E. L.; Berggren, K. K. *Science* **2009**, *321*, 939.

93. Drockenmuller, E.; Li, L. Y. T.; Ryu, D. Y.; Harth, E.; Russell, T. P.; Kim, H.-C.; Hawker, C. J. *Journal of Polymer Science, Part A: Polymer Chemistry* **2005**, *43*, 1028-1037.

94. Leiston-Belanger, J. M.; Russell, T. P.; Drockenmuller, E.; Hawker, C. J. *Macromolecules* **2005**, *38*, 7676-7683.

95. Reichmanis, E.; Houlihan, F. M.; Nalamasu, O.; Neenan, T. X. *Chem. Mater.*

**1991**, *3*, 394-407.

96. Shaw, J. M. G., J. D. *IBM J. Res. Develop.* **1997**, *41*, 81.

97. Du, P.; Li, M.; Douki, K.; Li, X.; Garcia, C. B. W.; Jain, A.; Smilgies, D.-M.; Fetters, L. J.; Gruner, S. M.; Wiesner, U.; Ober, C. K. *Advanced Materials (Weinheim, Germany)* **2004**, *16*, 953-957.

98. Li, M.; Douki, K.; Goto, K.; Li, X.; Coenjarts, C.; Smilgies, D. M.; Ober, C. K. *Chemistry of Materials* **2004**, *16*, 3800-3808.

99. Madorsky, S. L. *Thermal degradation of organic polymers*; Interscience: New York, 1964.

100. Bosworth, J. K.; Ruiz, R.; Paik, M. Y.; Schwartz, E. L.; Huang, J. Q.; Ko, A. W.; Smilgies, D. M.; Black, C. T.; Ober, C. K. *ACS Nano* **2008**, *2*, 1396-1402.

101. Bosworth, J. K.; Black, C. T.; Ober, C. K. *ACS Nano* **2009**.

102. Kim, Y. J.; Kang, H.; Leolukman, M.; Nealey, P. F.; Gopalan, P. *Chem. Mater.* **2009**, *21*, 3030-3032.

103. Han, E.; In, I.; Park, S.-M.; La, Y.-H.; Wang, Y.; Nealey, P. F.; Gopalan, P. *Adv. Mater.* **2007**, *19*, 4448-4452.

104. Gokan, H.; Esho, S.; Ohnishi, Y. *J. Electrochem. Soc.* **1983**, *130*, 143.

105. Asakawa, K.; Hiraoka, T.; Hieda, H.; Sakurai, M.; Kamata, Y.; Naito, K. *Journal of Photopolymer Science and Technology* **2002**, *15*, 465-470.

106. Lammertink, R. G. H.; Hempenius, M. A.; Van Den Enk, J. E.; Chan, V. Z. H.; Thomas, E. L.; Vancso, G. J. *Advanced Materials (Weinheim, Germany)* **2000**, *12*, 98-103.

107. Lammertink, R. G. H.; Hempenius, M. A.; Chan, V. Z. H.; Thomas, E. L.; Vancso, G. J. *Chemistry of Materials* **2001**, *13*, 429-434.

108. Lammertink, R. G. H.; Hempenius, M. A.; Thomas, E. L.; Vancso, J. *Journal of Polymer Science, Part B: Polymer Physics* **1999**, *37*, 1009-1021.

109. Lammertink, R. G. H.; Hempenius, M. A.; Van Den Enk, J. E.; Chan, V. Z. H.; Thomas, E. L.; Vancso, G. J. *Advanced Materials (Weinheim, Germany)* **2000**, *12*, 98-103.

110. Lammertink, R. G. H.; Hempenius, M. A.; Vancso, G. J.; Shin, K.; Rafailovich, M. H.; Sokolov, J. *Macromolecules* **2001**, *34*, 942-950.

111. Haupt, M.; Miller, S.; Glass, R.; Arnold, M.; Sauer, R.; Thonke, K.; Moller, M.; Spatz, J. P. *Advanced Materials (Weinheim, Germany)* **2003**, *15*, 829-831.

112. Freer, E. M.; Krupp, L. E.; Hinsberg, W. D.; Rice, P. M.; Hedrick, J. L.; Cha, J. N.; Miller, R. D.; Kim, H.-C. *Nano Letters* **2005**, *5*, 2014-2018.

113. Sundstrom, L.; Krupp, L. E.; Delenia, E.; Rettner, C. T.; Sanchez, M.; Hart, M. W.; Kim, H.-C.; Zhang, Y. *Appl. Phys. Lett.* **2006**, *88*, 243107.

114. Cheng, J. Y.; Ross, C. A.; Chan, V. Z. H.; Thomas, E. L.; Lammertink, R. G. H.; Vancso, G. J. *Advanced Materials (Weinheim, Germany)* **2001**, *13*, 1174-1178.

115. IBM, “Using self assembly to create airgap microprocessors.” Press Release, URL: http://www-03.ibm.com/press/us/en/presskit/21463.wss. Accessed October, 2009.

116. Black, C. T.; Guarini, K. W.; Milkove, K. R.; Baker, S. M.; Russell, T. P.; Tuominen, M. T. *Applied Physics Letters* **2001**, *79*, 409-411.

117. Hand, A. In *Semiconductor International*; Semiconductor International, 2008; Vol. 2009.

118. Rice, B.; SEMATECH, Ed.; SEMATECH, 2009; Vol. 2009.

119. Stoykovich, M. P.; Kang, H.; Daoulas, K. C.; Liu, G.; Liu, C.-C.; de Pablo, J. J.; Muller, M.; Nealey, P. F. *ACS Nano* **2007**, *1*, 168-175.

120. Li, H.-W.; Huck, W. T. S. *Nano Letters* **2004**, *4*, 1633-1636.

121. Chuang, V. P.; Ross, C. A.; Gwyther, J.; Manners, I. *Adv. Mater.* **2009**, *21*,

3789-3793.

122. Morikawa, Y.; Nagano, S.; Watanabe, K.; Kamata, K.; Iyoda, T.; Seki, T. *Advanced Materials* **2006**, *18*, 883-886.

123. Lee, J.-K.; Chatzichristidi, M.; Zakhidov, A. A.; Taylor, P. G.; DeFranco, J. A.; Hwang, H. S.; Fong, H. H.; Holmes, A. B.; Malliaras, G. G.; Ober, C. K. *J. Am. Chem. Soc.* **2008**, *130*, 11564-11565.

124. Nakashima, K.; Bahadur, P. *Adv. Coll. Int. Sci.* **2006**, *123-126*, 75-96.

125. Hillmyer, M. A.; Lodge, T. P. *J. Polym. Sci., Part A: Polym. Chem.* **2002**, *40*, 1-8.

126. Aizawa, M.; Buriak, J. M. *Journal of the American Chemical Society* **2006**, *128*, 5877-5886.

# CHAPTER TWO:

## SELF-ASSEMBLY OF MOLECULAR GLASS PHOTORESISTS USING NON-IONIC TRIBLOCK COPOLYMER SURFACTANTS*

* E. Schwartz, C. Chandler, V. Daga, J. Watkins, C. K. Ober. *To be submitted.*

### *2.1 Introduction*

The construction of microcircuitry relies on a technique called photolithography in order to define device layouts at the sub-micron scale. Photolithography refers to the process of exposing a radiation-sensitive polymeric material with ultraviolet light through a photomask, which contains a positive or negative replica of the patterns of lines and spaces that make up the final device layout. Current state-of-the-art photolithography uses a concept called 'chemical amplification' to convert ultraviolet photons into a chemical change in the polymer matrix. The materials that enable this conversion are called photoacid generators (PAGs), which contain a chromophore designed to absorb at the wavelength used for patterning, and will generate a strong acid that changes the solubility of neighboring reactive polymers in a developing solvent.[1] These systems require a thermal bake step in order for the PAG to diffuse through the polymer film and to carry out the solubility switch. The higher sensitivity gained by this approach usually comes at the expense of a loss in pattern fidelity, resulting from the excessive acid diffusion caused by the bake step and higher roughness in the patterned lines, relative to the initial photomask pattern, which is also usually produced using photolithography. These difficulties are compounded at the increasingly small resolutions required for the miniaturization of circuit geometries and concomitant increase in circuit density. So far, the industry has successfully commercialized a fabrication process using critical dimensions with a 45 nanometer half-pitch as of the time of this writing. [2] However, for sub-20 nanometer fabrication it appears as if traditional chemically amplified photoresists can no longer keep up with the pace of miniaturization, and new, innovative materials systems are required in order to advance into future eras of microfabrication.

Block copolymer self-assembly is one of the techniques under consideration to extend the range of high-resolution patterning.[3] Block copolymers are two chemically

distinct polymers connected in series by a covalent bond. In essence, the formation of mesoscopic features (10-100 nm) in a block copolymer is a thermodynamic phenomenon stemming from a balance of enthalpic and entropic forces in the melt.[4] These two forces are the repulsive force which opposes the mixing of the two kinds of polymer chains and the force of chain elasticity which pulls the chains back into a random coil configuration. The manipulation of a few variables, such as molecular weight, volume fraction, and the degree of incompatibility between the blocks, allows sufficient control over the size and shape of functional polymer units. For example, a decrease in the molecular weight of the block copolymer system will reduce the microdomain spacing, which is a common goal in block copolymer design for the lithography community.

Semiconductor materials suppliers are now aware of block copolymers after several recent laboratory successes, some of which have been successfully commercialized. In one example, simple surfactant macromolecules, such as poly(ethylene oxide-*block*-propylene oxide-*block*-ethylene oxide) (PEO-*b*-PPO-*b*-PEO, Pluronic$^{TM}$) have been used as sacrificial templates to create low-dielectric constant materials.[5, 6] In this approach, metal alkoxide or organic precursors are dissolved within the hydrophilic phase of the block copolymer in solution. With the addition of an acid catalyst, which also segregates to the hydrophilic phase, sol-gel reactions are allowed to take place within this template as the mixture evaporates, creating a progressively increasing concentration of surfactant and driving the organization of the precursors into liquid crystalline mesophases.[7] Finally, removal of the block copolymer template leaves behind a mesoporous framework of the formed reactant species.[8] This approach has been extended to produce metal oxide networks,[9] thermosetting epoxy resin,[10] and mesoporous carbon frameworks based on resol or formaldehyde precursors.[11,12]

A separate approach at the intersection of the field of block copolymers and semiconductor electronics uses the block copolymer as a lithographic template to replicate self-assembled morphologies into semiconductor substrates.[13] In one significant example of this approach, Li et al. integrated two levels of patternability into a single block copolymer system through the use of a high quantum yield negative-tone photoresist as the majority block of the block copolymer. [14] Using traditional resist chemistry, the authors fabricated 450nm photopatterns using the PHOST in the block copolymer as a photoresist and then used an additional development step to remove a degradable minority block within those photopatterns, creating a nanoporous stencil pattern.

Recently, Tirumala and coworkers have demonstrated this same principle by blending hydrogen-bonding additives, such as poly(4-hydroxystyrene) (PHOST) and poly(acrylic acid) (PAA), into PEO-containing triblock copolymer surfactants such as the surfactant systems mentioned above.[15,16] Without the blended additives, the blocks in the surfactant macromolecule were too weakly segregated for microphase segregation. However, with the additives, the resulting increase in repulsive interactions between the blocks allowed the block copolymer to undergo a disorder-order transition, which formed cylindrical and spherical phases with sub-20 nanometer resolution. In this work, we propose a similar approach, using instead a phenolic 'molecular glass' photoresist (MG2OH) as the blended additive, as shown in Figure 2.1.The crosslinking of the MG2OH within the Pluronic template should allow for a stabilization of the self-assembled morphology. Furthermore, the monodispersity and small molecular size (1-2 nm) of MG2OH should allow for more accurate pattern fidelity of the host triblock copolymer surfactant template, relative to their homopolymer counterparts.[17]

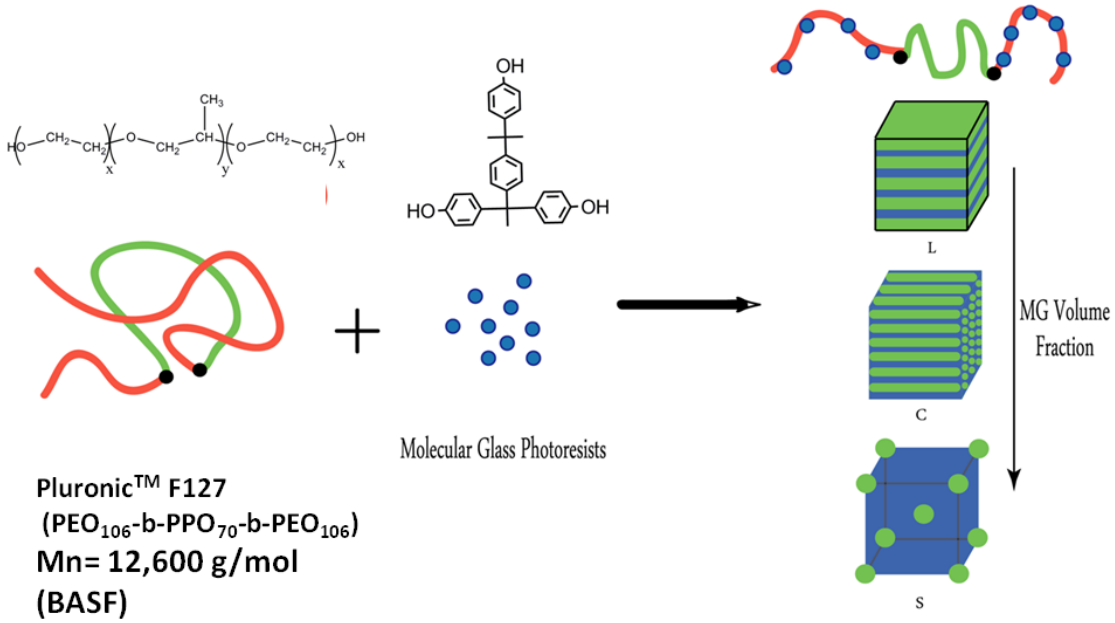


Figure 2.1. Schematic showing the concept of molecular glass templating using amphiphilic block copolymers, adapted from reference 16.

### *2.2 Experimental Methods*

#### *2.2.1 Materials*

Pluronic™ F127 ("PF127," $M_n$ = 12,600 g/mol, 70 wt% PEO), which has the structure PEO-*b*-PPO-*b*-PEO (PEO= poly(ethylene oxide) and PPO= poly(propylene oxide), was supplied as a gift from the BASF Corporation (Parsippany, NJ). α,α,α-tris(4-hydroxyphenyl)-1-ethyl-4-isopropylbenzene (MG2OH) were obtained from TCI America, ethanol (Pharmco), tetrakis(methoxymethyl)glycoluril (TMMGU, "Powderlink 1174," Cytec) and triphenylsulfonium triflate (TPST, Aldrich) were all purchased and used as received. Prime grade <100> silicon wafers <100> were obtained through Wafer Reclaim Services (WRS, Spring City, PA).

#### *2.2.2 Thin Film Preparation*

Silicon wafers were cleaved into small squares (3 $cm^2$) and covered with a freshly mixed piranha solution (7:3 $H_2SO4$:$H_2O_2$) heated at 70 °C (CAUTION: Extremely corrosive!) for 30 minutes in order to remove any organic contamination from the substrate. The pieces were then washed with copious amounts of water and soaked in a bath of ethanol:DI $H_2O$ (1:1, v/v) for 2 hours to completely oxygenate the surface. They were then washed with acetone and isopropanol and dried with a stream of dry nitrogen.

Crosslinked and single domain-thickness films of the F127/MG2OH system were prepared by spin coating 0.5 to 2 wt% solutions dissolved in 1:1 EtOH: ethyl acetate (v/v). The TMMGU crosslinking agent and TPST acid catalyst were added in varying amounts from 0 - 15 wt% and 5 wt%, respectively, and relative to the total mass of Pluronic/MG2OH in the solution. AFM images of the samples were obtained immediately afterwards. For MG2OH crosslinking, the wafers were exposed to a 248nm flood exposure using a JBA-1000 cure lamp (15 $mW/cm^2$), and then baked at

various temperatures immediately afterwards. To determine the effectiveness of the crosslinking step, each sample was soaked for 30 minutes in methanol, and the film thicknesses were then re-measured to verify the formation of a crosslinked network.

### *2.2.3 Characterization*

Film thickness was measured using a Woollam spectroscopic ellipsometer. Atomic force microscopy (AFM) was performed on a Veeco Dimension 3100 scanning force microscope operated in tapping mode under ambient conditions. Olympus OMCL-AC160-TS cantilever tips were used during operation (spring constant = 42 N/m, frequency = 300 kHz, tip radius < 10 nm).

For FTIR sample preparation, each specimen was prepared by drying the solution containing a MG2OH/F127 blend for 1 week at 55 °C under vacuum to remove all trace of solvent and water in the samples. After drying, these samples were added in 1 wt. % to dry KBr powder and pressed into a disc 13 mm in diameter and 1.5 – 2 mm in thickness. FTIR spectra were collected on a Mattson spectrometer using a wavenumber range from 400 to 4000 $cm^{-1}$, with a nominal resolution of 2 $cm^{-1}$. For each spectrum, 64 scans were collected and averaged.

Thermal analysis was performed on a TA Q1000 modulated differential scanning calorimeter (DSC). About 10 mg of the blend sample was placed in aluminum pans and heated from -50 °C to 150 °C at a 10 °C/minute heating rate to erase the thermal history, cooled, and then heated again. Data was acquired on the final heating ramp. An empty aluminum pan was used as a reference.

Small angle X-ray scattering (SAXS) experiments were performed at the W.M. Keck Nanostructures Laboratory at the University of Massachusetts Amherst using Rigaku-Molecular Metrology SAXS instrumentation (CuK$\alpha$, $\lambda = 0.1542$ nm) equipped with a 2-D wire array detector at a distance of 1.5 m from the sample.

Samples were prepared by casting from solutions of ethanol and ethyl acetate onto glass slides and drying overnight under vacuum at 80 °C. The blends were then packed into 1 mm thick washers and sealed between Kapton film. Data was acquired for 45 min for each sample set at either 80 or 25 °C under vacuum after thermal equilibration of at least 2 h. The resulting scattering data was azimuthally averaged and represented in plots of the arbitrary intensity versus the magnitude of the scattering vector, $q$, where $q = (4\pi/\lambda) \sin(\theta)$ and $2\theta$ is the scattering angle.

### *2.3 Results and Discussion*

#### *2.3.1 Thermal Analysis*

The key to the molecular glass templating concept is the localization of the functional molecular glass (MG2OH) molecule in the hydrophilic phase of the triblock copolymer. To confirm the selective blending of MG2OH with PEO, measurements of the effect of intermolecular interactions were performed using DSC. PEO is a semi-crystalline polymer miscible with many other polar molecules, so it was our hypothesis that a small phenolic molecule such as MG2OH could be blended with PEO.[18, 19] Figure 2.2 shows the DSC exothermic data of heat flow vs. temperature for increasing MG2OH content mixed with Pluronic F127 (PF127), relative to the total F127 weight. Neat PF127 shows an endothermic, well-defined PEO melting point ($T_m$) at 57 °C, as measured from the lowest point of the curve. The PEO melting curve becomes less well-defined and $T_m$ decreased monotonically as the MG2OH concentration was increased, as shown in Figure 2.2(b). From the monotonic decrease in $T_m$, the $\chi$ parameter for the PF127/MG2OH can be found to be equal to $-3.7 \times 10^{-4}$, indicating a thermodynamically miscible system (c.f. Appendix 2.6). Additionally, by integrating the area under each melting peak, the enthalpy of melting, $\Delta H_m$, for the PEO/MG2OH blend can be determined. This revealed a trend where $\Delta H_m$ decreased

linearly above ten percent MG2OH loading, as shown in Figure 2.2(c). We hypothesize that below 10 wt. %, the MG2OH additive molecules in the PEO domains may act as nucleation sites for crystallization, while above 10 % loading, the MG2OH still was able to nucleate crystals, but also acted to disturb the packing of the PEO polymer chains. At 60 wt. % MG2OH loading, the crystallization peak of the PEO was absent. Further evidence of the nucleation effect was found by noting the increase of the crystallization temperature ($T_c$) (or decrease in supercooling ($\Delta T$) necessary to form crystals) as the concentration of MG2OH rose.[20]

Blends of miscible polymeric systems typically show a single glass transition temperature which follows the Flory-Fox equation. A separate analysis of a pure PEO homopolymer/MG2OH blend showed a single $T_g$ value that increased with increasing concentration of MG2OH (c.f Appendix 2.6). The $T_g$ was only evident above 20%, possibly because the high degree of PEO crystallinity obscured the amorphous transition. The $T_g$ of the 30 wt.% MG2OH blend in PEO was -46 °C and increased to43 °C and -36 °C for the 40 wt.% and 50% MG2OH concentrations, respectively. The values approximately related to the Flory-Fox equation since the $T_g$ of PEO is equal to -59 °C and the MG2OH is equal to 94 °C. The above observations indicated miscibility between MG2OH and PEO. The specific nature of the intermolecular interactions will be discussed in the next section.

### *2.3.2 Evidence for Hydrogen Bonding*

The FTIR spectra of MG2OH, PF127, and their respective blends were obtained to verify the nature of the association between the phenolic MG2OH and PF127. All spectra are presented in Figure 2.3(a). The strong peak from 1050 to 1150 $cm^{-1}$ originated from the asymmetric stretching of the C-O-C bonds in both the PPO

a)

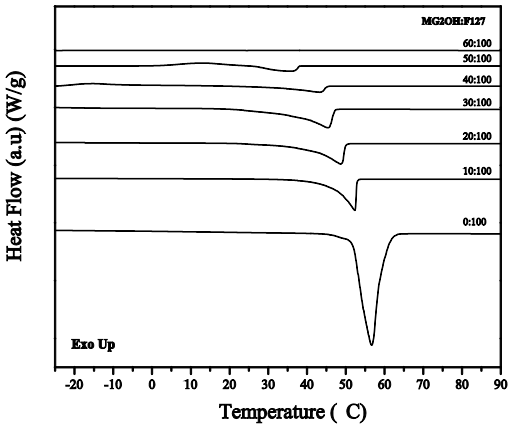


b)

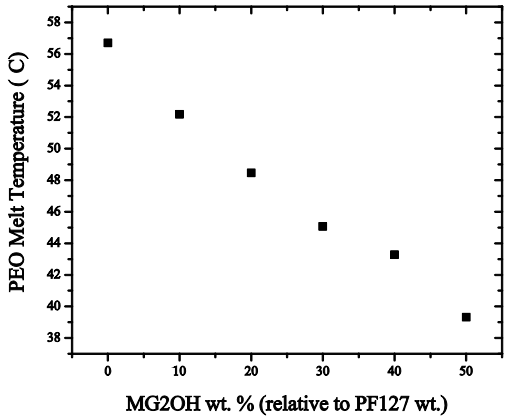


c)

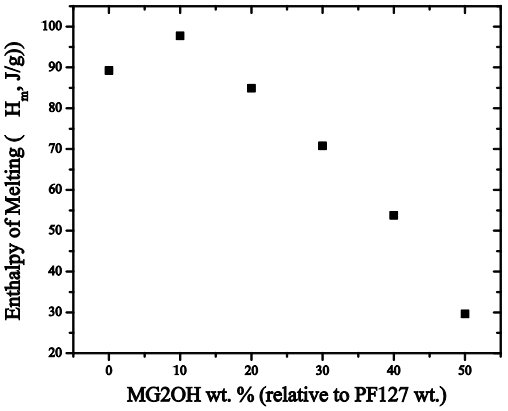


Figure 2.2. a) DSC overlay of the F127/MG2OH blends, b) the linear decrease in PEO melting temperature, and c) the decrease in the heat of melting, $\Delta H_m$ with increasing MG2OH loading

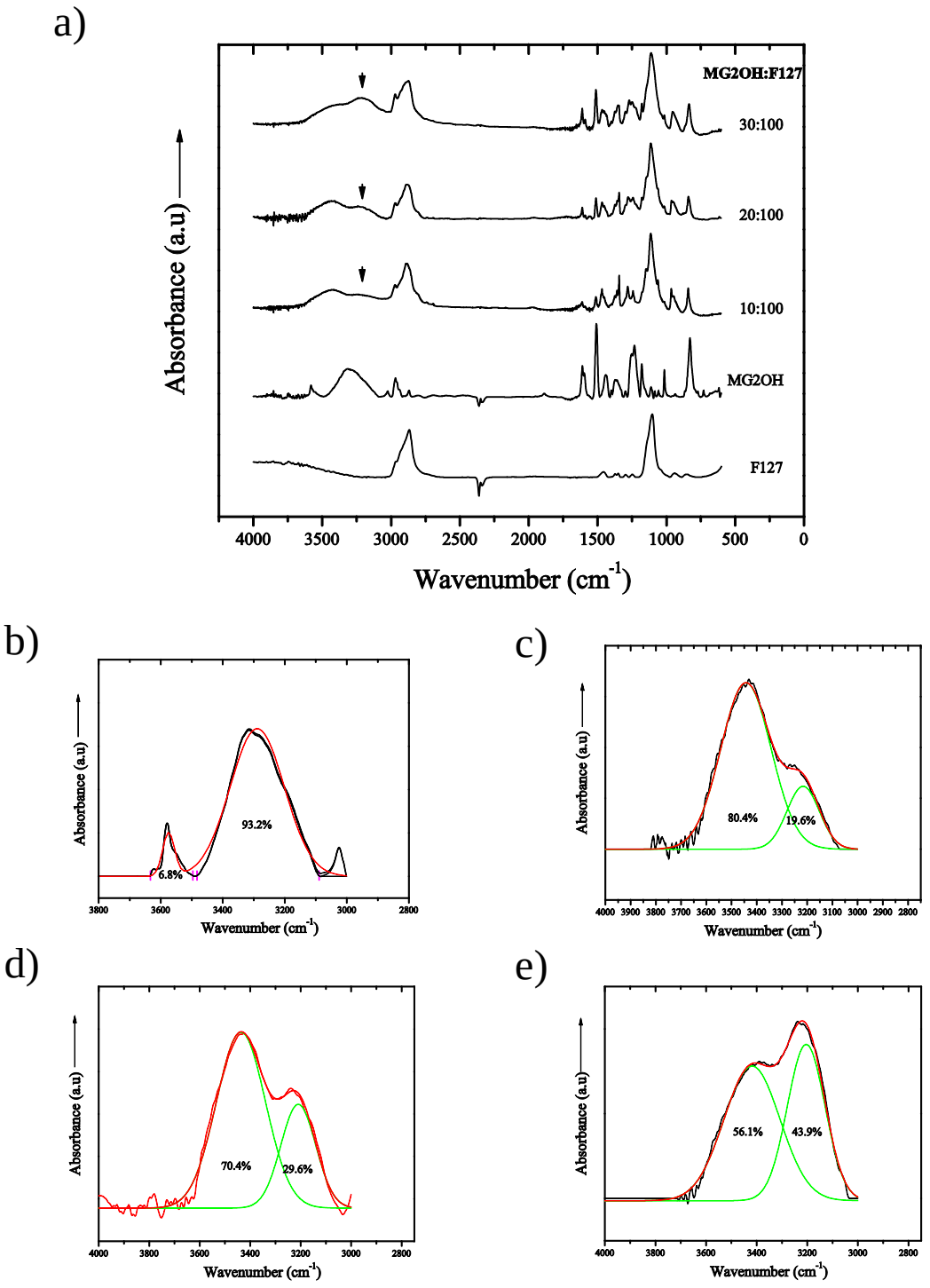


Figure 2.3. a) FTIR spectra overlay of F127, MG2OH and MG2OH:F127 blend compositions. (b-e) magnified –OH stretching region, showing fitted Gaussian peaks and relative area contributions from both self-associated MG2OH interactions (3415 $cm^{-1}$) and intermolecular (-OH---O-C) hydrogen bonding (3200 $cm^{-1}$).

and PEO blocks. These peaks appear broadened in the blend samples, while the peak at 960 $cm^{-1}$representing the helical structure of PEO, remained unchanged.[21] In the –OH region, pure MG2OH showed two peaks, one of which is a broad peak at 3300 $cm^{-1}$, and is ascribed to self-associated hydroxyl groups, and the other is a small peak at 3575 $cm^{-1}$ corresponding to non-associated "free" hydroxyl groups. In the case of the blends, we observed two overlapping peaks at 3200 and 3415 $cm^{-1}$, which are ascribed to the intermolecular hydrogen bonding of the MG2OH to the ether oxygen of the PEO phase, and the self-associated hydroxyl groups in the MG2OH, respectively. By fitting each one of these peaks using a Gaussian line shape and integrating the area under each curve, we noticed that the intermolecular association of the –OH groups in the MG2OH to the ether oxygen in the PEO domain grew stronger with the increasing concentration of MG2OH in the blend, relative to the peak corresponding to the self-associated MG2OH.[22] The relative area of this peak increased from 19.6 % to 43.9 % from the 10 wt. % to the 30 wt. % MG2OH/F127 blend, as shown in Figure 2.3(b-e), indicating increasing amount of hydrogen-bonding between MG2OH and PEO with increasing amounts of MG2OH in the blend.

### *2.3.3 Bulk Microstructure Analysis*

PEO crystallites are disadvantageous for our application since they may obscure or disrupt the morphology of the copolymer microdomains. If the blend is used for photolithography the three-dimensional spherulites would cause optical distortion and loss of resolution in the final developed patterns. Also, the PEO crystallization process may expel the photoacid generator out of the hydrophilic phase. Therefore, it was our best interest to remove crystallization by increasing the MG2OH concentration as much as possible.

As previously mentioned, the effective segregation strength of typically

disordered nonionic surfactants can be increased through the addition of such PEO-selective polymeric additives as PAA or PHOST.[16] Here we show the enhanced segregation strength of PF127 in the presence of the MG2OH molecule. The small characteristic domain size of block copolymers in addition to the electron density difference between the blocks made them well-suited to analysis using small angle x-ray scattering (SAXS) techniques. SAXS can be used to determine overall blend segregation strength, domain spacing, and ordered morphologies of the block copolymers in the bulk. This data was collected with the help of Curran Chandler of the University of Massachusetts, and presented here because it confirmed the bulk microstructure of the blends in the best possible way.

Figure 2.4 shows the SAXS profiles of MG2OH/F127 blends at two different temperatures, reported in arbitrary units of intensity. At room temperature, the samples with 20 and 30 wt. % MG2OH showed a sharp decrease in the full-width at half-maximum of the primary peak, in addition to the appearance of a second order reflection at $\sqrt{3}q^*$, indicative of a well-segregated, ordered cylindrical morphology. This peak width is related to the overall interfacial width of the domains and can be used to qualitatively assess changes in the segregation strength of the blend. The lack of a second order peak at the 40 wt. % MG2OH concentration suggests that the blend was driven back to disorder at higher additive concentrations as the system became overloaded with MG2OH. This is an important point, because although PEO crystallization was dramatically reduced via the addition of MG2OH, there was a limit to how much was possible to add before the ordered morphology was lost. Furthermore, Figure 2.4(b) shows that when PF127/MG2OH blends were heated to 80 °C, the system became disordered at all concentrations of MG2OH, as demonstrated by the broad primary scattering peak centered at ($q$*=0.55), and the loss of the second order peak. Additional scattering profiles of the copolymers blended with TMMGU,

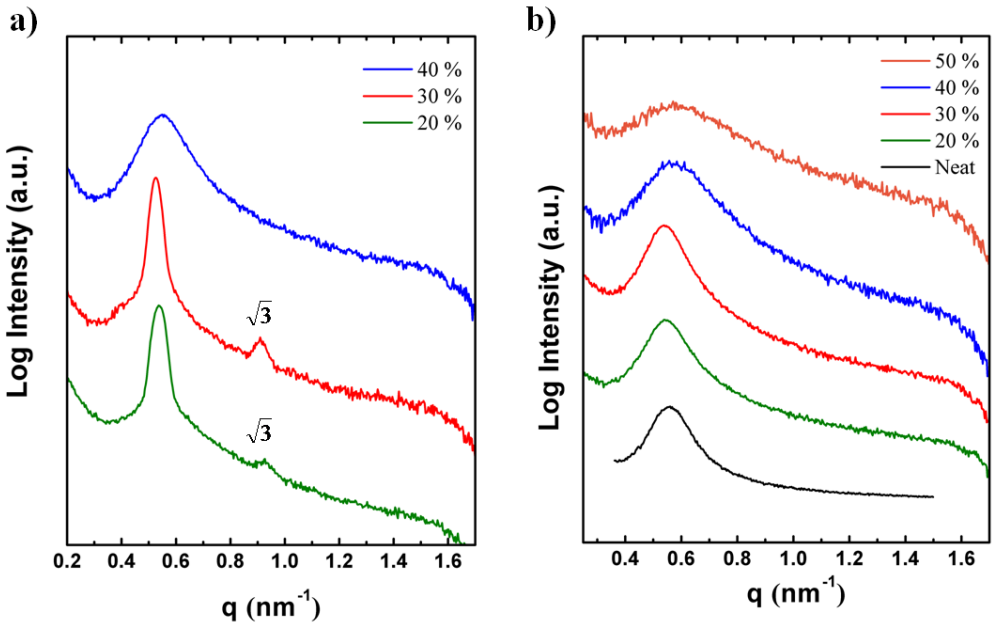


Figure 2.4. SAXS scattering profiles of PF127/MG2OH blends at a) 20 °C, and b) 80 °C. The legend in upper right corresponds to MG2OH weight percent relative to PF127 weight.

crosslinker (not shown) suggested that the additives had a negligible effect on the segregation strength and morphology.

### *2.3.4 Thin Film Characterization*

In order for cylindrical block copolymer morphologies to be useful as lithographic etch resists, the morphology must be oriented vertically to the substrate, or a single monolayer of the cylinders oriented parallel to the substrate is required. The PF127/MG2OH blends were easily dissolved in the solvent blend and spin-coated onto cleaned silicon wafers for the imaging of the morphology of the thin film, and dewetting was not observed. Ellipsometric measurements and AFM images were obtained for the films spun at varying solution concentrations and spin coating speeds in order to optimize the conditions required to form a monolayer of the phase separated block copolymer. Assuming no PEO wetting layer formation between the substrate and the cylinder monolayer, this should be nearly equivalent to the d-spacing observed by x-ray scattering of approximately 14 nm.

AFM was used to view the self-assembly of the MG2OH/PF127 blend films after spin coating a 15nm thick film. The differences in the mechanical properties between PPO and the PEO/MG2OH blend enabled the AFM cantilever probe to discriminate between the two blocks by the phase lag in probe tapping. The brighter domains represented the block with the stiffer mechanical properties, which in this case is the PEO/MG2OH blend, which formed the continuous matrix phase of the block copolymer. The PPO minority phase of the copolymer was represented by the darker regions. We found that as little as 10 wt. % (w/w PF127) MG2OH addition was necessary to induce ordering of the PF127 to form self-assembled cylinders oriented parallel to the plane of the substrate, as shown in Figure 2.5. The single layer of

cylinders showed an average PPO domain size of 6 – 7 nm, as measured by a line scan through the AFM image, and a periodicity of ~15 nm, which corresponded with the previously shown SAXS data. The cylinders appeared in a random orientation as indicated by the diffuse ring in a fast Fourier transform (FFT) of the image (not shown). As the concentration of MG2OH in the blend is increased to 30-40 wt. %, a mixed cylinder-sphere morphology was observed, as shown in Figure 2.5(d), indicating a possible order-order transition (OOT) towards an entirely spherical morphology. Above 40 % MG2OH, however, we observed featureless films.

### *2.3.5 Enhanced Long-Range Order Using Water Vapor Annealing*

Due to the fast evaporation of solvent used in the spin coating process, block copolymer morphologies are usually not at equilibrium immediately after spin coating. However, many applications in block copolymer lithography require long-range order for predictable registration of one domain relative to the other. It may be noted that the glass transition temperature of both PEO and PPO is well below ambient temperature (≈ -54 °C and -80 °C, respectively), and the $T_g$ of the F127/MG2OH 20% blend should also be well below room temperature. Therefore, the polymer morphology may be "annealing" while sitting at room temperature if the structure is not crosslinked.

Additional chain mobility may be quickly enhanced through a few processing tricks. For example, the MG2OH/F127 blended films were spin coated without any PAG and TMMGU from an ethanol/water (2:1 v/v) solution. No post-apply bake was performed on the films after spin coating, leaving residual water in the film that can act to further increase the mobility of the polymer chains in the film. The films were then 'aged' for 72 hours in a dessicator containing a 75% relative humidity atmosphere, and then dried in a dessicator prior to imaging.[24,25] Since the PEO

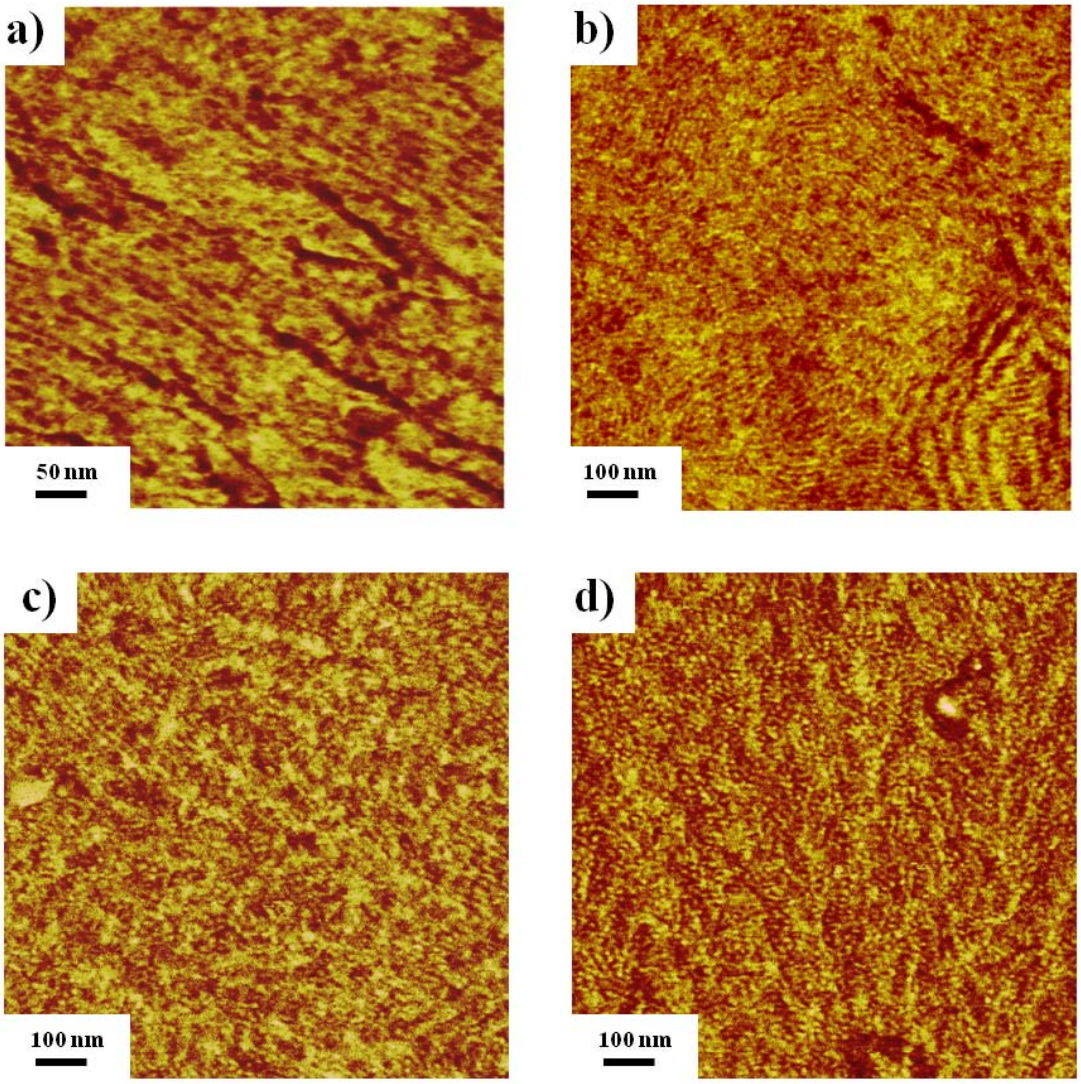


Figure 2.5. AFM phase images of PF127/MG2OH blends containing (a) 0 % MG2OH (disordered), (b) 10 % MG2OH (cylindrical), c) 20 % MG2OH (cylindrical), and d) 30 wt. % MG2OH (cylinder/sphere transition

majority phase is water-soluble, water vapor will plasticize the film, allowing the morphology to more quickly settle into an equilibrium state, hallmarked by a majority of cylinders lying in the same direction within a given area. Figure 2.6(a) shows a phase-mode AFM image of such a film, containing >20 cylinders lying in the same orientation. After the drying process, the films were able to be crosslinked at the same dose (20 mJ/cm$^2$) using PAG and TMMGU (Section 2.3.7), so it was assumed that the water vapor annealing process did not have any adverse effects on PAG activity.

### *2.3.6 Enhanced Long Range Order Using Metal Alkali Salts*

We have also observed a dramatic improvement in the ordering properties of these self-assembling systems through the addition of a metal alkali salt. The function of the salt is to complex with PEO units through ionic interactions of the metal cation with the lone pair electrons on the oxygen atom. The cation can also bridge between adjacent intra-chain PEO units, increasing the correlation length of the block copolymer morphology. A similar effect has also been reported in PS-b-PEO systems, up to a specific molar concentration of the cation relative to the oxygen atom.[26]

We saw similar behavior in the Pluronic/MG2OH blend system when blended with potassium iodide (KI) as the complexation agent. Figure 2.7(a-d) shows representative images from a series of F127/20 % MG2OH blend films mixed with increasing amounts of KI, and annealed in a humid environment for 1 day as discussed previously. The enhancement in ordering became evident at an [O]/[K] ratio equal to 64, but the best ordering was seen at an [O]/[K] ratio equal to 32, as defined by the largest number of cylinders lying in the same direction in several AFM scans. One research article has reported a “crystallization gap” after blending an amide-based potassium and lithium salts into PEO. In other words, PEO did not crystallize at a

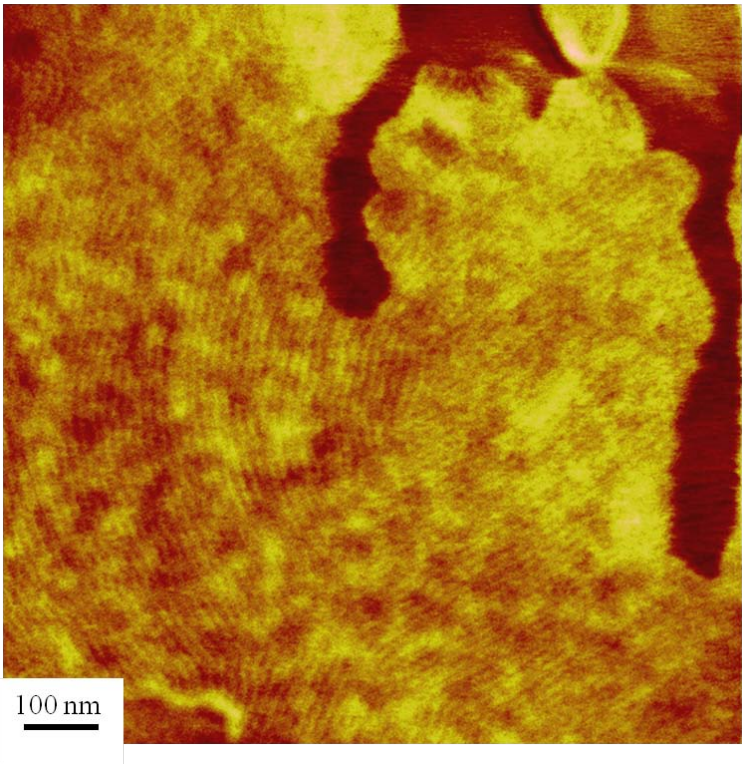


Figure 2.6. a) AFM images of F127/20% MG20H blend aged for three days in a humid (75% RH) environment without any PAG/TMMGU.

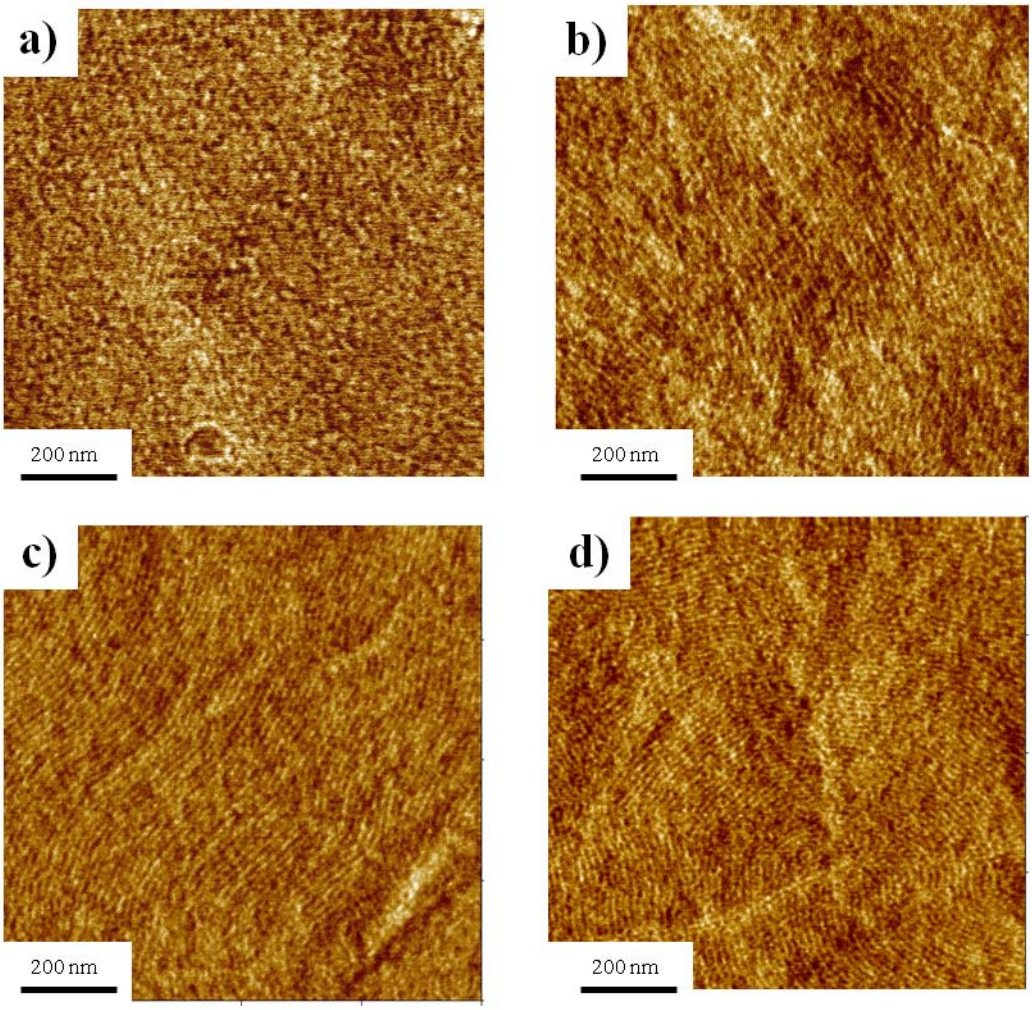


Figure 2.7. Series of AFM images shows how the addition of potassium iodide changes the ordering properties of the blend system through complexation with the PEO. a) [O]/[K] = 96, b) [O]/[K] = 64, c) [O]/[K] = 32, [O]/[K] = 16.

specific molar concentration range of the metal cation relative to the ethylene oxide unit.[27] Although this was not observed in our work, complexing metal salts such as these may have a dual function in these blends to decrease crystallinity and increase ordering in the block copolymer blends.

### *2.3.7 Thin Film Crosslinking Studies*

The crosslinking of the PF127/MG2OH blends followed a process flow typical for chemically amplified photoresists. Adapting a procedure reported by Dai et al.,[28] a sample containing 20 wt. % MG2OH was blended with 3% triphenylsulfonium triflate (PAG) and 9% tetramethoxymethylglycouril (TMMGU) and were exposed to 248 nm radiation. The photo-generated acid catalyzed the condensation of the methoxy groups on the TMMGU with the hydroxyl groups of the molecular glass. The wafers were then baked at various temperatures to speed the diffusion of acid through the film, forming a crosslinked, insoluble network, as shown in the schematic in Figure 2.8(a). It was interesting to note that even at 12 wt. % TMMGU, the tendency for the PEO component to crystallize was not completely eliminated in thick films, as observed from DSC data (not shown). However, at very small film thicknesses (<30 nm) PEO crystallization slowed dramatically, possibly due to the reduction of PEO chain diffusion and confinement effects at the substrate/ blend interface.[29]

Although a process flow typical for a chemically amplified photoresist was used, the blend did not behave like a typical photoresist. The contrast curve (Figure 2.8) indicated the sensitivity of this system was very high, and the resist formed a crosslinked gel beyond a dose of 10 mJ/cm$^2$ or greater, as indicated by the inability to dissolve the film in methanol afterwards. However, ellipsometric evaluation after development indicated that the entire film thickness of the PF127/MG2OH films did not take part in the crosslinking reaction. The normalized film thickness that remained

a)

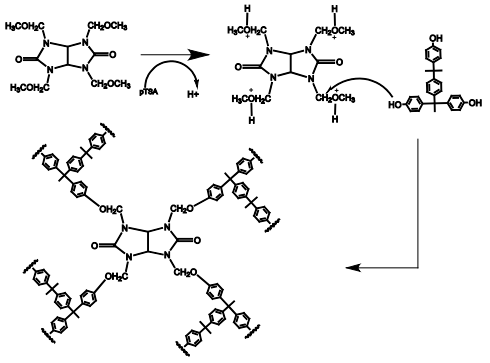

b)

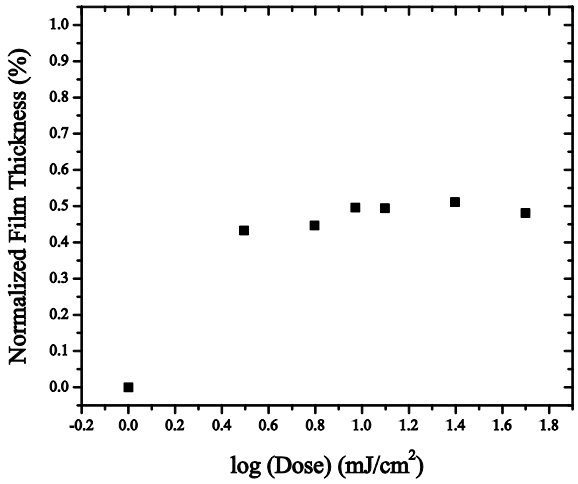


c)

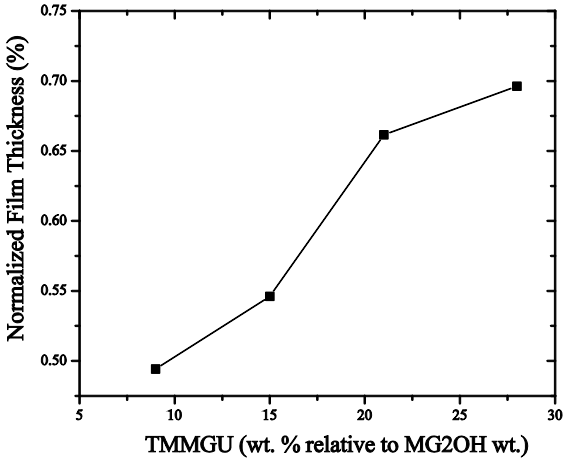


Figure 2.8. a) Schematic of chemically amplified crosslinking using PAG and TMMGU, b) Normalized film thickness vs. dose of 254nm radiation using 3% PAG, 9% TMMGU, and b) Normalized film thickness remaining versus increased TMMGU concentration in the PF127/ 20% MG2OH blend

after development (relative to the original film thickness) did not increase above 50% using only 9% TMMGU loading in the blend, as measured relative to the mass of MG2OH. This may have been due to the dissolution of PEO chains that did not incorporate into the MG2OH crosslinked network, or partial segregation of TMMGU into the hydrophobic PPO phase. We found that the fraction of film loss during development could be decreased by increasing the percent of TMMGU loading, as shown in Figure 2.8. The data showed a monotonic increase of the percent of film thickness remaining after development with increased TMMGU loading, given a fixed dose of 12.5 mJ/cm$^2$ used for exposure. We were able to achieve a normalized film thickness approaching 70% using a TMMGU concentration of 27.5 wt. %. However, adding this much TMMGU changed the film morphology to one of disordered spheres, requiring a compromise between the crosslink density and morphology of the system. We also tried adding more than 20 wt. % MG2OH into the blend, but this also caused an OOT upon addition of the PAG and TMMGU in the film.

An even bigger problem was the post-exposure bake (PEB) used to crosslink the film. The purpose of the PEB in lithography is to allow the polymer film enough mobility to allow for acid diffusion through the resist matrix and the subsequent solubility switch of the resist pattern. Due to the $T_g$ of both blocks of the host PF127 being below room temperature, the diffusion of acid and crosslinking of the MG2OH should be possible at relatively low temperatures, relative to typical lithographic processes. Considering that acid diffusion follows Arrhenius behavior, a more lengthy PEB was necessary at these low temperatures to achieve the same amount of diffusion achieved by a high temperature bake. However we did not find this to be the case, even if the film was allowed to sit for 12 hours after UV exposure at 25°C, or at 40 °C. We found that a PEB step of 80 °C for 180 seconds was sufficient to crosslink the films. However, afterwards the quality of the ordered morphology was completely

degraded, and featureless films are observed in AFM (not shown). This may be due to the previously discussed order-disorder transition, which occurs at or above 80 °C. Therefore, during the PEB step there are two competing processes. First is the rate of crosslinking of the MG2OH within the PEO domain to lock in the self-assembled structure, and second is the tendency for the system to disorder at temperatures above its ODT. In this case, the disordering is occurring first, destroying the morphology and then crosslinking it. More optimization will be necessary before photopatterning can be successfully performed on these materials, or more strongly hydrogen-bonding blend materials which are less susceptible to high temperature may be substituted for the MG2OH additive.

### *2.4 Conclusion*

Sub-10 nm self-assembled morphologies for both bulk and thin film systems have been generated by blending a commercially available, polymeric surfactant with a molecular glass photoresist. The blended systems contain a minority of PPO surrounded by a blended matrix of PEO and molecular glass photoresist. The miscibility of the blend was enabled by the strong multi-point intermolecular hydrogen bonds between the hydroxyl groups of the molecular glass and the alkyl ether of the PEO block, as evidenced by DSC and FTIR. Selective incorporation of MG2OH in the PEO led to an increase in the copolymer segregation strength as evidenced by narrowing of SAXS peak widths, and was also by shown from AFM to drive an order-order transition from a cylindrical to spherical morphology in single-layer films. MG2OH addition was also shown to significantly reduce crystallinity of the PEO matrix, but was unable to eliminate it completely, due to phase mixing at loadings greater than 40 wt.%. The technique is also applicable to other poly(alkylene oxide)-based nonionic surfactants with a range of different molecular weight and composition

ranges, offering the possibility of shrinking the feature size further. Based on these encouraging results, these type of hydrogen-bonded systems are expected to enable next-generation block copolymer lithographic resists exhibiting common diblock morphologies and having acceptable contrast in RIE plasmas.

### *2.5 Acknowledgements*

The authors would like to thank the Semiconductor Research Corporation for funding this research. Roy Lotz (Sleepy Hollow High School, Tarrytown, NY) is gratefully acknowledged for his help on this project. This work made use of various facilities of the Cornell Center for Materials Research (CCMR) with support from the National Science Foundation Materials Research Science and Engineering Centers (MRSEC) program (DMR 0520404). This work also made use of various facilities with Cornell's Nanobiotechnology Center (NBTC), in addition to the Cornell Nanoscale Facility, a member of the National Nanotechnology Infrastructure Network, which is supported by the National Science Foundation (Grant ECS-0335765).

## APPENDIX

### *2.6 Calculation of the PEO-MG2OH Interaction Parameter*

The thermodynamic parameters related to the mixing of the molecular glass (MG2OH) and pure poly(ethylene oxide) (PEO) can be determined by a quantitative analysis of the depression of the crystallization temperature of PEO with increasing MG2OH content.[30] This data can be used to understand the specific interaction of the MG2OH molecule with the PEO block in Pluronic™ triblock copolymer surfactants, and may be used to compare with that of other blended small molecule additives.

Increasing amounts of MG2OH were mixed with a pure PEO homopolymer ($M_n$=9,300 g/mol, Aldrich) in a good solvent. The molecular weight of the PEO homopolymer was selected to match closely with that of the PEO block in PF127 ($M_n$=8,820 g/mol). After slow drying of the solvent, and then drying under reduced pressure, the blends were analyzed using DSC, as shown in Figure 2.9. The PEO melting temperature was seen to decrease in a linear fashion, similar to the PF127/MG2OH data, as shown in Figure 2.10. From these values, the polymer-diluent interaction free energy can be calculated, as outlined in Mandelkern et al. [31]

The Flory-Huggins equation can be used to describe the free energy of mixing for a polymer and a small molecule diluent in the amorphous state.[32, 33] The chemical potential of the diluent $\mu_1$ in the mixture relative to that of the pure component $\mu_1^o$ can be written as

$$\mu_1 - \mu_1^o = RT\left[\ln(1-v_2) + (1-\frac{1}{x})v_2 + \chi_1 {v_2}^2\right] , \qquad \text{(Eq. 2.1)}$$

and the chemical potential of the blended PEO polymer relative to the pure PEO reference state is defined as

$$\mu_2 - \mu_2^o = RT\left[\ln(1-v_2) - (x-1)(1-v_2) + \chi_1(1-v_2)^2\right]. \qquad \text{(Eq. 2.2)}$$

In Equations (2.1) and (2.2), $\mu_2$ is the volume fraction of PEO present in the mixture, x

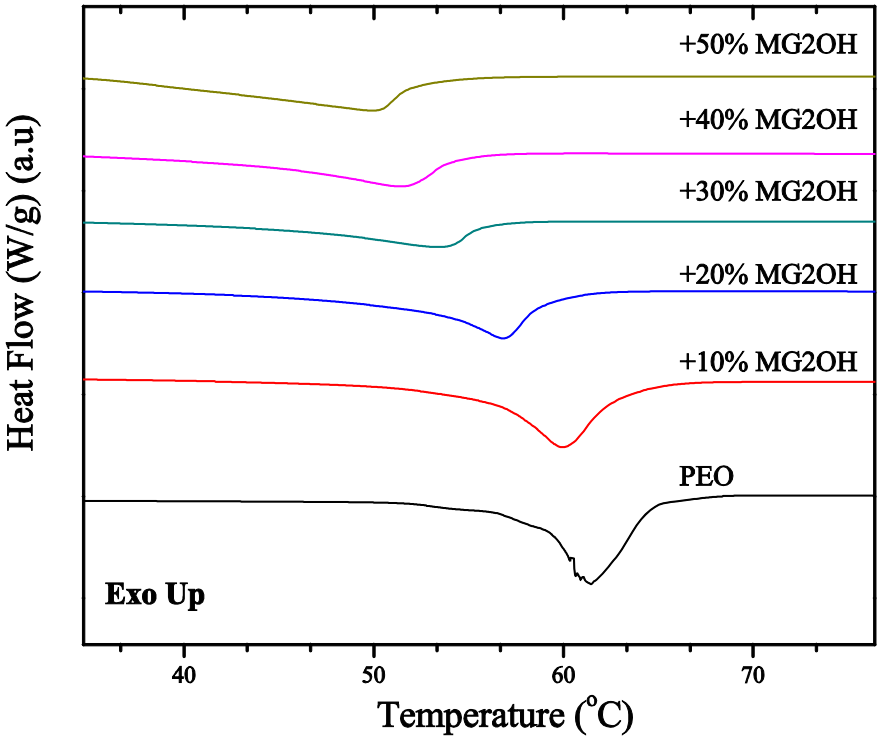


Figure 2.9. Raw DSC exotherms showing increasing MG2OH wt. % mixed into a pure PEO homopolymer (9,300 g/mol)

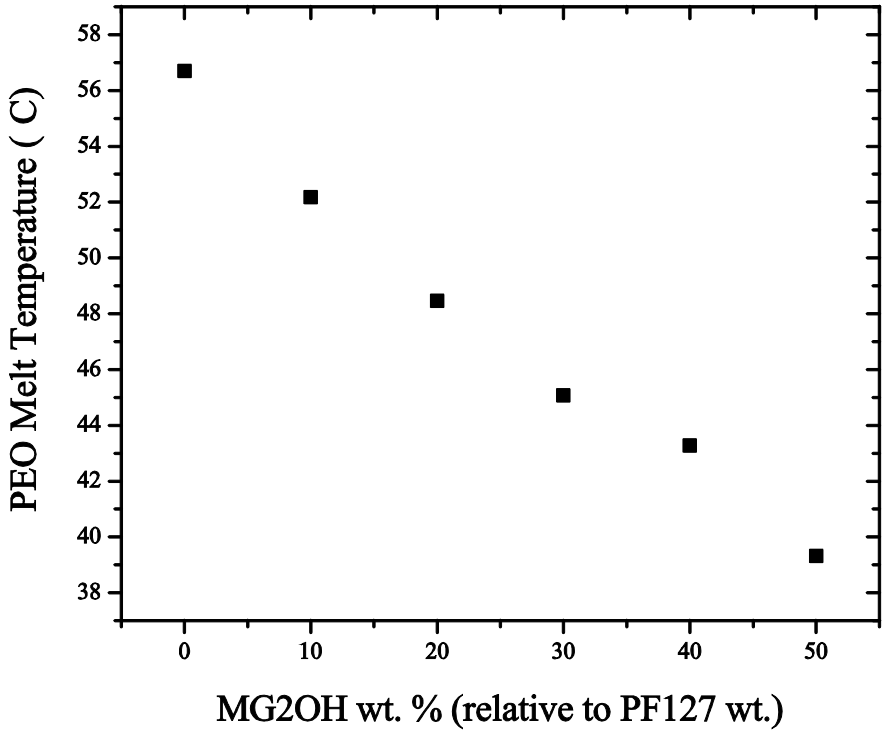


Figure 2.10. Depression of the melting point ($T_m$) of PEO homopolymer (9,300 g/mol) with increasing volume fraction ($v_1$) of MG2OH

Table 2.1. Relevant data for PEO/MG2OH blends.

| **MG2OH wt. %** | **MG2OH vol. %** | **$T_g$ (°C)** | **$T_c$ (°C)** | **$T_m$ (°C)** |
|---|---|---|---|---|
| 0 | 0 | - | - | 61.5 |
| 10 | 9.3 | - | - | 60.0 |
| 20 | 17.0 | - | - | 56.7 |
| 30 | 23.5 | -46.0 | -28.5 | 53.6 |
| 40 | 29.0 | -43.0 | -16.9 | 51.9 |
| 50 | 33.8 | -36.0 | 15.1 | 50.2 |

is the number of repeating units per molecule, and $\chi_1$ represents the polymer-diluent interaction free energy. The chemical potential per mole of polymer units can be obtained by dividing Eq. 2.2 above by $xV_1/V_u$, the number of units per molecule, as in

$$\mu_u - \mu_u^o = RT\frac{V_u}{V_1}\left[\ln\frac{v_2}{x} + (1-\frac{1}{x})(1-v_2) + \chi_1(1-v_2)^2\right] \quad \text{(Eq. 2.3)}$$

where $V_u$ and $V_1$ are the molar volumes of the polymer repeating unit and molecular diluent, respectively. For polymers of high molecular weight, Eq. 2.3 reduces to

$$\mu_u - \mu_u^o = RT\frac{V_u}{V_1}\left[(1-v_2) - \chi_1(1-v_2)^2\right] \quad \text{(Eq. 2.4)}$$

It can be assumed that the MG2OH is expelled from the crystalline lattice of PEO for steric reasons. Therefore, if an equilibrium exists in the system, then the chemical potential of the PEO in the amorphous and crystalline phase must be equal. At the melting point of a polymer-diluent mixture, it is required that

$$\mu_u^{\ c} - \mu_u^{\ o} = \mu_u^{\ l} - \mu_u^{\ o} \ . \quad \text{(Eq. 2.5)}$$

The superscripts *c* and *l* refer to crystalline and liquid phases, and the pure molten polymer is taken as the reference state. The difference in chemical potential between a crystalline polymer unit and one in the pure liquid state is defined as

$$\mu_u^{\ c} - \mu_u^{\ o} = -\Delta F_u \ = -(\Delta H_u - T\Delta S_u) \quad \text{(Eq. 2.6)}$$

If we assume that $\Delta H_u$ and $\Delta S_u$ do not vary with temperature, then by defining the ratio $\Delta H_u/\ \Delta S_u$ as equivalent to $T_m^{\ o}$ , Eq. 2.6 can be re-written as

$$\mu_u^{\ c} - \mu_u^{\ o} = \Delta H_u(1-\frac{T}{T_m^o}) \quad \text{(Eq. 2.7)}$$

After substitution of Eq. 2.4 for $\mu_u^{\ l} - \mu_u^{\ o}$ , we obtain the basic equation for the depression of the polymer melting temperature with added diluent:

$$\frac{1}{T_m} - \frac{1}{T_m^o} = \frac{RV_u}{\Delta H_u V_1}[(1-v_2) - \chi_1(1-v_2)^2] \ . \quad \text{(Eq. 2.8)}$$

For systems which show a continuous depression in melting point with decreasing polymer concentration, such as in the PEO/MG2OH system, Equation 2.8 can be rewritten in the form y = mx+b:

$$\frac{\frac{1}{T_m}-\frac{1}{T_m^o}}{v^1}=\frac{R}{\Delta H_u}\frac{V_u}{V_1}(1-\frac{BV_1}{R}\frac{v_1}{T_m}) \qquad \text{(Eq. 2.9)}$$

Therefore, a plot of the quantity $\frac{\frac{1}{T_m}-\frac{1}{T_m^o}}{v_1}$ vs. $v_1/T_m$ should yield a straight line, as shown in Figure 2.11. Any deviations in linearity may be due to differences in $\chi$ at the particular blend ratio. From the intercept of the straight line, $\Delta H_u$ can be deduced if the ratio $V_u/V_1$ is known, and the slope of the line can be related to B, the interaction energy density. Finally, B can be used to solve for $\chi$. For this calculation, the following constants have been used:

$M_{o\ (PEO)}$= 44 g/mol

$\rho_{(PEO}$=1.124 g/cm$^3$ (from Ref. 34)

$M_{o\ (MG2OH)}$ = 424 g/mol

$\rho_{(MG2OH)}$ = 1.1 g/cm$^3$ (estimate from other glass formers, c. f. Sha et al.) [35]

The calculation yields the following result for the thermodynamic parameters of the PEO/MG2OH system:

$\Delta H_u$=7.48 J/mol

B= -0.0428 J/cm$^3$

$\chi$= -0.0067 (at 20 °C)

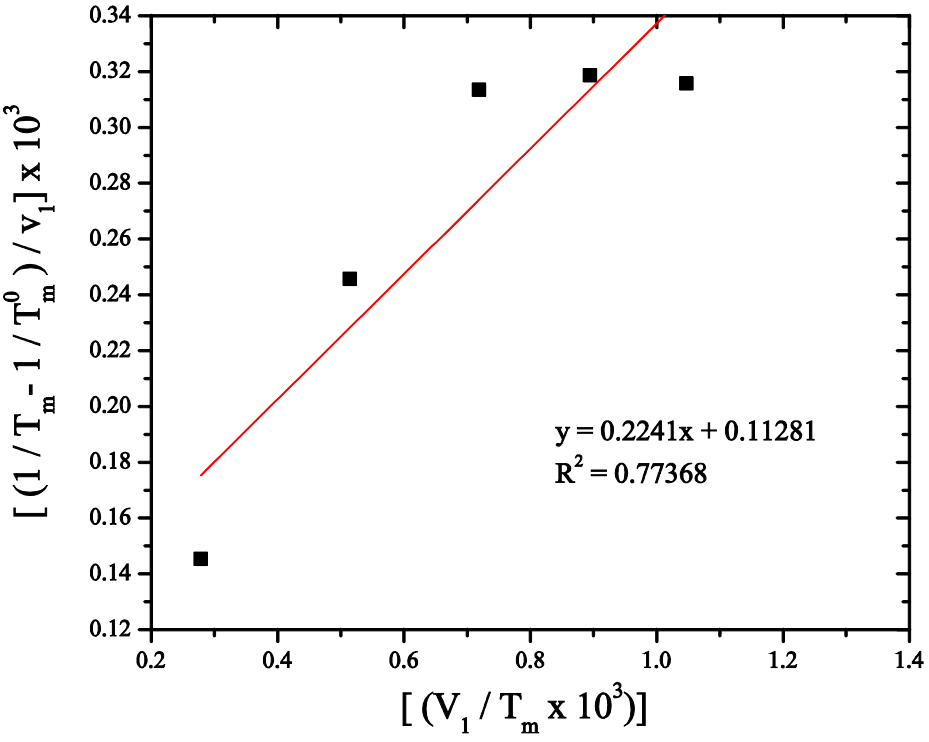


Figure 2.11. Plot of quantity $(1/T_m-1/T_m^{\ 0})/v_1$ against $v_1/T_m$ for PEO homopolymer mixed with MG2OH, and the associated linear trend line.

The calculated negative PEO-MG2OH interaction parameter strongly supports the experimental evidence that suggest the mixing of MG2OH and PEO. Furthermore, the $\chi$ parameter can be used as a useful comparison to gauge the interaction strength of other small molecule diluents in a block copolymer template. For example, when the same analysis is used for the blending of MG2OH into the Pluronics F127 system, $\chi$ is equal to $-3.7 \times 10^{-4}$ at room temperature, which is over an order of magnitude smaller than that shown in the present experiment. Differences in the molecular environment of the PEO block may contribute to the measured difference in $\chi$ between the PEO homopolymer and the PEO block in PF127. In the triblock, the neighboring poly(propylene oxide) domains may decrease the lamellar thickness of PEO crystallites compared to that of pure PEO homopolymer, as noted by Whitmore and Noolandi.[36] We observe a decrease in the melt temperature of the PEO block in Pluronics (56.7 °C) relative to that of the pure PEO homopolymer (61.4 °C). Floudas et al. has also reported a decrease in melting temperature and a reduction in crystallinity of PEO in the case of the a triblock PEO-*b*-PS-*b*-PEO compared to the PEO homopolymer.[37]

There are also several sources of error in this experiment. For example, for blends of semi-crystalline polymers and small molecule diluents, if the diluent becomes structurally integrated into the crystalline phase of the polymer, the chemical potentials of the crystalline PEO would become inaccurate as described in the lattice theory described above. Modifications to the theory may be taken into account as described in Mandelkern et al.[31] Also, the discussion described above made the assumption the melt temperature collected is from a system which is in equilibrium. This is probably not the case in our DSC experiment, since the temperature of the system is ramped at 10 °C/min or greater.

## REFERENCES


1. Reichmanis, E.; Houlihan, F. M.; Nalamasu, O.; Neenan, T. X., Chemical amplication mechanisms for microlithography. *Chem. Mater.* **1991,** *3* (3), 394-407.
2. Intel Intel Opens First High-Volume 45nm Microprocessor Manufacturing Factory. http://www.intel.com/pressroom/archive/releases/2007/20071025corp.htm (accessed May 25).
3. Bates, F. S.; Fredrickson, G. H., Block copolymers-designer soft materials. *Physics Today* **1999,** *52* (2), 32-38.
4. Bates, F. S.; Fredrickson, G. H., Block copolymer thermodynamics: theory and experiment. *Annual Review of Physical Chemistry* **1990,** *41*, 525-57.
5. Zhao, D.; Feng, J.; Huo, Q.; Melosh, N.; Fredrickson, G. H.; Chmelka, B. F.; Stucky, G. D., Triblock copolymer syntheses of mesoporous silica with periodic 50 to 300 angstrom pores. *Science* **1998,** *279*, 548.
6. Pai, R. A. H., R. ; Schulberg, M.T.; Sengupta, A. ; Sun, J-N. ; Watkins, J.J., Mesoporous silicates prepared using preorganized templates in supercritical fluids. *Science* **2004,** *303*, 507-510.
7. Brinker, C. J.; Lu, Y.; Sellinger, A.; Fan, H., Evaporation-induced self-assembly: nanostructures made easy. *Adv. Mater.* **1999,** *11* (7), 579-585.
8. Fan, H.; Brinker, J., Evaporation-induced self-assembly to functional nanostructures. *Studies in Surface Science and Catalysis* **2004,** *148* (Mesoporous Crystals and Related Nano-Structured Materials), 213-240.

9. Miyata, H. I., M.; Watanabe, M.; Noma, T., Preparation of highly ordered mesostructured tin oxide film with a microcrystalline framework through vapor-induced liquid-crystal templating. *Chem. Mater.* **2003,** *15*, 1334-1343.

10. Hillmyer, M. A.; Lipic, P. M.; Hajduk, D. A.; Almdal, K.; Bates, F. S., Self-assembly and polymerization of epoxy resin-amphiphilic block copolymer nanocomposites. *J. Am. Chem. Soc.* **1997,** *119*, 2749-2750.

11. Meng, Y.; Gu, D.; Zhang, F.; Shi, Y.; Cheng, L.; Feng, D.; Wu, Z.; Chen, Z.; Wan, Y.; Stein, A.; Zhao, D., A family of highly ordered mesoporous polymer resin and carbon structures from organic-organic self assembly. *Chem. Mater.* **2006,** *18*, 4447-4464.

12. Liang, C.; Hong, K.; Guiochon, G. A.; Mays, J. W.; Dai, S., Synthesis of a large-scale highly ordered porous carbon film by self-assembly of block copolymers. *Angew. Chem. Int. Ed.* **2004,** *43*, 5785-5789.

13. Bita, I.; Yang, J. K. W.; Jung, Y. S.; Ross, C. A.; Thomas, E. L.; Berggren, K. K., Graphoepitaxy of self-assembled block copolymers on two-dimensional periodic patterned templates. *Science* **2009,** *321*, 939.

14. Li, M.; Douki, K.; Goto, K.; Li, X.; Coenjarts, C.; Smilgies, D. M.; Ober, C. K., Spatially Controlled Fabrication of Nanoporous Block Copolymers. *Chemistry of Materials* **2004,** *16* (20), 3800-3808.

15. Tirumala, V. R. R., A. ; Agarwal, S. ; Lin, E.K. ; Watkins, J.J., Well ordered polymer melts from blends of disordered triblock copolymer surfactants and functional homopolymers. *Adv. Mater.* **2008,** *20*, 1603-1608.

16. Tirumala, V. R. P., R. A.; Agarwal, S.; Testa, J. J.; Bhatnagar, G.; Romang, A. H.; Chandler, C.; Gorman, B.P.; Jones, R. L.; Lin, E. K.; Watkins, J. J., Mesoporous silica films with long-range order prepared from strongly

segregated block copolymer/ homopolymer blend templates. *Chem. Mater.* **2007,** *19*, 5868-5874.

17. De Silva, A.; Felix, N. M.; Ober, C. K., Molecular glass resists as high resolution patterning materials. *Adv. Mater.* **2008,** *20*, 3355-3361.
18. Bang, J.; Kim, S. H.; Drockenmuller, E.; Misner, M. J.; Russell, T. P.; Hawker, C. J., Defect-Free Nanoporous Thin Films from ABC Triblock Copolymers. *J. Am. Chem. Soc.* **2006,** *128* (23), 7622-7629.
19. Freer, E. M.; Krupp, L. E.; Hinsberg, W. D.; Rice, P. M.; Hedrick, J. L.; Cha, J. N.; Miller, R. D.; Kim, H.-C., Oriented Mesoporous Organosilicate Thin Films. *Nano Letters* **2005,** *5* (10), 2014-2018.
20. Rong, M. Z.; Zhang, M. Q.; Zheng, Y. X.; Zeng, H. M.; Walter, R.; Friedrich, K., Structure-property relationships of irradiation grafted nano-inorganic particle filled polypropylene composites. *Polymer* **2001,** *42*, 167-183.
21. Ratna, D. A., T.N. ; Karger-Kocsis, J., Studies on polyethylene oxide and phenolic resin blends. *J. Appl. Polym. Sci.* **2008,** *108*, 2156-2162.
22. Coleman, M. M.; Painter, P. C., Hydrogen bonded polymer blends. *Prog. Polym. Sci.* **1995,** *20*, 1-59.
23. Tirumala, V. R. D., V. ; Bosse, A. W. ; Romang, A. ; Ilavsky, J.; Lin, E. K.; Watkins, J.J., Well-ordered polymer melts with 5 nm lamellar domains from blends of a disordered block copolymer and a selectively associating homopolymer of low or high molar mass. *Macromolecules* **2008,** *41*, 7978-7985.
24. Bell, L. N.; Labuza, T. P., *Moisture Sorption: Practical Aspects of Isotherm Measurement and Use*. 2nd ed.; American Association of Cereal Chemists: St. Paul, MN, 2000.

25. Urade, V. N.; Hillhouse, H. W., Synthesis of thermally stable highly ordered nanoporous tin oxide thin films with a 3D face-centered orthorhombic nanostructure. *J. Phys. Chem. B.* **2005,** *109*, 105338-10541.

26. Kim, S. Y. M., M.J.; Yang, L.; Gang, O.; Ocko, B.M. ; Russell, T.P., Salt complexation in block copolymer thin films. *Macromolecules* **2006,** *39*, 8473-8479.

27. Lascaud, S.; Perrier, M.; Vallee, A.; Besner, S.; Prud'homme, J.; Armand, M., Phase diagrams and conductivity behavior of poly(ethylene oxide)- molten salt rubbery electrolytes. *Macromolecules* **1994,** *27*, 7469-7477.

28. Dai, J. Y. C., S.W.; Hamad, A.; Yang, D.; Felix, N. ; Ober, C.K., Molecular Glass Resists for High Resolution Patterning. *Chem. Mater.* **2006,** *18*, 3404-3411.

29. Massa, M. V.; Dalnoki-Veress, K.; Forrest, J. A., Crystallization kinetics and crystal morphology in thin poly(ethylene oxide) films. *Eur. Phys. J. E.* **2003,** *11*, 191-198.

30. Nishi, T.; Wang, T. T., Melting point depression and kinetic effects of cooling on crystallization in poly(vinylidene fluoride)-poly(methyl methacrylate) mixtures. *Macromolecules* **1975,** *8* (6).

31. Mandelkern, L., *Crystallization of polymers*. McGraw-Hill: New York, 1964.

32. Huggins, M. L., *J. Phys. Chem.* **1942,** *46*, 151.

33. Flory, P. J., *J. Chem. Phys.* **1942,** *10*, 51.

34. Brandrup, J.; Immergut, E. H.; Grulke, E. A., *Polymer Handbook*. 4th ed.; Wiley-Interscience: New York, 1999.

35. Sha, J.; Lee, J.-K.; Kang, S.; Prabhu, V. M.; Soles, C. L.; Bonnesen, P. V.; Ober, C. K., Architectural effects on acid reaction-diffusion kinetics in molecular glass photoresists. *Chem. Mater.* **2010,** *22*, 3093-3098.

36. Whitmore, M. D.; Noolandi, J., Theory of crystallizable block copolymer blends. *Macromolecules* **1988,** *21*, 1482.

37. Floudas, G.; Tsitsillanis, C., Crystallization kinetics of poly(ethylene oxide) in poly(ethylene oxide)-polystyrene-poly(ethylene oxide) triblock copolymers. *Macromolecules* **1997,** *30*, 4381-4390.

# CHAPTER THREE:

## INTERFACE NEUTRALIZATION FOR LITHOGRAPHICALLY PATTERNABLE BLOCK COPOLYMERS

### *3.1 Introduction*

As traditional chemically amplified photoresist technology approaches its theoretical limits, new material innovations are required in order to extend lithographic patterning below the 20 nm critical dimension. Block copolymer self-assembly is one of the techniques under consideration to extend the range of high-resolution patterning into the molecular realm.[1] The formation of mesoscopic features (10-100 nm) are in essence a thermodynamic phenomenon.[2] They are a consequence of a balance in enthalpic and entropic forces: the repulsion force opposing the mixing of the two polymer chains and the force of chain elasticity which pulls the chains back into a randomly coiled configuration. The manipulation of a few variables, such as molecular weight, volume fraction, and the degree of incompatibility between the blocks, allows sufficient control over the size and shape of functional polymer units. If one of the blocks is selectively removable, many researchers have shown the ability to form nanoporous 'stencils' that can be used to resist the dry or wet etching processes used in traditional lithography.[3]

Some "hybrid" approaches for nanolithography aim to incorporate photochemical functionality into traditionally used self-assembling block copolymer templates.[16] One such system, poly(α-methylstyrene-*block*-4-hydroxystyrene) (PαMS-*b*-PHOST), has been used in our group for direct photo-patterning using 248 nm ultraviolet radiation, allowing precise placement of self-assembled structures via photolithography.[17] In conjunction with blended photoactive compounds, the majority component PHOST can be used as a negative-tone photoresist, while the PαMS block can be selectively removed to create nanoporosity inside the crosslinked areas. Previous work in our group has shown that annealing in a vapor of a good solvent, tetrahydrofuran, in addition to confining the cylinders inside silica trenches can be used to orient the cylindrical microdomains in the plane of the substrate with good

long-range order.[18] Selective solvents have also been used to reversibly switch the morphology to a spherical morphology, which can be "locked in" via the crosslinking of the PHOST matrix phase.[19,20]

In order to enable many lithographic applications, the microdomains of the block copolymer must be oriented vertically, such that removal of one of the phases exposes the substrate.[4] In thin films, however, this result is difficult to achieve due to the preferential attraction of one of the blocks to either the substrate or air interface. This induces the microdomains to orient parallel to the substrate, resulting in a multilayered structure of $nL_o$, with $n$ an integer value and $L_o$ the natural domain spacing of the block copolymer. On the other hand, a surface which does not preferentially attract either of the blocks should result in the entropically favorable structure of microdomains oriented perpendicular to the substrate. Kellogg et al. tested this hypothesis by coating one of the confining walls with a random copolymer (RC) designed to reduce preferential adsorption.[5] Mansky and coworkers built similar RC's which contained a hydroxyl end group on the polymer chains that could covalently bond to a silanol-coated silica surface via a dehydration reaction, creating a thin brush layer after washing off the excess (unbound) polymer.[6,7] The so called "neutrality condition" is usually based on an intermediate surface energy between that of the two polymers in an AB diblock copolymer, and is typically created by the careful synthesis of random copolymers containing a precise composition of each one of the respective blocks (A-*ran*-B). Assuming a well-segregated interface, in which both blocks have separate interactions with the substrate, the surface tension between the A-domain and the interface is equal to $\gamma_A = f_A\gamma_{AB}$, where $f_A$ is the A-segment of the random copolymer, and $\gamma_{AB}$ is the interfacial tension between A and B domains. Likewise, $\gamma_B = (1-f_A)\gamma_{AB}$. The preferential affinity of the surface is then $\Delta\gamma = \gamma_A - \gamma_B = (2f_A-1)\gamma_{AB,}$ and a "neutral surface" ($\Delta\gamma=0$) should result at $f_A=1/2$. The experimental reality, however, is

that $\Delta\gamma=0$ usually occurs at an off-symmetric composition, which may represent asymmetries in the system such as differences in the statistical segment lengths, or penetration into the brush by the block copolymer.[6,8,9] Other materials that have been used to create a "tunable" surface are organosilicates treated by variable doses of $UV/O_3$,[10,11] and self-assembled monolayers of polymers or alkoxysilanes.[12-14] Most of these surfaces have been tailored for poly(styrene-*block*-methyl methacrylate)(PS-*b*-PMMA), the most commonly used block copolymer for lithographic applications, and little has been done for other systems.[15]

Here, we demonstrate a neutral surface for the lithographically patternable PαMS-*b*-PHOST mentioned above, further proving the generality of the random copolymer approach. Since this polymer must be annealed at room temperature due to the thermally sensitive photoacid generators in the system, we show that additional control over the polymer/ solvent interface is necessary to induce vertical orientations in asymmetric block copolymers.

### *3.2 Experimental Method*

#### *3.2.1 Materials*

Styrene (St) and 4-*tert*-butoxystyrene (tBuOS) monomers were obtained from Aldrich. tBuOS was distilled under reduced pressure to remove inhibitor. α',α'-azoisobutyronitrile (AIBN) was used as received from Aldrich. An aqueous solution of hydrochloric acid (34 wt.%) was obtained from Fisher Scientific and used as received. An asymmetric poly(α-methylstyrene-block-4-hydroxystyrene) [PαMS-b-PHOST] diblock copolymer ($f_{P\alpha MS}$=0.34, $M_n$=53,000 g/mol, PDI=1.15) was synthesized as described previously.[17] All solvents were obtained from Aldrich and used as received unless otherwise noted. Silicon (100) wafers were obtained from Wafer Reclaim Services (Spring City, PA).

### *3.2.2 Synthesis of PS-ran-PHOST by Free Radical Polymerization*

All random copolymer samples were synthesized using free radical polymerization (FRP). A representative polymerization procedure is detailed below for sample **RC1**. A mixture of AIBN (0.246g, 1.5 mmol), St (4.68 g, 45 mmol), tBuOS (0.88g, 5 mmol) was dissolved in 30 mL of toluene, degassed by three freeze/thaw cycles, and sealed under nitrogen. The polymerization mixture was heated to 80 °C for 72 hours with magnetic stirring. The resulting mixture was concentrated under reduced pressure and precipitated into 500 mL of methanol. The polymer was purified by two additional cycles of dissolving in tetrahydrofuran and re-precipitation in methanol. Then, the polymer was filtered and dried under vacuum to give the random copolymer P(S-*ran*-tBuOS) as a white solid (3.78 g, 68% yield), $M_n$= 3900 g/mol, PDI=1.67. The fraction of styrene determined by NMR spectroscopy was 0.76. Deprotection of the tert-butoxy groups was performed by a hydrolysis reaction using a ten-fold molar excess of hydrochloric acid relative to poly(tBuOS) component of the random copolymer. P(S-*ran*-tBuOS) (3.0g) was dissolved in 30 mL dioxane, and equilibriated for 15 minutes at 80 °C, before adding a 36.5 wt.% (w/v) solution of hydrochloric acid dropwise (2.67 mL, 2.67 mmol) under vigorous stirring. The reaction was refluxed under nitrogen for 24 hours before precipitation in water. For purification, the polymer was dissolved in dioxane and re-precipitated in water three times. On the final precipitation step, the polymer was dried under reduced pressure to form **RC1** as a white powder (2.73g, 95.7%) .

### *3.2.3 Substrate Preparation*

Silicon (100) wafers with a native oxide layer of ~2 nm were cleaned using a Harrick oxygen plasma cleaner for 5 minutes, cleaved into 2 $cm^2$ squares and blown dry with a stream of high purity nitrogen before use.

### *3.2.4 Covalent Grafting of the Random Copolymers and Block Copolymer Film*

Random copolymer brush layers were generated by spin-coating of films of 1 wt.% P(S-*ran*-HOST) in methyl isobutyl ketone (MIBK) onto clean silicon wafers to give a film thickness of ~30 nm. The samples were annealed in a vacuum oven at 200 °C for various time intervals and quenched immediately to room temperature. During the annealing process, the hydroxyl groups on the PHOST side chain undergo a dehydration reaction with surface silanol groups to covalently bind the random copolymer to the substrate. The wafers were then soaked in a 1:1 mixture of MIBK:isopropanol for 12 hours to remove excess polymer and blown dry with a stream of nitrogen. The thickness of the remaining brush layers were measured by ellipsometry. PαMS-*b*-PHOST block copolymers were cast from 2 wt. % solutions in propylene glycol methyl ether acetate (PGMEA) onto the random copolymer brush layers. These samples were placed in a 1L teflon-sealed jar filled with ~2mL solvent and annealed for at least 8 hours at room temperature. Afterwards, the samples were immediately blown dry with a stream of nitrogen to lock in the annealed morphology.

### *3.2.5 Characterization*

$^{1}$H NMR spectra were recorded in solution with a Mercury 300 MHz spectrometer, using a deuterated chloroform solvent. The molecular weights of the polymers were measured by size exclusion chromatography using a Waters HPLC pump connected to a Waters 486 UV detector using tetrahydrofuran (THF) as an eluent at 40 °C and calibrated to poly(styrene) standards. The film thicknesses of the brush layers were measured with Woollam variable angle spectroscopic ellipsometer using a 300-1000 nm spectral range. For surface energy analysis, a Ramé-Hart Model 500 Advanced Goniometer was used to determine advancing contact angles using water and diiodomethane as test liquids. Data from at least 6 data sets were averaged

together for the measurements, which were analyzed in DROPimage Advanced software. Atomic force microscopy was performed on a Veeco Dimension 3100, using Olympus AC160TS scanning probe cantilevers (spring constant = 42 N/m, tip radius <10 nm) and the resulting images analyzed using Nanoscope software.

### *3.3 Results and Discussion*

#### *3.3.1 Synthesis and Characterization of P(S-ran-HOST)*

P(S-*ran*-tBuOS) random copolymer brushes were synthesized using classical AIBN-initiated free radical polymerization and then hydrolyzed to form P(S-*ran*-HOST), as shown in Figure 3.1. The two blocks of this random copolymer were designed to match closely to that of the two blocks in the block copolymer of interest, PαMS-*b*-PHOST. PαMS could not be used in the random copolymer because the ceiling temperature of PαMS ($T_c$=65 °C) prevented α-methylstyrene from polymerizing at the temperatures typically used to form free radicals from the thermal decomposition of the AIBN initiator (>60 °C). Therefore, PS was used as a substitute for PαMS, based on the similar surface energies of the two polymers (PS=40.7 mJ/m$^2$, PαMS=44.5 mJ/m$^2$).[21] The correct proportion of PS and PHOST polymers should theoretically result in a random copolymer surface that is equally attractive to both the PαMS and the PHOST blocks, leading to entropically favored vertically oriented block copolymer microdomains. Table 3.1 shows the molecular weight of the above mentioned FRP synthesis of P(S-*ran*-tBuOS) polymers. Size-exclusion chromatography of the polymers showed that the number-average molecular weight increased with increasing proportion of the tBuOS monomer in the synthesis feed, from 3900 g/mol RC1(10% tBuOS) to 7200 g/mol in RC6 (60% tBuOS), as exhibited in Figure 3.2. This may be due to the increased radical reactivity of 4-*tert*-

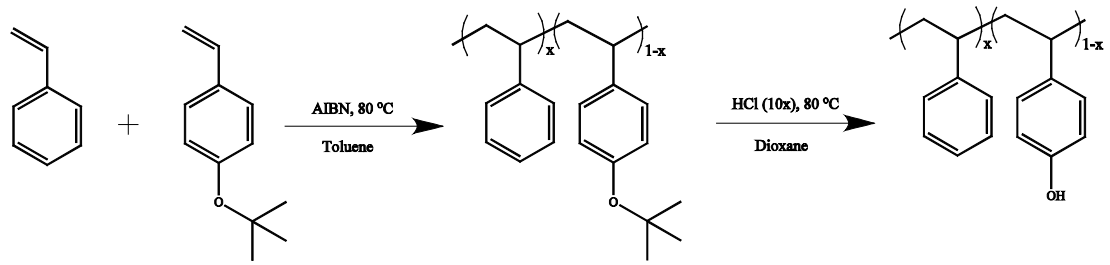


Figure 3.1. Synthesis of PS-*ran*-PHOST copolymers by classical free radical polymerization

Table 3.1. The resulting molecular weights of P(S-*ran*-tBuOS) copolymers, calculated by size-exclusion chromatography, and fraction of PtBuOS, as measured by $^{1}$H NMR Spectroscopy.

| | **Molar Feed Ratio** | | | | | | |
|---|---|---|---|---|---|---|---|
| | **Styrene** | **tBuOS** | **Yield** | **$M_n$** | **$M_w$** | **PDI** | **PtBuOs*** |
| | **(%)** | **(%)** | **(%)** | **(g/mol)** | **(g/mol)** | | **(%)** |
| **RC1** | 0.9 | 0.1 | 68 | 3,900 | 6,500 | 1.67 | 24.3 |
| **RC2** | 0.8 | 0.2 | 66 | 4,500 | 7,400 | 1.64 | 32.7 |
| **RC3** | 0.7 | 0.3 | 75 | 4,800 | 7,200 | 1.50 | 43.5 |
| **RC4** | 0.6 | 0.4 | 67 | 5,500 | 8,400 | 1.53 | 52.7 |
| **RC5** | 0.5 | 0.5 | 60 | 5,800 | 8,500 | 1.47 | 63.9 |
| **RC6** | 0.4 | 0.6 | 53 | 7,200 | 10,200 | 1.42 | 74.8 |

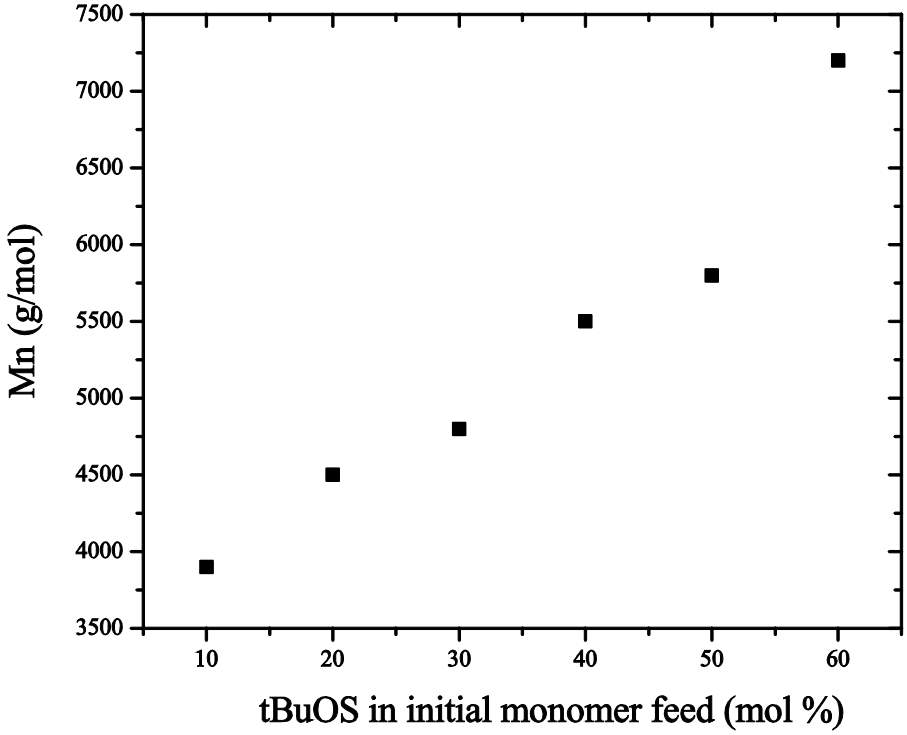


Figure 3.2**.** Molecular weight of the P(S-*ran*-tBuOS) polymers increased with increasing tBuOS in the monomer feed

butoxystyrene radical over that of the styrene radical, due to the inability of the 4-*tert*-butoxystyrene substituent to effectively stabilize a formed radical.[22] The reactivity ratio of a similar monomer pair (4-acetoxystyrene:styrene) has been reported as 1.22:0.89.[23] The effect of the molecular weight of the random copolymer involves a complex interplay of effects. For example, a longer grafted brush will interact to a greater extent and possibly intermix with the overlaying block copolymer chains. However, lower molecular weight polymers will have a higher grafting density, and are therefore less likely to undergo surface reconstruction under thermal or solvent annealing. [24]

One aspect of classical free radical polymerizations is the lack of control over the reaction, leading to polymers that have a higher polydispersity (PDI) compared to polymers produced using other "living" polymerization methods. The polymers produced for this study have a PDI of approximately 1.5. However, Gopalan and coworkers have shown that random copolymer PDI does not play a significant role in the formation of a neutral surface. In their study, random copolymer brushes synthesized by a nitroxide-mediated living FRP method were compared to those synthesized by a classical FRP method. They found that both sets of polymers worked equally well to orient lamellar microdomains of PS-*b*-PMMA vertically relative to the substrate, as long as the composition of the polymers remained within a certain range.[25] We analyzed the precise molar composition the PS and PtBuOS components of the random copolymers using $^{1}$H NMR spectroscopy (Figure 3.3), by integrating the signal of the *tert*-butyl protons (c.a 1.2 ppm) relative to that of the aromatic ring (c.a 7.0 ppm). Complete deprotection of the *tert*-butyl groups was verified by FTIR spectroscopy (Figure 3. 4). Characteristic bond stretching from the $C(CH_3)_3$ group is represented by a doublet peak at ~1370 and 1397 $cm^{-1}$.[26] After deprotection, this

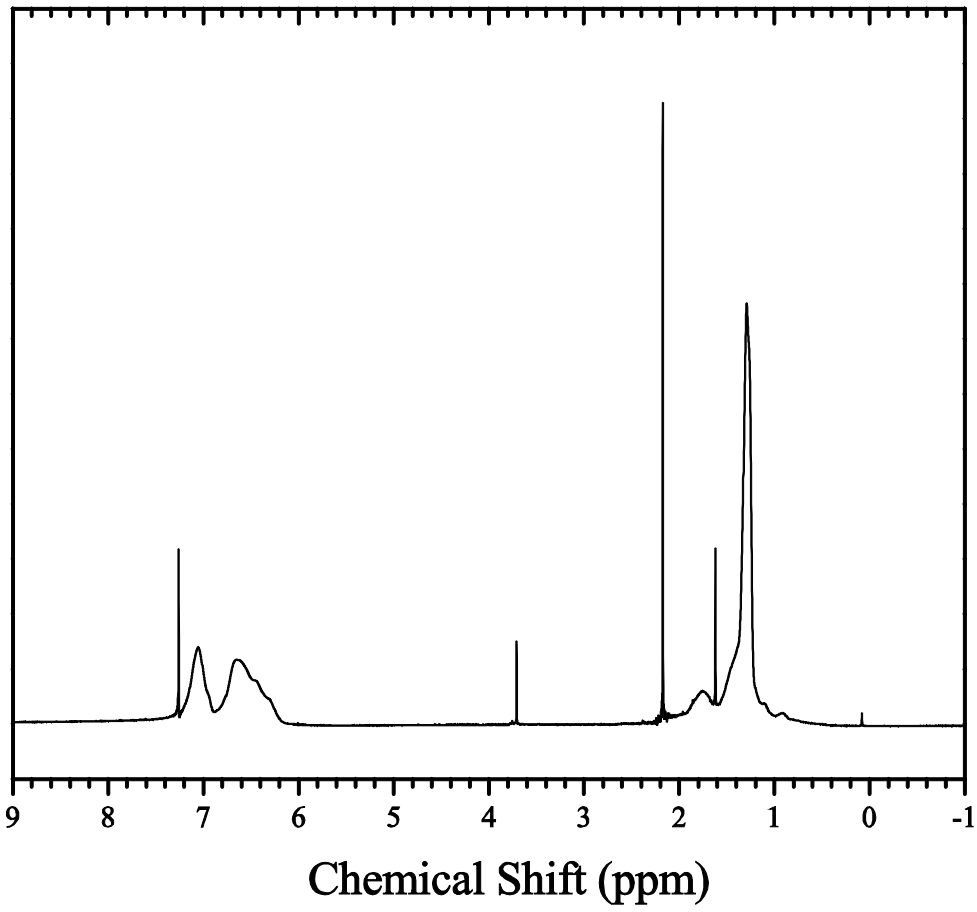


Figure 3.3**.** Representative $^{1}H$ NMR spectra of P(S-*ran*-tBuOS) polymer in $CDCl_3$.

a)

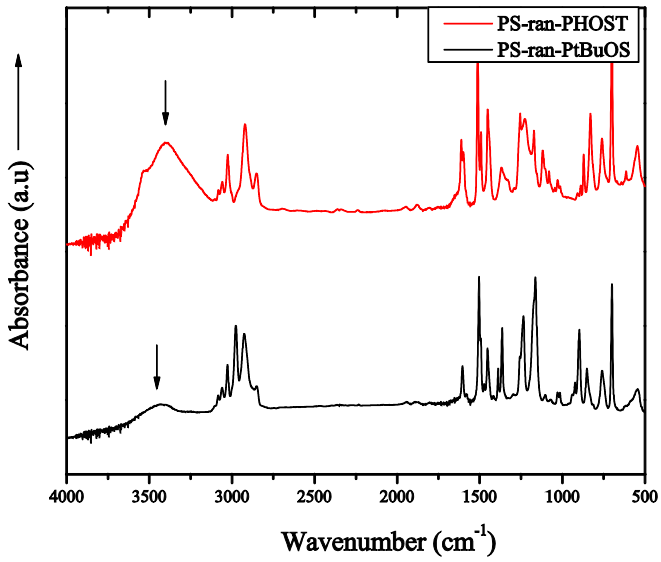


b)

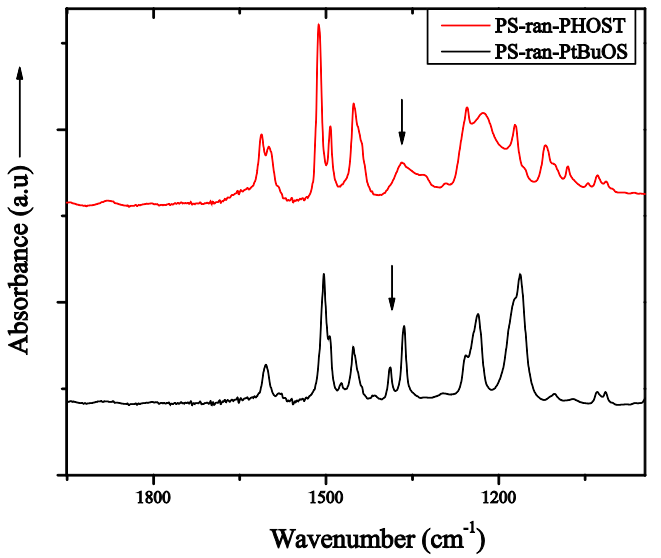


Figure 3.4. FTIR spectroscopy showing a) the total spectra of a representative P(S-*ran*-tBuOS) (bottom) and P(S-*ran*-HOST) (top) sample, and b) the disappearance of the characteristic $C(CH_3)_3$ doublet at 1397 and 1370 $cm^{-1}$ after the hydrolysis reaction.

doublet peak disappeared and was replaced by a broad stretch at ~3300 $cm^{-1}$, which is characteristic of the –OH groups in PHOST. This data provided strong evidence for the nearly complete deprotection of the tert-butyl groups to form P(S-*ran*-HOST).

### *3.3.2 Covalent Grafting of P(S-ran-HOST )to $SiO_x$*

The set of random copolymers, containing a high concentration of –OH groups from the PHOST block, were spin cast onto cleaned silicon wafers. In the first experiment, the wafers were baked above the glass transition temperatures of both PS and PHOST for three days in order to allow the –OH groups to diffuse to and bond with the silica surface. Afterwards, the baked wafers were soaked in a good solvent for at least 30 minutes to remove polymer that was not covalently bound to the silica surface. The resulting brush thicknesses were measured with an ellipsometer, and were found to be between 3.8 to 7.5 nm as the percent of PHOST ( and molecular weight) of the polymer increased, as shown in Figure 3. 5.

One of the samples baked for 3 days (RC4) was used as a benchmark to test the kinetics of brush grafting to the silica surface. A cleaned wafer was spin coated with the RC4 polymer and baked for sequential time intervals, and then the excess polymer was removed as before. The resulting brush thicknesses were plotted normalized to the brush length after three days. Figure 3.6 shows that approximately ~76% of the brush attached within the first hour of annealing, and then steadily increased thereafter. The high concentration of –OH groups along the polymer chain led to multipoint attachment of the polymer to the silica surface. These results show significantly improved grafting efficiency than other similar random copolymer brush surfaces, which only have –OH groups on the end of the polymer chain.[6]

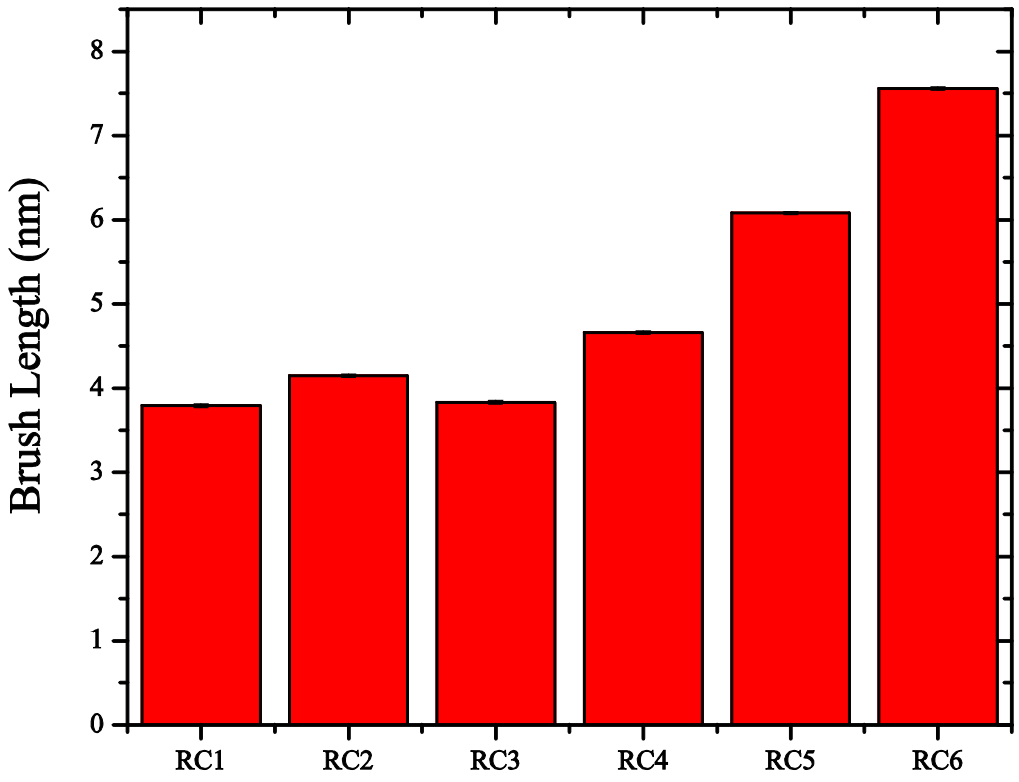


Figure 3.5. Random copolymer brush thickness after covalent grafting to the silica surface

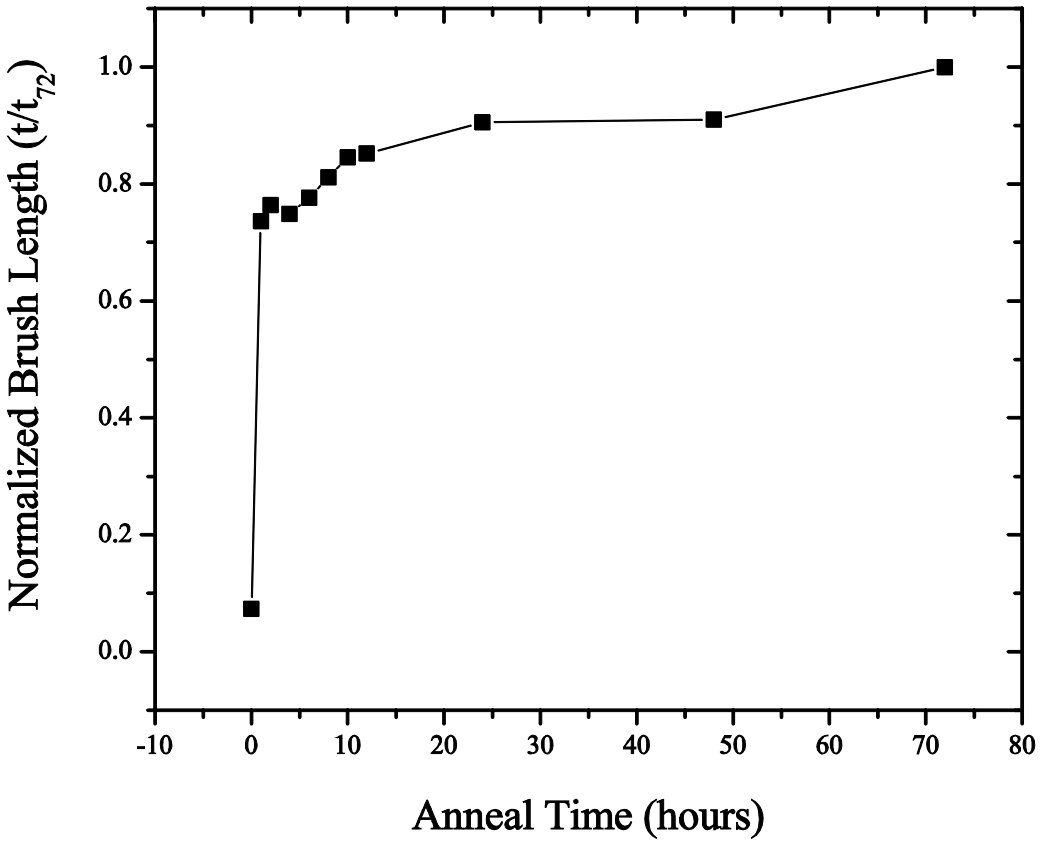


Figure 3.6. Brush length of P(S-*ran*-HOST, RC4) over time, normalized to the thickness of the brush after 72 hours.

### *3.3.3 Surface Energy Analysis*

Careful control of the molar fraction of PHOST ($f_{PHOST}$) in the random copolymer allowed for precise control over the surface energy of the random copolymer brush. First, the advancing contact angles of water and diiodomethane on the brush surface were measured, as shown in Table 3.2. Immediately evident was that the contact angles decreased as $f_{PHOST}$ increased, which translated to a more hydrophilic surface. These results were consistent with what was expected for the polymer brush surface: the presence of the –OH groups in PHOST made the surface more polar and should increase the hydrophilicity if the –OH groups are exposed to the air interface.

The surface energies of the RC-modified substrates were calculated from the contact angle data using the two-liquid harmonic method, and are shown in Figure 3.7(a).[21] The total surface energy measurements are composed of both dispersive and polar components, and also provide a confirmation of the behavior of the polymer on the molecular scale. The results showed that as $f_{PHOST}$ increased, the polar component of the surface energy increased by a small but significant amount, while the dispersive component remained the same. This result also pointed to the increased presence of the highly polar –OH groups of PHOST on the surface. The results also indicated that the RC-modified substrates featured surface energies that span from 47.39 ± 0.13 mJ $m^{-2}$ to 51.84 ±0.05 mJ $m^{-2}$. These values are located in between that of the PαMS (44.5 mJ $m^{-2}$) and PHOST (56.0 mJ $m^{-2}$) homopolymers, proving the ability to tune the surface energy of the RC substrate to balance the interfacial interactions in each block in PαMS-*b*-PHOST block copolymer.

Table 3.2. Contact Angles of Water and Diiodomethane ($CH_2I_2$) on P(S-*ran*-HOST) Brush Surfaces

| | **$f_{PHOST}$ (mol %)** | **$\theta_{water}$(°)** | **$\theta_{diiodomethane}$ (°)** |
|---|---|---|---|
| **RC1** | **18.1%** | **88.08 ± 0.34** | **34.51 ± 0.09** |
| **RC2** | **25.0%** | **86.39 ± 0.07** | **33.31 ± 0.06** |
| **RC3** | **34.6%** | **84.79 ± 0.04** | **31.78 ± 0.06** |
| **RC4** | **43.3%** | **83.43 ± 0.06** | **30.17 ± 0.05** |
| **RC5** | **54.9%** | **82.35 ± 0.13** | **30.19 ± 0.09** |
| **RC6** | **67.1%** | **81.42 ± 0.11** | **29.28 ± 0.05** |

a)

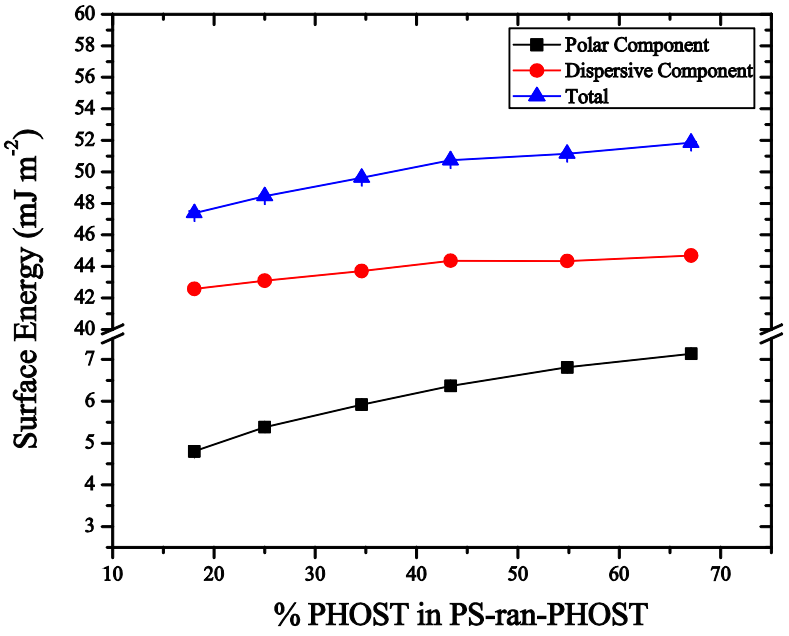


b)

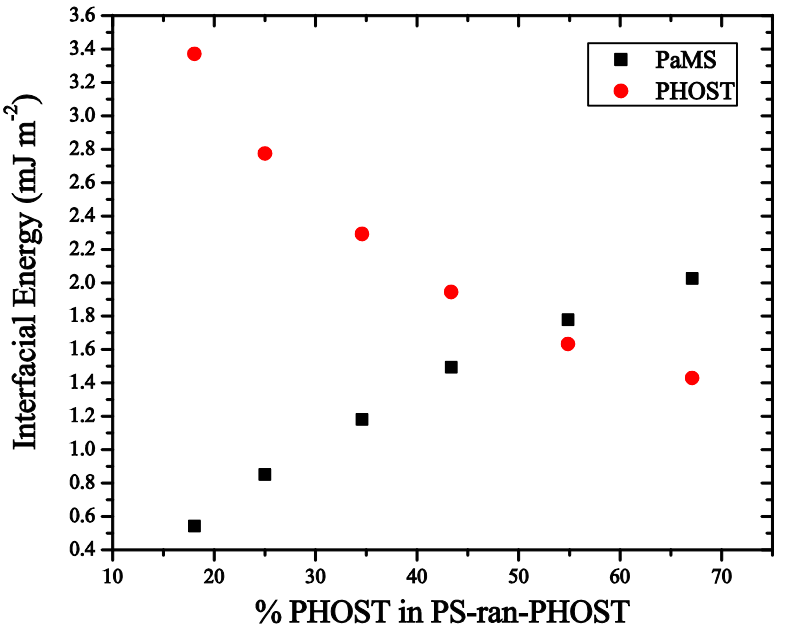


Figure 3.7. Surface energy of the RC substrates as a function of the percent of PHOST in the copolymer. Total surface energy (▲) is the sum of dispersive (●) and polar (■) components. (b) Interfacial energies of PαMS (■) and PHOST (●) against the RC substrate plotted as a function of the percent of PHOST in the copolymer.

To estimate the interfacial energy of either the PαMS or PHOST block against the various RC-brush modified substrates, we used the harmonic mean equation shown in Equation 3.1 [27]

$$\gamma_{polymer-RC} = \gamma_{polymer} + \gamma_{RC} - \frac{4\gamma^{d}_{polymer}\gamma^{d}_{RC}}{\gamma^{d}_{polymer} + \gamma^{d}_{RC}} - \frac{4\gamma^{p}_{polymer}\gamma^{p}_{RC}}{\gamma^{p}_{polymer} + \gamma^{p}_{RC}} \qquad \text{(Eq. 3.1)}$$

where $\gamma_{polymer\text{-}RC}$ is the interfacial energy between the polymer and the RC brush, $\gamma$ is the total surface energy, $\gamma^{p}$ is the polar component, and $\gamma^{d}$ is the dispersive component of the surface energy calculated from the contact angles shown in Table 3.2. The subscript "polymer" refers to either the PαMS or PHOST block in this case, and the subscript "RC" refers to the surface energy parameters for each random copolymer. Figure 3.7 (b) shows the estimated interfacial energies of PαMS and PHOST against the RC surface as a function of $f_{PHOST}$. It was found that the minimum interfacial energy of the PαMS against the RC substrate ($\gamma_{P\alpha MS\text{-}RC}$) occurred on the RC1 sample ($f_{PHOST}$ =18%). Therefore, the RC1-modified substrate was predicted to be preferential to the PαMS block. When the percentage of PHOST in the block copolymer was increased, the surface energy difference between PαMS and the RC surface became larger, and therefore, $\gamma_{P\alpha MS\text{-}RC}$ was increased. On the other hand, the surface energy difference between PHOST and the RC surface ($\gamma_{PHOST\text{-}RC}$) had its minimum when the percentage of PHOST was at its maximum in the series (RC6, $f_{PHOST}$ =67%), and increased with decreasing PHOST content. It was important to note that the interfacial energies, $\gamma_{P\alpha MS\text{-}RC}$ and $\gamma_{PHOST\text{-}RC}$, were nearly equivalent in the RC5 sample ($f_{PHOST}$ =55%), indicating the formation of a surface which exhibited no preferential interaction between either PαMS or PHOST blocks.

### *3.3.4 Solvent Annealing PαMS-b-PHOST on RC-Modified Surfaces*

Solvent annealing is a technique that has been used to gain mobility in polymer thin films without having to bake the film at a high temperature. [28, 29] The

reason for this is that the solvent vapor molecules act as a plasticizer, forcing the polymer chains apart and creating more "free volume" in the film. Since polymer films are typically constrained laterally and by a supporting substrate, the film swells dramatically in the z-direction, sometimes to over 250% of the original film thickness.[19] Thus, the polymer film experiences a significantly depressed $T_g$, the magnitude of which is a function of the size and concentration of the molecular diluent.[30] The softening of the film translates to an enhanced mobility of the polymer chains, allowing the chains to settle into a configuration which is closer to their thermodynamically favorable structure, although there is still some discussion over whether or not the solvent-annealed morphologies are actually a metastable state. For all practical purposes, however, the $T_g$ of the block copolymer returns instantly to its original (dry) $T_g$ (~180 °C) after the fast evaporation of the solvent vapor from the film, and the newly formed morphology becomes kinetically trapped.

PαMS-*b*-PHOST (18k/35k g/mol, 34% PαMS) was spin coated onto the RC-modified substrates as a thin film approximately 48 nm thick, approximately corresponding to the natural period of the block copolymer domain spacing ($L_o$). The films were exposed to a saturated vapor of tetrahydrofuran for eight hours and dried immediately with a blast of dry nitrogen. The top-view of the resulting films was imaged using an AFM and is shown in Figure 3.8. Immediately evident was the change of film morphology on the RC-modified substrates, as the surface energy changed. The preferential adsorption of the PαMS block on the RC1 substrate forced the cylinders to lie parallel to the substrate. As $f_{PHOST}$ is increased, a majority of parallel cylinders was observed in the AFM images until the RC4-modified substrate ($f_{PHOST}$=43.3). In this image, the film shows a mixture of dots and lines, which may correspond to a mixture of vertically and parallel-oriented cylinders in the film. Even the RC5 substrate, which is theoretically close to a neutral interfacial energy, showed

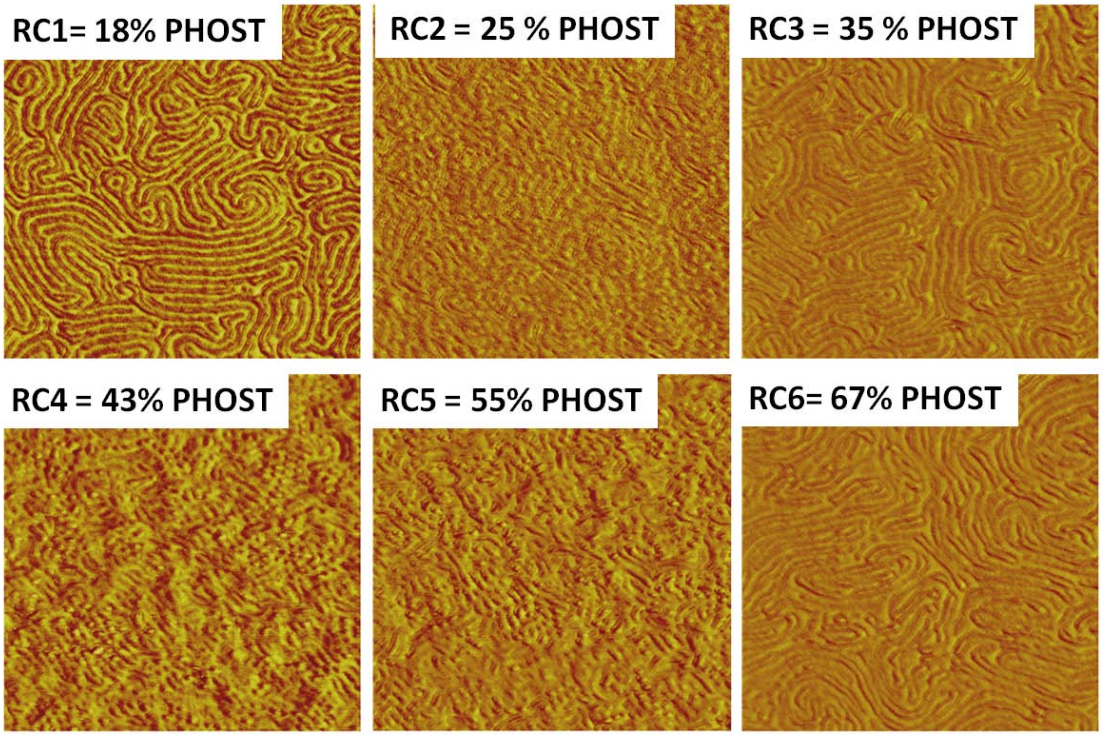


Figure 3.8. Phase-mode AFM images of PαMS-*b*-PHOST spin coated onto RC-modified substrates. a) RC1, $f_{PHOST}$ =18%, b) RC2, $f_{PHOST}$ =25%, c) RC3, $f_{PHOST}$ =35%, d) RC4 $f_{PHOST}$ =43%, e) RC5, $f_{PHOST}$ =55% f) RC6, $f_{PHOST}$ =67%. All images are 2.0 $\mu m^2$ and the data scale is equal is from 0° to 5°.

the same mixture of dots and lines. The results showed that although the substrate may be neutralized by the random copolymer brush surface, the tetrahydrofuran vapor used for the processing may be slightly selective towards the PαMS block, as noted by the solubility parameter for THF (19.33 $Mpa^{1/2}$) being nearly equivalent to that of the PαMS (19.4 $Mpa^{1/2}$), in addition to THF's relatively low dielectric constant (7.8), which classifies it as relatively nonpolar.[23] The lack of sufficient polarity may have caused a preferential attraction of the PαMS cylinders to the polymer/vapor interface. Therefore, a modification of the polymer/solvent vapor interface was also necessary to avoid preferential wetting on the top of the film.

The adjustment to the polymer/solvent vapor interface was executed by blending a more polar solvent in with THF in the solvent annealing chamber. Our strategy was to blend THF with a non-selective, low vapor pressure solvent that is slightly more polar than THF. Selective solvents for the PHOST block that have a high vapor pressure have been shown to cause an order-order transition (OOT) through a selective swelling of the phase with solvent vapor and a resultant increase in volume fraction. [18] An OOT is not desirable in this case, so we selected a higher boiling point solvent. The polarity of a solvent can be quantified in several different ways, including the polar and H-bonding component of the Hansen solubility parameter, the dielectric constant, or the surface tension. The two solvents studied to accomplish the polarity modification are two gycol ethers, propylene glycol monomethyl ether acetate (PGMEA), and dipropylene glycol methyl ether (DPM). The relevant parameters for each are compared to THF in Table 3.3. The gycol ethers are well known to be good solvents for both hydrophobic and hydrophilic materials, and it has been previously reported that PαMS-*b*-PHOST solutions spin coated from PGMEA showed perpendicular orientations, making these solvents a good starting point for our studies.[17]

PαMS-*b*-PHOST solutions were spin coated onto the RC5 substrate and annealed in a blend of DPM:THF (1:1 v/v) for 12 hours and then promptly dried. AFM microscopy of the dried films, shown in Figure 3.9, showed a well-ordered array of dots occurring over large areas of the sample. Evidently, introducing the small amount of DPM solvent vapor acted to avoid the preferential wetting of the PαMS cylinders to the polymer/solvent vapor interface. However, cross-sectional techniques or x-ray scattering must be performed to study the morphology throughout the depth of the film

### *3.4 Conclusion*

A random copolymer P(S-*ran*-HOST) was designed and synthesized to avoid preferential block wetting conditions in the lithographically patternable block copolymer system, PαMS-*b*-PHOST. Neutral surface interactions are required to orient the microdomains vertically for many lithographic applications for this system. Solvent annealing at room temperature has been shown to induce long-range order in this system. However, using solvent vapor processing exposed the block copolymer to another interface that must be tuned to avoid preferential block wetting. This was accomplished by modifying the polarity of the solvent vapor in the annealing chamber. Future work will focus on perfection of the vertical orientation of this block copolymer system throughout the depth of the film.

.

Table 3.3. Relevant parameters related to the solvent annealing of PαMS-*b*-PHOST

| **Solvent** | **Boiling Point (°C)** | **Vapor Pressure (mm Hg)** | **Dielectric Constant** | **Surface Tension (dynes/cm)** |
|---|---|---|---|---|
| THF | 66 | 143 | 7.6 | 28 |
| Propylene glycol methyl ether acetate (PGMEA) | 146 | 3.7 | 8.04 | 28.9 |
| Dipropylene gycol methyl ether (DPM) | 190 | 0.4 | 10.44 | 28.8 |

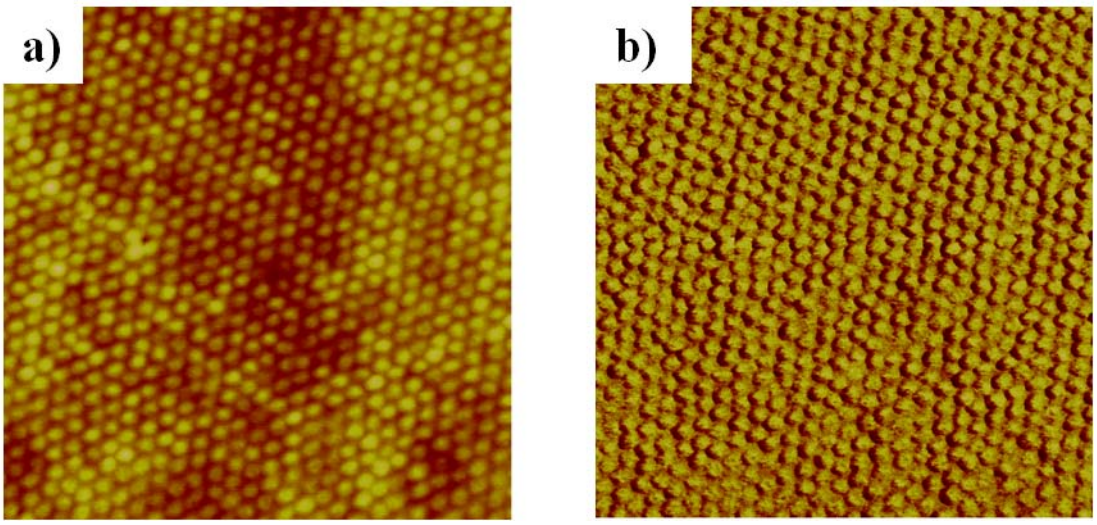


Figure 3.9. AFM images showing a) height and b) phase information for PαMS-*b*-PHOST films on RC5 surface, annealed for 12 hours in a DPM:THF (1:1 v/v) blend. The image areas are 1μm$^2$ and the data scales represented are 10 nm and 10°, respectively.

### *3.5 Acknowledgments*

The authors would like to thank the Semiconductor Research Corporation for funding this research. Zhen Dai, Corissa Lee, Trevor Goff, and Eric Sterling are gratefully acknowledged for their help on this project. This work made use of various facilities of the Cornell Center for Materials Research (CCMR) with support from the National Science Foundation Materials Research Science and Engineering Centers (MRSEC) program (DMR 0520404). This work also made use of various facilities with Cornell's Nanobiotechnology Center (NBTC), in addition to the Cornell Nanoscale Facility, a member of the National Nanotechnology Infrastructure Network, which is supported by the National Science Foundation (Grant ECS-0335765).

## REFERENCES


1. Bates, F. S.; Fredrickson, G. H., Block copolymers-designer soft materials. *Physics Today* **1999,** 52, (2), 32-38.
2. Bates, F. S.; Fredrickson, G. H., Block copolymer thermodynamics: theory and experiment. *Annual Review of Physical Chemistry* **1990,** 41, 525-57.
3. Segalman, R. A., Patterning with block copolymer thin films. *Materials Science & Engineering, R: Reports* **2005,** R48, (6), 191-226.
4. Park, M.; Harrison, C.; Chaikin, P. M.; Register, R. A.; Adamson, D. H., Block copolymer lithography: periodic arrays of ~1011 holes in 1 square centimeter. *Science (Washington, D. C.)* **1997,** 276, (5317), 1401-1404.
5. Kellogg, G. J.; Walton, D. G.; Mayes, A. M.; Lambooy, P.; Russell, T. P.; Gallagher, P. D.; Satija, S. K., Observed surface energy effects in confined diblock copolymers. *Physical Review Letters* **1996,** 76, (14), 2503-6.
6. Mansky, P.; Liu, Y.; Huang, E.; Russell, T. P.; Hawker, C., Controlling polymer-surface interactions with random copolymer brushes. *Science (Washington, D. C.)* **1997,** 275, (5305), 1458-1460.
7. Huang, E.; Pruzinsky, S.; Russell, T. P.; Mays, J.; Hawker, C. J., Neutrality Conditions for Block Copolymer Systems on Random Copolymer Brush Surfaces. *Macromolecules* **1999,** 32, (16), 5299-5303.
8. Mansky, P.; Russell, T. P.; Hawker, C. J.; Mays, J.; Cook, D. C.; Satija, S. K., Interfacial Segregation in Disordered Block Copolymers: Effect of Tunable Surface Potentials. *Physical Review Letters* **1997,** 79, (2), 237 LP - 240.
9. Mansky, P.; Russell, T. P.; Hawker, C. J.; Pitsikalis, M.; Mays, J., Ordered Diblock Copolymer Films on Random Copolymer Brushes. *Macromolecules* **1997,** 30, (22), 6810-6813.

10. Suh, H. S.; Kang, H.; Liu, C.-C.; Nealey, P. F.; Char, K., Orientation of block copolymer resists on interlayer dielectrics with tunable surface energy. *Macromolecules* **2010,** 43, 461-466.
11. Kim, H.-C.; Wallraff, G.; Kreller, C. R.; Angelos, S.; Lee, V. Y.; Volksen, W.; Miller, R. D., Photopatterned nanoporous media. *Nano Lett.* **2004,** 4, (7), 1169.
12. Genzer, J.; Kramer, E. J., Wetting of substrates with phase-separated binary polymer mixtures. *Physical Review Letters* **1997,** 78, (26), 4946-4949.
13. Peters, R. D.; Yang, X. M.; Kim, T. K.; Sohn, B. H.; Nealey, P. F., Using Self-Assembled Monolayers Exposed to X-rays To Control the Wetting Behavior of Thin Films of Diblock Copolymers. *Langmuir* **2000,** 16, (10), 4625-4631.
14. Albert, J. N. L.; Baney, M. J.; Stafford, C. M.; Kelly, J. Y.; Epps, T. H., Generation of monolayer gradients in surface energy and surface chemistry for block copolymer thin film studies. *ACS Nano* **2009,** 3, (12), 3977-3986.
15. Russell, T. P.; Thurn-Albrecht, T.; Tuominen, M.; Huang, E.; Hawker, C. J., Block copolymers as nanoscopic templates. *Macromolecular Symposia* **2000,** 159, (Polymer Science and Industrial Research in the Fast-Changing Age), 77-88.
16. Saavedra, H. M.; Mullen, T. J.; Zhang, P.; Dewey, D. C.; Claridge, S. A.; Weiss, P. A., Hybrid strategies in nanolithography. *Rep. Prog. Phys.* **2010,** 73, 036501.
17. Li, M.; Douki, K.; Goto, K.; Li, X.; Coenjarts, C.; Smilgies, D. M.; Ober, C. K., Spatially Controlled Fabrication of Nanoporous Block Copolymers. *Chemistry of Materials* **2004,** 16, (20), 3800-3808.
18. Bosworth, J. K.; Ruiz, R.; Paik, M. Y.; Schwartz, E. L.; Huang, J. Q.; Ko, A. W.; Smilgies, D. M.; Black, C. T.; Ober, C. K., Control of Self Assembly of

Lithographically-Patternable Block Copolymer Films. *ACS Nano* **2008,** 2, (7), 1396-1402.

19. Paik, M. Y.; Bosworth, J. K.; Smilges, D.-M.; Schwartz, E. L.; Andre, X.; Ober, C. K., Reversible morphology control in block copolymer films via solvent vapor processing: an in-situ GISAXS study. *Macromolecules* **2010,** 43, 4253-4260.
20. Bosworth, J. K.; Black, C. T.; Ober, C. K., Selective area control of self-assembled pattern architecture using a lithographically patternable block copolymer. *ACS Nano* **2009,** 3, (7), 1761-1766.
21. Wu, S. J., *J. Polym. Sci.* **1971,** C34, 19.
22. Odian, G., *Principles of Polymerization.* 2nd ed.; Wiley-Interscience: New York, 1981.
23. Brandrup, J.; Immergut, E. H.; Grulke, E. A., *Polymer Handbook*. 4th ed.; Wiley-Interscience: New York, 1999.
24. Stuen, K. O.; In, I.; Han, E.; Streifer, J. A.; Hamers, R. J.; Nealey, P. F.; Gopalan, P., Imaging layers for the directed assembly of block copolymer films: Dependence of the physical and chemical properties of patterned polymer brushes on brush molecular weight. *Journal of Vacuum Science & Technology, B: Microelectronics and Nanometer Structures* **2007,** 25, (6).
25. In, I.; La, Y.-H.; Park, S. M.; Nealey, P. F.; Gopalan, P., Side-chain grafted random copolymer brushes as neutral surfaces for controlling the orientation of block copolymer microdomains in thin films. *Langmuir* **2006,** 22, 7855-7860.
26. Gordon, A. J.; Ford, R. A., *Chemist's Companion: A handbook of practical data, techniques, and references*. Wiley-Interscience: New York, 1972.
27. Wu, S. J., *Polymer Interface and Adhesion*. Marcel Dekker: New York, 1982.

28. Kim, G.; Libera, M., Morphological Development in Solvent-Cast Polystyrene-Polybutadiene-Polystyrene (SBS) Triblock Copolymer Thin Films. *Macromolecules* **1998,** 31, (8), 2569-2577.

29. Jeong, U.; Ryu, D. Y.; Kho, D. H.; Kim, J. K.; Goldbach, J. T.; Kim, D. H.; Russell, T. P., Enhancement in the orientation of the microdomain in block copolymer thin films upon the addition of homopolymer. *Advanced Materials (Weinheim, Germany)* **2004,** 16, (6), 533-536.

30. Chow, T. S., Molecular interpretation of the glass transition temperature of polymer-diluent systems. *Macromolecules* **1980,** 13, (2), 362-364.

31. Chen, Y.; Wang, Z.; Gong, Y.; Huang, H.; He, T., Solvent-Induced Novel Morphologies in Diblock Copolymer Blend Thin Films. *Journal of Physical Chemistry B* **2006,** 110, (4), 1647-1655.

# CHAPTER FOUR:

## HIGH REFRACTIVE INDEX PHOTORESISTS FOR NEXT GENERATION LITHOGRAPHY BASED ON HAFNIUM-OXIDE NANOPARTICLES[*]

[*] Markos Trikeriotis, Evan L. Schwartz, Marie E. Krysak, Woo Jin Bae, Peng Xie, Neal Lafferty, Bruce Smith, Emmanuel Giannelis, Christopher K. Ober. *To be submitted.*

### *4.1 Introduction*

The extension of optical lithography for future semiconductor devices will be made possible through synergistic innovations in applied optics and materials chemistry.[1] The demand for increasing circuit density calls for a concomitant decrease in the patterned half-pitch (HP). Decreases in HP will come from one of three sources: a) a decrease in the exposure wavelength (λ), b) an increase in the numerical aperture (NA) of the imaging system, or c) a decrease in the process factor (k), as given by the following equation:

$$CD = \frac{k\lambda}{NA}. \qquad \text{[Eq. 4.1]}$$

Modern photolithographic systems commonly use a 193nm wavelength (ArF) excimer laser for lithographic exposure. Since replacing these tools with even lower wavelength extreme ultraviolet (λ=13.5 nm) scanners would be extremely expensive,[2] it is becoming increasingly likely that companies doing high-volume lithographic patterning will aim to push the currently used 193nm systems with higher-NA lenses, fluids and resist systems down to the 15nm node, expected to be reached in 2013.[3] As an example of this approach, research well over 100 years old showed that the introduction of an immersion liquid between the final optical lens and the resist film leads to an increase in the NA of the optical system and improved depth of focus (DOF) of the imaging system.[4] Ultra-pure water is now the commercially accepted first-generation immersion fluid, which allows for an NA equal to 1.35, and the production of 45nm half-pitch features.[5] While research in these advanced optical lenses and fluids has advanced admirably,[6, 7] the materials technology for next-generation photoresists still remains a question.

There are two requirements that next generation photoresists must meet in order to be applicable to high-NA lithography. First, it has been found through

extensive simulations that the use of high-NA optics requires a corresponding resist material with a refractive index > 1.9.[8,9] A high-RI resist has also been found to be beneficial in increasing the mask error exposure factor and improving the DOF.[10] Second, these resists must show improved etch resistance during the pattern transfer step. This is important because as the patterned CD drops below 32 nm, the tendency for the features to collapse after the development step becomes much greater. Pattern collapse can be remedied by decreasing the aspect ratio of the patterned features, which is equivalent to the use of a thinner resist film. Therefore, compared to the amount of etching into the substrate performed for thick 248nm resist films, the relatively thin next-generation resist films must be able to withstand an equivalent amount of etching into the substrate.

Although the theory is in place, the design of practical materials that match the refractive index requirements mentioned above have been fraught with difficulty. The strategy towards increasing the RI of a polymeric photoresist has been to use monomers containing highly polarizable elements such as lead, sulfur, nitrogen, or phosphorus.[11,12] Unfortunately, the addition of these elements causes a simultaneous increase in the absorbance of the resist, leading to an unacceptable tradeoff in material properties. Recently, hafnium oxide ($HfO_2$, or hafnia) has emerged as a material of choice for high-RI resist systems, due to the discovery that pure hafnia has an RI approaching 2.90 at the 193nm wavelength.[7] Hafnia has become a very important material due to its large dielectric constant ($\varepsilon \sim 30$), high melting point (2758 °C) and great chemical stability. In fact, in early 2007, the semiconductor industry began replacing $SiO_2$ with $HfO_2$ in 45nm node metal-oxide-semiconductor (MOS) devices, based on the discovery that hafnia enables a thinner gate dielectric, while also reducing leakage current.[13, 14]

There are examples of the use of hafnium in other areas of engineering, as well. In the field of 3-D holographic lithography, high-refractive index monomers have been used extensively to create photonic band gap structures. In one example, zirconium or hafnium acrylate monomers are mixed with a radical photoinitiator (Irgacure) and excited with a laser to form a crosslinked network via the propagation of the photo-generated radical.[15,16] An example of non-chemically amplified lithography, the resolution of these systems is limited to sub-micron features by the use of visible wavelength lasers ($\lambda$ = 632.8 nm). For future high-resolution lithography, we demonstrate that this same concept can be exploited using lower wavelength, higher energy photons such as those originating from an ArF excimer laser.

Concurrently, efforts have been ongoing in the design of photoresists with alternative molecular architectures, including those with a smaller pixel size and new elemental compositions. One of these new design trends focuses on the use of monodisperse 1-2 nm molecules known as molecular glasses, due to their ability to form amorphous films upon spin coating.[17,18] Molecular glasses offer many of the same performance features of polymers, such as good film-formability and high glass transition temperature ($T_g$), combined with a reduced "pixel" size of the imaging unit to allow for the possibility of higher achievable resolutions. In a typical resist design, a central core of the molecule is selected that will increase etch resistance and glass transition temperature of the molecule, while the shell of the molecule typically consists of a mixture of phenolic and photolabile lipophilic molecules for a combination of adhesion and sensitivity of the resist. Within this design framework, inorganic components have been used to increase etch resistance of the central core of the molecule without sacrificing glass transition temperature or UV transparency. Some examples from our research group have included the use of boron or silicon in

the resist design. [19-21] Previous work in other research groups have shown the feasibility of using a small silicon nanoparticle as a central core for a photoresist, surrounded by a polymer containing an acid-labile protecting group such as *tert*-butyl acrylate. [22] Along these lines, the aim of our work is to develop a photoresist featuring high-refractive index hafnia nanoparticles that will be suitable for high-throughput lithographic patterning using far ultraviolet (ArF), extreme ultraviolet (EUV) and e-beam radiation sources. Contrary to the trend in lithography, however, the patterning mechanism for these nanoparticles does not use chemical amplification. Instead, a non-chemically-amplified, negative-tone process was used, as shown in Figure 4.1. The hafnia nanoparticles are covered with an organic ligand containing an unsaturated bond that can cause the crosslinking of neighboring nanoparticles upon exposure to photo-generated radicals. Alternatively, this resist is also capable of positive-tone patterning, although this route will not be discussed in this chapter. The first half of the chapter will discuss the synthesis and characterization of the hafnia nanoparticles, while the second half of the chapter will discuss the performance of this new resist material with 193nm interference lithography.

## *4.2. Experimental Methods*

### *4.2.1 Materials*

All materials were used as received from Aldrich unless otherwise noted. Methacrylic acid was distilled using a Büchi ball-tube distillation apparatus (Büchi B585) to remove inhibitors and other impurities.

### *4.2.2 Synthesis of Hf-MAA*

A similar synthesis of hafnia nanoparticles has been described in a previous publication.[23] To a three-neck round bottom flask, 5 g (12 mmol) of hafnium

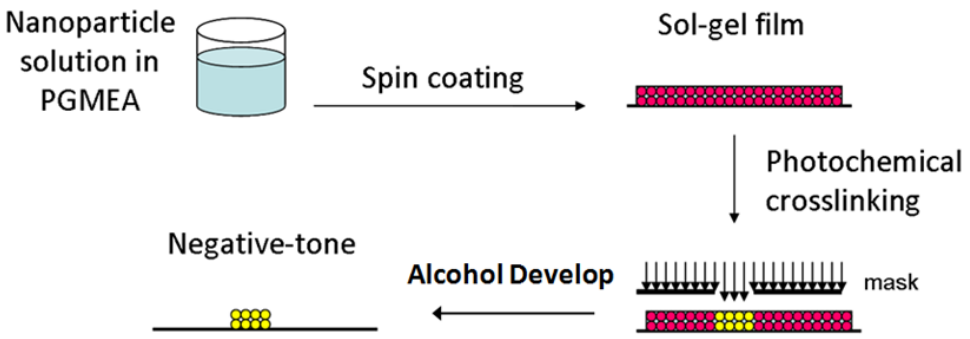


Figure 4.1. Schematic showing the process flow for the negative-tone lithographic patterning of Hf-MAA

isopropoxide precursor and 25 ml (286 mmol) of methacrylic acid were added along with a magnetic stir bar. After sealing the flask with two rubber septa and a condenser, the solution was allowed to equilibrate at 65 °C under reflux while stirring at 300 rpm for 15 minutes. Separately, 9 ml of methacrylic acid was mixed with 1 ml of deionized water (55.5 mmol) in a syringe until a homogenous solution was formed. To start the hydrolysis and condensation reaction, the water/MAA solution was slowly injected into the reaction flask over the course of one minute. During the injection, the precursor suspension turned from turbid to clear. After 18 hours, an additional injection of (9 ml of MAA and 1 ml of $H_2O$) was added with a syringe. After 2 additional hours, the reaction was stopped and the nanoparticles precipitated by adding a 2:1 volume of DI $H_2O$ into the reaction flask. The white nanoparticle aggregates were centrifuged at 8000 rpm for 8 minutes to separate them from the supernatant and the supernatant was decanted off. A cycle of dissolving the aggregates in acetone, precipitating in DI $H_20$ and then separating the aggregates via centrifuge was performed 4 times to remove excess methacrylic acid. After the final wash step, the supernatant was decanted and the nanoparticles were placed in a vacuum oven at room temperature for at least twenty-four hours to form a dry white powder (yield ~70%).

### *4.2.3 Film Preparation*

The nanoparticles were dissolved in 10 wt. % (w/v) in propylene glycol methyl ether acetate (PGMEA) along with 0-5 wt. % (relative to Hf-MAA weight) of the radical photoinitiator 2,2-dimethoxy-2-phenyl acetophenone (DPAP). After the solution became transparent after 3-4 minutes, it was passed through a 0.2 μm nylon filter twice. Freshly cleaned 4'' silicon wafers were dehydrated by heating on a hotplate at 200 °C for 1 minute and then cooled to room temperature prior to spin

coating. A bottom anti-reflection coating (BARC) underlayer (ARC29A-8) was supplied by RIT and spun onto the dehydrated Si wafer at 1000 rpm for 60 seconds, baked at 200 °C for 90 seconds to remove casting solvent and to initiate the thermal crosslinking of the underlayer, and then cooled back down to room temperature prior to the spin coating of the resist on top. 0.5 mL of the Hf-MAA resist solution was dropped on the center of the wafer, and the wafer was spun at 2000 rpm for 60 seconds to give a smooth film. The film thickness was controlled by either changing the solution concentration (7-15 wt.%) or the spin speed from 1,000-5,000 rpm. After spin coating, the film was baked for 60 seconds at 130°C on a hotplate to remove residual casting solvent and immediately taken for lithographic exposure. Plasma etching of the films were performed on a Plasmatherm 72 etcher ($SF_6$= 13 sccm, $O_2$ = 40 sccm), with a system pressure of 50 mTorr, and a power equal to 100 W.

### *4.2.4 Interference Lithography*

A Talbot interference lithography system using a compact prism printed periodic line/space patterns of variable pitch using a Lambda Physik OPTex Pro 193nm ArF excimer laser with line-narrowing T-Module. This system has been described previously.[24] This optical setup used a spatially coherent light beam that passes through the center of the optical path. The beam was split by passing through a 1:1 duty ratio chromeless phase grating, and only the $1^{st}$ and $-1^{st}$ diffraction orders were used as the interference waves. After beam splitting, the waves passed through a specially-designed Smith-Talbot prism which had a reflective coating on the prism facets. The angle of the facets, combined with the phase grating pitch, defined the arrival angle of the light at the wafer and the ultimate numerical aperture of the imaging system. Different prisms have been designed, allowing for the patterning of a variety of half-pitch lines, as shown in Table 4.1.

Table 4.1. Prism designs created for the Talbot interferometer and the resulting half-pitch of the intensity modulation.

| NA | Half-pitch (nm) |
|---|---|
| 0.32 | 150 |
| 0.54 | 90 |
| 0.80 | 60 |
| 1.05 | 45 |
| 1.20 | 40 |
| 1.35 | 36 |

### *4.2.5 Characterization*

The size of the nanoparticles was measured by dynamic light scattering using a Malvern Zetasizer Nano-ZS by dispersing them in 5 mg/mL, twice filtered solution in PGMEA. Thermal analysis was performed on a TA Q1000 modulated differential scanning calorimeter (DSC). About 10 mg of the blend sample was placed in aluminum pans and heated from 25 °C to 250 °C at a 15 °C/minute heating rate to erase the thermal history, cooled to room temperature, and then heated again. Data was acquired on the first heating ramp. An empty aluminum pan was used as the reference. To measure the thermal degradation of the blend components, a TA Instruments Q500 Thermogravimetric Analyzer (TGA) was used to heat the samples from room temperature to 550 °C at a heating rate of 5 °C/minute under a nitrogen atmosphere. High-resolution transmission electron microscopy (HR-TEM) was performed on a field emission Tecnai FEI F20 TEM operating at 200 kV.

The imaging of the patterned nanoparticles was performed using a LEO 1550 scanning electron microscope (SEM) equipped with a field emission gun, operating at 8 kV. For FTIR sample preparation, the nanoparticles were dried under reduced pressure to remove residual water, and then added in 1% (w/w) to dry KBr powder and pressed into a disc 13 mm in diameter and 1.5 – 2 mm in thickness. FTIR spectra were collected on a Mattson spectrometer using a wavenumber range from 400 to 4000 $cm^{-1}$, with a nominal resolution of 2 $cm^{-1}$. For each spectrum, 64 scans were collected and averaged. For optical absorbance measurements of the nanoparticle films, the films were spin coated on cleaned quartz wafers, baked at 130 °C for 1 min, and then measured using a Shimadzu UV-3101 UV/Vis Spectrophotometer. The film thickness was measured on a Woollam Variable-Angle Spectroscopic Ellipsometer (VASE), using a Cauchy optical model fitting procedure.

### *4.3 Results and Discussion*

#### *4.3.1 Hydrolysis and Condensation Mechanism*

The synthesis of the hafnia nanoparticles was performed using a traditional hydrothermal technique. Previous work has shown that it is also possible to synthesize $HfO_2$ nanocrystals via non-hydrolytic procedures, by reacting hafnium isopropoxide with hafnium halides at high temperature in a strongly coordinating solvent, although these procedures will not be discussed in detail here.[25, 26] The metal alkoxide precursor used in our study, hafnium isopropoxide, is mixed in a large molar excess of methacrylic acid to produce a turbid mixture in an air atmosphere. After the mixture equilibrated at 65 °C, a precise amount of water was injected and the mixture turned transparent, signifying the solvation of the metal alkoxide and the start of the hydrolysis and condensation reactions. While the humidity in the air may have had some small effect on the hydrolysis step, this effect was minimal considering the total amount of water that was added over the course of the reaction (2 mL). A typical hydrolysis reaction for a tetravalent metal alkoxide can be chemically identified by the following reaction mechanism:[27]

Hydrolysis: $Hf(OR)_4 + H_20 \rightarrow HO\text{-}Hf\text{-}(OR)_3 + ROH$

$\rightarrow\rightarrow Hf(OR)_4 + 4H_20 \rightarrow Hf\text{-}(OH)_4 + 4ROH,$ [Eq. 4.2]

where R represents the isopropoxide ligand used in our reactions. The reaction byproduct (ROH), therefore, is isopropanol. Other hafnium precursors, such as hafnium tert-butoxide and hafnium n-butoxide, have substantially different reaction kinetics and were not investigated in detail in this study. Hydrolysis was quickly followed by condensation reactions, in which hydrolyzed atoms were chemically bound to form the shape of the nanoparticle:

Condensation: $(OR)_3Hf\text{-}OH + HO\text{-}Hf\text{-}(OR)_3 \rightarrow (OR)_3Hf\text{-}O\text{-}Hf(OR)_3 + H_20$

$\rightarrow\rightarrow$ highly branched network structure [Eq. 4.3]

### *4.3.2 The Role of Methacrylic Acid*

The large molar excess of methacrylic acid (MAA) in the reaction has multiple functions. First, it provided an acid catalyst for the hydrolysis step. The pKa of methacrylic acid is 4.66, from a literature value.[28] Second, MAA monomer chemically modified the metal alkoxide precursor with a shell of methacrylic acid ligands, which retarded the hydrolysis and condensation reaction rate by sterically hindering the entry of other hydrolyzed hafnia isopropoxide molecules. As the sol-gel reaction occurred, esterification reactions took place on the shell of the nanoparticle to covalently bind the –COOH functional group from MAA to the Hf-OH groups on the nanoparticle via an acid catalyzed nucleophilic acyl substitution. Other functional groups, such as phosphonates, have been used to strongly bind to metal oxide nanoparticles.[29] Since the reaction is conducted at a relatively low temperature (65 °C), it is likely that not all Hf-OH has been completely capped with methacrylic acid ligands and the particles may not be completely condensed. Finally, the surface modification of the Hf-OH nanoparticles by MAA also allows the nanoparticles to be dissolved into a clear solution up to 60-70 wt. % in propylene glycol methyl ether acetate (PGMEA). The same MAA functional group also contained the highly reactive vinyl bond which allowed the crosslinking of neighboring nanoparticles to each other under heat or ultraviolet radiation, as shown in Figure 4.2.

### *4.3.3 Effect of Synthesis on Nanoparticle Size*

The size of the nanoparticles in solution was measured by dynamic light scattering. All nanoparticles showed mean diameters of 1-3 nm, but we found that the size of the nanoparticles varied according to the synthesis conditions. The particles that were synthesized in a large molar excess (~24x) of methacrylic acid relative to the

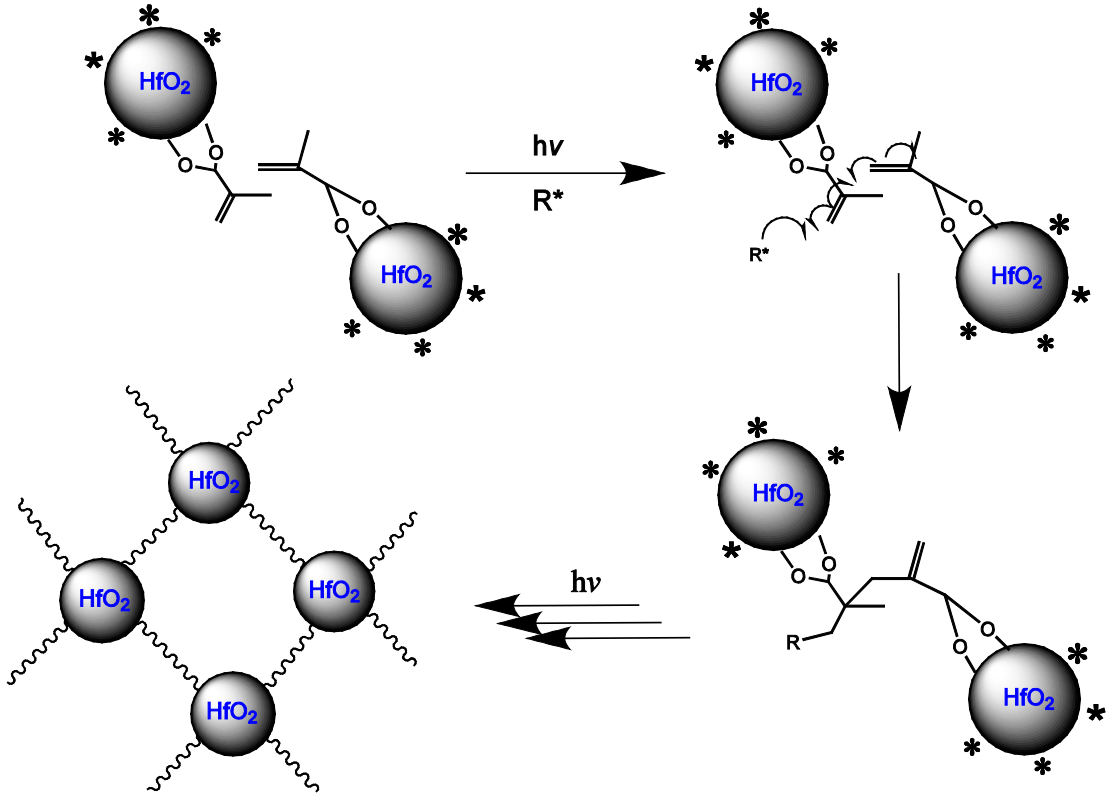


Figure 4.2. A schematic of the crosslinking reaction between neighboring Hf-MAA particles, catalyzed by a free radical generated either by direct exposure to UV light, a photo-radical initiator struck by UV light, or heat. This reaction can continue as the radical source is re-generated, resulting in a crosslinked hafnia network.

hafnia precursor showed mean particle diameters of ~1.6nm, whereas the particles synthesized in an ethanol solvent and only ~10x molar excess showed mean particle diameters of around 2.1nm, as shown in Figure 4.3(a). The dispersity of the nanoparticles, which describes the width of the particle size distribution, averaged around 0.18. As a rule of thumb for nanoparticles, dispersity values below 0.2 are considered to be monodisperse.[30] A representative high-resolution TEM image of the nanoparticle is also shown in Figure 4.3(b), showing crystalline lattice fringes equal to 3.2 angstroms, which match a hafnium crystal structure. The small size of the nanoparticles is important because larger particles will begin to scatter 193nm wavelength light and render the films too opaque for lithography. There has also been some evidence to show that quantum confinement effects can cause a blue shift in the absorbance peak (<<190nm) for silicon nanoparticles at sub-5nm length scales which further motivated us to keep the nanoparticle size small.[31]

### *4.3.4 Chemical Bonding of MAA*

FTIR provided quantitative proof of the covalent binding of the methacrylic acid ligand to the hafnia core. As shown in Figure 4.4, strong peaks appeared at 1470 and 1510 $cm^{-1}$, corresponding to the asymmetric and symmetric stretching of the C-O bond. A broad stretching band was observed around $\nu$ =3300 $cm^{-1}$, and can be attributed to either –OH groups remaining on the hafnia core or to water that is bound on the nanoparticles. A small peak at $\nu$ = 2970 $cm^{-1}$ was assigned to antisymmetric – $CH_3$ stretching. The $CH_2$ wag vibration can be found at ~950 $cm^{-1}$.[32]

FTIR can also differentiate between the two different binding geometries (mono-dentate and bi-dentate) of the oxygen atoms in methacrylic acid to the nanoparticle core. The monodentate mode [$CH_2$=C($CH_3$)-COO-Hf], is denoted by only one oxygen atom is attached to the Hf atom, whereas the bidentate configuration,

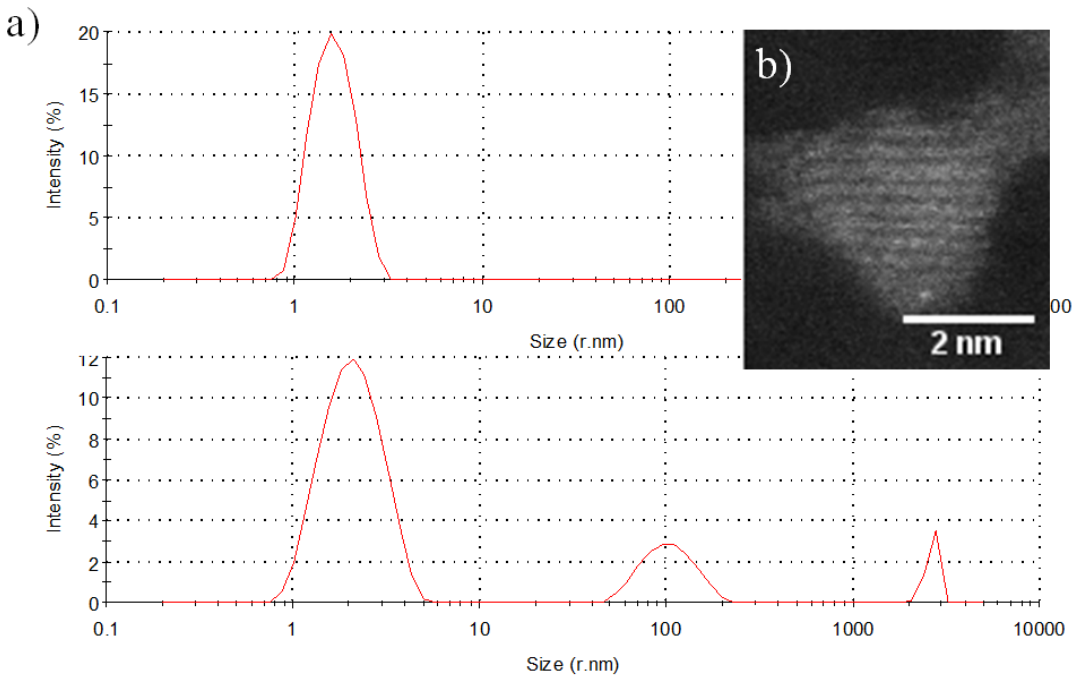


Figure 4.3. a) Dynamic light scattering particle size distributions by intensity. The top graph shows the distribution of particles synthesized in a solvent of methacrylic acid, showing a particle size of 1.6nm. The bottom graph shows the 2.1nm size of particles synthesized in ethanol, with a 10x molar excess of methacrylic acid. B) shows a high-resolution TEM image of a similarly produced hafnia nanoparticle, showing lattice fringes of 3.2 angstroms, which match that of hafnium.

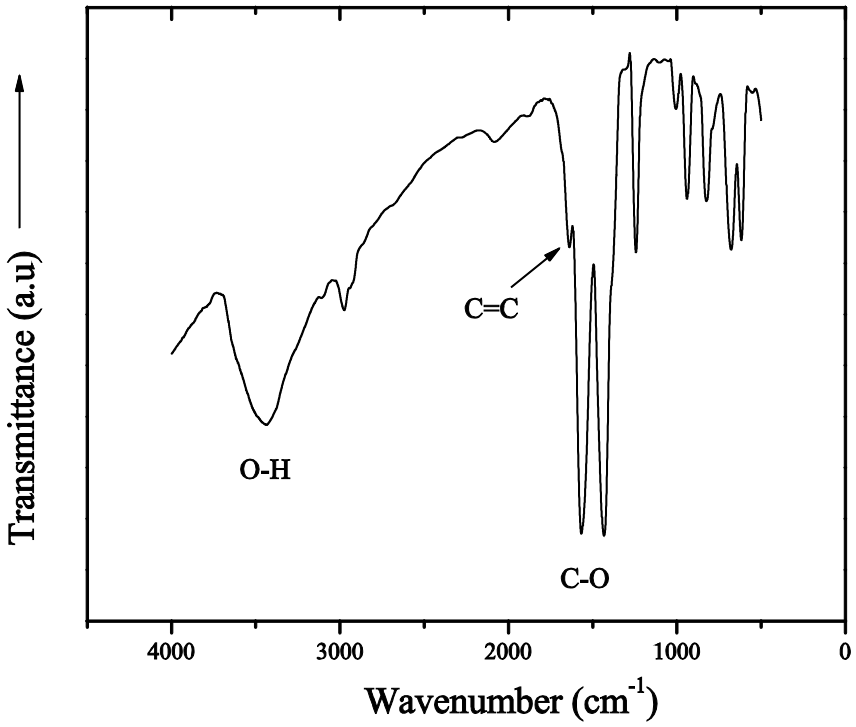


Figure 4.4. FTIR spectra of purified Hf-MAA

is denoted by both oxygen atoms covalently binding to the $HfO_2$ core [$CH_2$=C($CH_3$)-(Hf-O)C(O-Hf)].[33] Due to the lack of the C=O stretch at $\nu$~1700 $cm^{-1}$, FTIR confirmed that the methacrylic acid was attached via the bidentate geometry. The bidentate binding geometry is also known as the more stable configuration of the two.[34]

### *4.3.5 Nanoparticle Organic Content and Purification*

Once the hydrolysis/condensation reaction was complete the nanoparticles were precipitated in a 2:1 excess of water to form aggregates. After centrifugation, the aggregates can be washed with water to remove excess methacrylic acid. However, MAA removal from the center of the aggregate via water washing was inefficient due to slow diffusion. We found that a more efficient purification technique to remove the trapped MAA inside the nanoparticle aggregate involved consecutive cycles of re-dissolving the nanoparticles in acetone, precipitating in water, centrifuging the nanoparticles and then repeating these steps until all the free MAA was removed. Since MAA is soluble in water and the MAA-bound nanoparticles are not, we were able to release the free methacrylic acid into water using this process, which is then poured off during the decanting process.

We checked the efficiency of methacrylic acid removal via DSC. Figure 4.5 shows the heat flow of the nanoparticle powders during the first heating cycle. The heat flow trace showed a large endothermic peak between 160-175 °C, corresponding to the onset of methacrylic acid monomer evaporation (b.p =163 °C). The area under the MAA endothermic peak could be related to the total enthalpy of vaporization of the unbound MAA monomer, and was seen to decrease with each purification step until it remained approximately constant after 3 cycles, as shown in Table 4.2. Interestingly, after the first dissolve/precipitate cycle this peak broadened and shifted

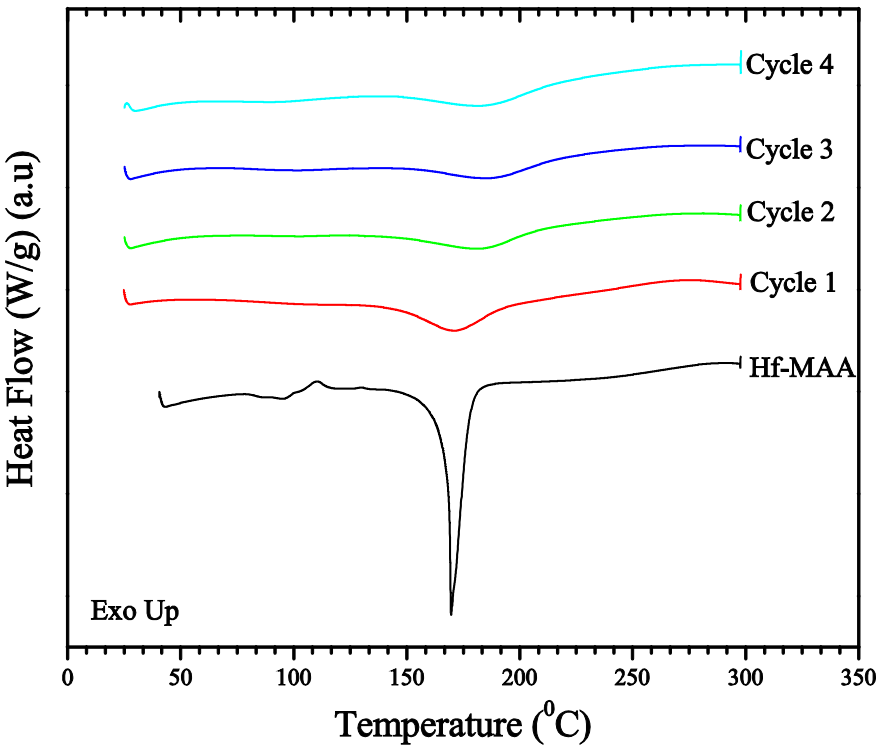


Figure 4.5. The first heating cycle of a DSC curve showed a prominent peak of methacrylic acid evaporation. The area under the peak can be correlated to the latent heat of vaporization of unbound MAA monomer.

Table 4.2. The change in the latent heat of vaporization of methacrylic acid with increased dissolve/precipitate purification cycles of Hf-MAA powder, as determined by integrating the area under the endothermic peak in the first heating cycle of DSC.

| # dissolve/ precipitate cycles | Center of peak (°C) | Latent heat of vaporization (J/g) |
|---|---|---|
| **0** | 169.70 | 138.7 |
| **1** | 171.50 | 54.21 |
| **2** | 182.90 | 55.58 |
| **3** | 187.05 | 45.59 |
| **4** | 184.24 | 30.27 |

to higher temperatures. This may be due to a shift in the location of the majority of free MAA from around the outside of the nanoparticle towards the interior of the nanoparticle aggregate, where it became harder to remove. No evidence of a glass transition temperature was found in any of the heating cycles in DSC.

The organic content of the nanoparticle powders was also quantified via thermogravimetric analysis (TGA), as shown in Figure 4.6. The weight loss of Hf-MAA occurred in two distinct steps. The first weight loss occurred during the 100-200°C temperature ramp, where adsorbed solvents and free methacrylic acid (b.p. = 163 °C) are evaporated from the powder. The second weight loss step occurred from 400-500 °C, corresponding to the decomposition of the bound organic ligand on the surface of the nanoparticle. Before purification, the total weight loss upon heating to 550°C averaged about 40-50%, meaning that 50-60% by weight of the nanoparticles consisted of the inorganic hafnium oxide species, which remained stable at 550 °C.

Higher inorganic contents are expected to lead to a higher etch resistance in the final patterned film due to the chemical stability of hafnium oxide, so it was to our benefit to try to increase the inorganic content as much as possible. Figure 4.6 shows the TGA curves from the as-synthesized Hf-MAA powder, in addition to the Hf-MAA purified by the cumulative purification cycles mentioned above. The TGA traces showed that the as-synthesized Hf-MAA, containing up to 49% organic content in this case, dropped to 28% after three purification cycles. The small difference in weight loss between the third and fourth dissolve/precipitate cycle corresponded with previously shown DSC data which showed that most free methacrylic acid had been removed by this point.

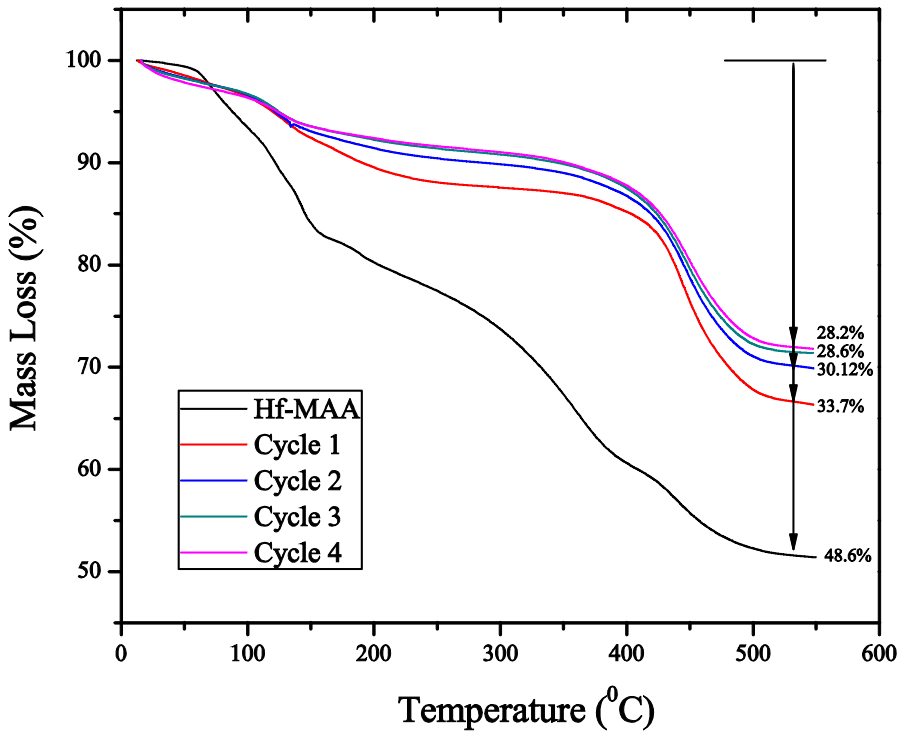


Figure 4.6. The total decrease in organic content dropped to ~28% after removal of free methacrylic acid and remained approximately steady with additional dissolve/precipitate cycles. The leftover organic content was methacrylic acid ligand bound to the hafnia core, which started to decompose at c.a 400 °C.

### *4.3.6 Optical Properties of Hf-MAA*

#### *4.3.6.1 Effect of MAA Impurities on Film Absorbance*

A close examination of the optical properties of the nanoparticles was very important to determine optimal imaging conditions in photolithography. Practically speaking, photoresists must maintain an optical absorbance of less than 4/μm at the chosen imaging wavelength in order to ensure a homogenous distribution of light through the film stack.[35] Resists that are too highly absorbing can suffer from "T-topping" as a result of too much radiation being absorbed at the top of the film. Conversely, if the bottom of the resist film does not receive the requisite dose of radiation, the patterned lines may lift-off as a result of poor adhesion to the substrate. The individual chemical and physical contributions to the nanoparticle resist absorbance will be individually discussed in the following paragraphs.

We measured the optical absorbance of the nanoparticle films spin coated on a quartz substrate at 193nm using a UV spectrophotometer. The same films were also spun onto silicon wafers for an accurate measurement of the film thickness via ellipsometer to find the absorbance per micron of resist. We found that most of the films fell into a range of absorbance from 7-9/μm at 193nm, depending on the extent of removal of the free methacrylic acid. Figure 4.7 shows the absorbance of the unpurified resist at around 8.9/μm, and also the decrease in the absorbance to 7.7/μm after complete removal of the methacrylic acid. We also observed a small (2 nm) hypsochromic shift in the absorbance peak from 204 nm to 202 nm once the nanoparticles were completely purified, possibly due to the change in the electronic environment of the nanoparticles after the free methacrylic acid was removed. It is well known that solvent effects can have a significant effect on the absorption peak for unsaturated carbonyl compounds. [28]

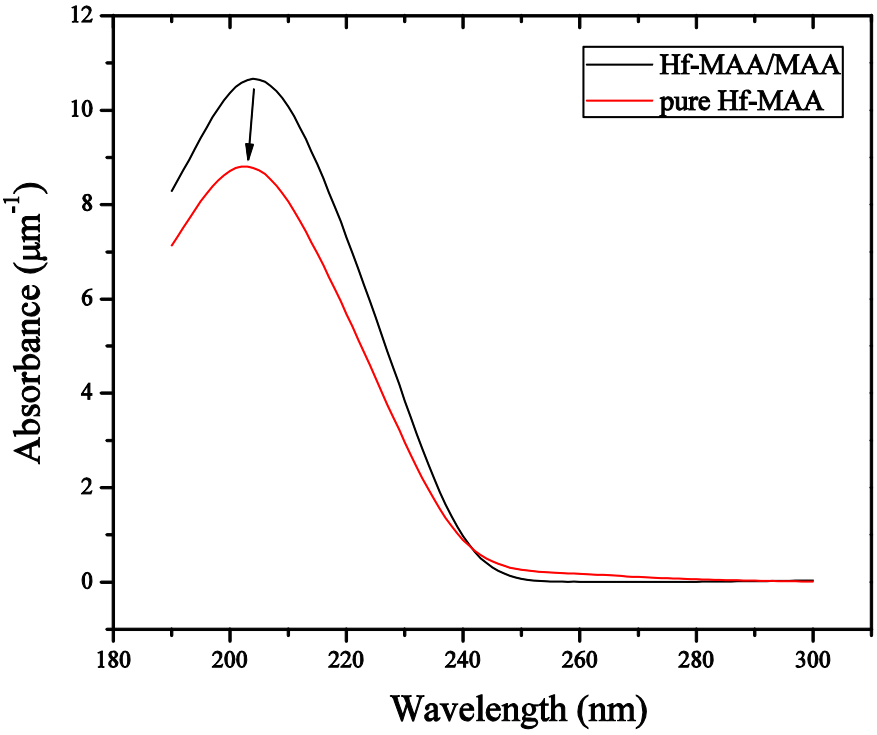


Figure 4.7. Shows the absorbance drop and small shift after purifying Hf-MAA by removing excess methacrylic acid

#### *4.3.6.2 Effect of Electronic Environment on Spectral Peak*

The unsaturated $CH_2$ double bond in both the free and bound MAA is another component of film opacity at 193nm. The effects of the unsaturation can be seen by baking the film at 130°C for thirty minutes, inducing thermal crosslinking of the nanoparticles via the conversion of double bonds to single bonds. The resulting films do not lose any thickness after immersion in PGMEA for 1 hr, indicating complete crosslinking. In this case, the film absorbance dropped to 4/μm and still retained the same spectral shape (not shown).

Despite the existence of the element hafnium and $–CH_2=CH_2-$ double bonds, it was interesting to observe that the salient absorption peak in the UV/Vis spectroscopy of Hf-MAA films most closely matched to a $\pi \rightarrow \pi^*$ transition, similar to that found in the C=O bond in the methacrylic acid monomer. In fact, by comparing the absorbance peak ($\lambda_{max}$) of the free MAA monomer in water with that of the MAA-bound nanoparticles, we found an almost perfect match in spectral shape. However, the attachment of the ligand to the hafnia core leads to a +5 nm shift of the $\lambda_{max}$, from 198 nm to 204 nm, possibly due to electron donation from the hafnia core towards the conjugated system. Woodward and Fieser were among the first to empirically predict $\lambda_{max}$ based on the substituent groups surrounding unsaturated carbonyl systems in UV/Vis spectroscopy.[36] Using these same principles, we found that an electronic shift in $\lambda_{max}$ of up to 10 nm was possible by altering the electronic substituent surrounding the carbonyl group on the acrylic acid backbone. For example, we found that substituting electron withdrawing groups such as $–CF_3$ in the 2-position of the ligand shifted the peak towards lower wavelengths <190 nm (hypsochromic shift), while electron donating groups, such as a propyl group, shifted the peak towards higher wavelengths (bathochromic shift), relative to the original Hf-MAA material, as shown in Figure 4.8. Synthesized hafnia-acrylic acid and hafnia-trifluoromethyl acrylic acid

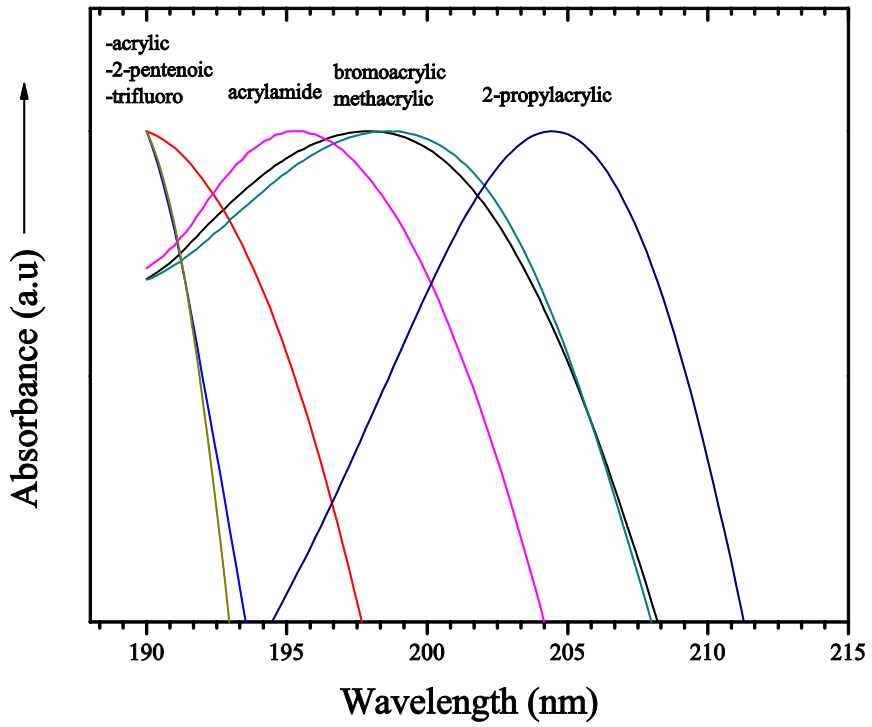


Figure 4.8. The spectral peak of a variety of monomeric acrylic acid derivatives in water. The electronic substituent surrounding the carbonyl group can affect the absorption peak by shifting it ± 10 nm.

nanoparticle $\lambda_{max}$ (c.f Appendix 4.8) also showed the same +5nm shift relative to the free ligand, as displayed in Figure 4.9. Besides the use of an acrylic acid backbone, an acrylamide ligand may also be used to bind to nanoparticles. By substituting an amine group for the –OH, $\lambda_{max}$ of free acrylamide monomer appears 5-10nm higher than acrylic acid as a result of increased electron donation towards the conjugated system. While we have not yet succeeded in synthesizing a nanoparticle using the acrylamide-based ligand series, it may become a promising route to shift the absorbance peak further away from 193nm while still maintaining the vinyl functionality to crosslink the nanoparticles with exposure to UV light.

#### *4.3.6.3 Refractive Index of Hf-MAA*

The refractive index of the resist was also important for modeling the standing waves that result from the constructive and destructive interference of light reflecting from the substrate back up through the resist. Standing waves can cause intensity maxima along the resist cross-section, which can result in undulations in the sidewall profile of a negative-tone photoresist. A bottom anti-reflection coating (BARC) can be spin coated and crosslinked before application of the photoresist to eliminate most of these reflections.

In collaboration with the Rochester Institute of Technology, we have simulated the light absorption through the resist cross-section in order to predict imaging performance using ILSim$^{TM}$.[37] ILSim is an interference lithography simulator based on full vector interference theory, ideally suited to predict imaging performance at the high NA values predicted for use in 193nm immersion lithography. The inputs to the simulation are the refractive index (n) of Hf-MAA (previously measured to be 2.0 at 193nm),[7] imaging wavelength (193 nm), substrate choice (Si), numerical aperture (0.32) and film thickness (100 nm) . Simulation results show that the

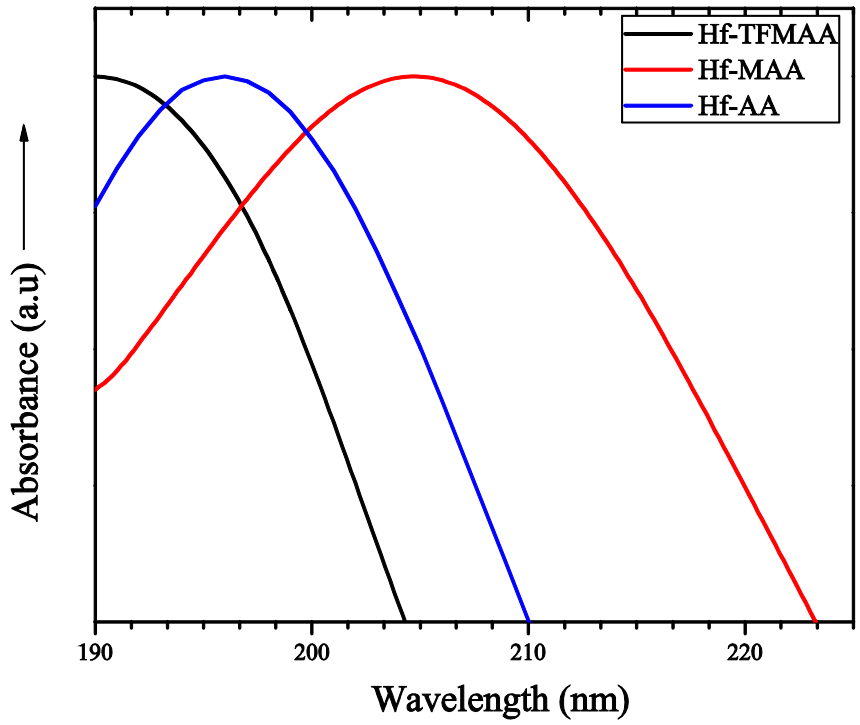


Figure 4.9. Absorbance peak shifts depend on the electronic nature of the substituents. However, attaching the ligand to the hafnia core results in a slight +5nm shift in the absorbance peak relative to that of the monomeric version of the ligand.

extinction coefficient will dramatically change the absorption path of the light through the resist. Two different k-value inputs for the simulation are shown here (0.1 and 0.2), corresponding to absorbance values of 6.5/μm and 13/μm, which bordered the range of measured absorbance values for our nanoparticle batches. The simulations were also run with and without a thick BARC layer to examine the effect of standing wave reflections on the resist profile. The simulation results (Figure 4.10) show the apparent necessity of the BARC layer to control standing wave reflections and allow 193nm light to propagate all the way through the 100nm film stack. The intensity maxima along the film cross-section shown here would manifest as undulating ridges in the patterned line. These images also illustrate the importance of decreasing the absorbance of Hf-MAA as much as possible to reduce the high absorbance that can occur at the top of the film, which can cause T-topping or a skin layer on the surface of the resist.

### *4.3.7 Free Radical Polymerization and Photobleaching*

The absorbance of Hf-MAA may depend critically on the concentration of highly absorbing double bonds originating from the methacrylic acid ligand. Since we have seen UV absorbance peaks from the film which look much like that of the methacrylic acid monomer, this effect should not be underestimated. During the exposure, 193nm radiation is efficiently converted into a free radical through an added photoinitiator in the resist solution, 2,2-dimethoxy-2-phenyl acetophenone (DPAP). A free radical is essentially a molecule which contains an unpaired electron which can electronically react with an unsaturated molecule, such as the MAA monomer. In the vinyl group of MAA, one pair of electrons is held in a stable sigma bond, and another pair is more loosely held in a pi bond. The radical uses one electron from the pi bond to form a more stable bond with the carbon atom, transforming the double bond into a

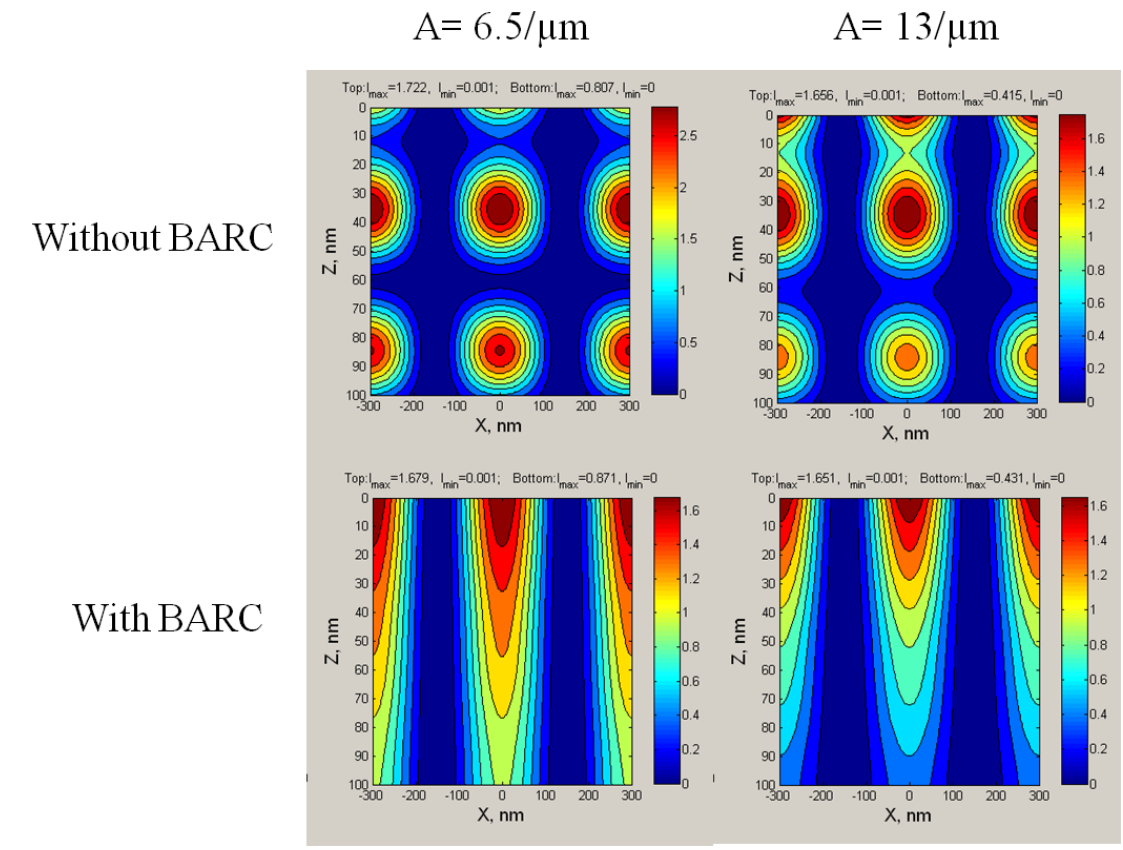


Figure 4.10. ILSim lithography simulation results of Hf-MAA nanoparticle resist films at 0.32 NA with different extinction coefficients, with and without control of substrate reflection using a BARC.

single bond. The other electron in the pi bond is transferred to the second carbon atom, turning the entire molecule into another radical. In this way, new monomers can be added to the end of the chain to form a polymer, as shown previously in Figure 4.2. The "addition" polymerization continues until the supply of monomer is exhausted, two radical-containing species combine, or if the radical is scavenged by an inhibitor molecule like oxygen.[38]

In any case, the theoretically highly absorbing unsaturated bond in the methacrylic acid is converted to a relatively non-absorbing saturated one as the resist is crosslinked, which could lead to an effective "photo-bleaching" of the resist during exposure. To examine the possibility of Hf-MAA photobleaching as a result of the conversion of double bonds during exposure, a real-time test of 193 nm transmission through the Hf-MAA resist film as a function of 193 nm dose was performed. For this experiment we first measured the energy of 10 averaged 193 nm pulses of a 0.4 cm diameter without any obstructions in the optical path, as measured by a Coherent™ LabMax laser energy photometer with a direct USB connection to a computer for data capture and storage. We found this value to be 11.21 +/- 0.51 μJ. Then, we placed a blank quartz wafer in the optical path, and found the transmission dropped to 8.73 +/- 0.41 μJ. Finally, we coated the same quartz wafer with a Hf-MAA film, baked it at 130°C for 60 seconds to remove residual PGMEA spin coating solvent, and then again placed the quartz in the optical path. Upon the start of the 200 Hz pulses of 193nm radiation, we captured the initial transmission of 193nm light through the resist film, quickly followed by the bleaching of the resist, as shown in Figure 4.11.

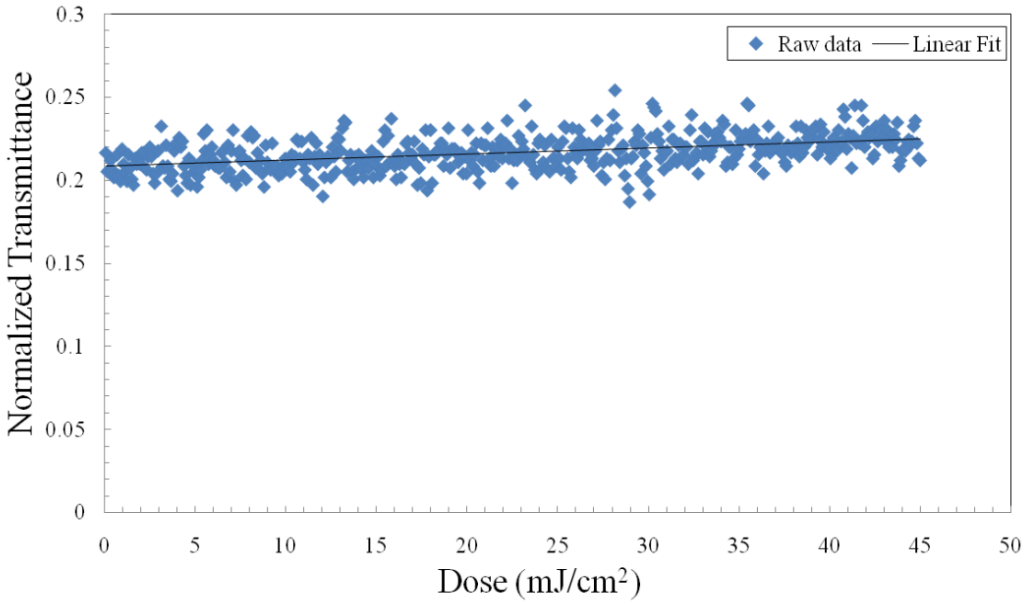


Figure 4.11. Scatter plot and linear trend line displaying the normalized transmittance of 193nm photons through the Hf-MAA film coated on a quartz wafer as a function of dose per unit area. With increasing dose, the transmittance of the material increased slightly, presumably due to the vinyl polymerization of MAA.

Dill's A parameter was used to quantitatively describe the photobleaching of the photoresist as a function of dose per unit area,

$$A = \frac{1}{d}\ln[\frac{T_0}{T_f}]\,.^{39} \qquad \text{[Eq. 4.4]}$$

In this equation, $d$ is equal to the film thickness, and $T_o$ and $T_f$ are equal to the initial transmittance of the resist and transmission of the resist when it is fully exposed, respectively. Assuming a film thickness equal to 90 nm and a full exposure dose of 45 mJ/cm$^2$, we found that Dill's A parameter was less than 1.0 μm$^{-1}$. Although this drop in absorbance may make some small difference in the quality of the patterned line-shape, we concluded that Hf-MAA is not a significant photobleaching material at doses traditionally used for lithography (<100 mJ/cm$^2$).

### *4.4 193nm Interference Lithographic Patterning of Hf-MAA*

#### *4.4.1 Exposure Dose Optimization*

Before the application of the interference optics, the response of HF-MAA to 193nm photons was examined. A characteristic curve was constructed to quantify the lithographic contrast of the resist as well as to find the correct dose for patterning. Hf-MAA was spin coated with a small amount (~1 wt.%) of the free radical photoinitiator DPAP. The characteristic curve was constructed by exposing the resist to varying doses of radiation and measuring the film thickness remaining after development for each exposed area. In negative resists, the resist does not crosslink and form a gel until a certain dose has been reached, which is known as the interface gel dose ($D_g^i$). With increasing exposure dose, the film thickness becomes greater until it equals the value of the initial film thickness. The normalized film thickness versus the log (base 10) of the exposure dose for Hf-MAA is shown in Figure 4.12, showing the high contrast of Hf-MAA under 193 nm radiation. The lithographic contrast can be quantified by the following equation,

$$\gamma_n = \frac{1}{\log D_g^0 - \log D_g^i} \ , \qquad \text{(Eq. 4.5)}$$

where $D_g^0$ is the dose required to produce 100% initial film thickness, and is determined by extrapolating the linear portion of the normalized thickness versus dose plot to a value of 1.0 normalized film thickness.[40] In this particular batch of Hf-MAA, the lithographic contrast is equal to 4.2, as shown in Figure 4.12. The lithographically useful dose, or sensitivity, is usually somewhere between 0.5-0.8 x $D_g$, and is qualitatively defined as the dose at which the feature size matches that of the target pattern. However, the sensitivity was seen to vary depending on the particular batch of nanoparticles used for patterning, perhaps due to slightly varying amounts of free methacrylic acid content.

Armed with the above information about the material properties of Hf-MAA, the resist was exposed to 193nm photons using an Amphibian ArF excimer laser-based interferometric lithography (IL) system at the Rochester Institute of Technology. The variable NA system used a line-narrowed compact excimer laser and projection optics for Talbot interference imaging using a phase grating mask. At the intersection of two intersecting beams of 193nm light, the resulting interference produces a sinusoidal pattern featuring 100% intensity modulation. A photoresist positioned at the point of intersection will be exposed by the interference pattern, printing a high-resolution line/space pattern. Although IL is limited in the geometry of patterns it can create, the simplicity of the technique was perfect for the study of this new photoresist material. For example, the period of the pattern could be easily adjusted by changing the numerical aperture, thereby changing the angle of intersection of the coherent beams of light, and the half-pitch (as shown previously in Table 4.1). Therefore, IL enabled systematic studies of the behavior of Hf-MAA as a function of pitch.[41]

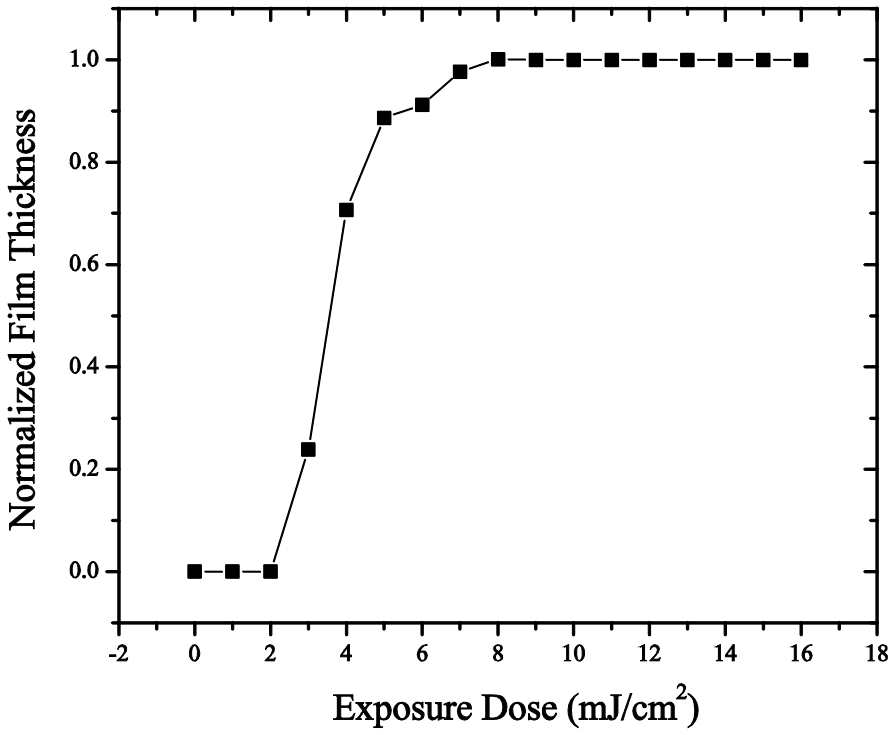


Figure 4.12. Characteristic curve showing of Hf-MAA under 193nm radiation

A 4x4 dose array of spots was printed with exposure doses varying from 5-45 $mJ/cm^2$ on a freshly coated wafer and developed in an alcohol that allowed for a controlled dissolution of the unexposed film. We found that at the theoretically predicted 300 nm pitch produced using the 0.32 NA prism, correctly exposed spots [Figure 4.13(b)] showed an optical diffraction pattern of a bright green color along the long axis of the elliptical spot (Figure 4.13(b), inset), allowing a visual check on the quality of the exposed lines/spaces before SEM analysis. By cleaving the elliptical spot along its long axis and analyzing the sample tilted 70° in the SEM, these correctly exposed spots showed lines and spaces of 150nm half-pitch. Underexposed spots showed lines less than 150 nm [Figure 4.13(a)], whereas overexposed spots showed lines greater than 150 nm [Figure 4.13(c)] or, in the worst cases, excessive bridging or merging of neighboring lines [Figure 4.13(d)]. In all spots, the dose of 193nm radiation can decrease from the center out to the edge of the interference field, so care was taken to select lines in the center of the exposure spot for SEM imaging. The correctly exposed spots, however, suffered from T-topping along the resist cross-section, which could be corrected with additional optimization of the resist formulation, as discussed in the following section. Contrary to our simulation results, no effect of standing waves was observed in the 0.32 NA patterns, even without the use of a BARC underlayer.

### *4.4.2. Photoinitiator Optimization*

A major component of our resist system was the radical photoinitiator, DPAP, used to catalyze the radical crosslinking of neighboring Hf-MAA nanoparticles. The chemical structure of this molecule is shown in Figure 4.14(a), which generates a free radical by unimolecular bond cleavage. Previous work on the Hf-MAA resist system has shown that the concentration of DPAP can have a major effect on the quality of

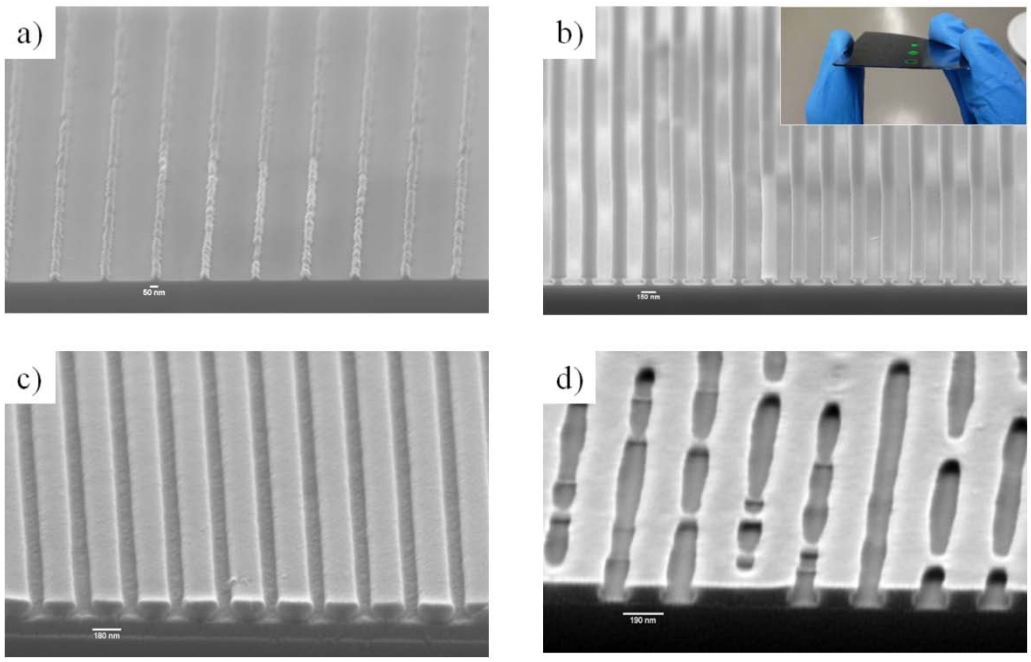


Figure 4.13. A range of exposure doses showing (a) underexposed (b) correctly exposed, (c) overexposed, or (d) the merging or bridging of lines due to overexposure. The inset in (b) shows the optical diffraction grating produced by interference patterning at 0.32 NA.

the three-dimensional lineshape, perhaps due to the high absorbance of the aromatic groups in the molecule. In fact, previous results have shown an increase in film absorbance by about 0.3 $\mu m^{-1}$ for every 1 % DPAP added to the resist solution.

To see what effect this molecule would have on the patterning properties, DPAP was blended in varying concentrations relative to the mass of Hf-MAA. Interestingly, the optimum exposure dose increased with increasing DPAP concentration. This may be due to a higher likelihood of termination of the photo-induced radicals by recombination at higher concentrations in the film. Therefore, we had to create 4x 4 exposure dose arrays to optimize the dose for every different DPAP concentration. After cleaving the patterns which showed the best optical diffraction through the center of the spot, the substrate was tilted 90° in the SEM relative to the electron beam, and the contact angle between the patterned line and the substrate was examined. The goal was a 90° contact angle between the substrate and the resist through the entire resist film thickness. Improperly patterned lines may show 'T-topping' as exemplified by acute (<90°) angles of the patterned resist at both the substrate and air interface. Lines exhibiting footing may have obtuse (>90°) angles between the resist and substrate, and can be due to high absorbance at the substrate/polymer interface or also under-developing the film.

We observed a clear dependence on the concentration of DPAP in the film and the amount of T-topping in the patterned line. For example, a Hf-MAA film containing 5% DPAP relative to Hf-MAA exhibited a dramatic degree of T-topping, as shown in Figure 4.14(b). The DPAP in this case caused such a high absorbance that a much lower dose was received at the bottom of the film than the top, causing a "mushroom cap" shape. By dropping the DPAP concentration to 2% we saw much less T-topping, as shown in Figure 4.14(c). Dropping the DPAP concentration further to 1 wt.% displayed an array of lines with nearly square profiles with 90° substrate

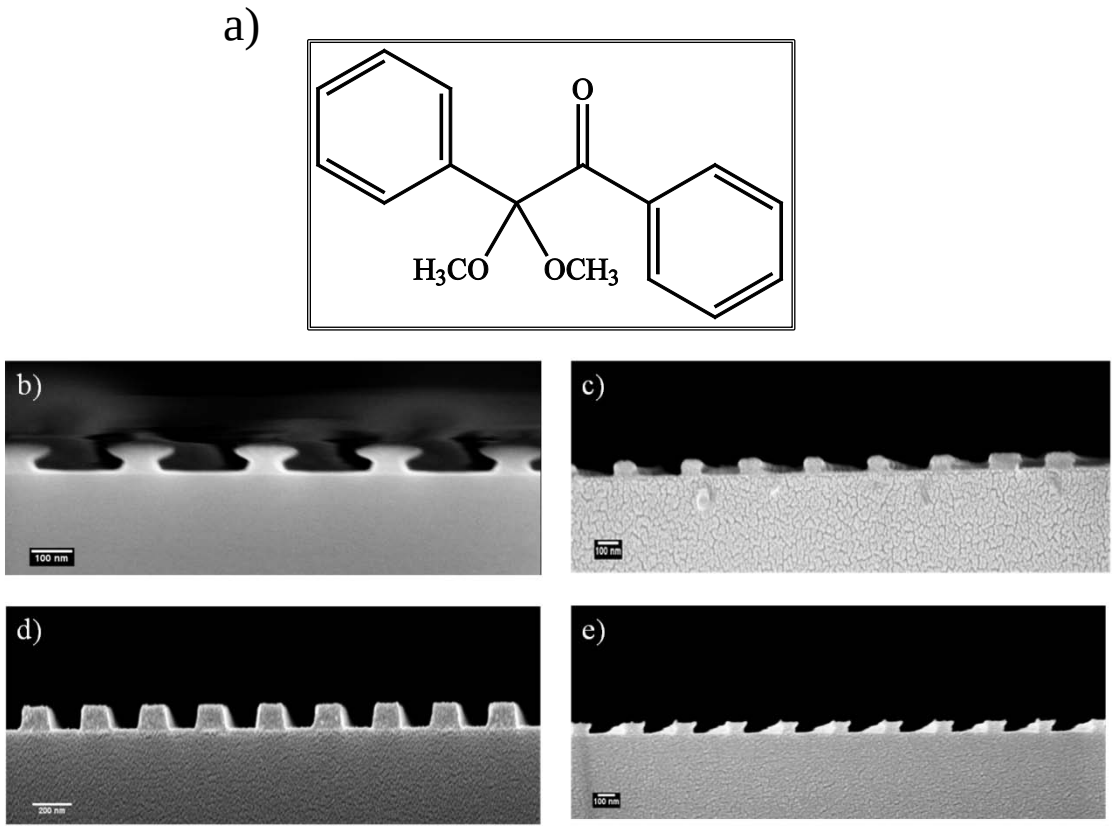


Figure 4.14. Varying the DPAP concentration led to changes in the resist profile. a) shows the chemical structure of DPAP, b-e) shows 5%, 2%, 1%, and 0% DPAP concentrations, respectively, relative to Hf-MAA in the resist solution.

contact angles, displayed in Figure 14(d). The SEM image for the 1% DPAP sample tilted 70° is shown in Figure 4.15, showing no defects along the length of the patterned line. Interestingly, we also found that Hf-MAA could crosslink without any photoradical initiator [0% DPAP, Figure 4.14(e)], although the doses required in these films were slightly higher, and the resist cross-section showed crowns on top of the patterned line that were not seen in any other case.

### *4.4.3. Imaging at Higher NA*

Hf-MAA was also tested using higher numerical apertures in the effort to determine the highest resolution possible with this system. Samples containing a 33% organic content were spin coated without any BARC layer to control standing wave reflections, and the resist was exposed using a 0.54 NA prism under interference conditions, which printed lines at 90 nm half-pitch. We found the optimal exposure dose for this system was 11 mJ/cm$^2$, which was similar to other results obtained using the same nanoparticle batch. The spin coating solvent, PGMEA, made for an efficient developer which cleared all unexposed film within seconds. However, this development was too fast to be accurately reproduced, so we used a blend of PGMEA with 4-methyl-2-pentanol (MP), in a MP:PGMEA ratio of 4:1 to slow the dissolution rate to about thirty seconds. The result, as shown in Figure 4.16(a), was a well-resolved pattern with no T-topping, a pitch of 173nm, and no bridging defects or merged lines. Upon closer examination; however, we did find a residual nanoparticle layer between the lines of a 10nm thickness, as shown in the inset in Figure 4.16a. We attributed the inability to clear this residual layer to poor control over the kinetics of the development process. Efforts are currently underway to widen the process window for development and obtain more reproducible results.

The next target was 0.80 NA, which prints lines of a 60nm half-pitch. For this

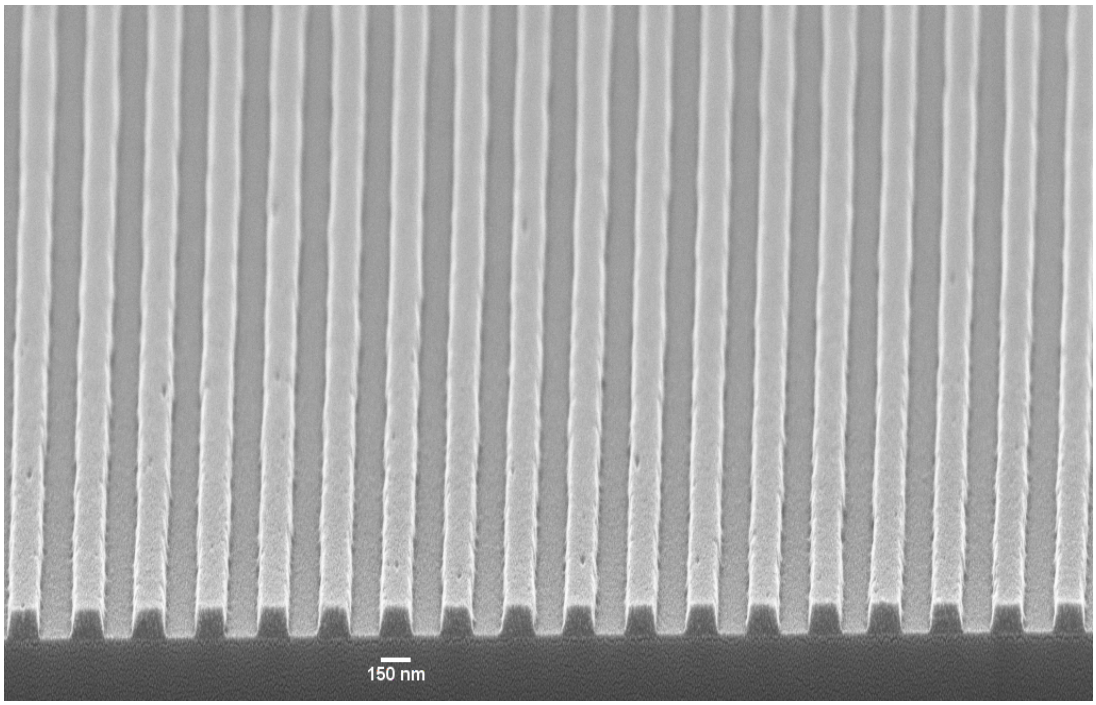


Figure 4.15. 150 nm line/space patterns of Hf-MAA at 0.32NA using a 1% DPAP concentration at a correct exposure dose. For this batch, the correct exposure dose was 25 mJ/cm$^2$. The corresponding 90° cross-section of this film is shown above in Figure 4.14(d).

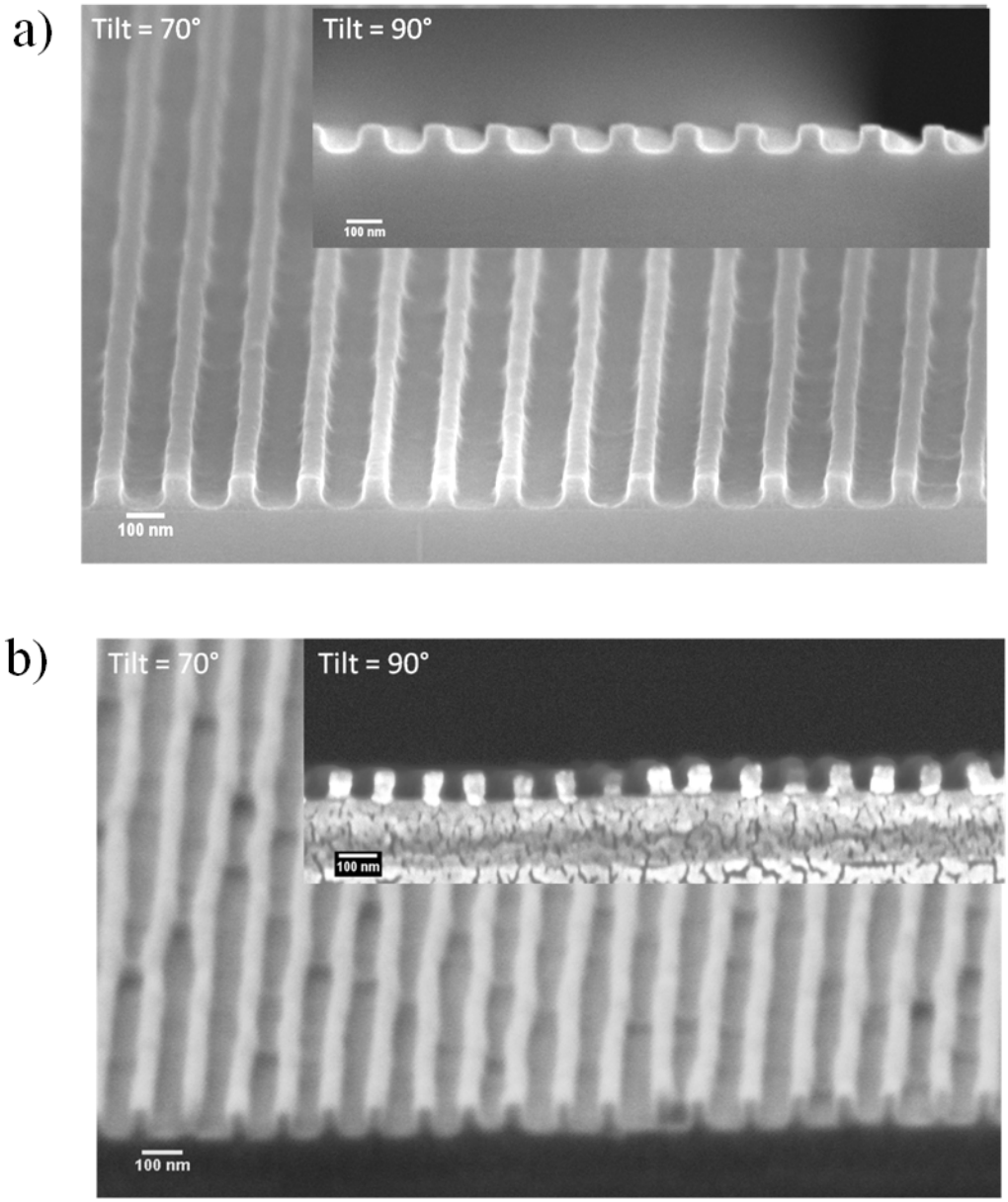


Figure 4.16.a) Lithographic patterning of Hf-MAA at 0.54 NA, showing 90 half-pitch patterns, and b) 0.80NA imaging, showing 60 nm half-pitch patterns with a high aspect ratio

numerical aperture, it was very important to minimize any reflection from the substrate, so we spun Hf-MAA on a thick BARC layer (~150nm) to minimize the standing wave effect. The exposure was performed on an optical bench-top setup, using mirrors to control the correct entrance angle of light onto the substrate. The same 11 mJ/cm$^2$ exposure dose was used for this exposure, and the Hf-MAA film thickness was 83 nm. This time, a MP:PGMEA blend of 7:3 (v:v), and a developing time of 5 seconds was used for development. The result is shown in Figure 4.16(b) showing very high aspect ratio lines with no evidence of pattern collapse or merging of neighboring lines. The lines suffered from excessive swelling during the development step, which caused "snaking" of the lines. The snaking effect is caused by a resist that is expanding in the z-direction due to solvent swelling, but cannot expand freely in the plane of the substrate due to the adherence of the film to the wafer. The line must increase its length in some way to relieve stress, so it does this by generation of a sinusoidal, snake-like appearance that persists even after drying.[42] Previous research has shown that it is possible to remove some of the snaking effect by rinsing the film in a series of developing solvents which have a gradually decreasing affinity for the polymer film.[43] Efforts are currently underway to widen the process window for development and obtain more reproducible results without these effects from excess swelling. Future work will also focus on patterning Hf-MAA with a solid immersion lens, a technique which allows for patterning below the optical diffraction limit at sub-30nm resolution. [44]

### *4.5 Etch Rate Characterization of Hf-MAA*

The ability to transfer the photo-defined pattern into the underlying substrate is the final step in a lithographic process. There are many different types of chemistries used for pattern transfer, including both dry and wet techniques. In the semiconductor

industry, reactive ion etching (RIE) is traditionally used to create a positive replica of the resist pattern into the underlying silicon substrate. Typically, a reactive ion etch step using fluorinated gases such as $CF_4$ and $SF_6$ is used to etch silicon. Depending on the voltage on the electrodes that is used to drive the highly energetic ions into the sample, chemical reactions can take place within the resist, or the ions may transfer their kinetic energy into the resist molecules to physically remove material via a sputtering mechanism.[45] Therefore, the photoresist must be able to withstand the harsh conditions of these plasmas to allow for the creation of high-aspect ratio nanopatterned silicon.

Not surprisingly, the etch durability of a photoresist is dramatically enhanced by the incorporation of inorganic species. Compared to organics, inorganic molecules have a higher atomic mass that can resist physical sputtering mechanisms as well as an ability to form chemically stable oxides on exposure to oxygen plasmas.[46] Since the majority of the Hf-MAA resist was composed of hafnium, we expected the resist to be extremely durable to RIE plasmas. We also expected the completely purified Hf-MAA to be slightly more durable than the unpurified Hf-MAA due to the increase in inorganic content. In order to test this hypothesis, we exposed the Hf-MAA material previously shown to have a decreasing amount of organic content (quantified in Figure 4.6) to a blend of $SF_6$ and $O_2$ plasmas. A certain percentage of oxygen is commonly added to RIE in order to make the etching more selective to silicon.[47] The recipe used in this study was previously found to etch silicon at a rate of 100 nm/ min, usually with a selectivity of 6.5:1 relative to an organic photoresist. The samples were labeled according to how many cumulative dissolve/precipitate cycles they experienced, so ‘w0’ stands for the unpurified material with 48.6% MAA content, ‘w1’ contains 33.7% MAA, ‘w2’ contains 30.1% MAA, and ‘w3’ contains 28.6% MAA. Along with the Hf-MAA films of varying organic content, we also included a control film of

poly(4-hydroxystyrene) (PHOST), an industry standard 248 nm negative-tone photoresist, and measured the film thickness loss for each film using an ellipsometer. The results are shown in Figure 4.17. We found all of the Hf-MAA films to be much more durable than PHOST overall. The etch rates of Hf-MAA were at least 13 times slower than PHOST, even in the case of the unpurified Hf-MAA.

However, we were surprised to observe nonlinear etching behavior for Hf-MAA, making it difficult to quantitatively assign an etch rate for each Hf-MAA organic content film. In fact, the nanoparticle films showed three etching regimes, each with slightly different behavior. The first regime showed a very high etch resistance for all Hf-MAA films. In this regime, the nanoparticle films with the highest organic content ('w0' and 'w1') performed slightly better (<1nm/min) than the films with the lower organic contents ('w2' and 'w3'), which lost about 3 nm in the first 30 seconds, and then leveled off immediately afterwards.

The second regime featured a much higher etch rate than the first, and it started at two different times for the unpurified and purified samples, respectively. In the case of 'w0', significant amounts of etching began between 60-90 seconds. For the rest of the samples, etching began after the 90 second mark. It is noteworthy that the etch rate for the 'w0' sample in this regime approached that of PHOST (106 nm/min).

The third regime (5-8 minute cumulative etching time) showed very little change in the film thickness for all organic content films, as if the films had become completely resistant to plasma. However, we did observe that the films with the highest organic content started to become very rough and cracked past five minutes, which made an accurate film thickness measurement difficult to obtain. The 'w2' and 'w3' films, however, remained perfectly intact, even after 8 minutes of $SF_6/O_2$ etching. To test the limits of etch durability for this material, another sample ('w4'), featuring 28.2% organic content, was exposed to 15 minutes of the same $SF_6/O_2$

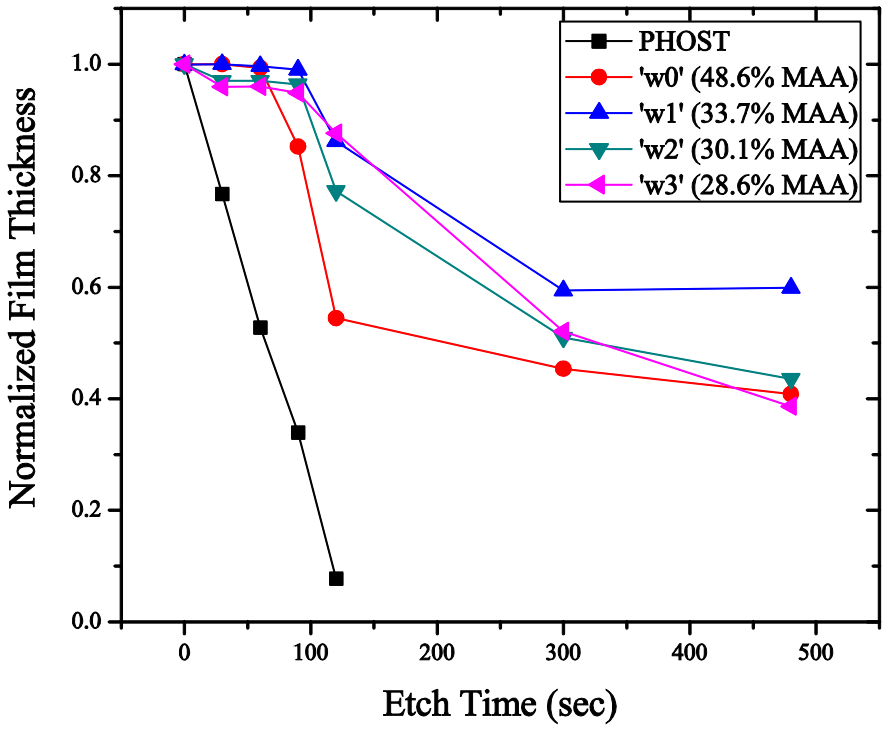


Figure 4.17. The etch resistance of Hf-MAA films with decreasing organic content, due to consecutive cycles of purification, show nonlinear etching behavior under standard silicon etching conditions in $SF_6/O_2$ plasma.

etchant and only lost about 31 nm of thickness. This corresponds to an etch rate of about 2nm/ min over this time period. To the best of the author's knowledge, this kind of performance is unparalleled among commercially available photoresists and can only be due to the high inorganic content in the film and/or the formation of an oxide 'etch stop' which is extremely resistant to plasma etching.

The variation of Hf-MAA etching behavior among the different batches may be due to one or more factors. The first probable cause is a vertical segregation of the organic (free methacrylic acid) and inorganic (Hf-MAA) phases in the film. For example, by looking at the dataset for the highest organic content 'w0' sample, in the first regime there seems to be an inorganic layer at the top of the film which etches very slowly, followed by a fast-etching organic layer in the second regime, and then another slow-etching inorganic layer in the third regime. The low organic 'w3' sample seemed to be less susceptible to this kind of behavior, because the three etching regimes are not as well defined. For a more quantitative definition of this difference, a linear trend line was fitted to each of the Hf-MAA data sets, and the $R^2$ 'goodness of fit' correlation was compared between each of the samples. The results are shown in Table 4.3. While 'w0' fits very poorly to a linear trend line ($R^2$=0.76), the 'w3' sample fit is much better ($R^2$=0.95). Therefore, the more linear etching behavior in the w3 sample may be due to less phase segregation in the film. Of course, more quantitative depth-profiling techniques must be used in order to verify this hypothesis. Other factors for the non-linear etching behavior may be due to variation in the energy of the plasma in the tool over time, the fluorine atoms in the plasma reacting with hafnia to form a polymer, or some crosslinking or degradation reactions due to oxidation that may have occurred during the processing of the film.

Table 4.3. The linear trendlines fit to the $SF_6/O_2$ RIE etching of Hf-MAA

| Sample Name | Organic Content (%) | Linear Trendline Slope (nm/sec) | $R^2$ Correlation |
|---|---|---|---|
| **PHOST** | 100 | 1.77 | 0.9982 |
| **w0** | 48.6 | 0.098 | 0.7623 |
| **w1** | 33.7 | 0.104 | 0.8776 |
| **w2** | 30.12 | 0.117 | 0.9136 |
| **w3** | 28.6 | 0.127 | 0.9552 |

### *4.6 Conclusion*

This chapter discussed the development of a new type of photoresist for next-generation lithography, one that is composed of inorganic nanoparticles with a potential for a high refractive index. We have synthesized these nanoparticles with a hafnium precursor, coated with a methacrylic acid ligand. The ligand lead to excellent solubility and film formation, and also enabled a switch in solubility after exposure to high energy photons. Decreasing the amount of organic surrounding the hafnia nanoparticles lead to many changes in the materials properties, such as etch resistance, dissolution rate, and overall lithographic performance. We have found that this material showed excellent patterning performance using 193nm two-beam interference lithography, in addition to etch resistance greater than ten times better than the industry standard poly(4-hydroxystyrene). In collaboration with SEMATECH, work is underway to test this material using extreme ultraviolet lithography at their resist development center in Albany, NY. This enhancement enables the use of thinner resist films, which decreases material cost for the semiconductor fabrication facilities and also decreases the chance of pattern collapse in chip layouts that use sub-45 nm critical dimensions. Apart from lithographic applications, this nanoparticle crosslinking strategy may find other uses in diverse areas such as energy harvesting, photocatalysis, or biotechnology which can capitalize on the vast amount of functional surface area created after patterning of metal oxide nanoparticles on the nanometer scale.[48]

### *4.7 Acknowledgements*

The authors would like to thank Markos Trikeriotis, Marie Krysak, Nathan Lee, Woo Jin Bae, Peng Xie, Neal Lafferty, Bruce Smith, and Emmanuel Giannelis for a fruitful collaboration on this project. We also would like to thank Paul

Zimmerman, Warren Montgomery and Prof. Xiao “Matthew” Hu for helpful discussions on this work. E.L.S. would like to thank the Semiconductor Research Corporation, Motorola and SEMATECH for financial support. This work made use of various facilities of the Cornell Center for Materials Research (CCMR) with support from the National Science Foundation Materials Research Science and Engineering Centers (MRSEC) program (DMR 0520404). This work also made use of the Cornell Nanoscale Facility, a member of the National Nanotechnology Infrastructure Network, which is supported by the National Science Foundation (Grant ECS-0335765).

# APPENDIX

## *4.8 Fluorinated Hafnia Nanoparticle Topcoat for 193nm Immersion Lithography*

### *4.8.1 Introduction*

One of the main requirements for 193nm immersion lithography is the ability to contain a droplet of fluid, usually water, in between the lens element and the resist. As the tool rapidly scans laterally to expose various die on the wafer, the droplet of water must move along with the lens at an extremely fast velocity (~400 mm/sec). Although the water in the lens/wafer gap is replenished continually, water loss in the lens/wafer gap must be kept to an absolute minimum as the wafer moves laterally, since the evaporation of any residual water droplets may cause various patterning defects.[49] Therefore, the surface tension of the resist interface becomes very important to consider, especially in relation to the viscous and inertial forces of the fluid drop as it moves along the wafer. For any resist material, these forces become dominant at a critical velocity, above which water is left behind as it is dragged along the wafer. The magnitude of this critical velocity will influence the maximum acceptable scan rate, which ultimately determines wafer throughput.[49]

This fundamental interaction at a polymer/ water interface is straightforward to characterize using contact angle measurements. Besides measuring the static contact angle, the advancing and receding contact angles are very important for immersion lithography, corresponding to the contact angle of water on the leading and trailing edge of the droplet, respectively, as it moves along a surface. Generally speaking, lower contact angles (<50°) correspond to hydrophilic surfaces and higher surface energy, and higher water contact angles (>90°) correspond to hydrophobic surfaces and lower surface energy. The lower surface energies are more highly desired in this case, because these relatively non-wetting surfaces will experience less film pulling and inertial instability as the droplet moves along the wafer. Traditional resists are

somewhere in between these two extremes, with static water contact angles between 60-80° and receding angles around 40-50°, leaving a lot of room for improvement through the use of a topcoat material. Usually, topcoat layers are spin coated on top of the resist to lower the surface energy of the water/resist interface; however, the topcoat solvent must be orthogonal to the underlying resist matrix in order to avoid intermixing of the two layers. We have designed a hafnia nanoparticle with a ligand composed of 2-trifluoromethacrylic acid, which is designed for use as a hydrophobic topcoat material for immersion lithography.

### *4.8.1 Materials*

Hafnium isopropoxide isopropanol adduct, 2-trifluoromethacrylic acid (TFMAA), and 2,2-Dimethoxy-2-phenylacetophenone (DPAP) were used as received from Aldrich. All solvents were also used as received from Aldrich unless stated otherwise.

### *4.8.2 Synthesis*

To an air-sealed three-neck flask with a magnetic stir bar, hafnium isopropoxide (1g, 2.4 mmol) was added to 10 ml of ethanol. The mixture was left to equilibrate for 15 minutes at 65 °C under reflux while stirring at 350rpm. Meanwhile, 2g of TfMAA (14 mmol, 5.8x molar excess relative to hafnium isopropoxide) was mixed with 10 mL ethanol in a separate container until the solution became clear. 1.5 mL of this solution was added to 0.2 mL $H_20$, and was then injected into the reaction flask after equilibration. After 18 hours, the remaining 2.5 mL of the TFMAA/EtOH solution was mixed with another 0.2 mL $H_20$ and injected into the reaction flask with a syringe. After an additional 2 hours, $H_2O$ (~2:1 v/v) was added to the reaction to precipitate the nanoparticles. The resulting white aggregate powder was washed with

deionized water four times to remove some unbound TfMAA monomer, and then dried in a vacuum oven at room temperature for 12 hours.

### *4.8.3 Film Preparation*

The nanoparticles were dissolved in 2.5 wt. % (w/v) in trifluorotoluene. After the solution became transparent after 3-4 minutes, it was passed through a 0.2 µm nylon filter twice. Freshly cleaned 2 x 2'' squares of silicon were dehydrated by heating on a hotplate at 200 °C for 1 minute and then cooled to room temperature prior to spin coating. 0.5 mL of the Hf-TfMAA resist solution was dropped on the center of the wafer, and the wafer was spun at 2000 rpm for 60 seconds to give a smooth film. The film thickness was controlled by either changing the solution concentration (7-15 wt.%) or the spin speed from 1,000-5,000 rpm. After spin coating, the film was baked for 60 seconds at 130°C on a hotplate to remove residual casting solvent and immediately taken for testing.

### *4.8.4 Results and Discussion*

Contrary to methacrylic acid, which is a liquid that can be used as a solvent for the nanoparticle synthesis, 2-trifluoromethacrylic acid (TFMAA) is a solid. Therefore, it was necessary to carry out the reaction in a solvent of anhydrous ethanol in order to dissolve both the hafnium isopropoxide precursor and the TFMAA ligand. After the synthesis, the Hf- TFMAA nanoparticles were precipitated and washed with distilled water. Figure 4.18 shows the FTIR spectrum of the Hf-TFMAA nanoparticles dispersed in a KBr pellet. Characteristic $C=CH_2$ peaks (1660 $cm^{-1}$) and $–CF_3$ peaks (1130, 1250 $cm^{-1}$) were evident in the spectra, in addition to a broad –OH stretch (~3400 $cm^{-1}$), which indicated an impurity of TFMAA monomer that did not get washed away by the water washing steps. TGA showed these nanoparticles were

composed of 45% organic material, including the impurity. The size of the nanoparticles was measured at 2.1 nm, as measured by dynamic light scattering.

We found that Hf-TFMAA nanoparticles were at least partially soluble in fluorinated solvents, such as hydrofluoroethers and trifluorotoluene, motivating possible applications in orthogonal processing.[50, 51] The hydrofluoroether solvent that we tested was called Novec 7300$^{TM}$, manufactured by 3M Corporation. This family of solvents is typically used for cleaning residue from electronics components.[52] Hf-TFMAA, however, was only sparingly soluble (<1 wt.%) in this solvent, as shown in Figure 4.19(a). Trifluorotoluene (TFT), one of the strongest fluorinated solvents, dissolved Hf-TFMAA in up to 2.5 wt. % (w/w) concentration, as shown in the photo in Figure 4.19(b). We spin coated smooth films of Hf-TFMAA from the TFT solution onto cleaned silicon, as well as quartz wafers for absorbance measurements. The absorbance of these films were measured at 6.5/μm at 193nm, slightly lower than the absorbance of Hf-MAA, meaning a very thin coating of this material would have little effect on the optical properties of the film stack.

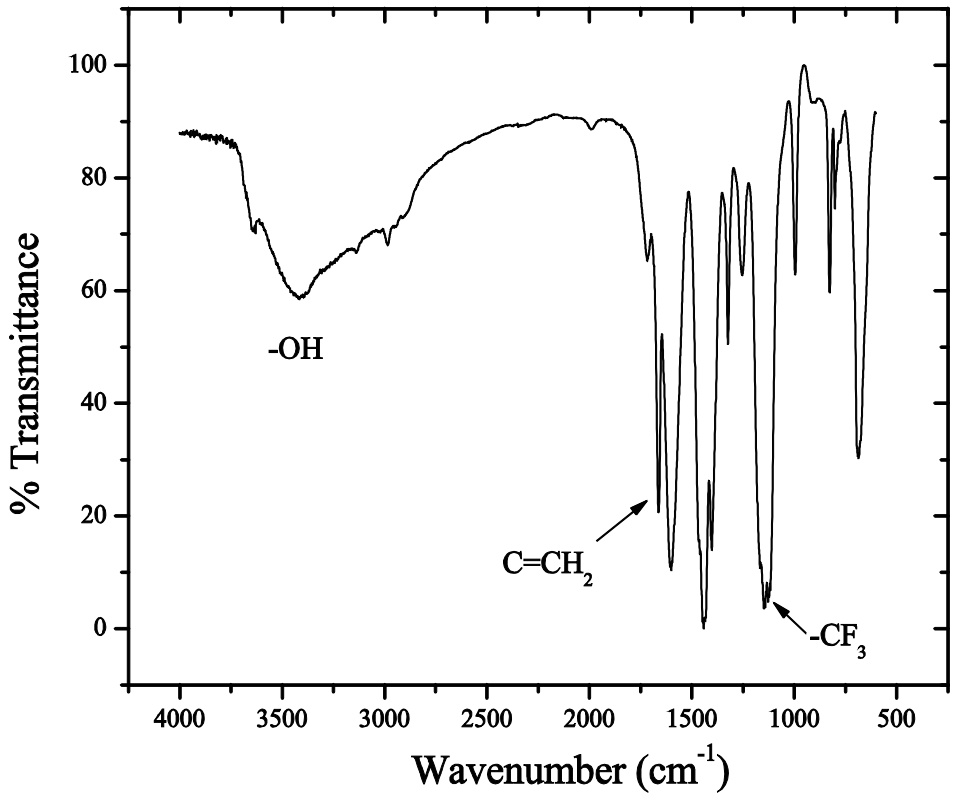


Figure 4.18. FTIR spectra of Hf-TFMAA

a) b)


c) d)

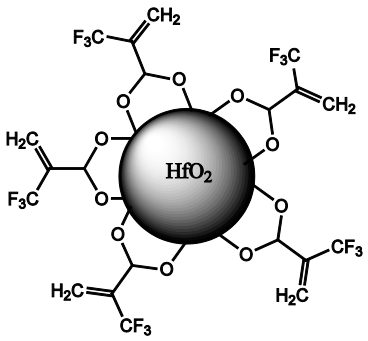


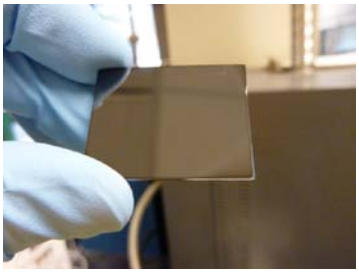

Figure 4.19.Vials containing Hf-TFMAA dissolved in a) Novec 7300, b) trifluorotoluene (TFT), c) schematic of Hf-TfMAA nanoparticles (the number of ligands may differ from what is shown here) d) smooth amorphous film of Hf-TFMAA spin coated from TFT solution

The ability to crosslink Hf-TFMAA using free radical polymerization was tested using the radical initiator 2,2-Dimethoxy-2-phenylacetophenone (DPAP), which dissociates upon UV irradiation to form free radicals. Due to the strongly negative inductive effects originating from the three fluorine atoms on the TFMAA ligand, we found that Hf-TFMAA nanoparticles would not crosslink to one another. [53] However, Hf-TFMAA did crosslink when blended with Hf-MAA nanoparticles in a 1:1 (w/w) ratio, forming films that were slightly greater than the spin coated film thickness as a result of swelling in the TFT developing solvent.

The water contact angle on the spin-coated Hf-TFMAA films was tested to give some insight into how the material would behave as a topcoat material for lithography. A goniometer with video capabilities was used in order to capture advancing and receding contact angles, as shown in Table 4.4 . The results showed that the advancing contact angle of Hf-TFMAA increased by about 11° relative to the Hf-MAA. The receding contact angles of Hf-TFMAA were increased by about 6° relative to Hf-MAA. The contact angles of the 50/50 blend of Hf-TFMAA/Hf-MAA materials were both slightly higher than a simple weighted average of the respective Hf-TFMAA and Hf-MAA contact angles, indicating a possible vertical phase segregation of the Hf-TFMAA nanoparticles to the air interface. The contamination from the TFMAA monomer left over from the reaction may have lowered the contact angle of these films, especially since the monomer is soluble in water. Further work on this system must be done to purify these materials further and re-test the surface energy. These nanoparticles could also have other potential uses as a hydrogen bond acceptor due to the strongly electronegative effect of the fluoro subsituents.[54]

Table 4.4. Advancing and receding water contact angles on Hf-TFMAA surfaces

| Hf-TFMAA/ Hf-MAA | Advancing Contact Angle (°) | Receding Contact Angle (°) |
|---|---|---|
| **100/0** | 95.9 ± 2.34 | 25.83 ± 3.93 |
| **0/100** | 84.68 ± 1.68 | 19.63 ± 1.09 |
| **50/50 crosslinked** | 92.53 ± 2.54 | 20.28 ± 4.89 |
| **50/50 uncrosslinked** | 94.40 ± 1.72 | 15.60 ± 1.57 |

## REFERENCES


1. Sanders, D. P., Advances in patterning materials for 193nm immersion photolithography. *Chem. Rev.* **2010,** *110*, 321-360.
2. Wu, B.; Kumar, A., Extreme ultraviolet lithography: A review. *J. Vac. Sci. Tech. B* **2007,** *25*, 1743.
3. Borodovsky, Y., Intel's 193nm ArF Lithography Platform. In *Lithovision 2010*, San Jose, CA, 2010.
4. Born, M.; Wolf, E., *Principles of Optics*. Pergamon: New York, 1980.
5. Smith, B. W.; Bourov, A.; Fan, Y.; Zavyalova, L.; Lafferty, N.; Cropanese, F. In *Approaching the numerical aperture of water immersion lithography at 193 nm*, Proc. SPIE: Optical Microlithography XVII, Smith, B. W., Ed. 2004; pp 273-284.
6. Bremer, L.; Tuinier, R.; Jahromi, S., High refractive index nanocomposite fluids for immersion lithography. *Langmuir* **2009,** *25*, 2390-2401.
7. Zimmermann, P. A.; Rice, B.; Rodriguez, R.; Zettel, M. F.; Trikeriotis, M.; Wang, D.; Yi, Y.; Bae, W. J.; Ober, C. K.; Giannelis, E. P., The use of nanocomposite materials for high refractive index immersion lithography. *J. Photopolym. Sci. Tech.* **2008,** *21* (5), 621.
8. Zhou, J.; Fan, F.; Bourov, A.; Smith, B. W., Inorganic immersion fluids for ultrahigh numerical aperture 193 nm lithography. *Applied Optics* **2006,** *45*, 3077.
9. Smith, B.; Zhou, J., Snell or Fresnel: the influence of material index on hyper-NA lithography. *Proc. SPIE* **2007,** *6520*, 65200A.

10. Conley, W.; Warrick, S.; Garza, C.; Goirand, P.-J.; Gemmink, J.-W.; Van Steenwinckel, D. 3rd Int'l Symposium on Immersion Lithography, Kyoto, Japan, Kyoto, Japan, October; Kyoto, Japan, 2006.
11. Zimmerman, L.; Weibel, M.; Caseri, W.; Suter, U. W., High refractive index films of polymer nanocomposites. *J. Mater. Res.* **1993,** *8* (7), 1742-1748.
12. Liu, J.-G.; Ueda, M., High-refractive index polymers: fundamental research and practical applications. *J. Mater. Chem.* **2009,** *19*, 8907-8919.
13. Intel, C. Intel's transistor technology breakthrough represents biggest change to computer chips in 40 years. http://www.intel.com/pressroom/archive/releases/2007/20070128comp.htm (accessed July 5).
14. Wilk, G. D.; Wallace, R. M.; Anthony, J. M., High-K gate dielectrics: current status and materials properties considerations. *J. Appl. Phys.* **2001,** *89*, 5243-5275.
15. Krug, H.; Tiefensee, F.; William Oliveira, P.; Schmidt, H., Organic-inorganic composite materials: optical properties of laser patterned and protective coated waveguides. *Proc. SPIE: Sol-Gel Optics II* **1992,** *1758*, 448.
16. Saravanamuttu, K.; Blanford, C. F.; Sharp, D. N.; Dedman, E. R.; Turberfield, A. J.; Denning, R. G., Sol-gel organic-inorganic composites for 3-d holographic lithography of photonic crystals with submicron periodicity. *Chem. Mater.* **2003,** *15* (2301-2304).
17. Yoshiiwa, M.; Kageyama, H.; Shirota, Y.; Wakaya, F.; Gamo, K.; Takai, M., Novel class of low molecular-weight organic resists for nanometer lithography. *Appl. Phys. Lett.* **1996,** *69* (17), 2605.
18. De Silva, A.; Felix, N. M.; Ober, C. K., Molecular glass resists as high resolution patterning materials. *Adv. Mater.* **2008,** *20*, 3355-3361.

19. Krysak, M.; De Silva, A.; Sha, J.; Lee, J.-K.; Ober, C. K., Molecular glass resists for next-generation lithography. *Proc. SPIE: Advances in Resist Technology and Processing XXVI* **2010,** *7273*, N/1-N/8.

20. Dai, J.; Ober, C. K. In *Novel resists with nontraditional compositions for EUV lithography*, Proc. SPIE: Advances in Resist Technology and Processing XXI, Santa Clara, CA, USA, Santa Clara, CA, USA, 2004; p 508.

21. Bravo-Vasquez, J. P.; Kwark, Y.-J.; Ober, C. K.; Cao, H. B.; Deng, H.; Meagley, R. P., Silicon backbone polymers as EUV resists. *Proc. SPIE: Advances in Resist Technology and Processing XXI* **2004,** *5376*, 739.

22. Sondi, I.; Fedynyshyn, T. H.; Sinta, R.; Matijevic, E., Encapsulation of nanosized silica by in-situ polymerization of tert-butyl acrylate monomer. *Langmuir* **2000,** *16*, 9031-9034.

23. Bae, W. J.; Trikeriotis, M.; Sha, J.; Schwartz, E. L.; Rodriguez, R.; Zimmerman, P. A.; Giannelis, E. P.; Ober, C. K., High refractive index and high transparency HfO2 nanocomposites for next generation lithography. *J. Mater. Chem.* **2010,** *20*, 5186-5189.

24. Bourov, A.; Fan, Y.; Cropanese, F. C.; Lafferty, N. V.; Zavyalova, L.; Kang, H.; Smith, B. W., Immersion microlithography at 193 nm with a Talbot prism interferometer. *Proc. SPIE* **2004,** *5377*, 1573.

25. Trikeriotis, M.; Rodriguez, R.; Zettel, M. F.; Bakandritsos, A.; Bae, W. J.; Zimmerman, P. A.; Ober, C. K.; Giannelis, E. P., *Proc. SPIE* **2009,** *7273*, 72732A.

26. Tang, J.; Fabbri, J.; Robinson, R. D.; Zhu, Y.; Herman, I. P.; Steigerwald, M. L.; Brus, L. E., Solid-solution nanoparticles: use of a nonhydrolytic sol-gel synthesis to prepare HfO2 and HfxZr1-xO2 nanocrystals. *Chem. Mater.* **2004,** *16*, 1336-1342.

27. Brinker, C. J.; Scherer, G. W., *Sol-gel science: the physics and chemistry of sol-gel processing*. Academic Press, Inc.: San Diego, CAS, 1990.

28. Sorensen, T. S., The pKa of protonated a, B-unsaturated carboxylic acids. *Can. J. Chem.* **1964,** *42*, 724-730.

29. Guerrero, G.; Mutin, P. H.; Vioux, A., Mixed nonhydrolytic/hydrolytic sol-gel routes to novel metal oxide/phosphonate hybrids. *Chem. mater.* **2000,** *12*, 1268-1272.

30. Malvern FAQ: What does polydispersity mean? http://www.malvern.com/malvern/kbase.nsf/allfaqbyno/KB000780?opendocument (accessed July 6).

31. Li, C.; Xiyu, S.; Zhenyu, W.; Bingsuo, Z.; Jiahua, D.; Sishen, X., Quantum confinement effect of ZnO nano-particles *Chem. J. Int.* **2002,** *9*, 45.

32. Orgill, M.; Baker, B. L.; Owen, N. L., FTIR studies of conformational isomerism in acrylates and acrylic acids. *Spectrochimica Acta Part A* **1999,** *55*, 1021-1024.

33. Nakamoto, K., *Infrared and Raman Spectra of Inorganic and Coordination Compounds*. John Wiley & Sons: New York, 1986.

34. Huang, J. Y.; Shao, Y. X.; Huang, H. G.; Cai, Y. H.; Ning, Y. S.; Tang, H. H.; Liu, Q. P.; Alshahateet, S. F.; Sun, Y. M.; Xu, G. Q., Binding Mechanisms of Methacrylic Acid and Methyl Methacrylate on Si(111)-Effect of Substitution Groups. *J. Phys. Chem. B* **2005,** *109*, 198381-19838.

35. Rice, B. J., High-index materials research key to extending immersion lithography. *Solid State Technology* February, 2008, pp 28-33.

36. Woodward, R. B., Structure and the Absorption Spectra of α,β-Unsaturated Ketones. *J. Am. Chem. Soc.* **1941,** *63*, 1123.

37. Fan, Y. B., Anatoly; Zavyalova, Lena; Zhou, Jianming; Estroff, Andrew; Lafferty, Neal; Smith, Bruce W., ILSim: a compact simulation tool for interferometric lithography. *Proc. SPIE: Optical Microlithography* **2005,** *5754*, 1805-1816.

38. Decker, C.; Elzaouk, B., Laser-induced crosslinking polymerization of acrylic photoresists. *J. Polym. Sci.* **1997**, 833-844.

39. Dill, F. H.; Hornberger, W. P.; Hauge, P. S.; Shaw, J. M., Characterization of positive photoresist. *IEEE Trans. Elec. Dev.* **1975,** *ED-22* (7), 445-452.

40. Thompson, L. F., Resist Processing. In *Introduction to Microlithography*, Thompson, L. F.; Willson, C. G.; Bowden, M. J., Eds. American Chemical Society: Washington, D.C., 1994; p 277.

41. Hinsberg, W.; Houle, F. A.; Hoffnagle, J.; Sanchez, M.; Wallraff, G.; Morrison, M.; Frank, S., Deep-ultraviolet interferometric lithography as a tool for assessment of chemically amplified photoresist performance. *J. Vac. Sci. Technol. B.* **1998,** *16*, 3689-3694.

42. Willson, C. G., Organic Resist Materials. In *Introduction to Microlithography*, Thompson, L. F.; Willson, C. G.; Bowden, M. J., Eds. American Chemical Society: Washington, D.C., 1994; p 209.

43. Novembre, A. E.; Kowalski, L. M.; Frakoviak, J.; Mixon, D. A.; Thompson, L. F., GMC (glycidyl methacrylate -chlorostyrene copolymer): a negative-acting resist used in the fabrication of chromium photomasks. *Solid State Technol.* **1988,** *16* (6), 1997.

44. Wu, Q.; Feke, G. D.; Grober, R. D.; Ghislain, L. P., Realization of numerical aperture 2.0 using a gallium phosphide solid immersion lens. *Appl. Phys. Lett* **1999,** *75*, 4064-4067.

45. Mucha, J. A.; Hess, D. W.; Aydil, E. S., Plasma Etching. In *Introduction to Microlithography*, Thompson, L. F.; Willson, C. G.; Bowden, M. J., Eds. American Chemical Society: Washington, D.C., 1994; pp 386-390.

46. Taylor, G. N.; Wolf, T. M., Behavior of Si-containing polymers under $O_2$ RIE etch conditions. *Polym. Eng. Sci.* **1980,** *20*, 1087.

47. Mucha, J. A.; Hess, D. W.; Aydil, E. S., Plasma Etching. In *Introduction to Microlithography*, Thompson, L. F.; Willson, C. G.; Bowden, M. J., Eds. American Chemical Society: Washington, D.C., 1994; p 452.

48. Sanchez, C.; Julian, B.; Belleville, P.; Popall, M., Applications of hybrid organic-inorganic nanocomposites. *J. Mater. Chem.* **2005,** *15*, 3559-3592.

49. Wei, Y.; Brainard, R. L., *Advanced processes for 193nm immersion lithography*. Society of Photo-Optical Instrumentation Engineers (SPIE): Bellingham, WA, 2009.

50. Zakhidov, A. A.; Lee, J.-K.; Fong, H. H.; DeFranco, J. A.; Chatzichristidi, M.; Taylor, P. G.; Ober, C. K.; Malliaras, G. G., Hydrofluoroethers as orthogonal solvents for the chemical processing of organic electronic materials. *Adv. Mater.* **2008,** *20*, 3481-3484.

51. Taylor, P. G.; Lee, J.-K.; Zakhidov, A.; Malliaras, G. M.; Ober, C. K., Orthogonal patterning of PEDOT:PSS for organic electronics using hydrofluoroether solvents. *Adv. Mater.* **2009,** *21*, 2314-2317.

52. Kehren, J., HFE's offer a cost-effective, environmentally safe alternative to aqueous cleaning. *Data Storage* **2001**.

53. Ito, H.; Wallraff, G. M.; Fender, N.; Brock, P. J.; Hinsberg, W. D.; Mahorowala, A.; Larson, C. E.; Truong, H. D.; Breyta, G.; Allen, R. D., Development of 157 nm positive resists. *J. Vac. Sci. Technol. B.* **2001,** *19* (6), 2678-2684.

54. Yilmaz, E.; Mosbach, K.; Haupt, K., Influence of functional and cross-linking monomers and the amount of template on the performance of molecularly imprinted polymers in binding assays. *Anal. Commun.* **1999,** *36*, 167-170.

# CHAPTER FIVE:

## ENHANCED FUNCTIONALITY OF LITHOGRAPHICALLY PATTERNABLE BLOCK COPOLYMERS THROUGH HAFNIA NANOPARTICLE CO-ASSEMBLY

### *5.1 Introduction*

Today's semiconductor devices feature billions of transistors in total areas often not much bigger than a quarter. Over fifty years of manufacturing expertise and research investment have enabled this development, but the march to higher circuit densities and smaller feature sizes is becoming exceedingly challenging with every new technology generation. The workhorse technology behind these advances is a technique called photolithography, which relies on high-energy ultraviolet photons to transfer circuit information through a radiation-induced solubility switch in a thin polymer film "photoresist."

Lithography using self-assembling block copolymers is another potential approach for nanoscopic structure control. Self-assembly can be defined as a process in which disordered materials spontaneously organize into more ordered structures with atomic or molecular-level precision without human intervention.[1] Block copolymers consist of two or more polymer segments linked at one of their ends with a covalent bond. A combination of entropic and enthalpic effects originating from the molecular interaction of the two immiscible polymers drives the formation of periodic patterns such as spheres, cylinders and lamellae in the mesoscopic (10-100 nm) regime.[2] Similar to traditional polymeric photoresists used in photolithography, they can be dissolved in an organic solvent and spin coated from solution as a thin film. The selective removal of one of the periodic features, either by wet or dry etching techniques, allows the remaining pattern to 'resist' future dry etching steps for the transfer of the self-assembled pattern into any semiconducting substrate. Therefore, with feature sizes less than 50 nm, this class of material is capable of producing etched pattern densities greater than $10^{11}$ per square centimeter, without the use of an expensive lithographic toolset.[3] Furthermore, the size and periodicity of the self-assembly typically scales with the polymer molecular weight, giving the polymer

chemist control over the critical dimension (CD) of the microdomain structures. Many semiconductor applications, such as CMOS capacitors,[4] field effect transistors,[5] and airgap insulation[6] have been revolutionized using the nanoscale features of block copolymers.

An important part of any photolithographic process is the ability of the photoresist to "resist" plasma etching, which is commonly used to scribe the lithographic pattern into the substrate. As such, the etch resistance of a film is a very important parameter that will define the success of the material in post-lithographic pattern transfer steps. A photoresist with poor etch resistance will require a very thick spin-coated film in order to etch a significant amount into the substrate, whereas a material with good etch resistance will not require as thick of a film in order to accomplish the same. In block copolymer lithography, this concept is especially true, since the thickness of the block copolymer film is limited by the difficulty of inducing long-range order in films greater than 400 nm.[7] As a result, a block copolymer matrix requires very high etch resistance.

There have been many efforts to incorporate inorganic additives into block copolymer matrices to increase etch resistance, in addition to improving many other material properties. At least four different approaches have been put forward, including polymerization of inorganic-containing monomers,[8, 9] "in-situ" reduction of metal salts or sol-gel synthesis of inorganic precursors within block copolymer microdomains,[10,11] phase-selective evaporation or sputtering of metals onto amphiphilic block copolymer films,[12] and "co-assembly" of inorganic polymers or nanoparticles into specific block copolymer phases during solvent evaporation.[13,14] The latter approach appears straightforward, but is actually quite complex.

There are a couple key criteria that must be met in order to successfully blend inorganic nanoparticles into a host block copolymer microdomain. First, the size of the

inorganic particle must be less than the corresponding dimensions of the block in which it is mixed. For polymers, this dimension is approximately equal to the root mean square end-to-end distance of the chain, or $6^{1/2}$ times the radius of gyration ($R_g$) of the ideal chain.[15] As the nanoparticle size approaches $R_g$, a competition occurs between the translational entropy of the nanoparticles and the conformational entropy of the polymer. Above $R_g$, the nanoparticles will be expelled from the host polymer in order to avoid the excessive entropic penalty of having to wrap around the nanoparticle. Second, enthalpic interactions are required to drive the inorganic component into the host polymer matrix. These may include ionic, dipole-dipole, or hydrogen-bonding interactions. For example, the alkyl ether bond in polyethylene oxide has been used for hydrogen bonding with a polymeric silsesquioxane containing hydroxyl groups.[13] The same functionality on the negative-tone photoresist, poly(4-hydroxystyrene) (PHOST), has also been exploited to incorporate functionalized nanoparticles to enhance the properties of gate dielectric materials.[16] However, to the best of the author's knowledge, a PHOST-based block copolymer has never been used for nanoparticle co-assembly.

We propose a combination of chemically amplified block copolymer lithography (CABL, Chapter 3), using the lithographically patternable PαMS-*b*-PHOST block copolymer [Figure 5.1(a)], with the blending of inorganic hafnium oxide nanoparticles, [Hf-MAA, Chapter 4, Figure 5.1(b)]. The incorporation of inorganic nanoparticles will strengthen the etch resistance of the self-assembled template after removal of the PαMS minor phase. The purpose of this study was to determine if enthalpic interactions can be used to drive segregation of the nanoparticles into the block copolymer and to investigate what effect nanoparticle addition has on the etch resistance and patternability of the matrix phase, in addition to the degradability of the PαMS phase relative to PHOST.

a)

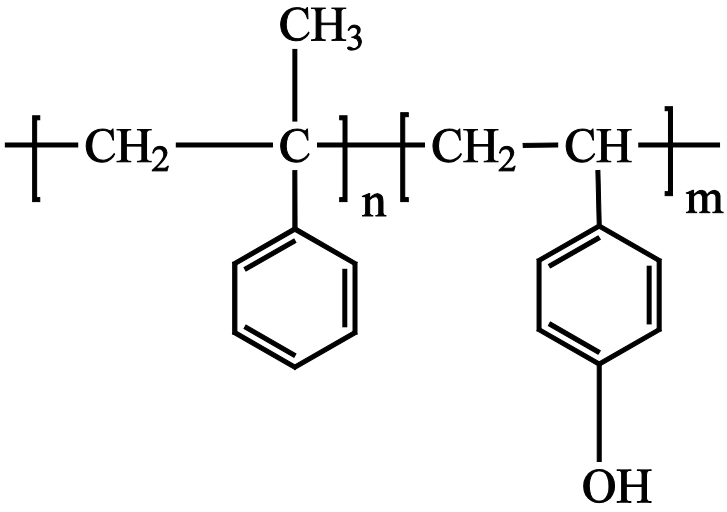


b)

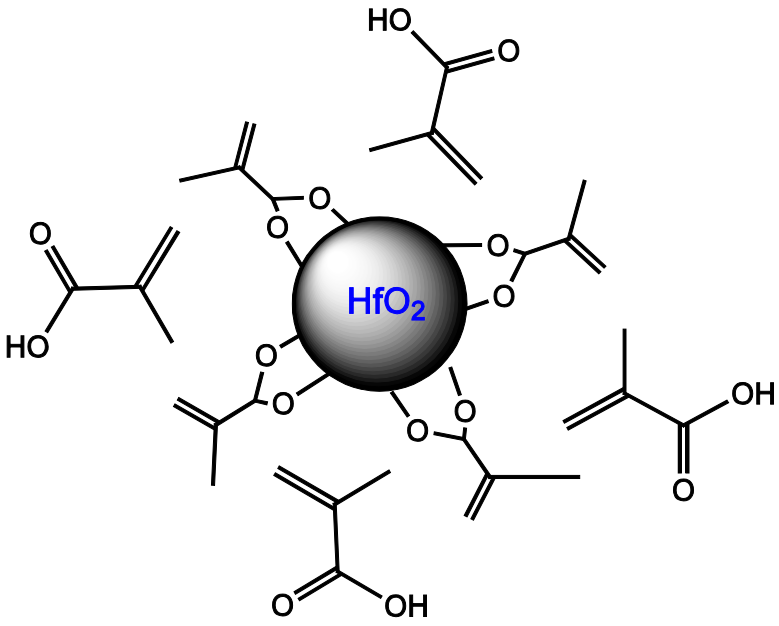


Figure 5.1. The chemical structure of (a) poly(α-methylstyrene-*block*-4-hydroxystyrene) (PαMS-*b*-PHOST) and (b)Hf-MAA/MAA .

### *5.2 Experimental Method*

#### *5.2.1 Materials*

PαMS-*b*-PHOST was synthesized according to established literature procedures.[17] Methacrylic acid (99%) was obtained from Aldrich and distilled under reduced pressure. Silicon wafers were obtained from WRS (Spring City, PA). All other materials and solvents were obtained from Aldrich unless otherwise noted in the text.

#### *5.2.2 Synthesis of Hf-MAA*

A similar synthesis of hafnia nanoparticles has been described in a previous publication.[18] To a three-neck round bottom flask, 5 g (12 mmol) of hafnium isopropoxide precursor and 25 ml (286 mmol) of methacrylic acid were added along with a magnetic stir bar. After sealing the flask with two rubber septa and a condenser, the solution was allowed to equilibrate at 65°C under reflux while stirring at 300 rpm for 15min. Separately, 9 ml of methacrylic acid was mixed with 1 ml of de-ionized water (55.5 mmol) in a syringe until a homogenous solution was formed. To start the hydrolysis and condensation reaction, the water/MAA solution was slowly injected into the reaction flask over the course of one minute. During the injection, the precursor suspension turned from turbid to clear.

After 18 hours, an additional injection of (9 ml of MAA and 1 ml of $H_2O$) was added with a syringe. After 2 additional hours, the reaction was stopped and the nanoparticles precipitated by adding a 2:1 volume of DI $H_2O$ into the reaction flask. The white nanoparticle aggregates were centrifuged at 8000 rpm for 8 minutes to separate them from the supernatant and the supernatant was decanted off. A cycle of suspending the nanoparticles in water, separating the aggregates via centrifuge, and decanting the water was performed 4 times. After the final wash step, the supernatant

was decanted and the nanoparticles were placed in a vacuum oven at room temperature for at least twenty-four hours to form a dry white powder (yield ~70%). TGA showed these nanoparticles to have an organic content of approximately 40%.

### *5.2.3 Bulk TEM Sample Preparation*

2 mL of a 5 wt.% solution of PαMS-*b*-PHOST was dissolved in THF, filtered through a 0.45 μm nylon filter, and charged into small (5mL) Teflon beakers. The beakers sat on a thick layer of paper towels, underneath an inverted crystallization dish. A separate reservoir of pure THF underneath the dish was used to slow the THF evaporation from the Teflon beakers. The solutions were left to slowly dry for 4 days, and then annealed under vacuum at 200 °C for 3 days. The resulting bulk films of the block copolymers were embedded in epoxy and cured overnight at 65 °C. The hardened epoxy was cut to 50 nm slices using a Leica Ultracut UCT microtome equipped with a diamond knife at room temperature. The slices were picked up from a water bath onto copper TEM grids.

### *5.2.4 Thin Film Preparation*

The polymers were mixed with 4 wt. % (w/w) of the crosslinking agent tetramethoxymethylglycouril (TMMGU, Cytec Industries), and 1.5 wt.% of the photoacid generating species triphenylsulfonium triflate (TPST, Aldrich), relative to the block copolymer. The PαMS-*b*-PHOST was dissolved in propylene glycol monomethyl ether acetate (PGMEA) and left overnight under magnetic stirring. Any unwanted organic contamination on the silicon wafers was cleaned using a 3:1 mixture of sulfuric acid: hydrogen peroxide “Piranha” solution maintained at 75 °C, in addition to producing a consistently hydrophilic surface. The film thickness was varied according to the solution concentration and spin speed. The freshly spin coated wafers were placed in a closed Teflon-sealed glass jar with a small reservoir of

tetrahydrofuran solvent for varying amounts of time. The empty volume of the vessel and solvent surface area was systematically varied in order to find optimal conditions for the annealing process. The films were removed from the vessel just before dewetting of the polymer film took place, as seen from the random nucleation of holes on the film surface.

### *5.2.5 Characterization Methods*

The size of the nanoparticles was measured by dynamic light scattering using a Malvern Zetasizer Nano-ZS. Thermal analysis was performed on a TA Q1000 modulated differential scanning calorimeter (DSC). About 10 mg of the blend sample was placed in aluminum pans and heated from 25 °C to 250 °C at a 15 °C/minute heating rate to erase the thermal history, cooled to room temperature, and then heated again. Data was acquired on the first heating ramp, using an empty aluminum pan was used as the reference. To measure the thermal degradation of the blend components, a TA Instruments Q500 Thermogravimetric Analyzer (TGA) was used to heat the samples from room temperature to 550 °C at a heating rate of 5 °C/minute under a nitrogen atmosphere. Volume fractions of the Hf-MAA nanoparticles were quantified following the procedure detailed in Warren et al.[14] For FTIR sample preparation, after drying the nanoparticles in vacuum to remove residual water they were added in 1% (w/w) to dry KBr powder and pressed into a disc 13 mm in diameter and 1.5 – 2 mm in thickness. FTIR spectra were collected on a Mattson spectrometer using a wavenumber range from 400 to 4000 $cm^{-1}$, with a nominal resolution of 2 $cm^{-1}$. For each spectrum, 64 scans were collected and averaged. For optical absorbance measurements of the nanoparticle films, the films were spin coated on cleaned quartz wafers, baked at 130 °C for 1 min, and then measured using a Shimadzu UV-3101 UV/Vis Spectrophotometer. Film thicknesses were measured with a Woollam

Spectroscopic Variable Angle Ellipsometer (for film thicknesses below 50 nm) or with a FilmMetrics F20 reflectometer (for film thicknesses greater than 50 nm). To probe the top surface of the film, atomic force microscopy (AFM) was carried out in ambient conditions using a Veeco Dimension 3100 scanning probe microscope operating in tapping mode. Olympus cantilever Si tips were used (resonant frequency = 300 kHz, force constant= 42 N/m, tip radius <10 nm). Digital Instruments Nanoscope© software was used for AFM image processing, along with power spectral density analysis for measurement of the spatial period. Bright field transmission electron microscopy (TEM) was performed using an FEI Tecnai F12 microscope operating at 120 kV. TEM images were analyzed using ImageJ software. For oxygen plasma reactive-ion etching, the experiment was carried out using a Glenn 1000 oxygen plasma resist ashing tool at the Cornell Nanofabrication Facility (50W, 0.3 mTorr, 42 sccm $O_2$). For $SF_6/O_2$ etching, the PT72 etcher was used ($SF_6$=13 sccm, $O_2$=40 sccm, 50 mTorr, 100 W). The Samco UV/Ozone Cleaner 'UV1' was used for the PαMS removal study, with an oxygen flow rate of 5 mL/min, UV lamp turned on, the ozone generator off, and a hotplate temperature of 80 °C. SAXS experiments were performed using a rotating anode x-ray tube using the CuKα line (λ=0.154 nm) in the Gruner Lab in Clark Hall, and a total exposure time of twenty minutes.

## *5.3 Results and Discussion*

### *5.3.1 Synthesis of Hf-MAA*

The growth of Hf-MAA nanoparticles proceeded from a hafnia isopropoxide precursor in the presence of water and methacrylic acid at 80 °C. The size of the nanoparticles was shown to be ~2 nm as shown by dynamic light scattering and TEM (Chapter 4). TGA data showed a weight loss of ~40% upon heating to 550 °C. A distinct drop in weight at around the boiling point of methacrylic acid (~163 °C)

indicated the presence of approximately 10 wt. % methacrylic acid monomer that was not purified from the material (Chapter 4). As a result, FTIR of the nanoparticles showed distinct peaks around 3300 cm-1, characteristic of the –OH and –COOH stretch (Chapter 4).

### *5.3.2 Thermal Analysis of PHOST–Hf-MAA Interaction*

Previous work has shown that carboxylic acids bind strongly to metal oxide surfaces, presenting various functional groups outward and providing opportunities for enthalpic interactions with host polymers.[19] We have exploited enthalpic interactions in order to enhance compatibility of hafnia nanoparticles with the majority block of a lithographically patternable block copolymer, poly(4-hydroxystyrene), or PHOST. As one example, hydrogen bonding interactions between methacrylic esters and PHOST polymers are well known in the literature.[20]

The thermal interaction of Hf-MAA with the PαMS and PHOST homopolymers was investigated using a DSC, as shown in Figure 5.2(a) and 5.2(b), respectively. The addition of the Hf-MAA nanoparticles increased the glass transition temperature ($T_g$) of PHOST significantly, but the $T_g$ of PαMS remained unaffected. The strong PHOST-Hf-MAA interactions hinder the segmental motion of the polymer chains as the temperature of the sample is increased, creating a higher and broader glass transition temperature range.[21, 22] The 20 wt.% Hf-MAA sample showed the highest $T_g$ increase ($T_g$ = 213 °C), followed by the 40 wt. % Hf-MAA (Tg= 211 °C), and then the 60 wt. % Hf-MAA blend (201 °C). The decrease in $T_g$ in the 40% and 60 % samples may signify an increasing amount of macrophase separation the nanoparticles from the PHOST matrix, which would bring the $T_g$ back down towards its original value (172 °C). This

a)

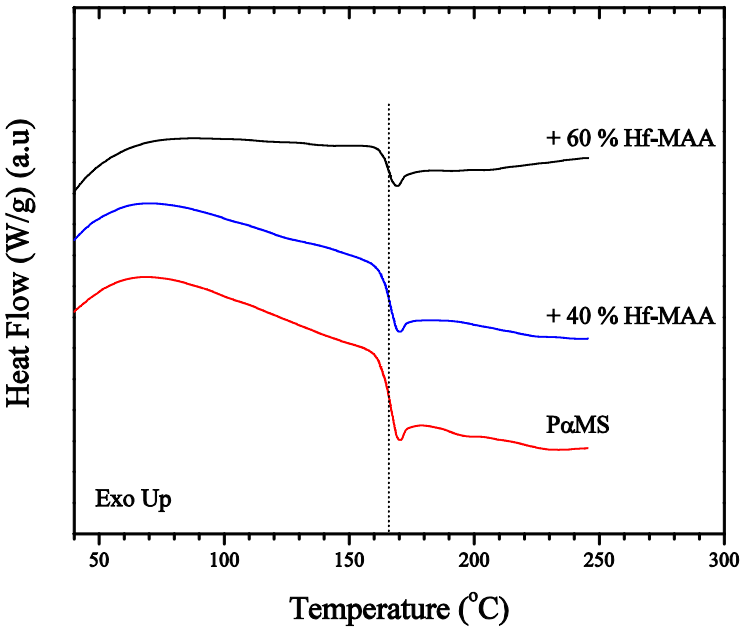


b)

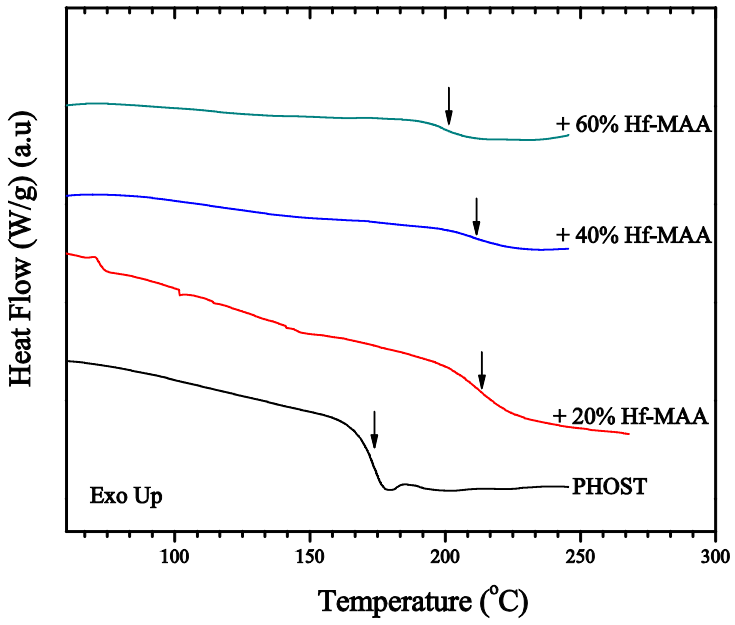


Figure 5.2. DSC exotherms of a) PαMS and b) PHOST, both blended with Hf-MAA/MAA nanoparticles.

data strongly supported selective blending of Hf-MAA into the PHOST phase. It is worth noting, however, that the Hf-MAA used in this study contains about 10 wt. % impurity of methacrylic acid monomer left over from the synthesis. The free methacrylic acid monomer may help to compatibilize the nanoparticle with the PHOST phase. Further study must be done to see if completely purified Hf-MAA will still exhibit the same strong interaction with PHOST polymer.

### *5.3.3 TEM Characterization of Hf-MAA/PαMS-b-PHOST Bulk Films*

Although understanding the behavior of each of the homopolymers blended with Hf-MAA is critical and will be explored in greater detail later in the chapter, the final application of the Hf-MAA addition will be inside the PHOST block of PαMS-*b*-PHOST. Hf-MAA nanoparticles were blended in a good solvent from 0 to 60 wt. % (relative to the weight of the PHOST phase) into PαMS-*b*-PHOST (27K/11K g/mol, 29% PHOST). A two-dimensional projection of the the bulk films was analyzed using TEM for visual proof of nanoparticle localization within the PHOST domain.

Without any Hf-MAA loading, the neat block copolymer displayed a lamellar morphology with a d-spacing of approximately 30 nm, as shown by the TEM image in Figure 5.3(a). In the nanoparticle loaded samples, no chemical vapor staining was necessary due because the high atomic number nanoparticles acted as a selective contrast agent for the PHOST block.[23]

There were a couple significant observations from this study. First, it was found that the nanoparticles showed no preference for the PαMS/PHOST interface. This was a question since the particles contain chemical groups which are similar to both the PαMS and PHOST block (the $–CH_3$ end-group on the MAA ligand, and the –OH groups in Hf-OH, respectively). Second, the nanoparticles started to macrophase separate out the PHOST phase at 40 wt. %, indicating a limit for how much inorganic

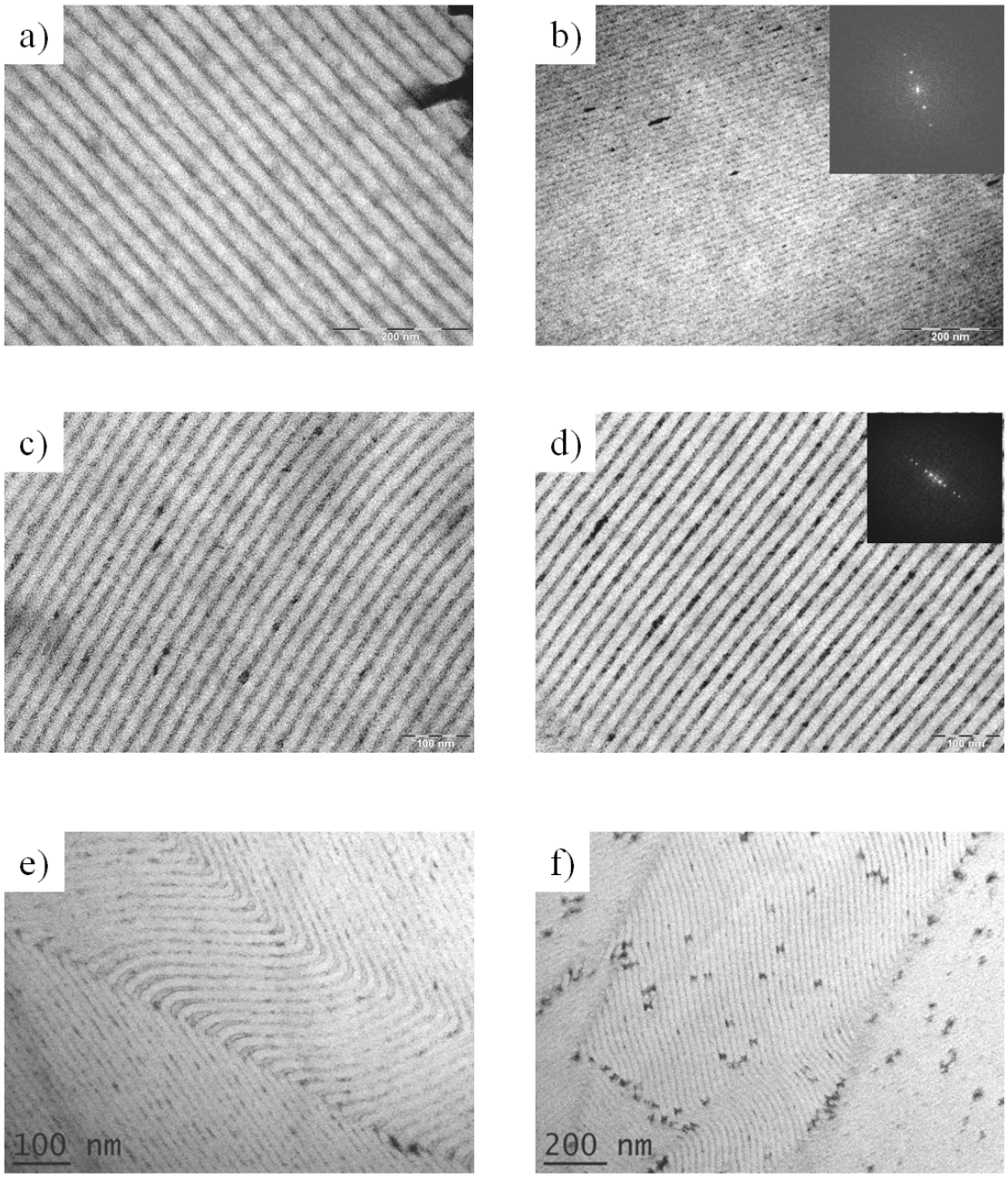


Figure 5.3. Transmission electron microscopy images of a PαMS-*b*-PHOST block copolymer (27K/11K g/mol, 29% PHOST) with a) 0% Hf-MAA, in which the PHOST phase is stained dark with 20 minutes of vapor from a fresh ruthenium tetroxide solution, b) 10% Hf-MAA, c) 20% Hf-MAA, d) 30% Hf-MAA, e) 40% Hf-MAA, f) 50% Hf-MAA, all measured by weight relative to the weight of the PHOST block.

can be incorporated into the block copolymer before macrophase separation. This was equivalent to a maximum total volume fraction of approximately 25% relative to the PHOST phase. No order-order phase transitions were observed with increasing loading into the PHOST block, even though the addition of the Hf-MAA represented large changes in the volume fraction of the PHOST block. Third, even at Hf-MAA concentrations lower than 40 wt. %, aggregation of nanoparticles into some individual block domains was observed. The nanoparticles may have started to aggregate during the slow drying sample preparation of the TEM sample, when the concentration of the nanoparticles rose above their solubility limit in the tetrahydrofuran drying solvent. Local aggregation was also evident at points of curvature in the lamellar microdomains, corresponding to other literature reports that discuss blended additives in block copolymers that tended to segregate to the points of curvature to mitigate the bending stress in the polymer chains.[24]

We found that the domain spacing was not consistent between different Hf-MAA loaded samples, for a couple reasons that all stem from the TEM sample preparation technique.[25] For starters, the microtome may slice through the lamellae at different angles, producing a two-dimensional projection of the sample that will vary from one grain of microdomains to another, and also from sample to sample. Also, the microtome introduces a large component of shear into the samples that may stretch or compress the microdomains. Lastly, since TEM only produces a projection of a three-dimensional bulk film, and only small areas of the block copolymer can be averaged at one time, it cannot produce an accurate measurement of the periodicity.

### *5.3.4 SAXS Characterization*

For measurement of the d-spacing of the bulk Hf-MAA blended block copolymers, we turned to small-angle x-ray scattering (SAXS). Due to the x-ray spot

(area~3 $mm^2$) passing through a three-dimensional bulk film, SAXS measures an ensemble average of periodicity from a very large number of microdomains. The film containing 0% Hf-MAA only showed a diffuse powder ring, and did not show any first order peak (q*), possibly due to the small electron density difference between the domains. Upon blending increasing amounts of the nanoparticles, a strong first order (q*) scattering peak, in addtion to a weak second order ($q^1$) peak was observed. The spacing of $q^1$ was approximately a factor of two greater than the first, confirming a lamellar morphology (not shown).

A noteworthy observation was made regarding the the q* peak, as presented in Figure 5.4. We found that the q* peak was actually composed of two overlapping peaks, one at q = 0.214 $nm^{-1}$ (d= 29 nm), and one at q=0.174 $nm^{-1}$ (d=36 nm). The relative area of the latter peak (q=0.174 $nm^{-1}$) increased with an increasing concentration of nanoparticles in the blend, indicating a possible expansion of the PHOST phase with nanoparticle loading. It is currently unclear why a statistical distribution of d-spacings was not formed with increasing nanoparticle loading, which would create a more broad peak. Instead, there seemed to be a discrete jump from the original BCP period (29 nm) to the Hf-MAA blended BCP period (36 nm) that created two distinct humps in the q* peak. Further investigations into this topic are ongoing.

### *5.3.5 Plasma Etching Studies for Pattern Transfer*

As discussed previously, oxygen and fluorocarbon plasmas are used to etch organic and inorganic materials, respectively. The etch resistance of PHOST to oxygen ($O_2$) and fluorocarbon ($SF_6$) gas plasmas may be dramatically affected by the incorporation of Hf-MAA, leading to more efficient pattern transfer of the self-assembled PαMS-*b*-PHOST pattern into silicon substrates. Data shown in the previous chapter (Chapter 4) indicate that the Hf-MAA nanoparticles by themselves show etch

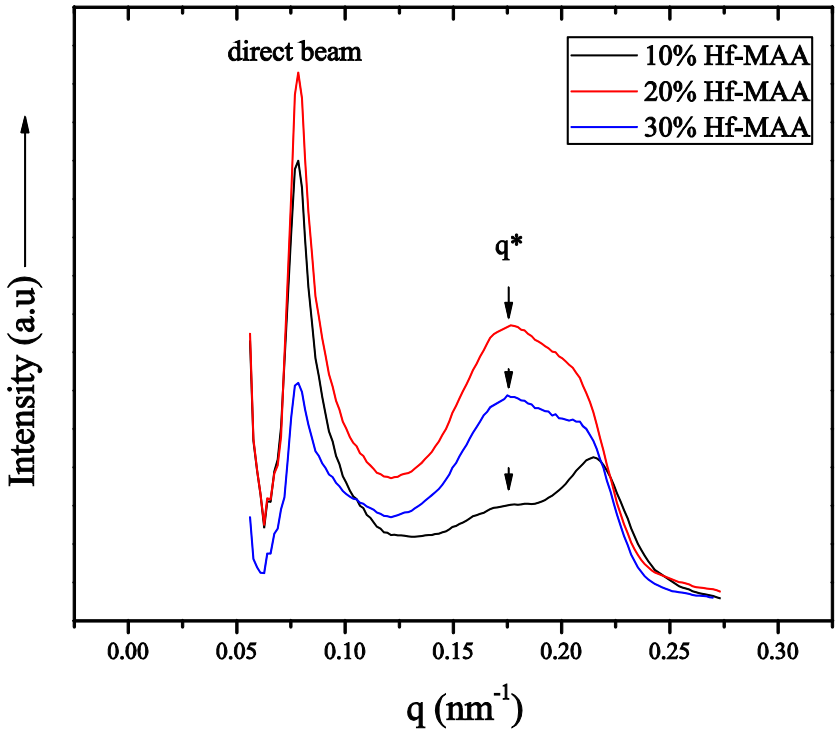


Figure 5.4. SAXS scattering profiles of the q* peak in the10%, 20% and 30% Hf-MAA samples

resistance over 12 times greater than a pure PHOST homopolymer. Increasing concentrations of Hf-MAA nanoparticles were blended into a PHOST homopolymer as a homogeneous mixture and spin cast as a smooth film up to 60 wt. %. The films were exposed to each type of plasma gas for sequential time intervals and measured with an ellipsometer after each interval to measure the etch rate quantitatively. All etch rate data fit very well with a linear regression analysis ($R^2 \sim 0.99$) and the absolute value of the slope from the trendline was taken as the etch rate. The etch rate of each film was compared to a reference pure PHOST homopolymer film, and the results are shown in Figure 5.5.

For the oxygen plasma gas treatment, the decrease in etch rate above 10% Hf-MAA addition was immediately evident. It is unclear why the 10% loading of Hf-MAA actually increased the etch rate of PHOST slightly. It is noteworthy that the oxygen etch rate of PHOST+Hf-MAA did not surpass that of the PαMS block until greater than 30% Hf-MAA loading. The enhancement in PαMS $O_2$ plasma etch resistance over that of PHOST comes from the absence of oxygen in the PαMS chemical structure, as proven empirically by Ohnishi et al.[26] This value should be taken into consideration if the PαMS in the block copolymer is removed via a dry oxygen plasma etching step, otherwise, the PαMS block can be removed using a combination of heat and ultraviolet radiation, as described in Section 5.3.6.

The fluorocarbon gas plasma recipe chosen for this study is traditionally used to etch bulk silicon at a rate of 100 nanometers per minute. The total decrease in the etch rate after nanoparticle loading was relatively less than that for the oxygen plasma. However, the 40 wt. % Hf-MAA sample showed an etch rate that was over 20% less than that of pure PHOST, demonstrating a marked improvement in the ability to transfer self-assembled PαMS-*b*-PHOST patterns into silicon substrates. For this type of plasma, the chemical structure of PαMS does not give any advantage relative to the

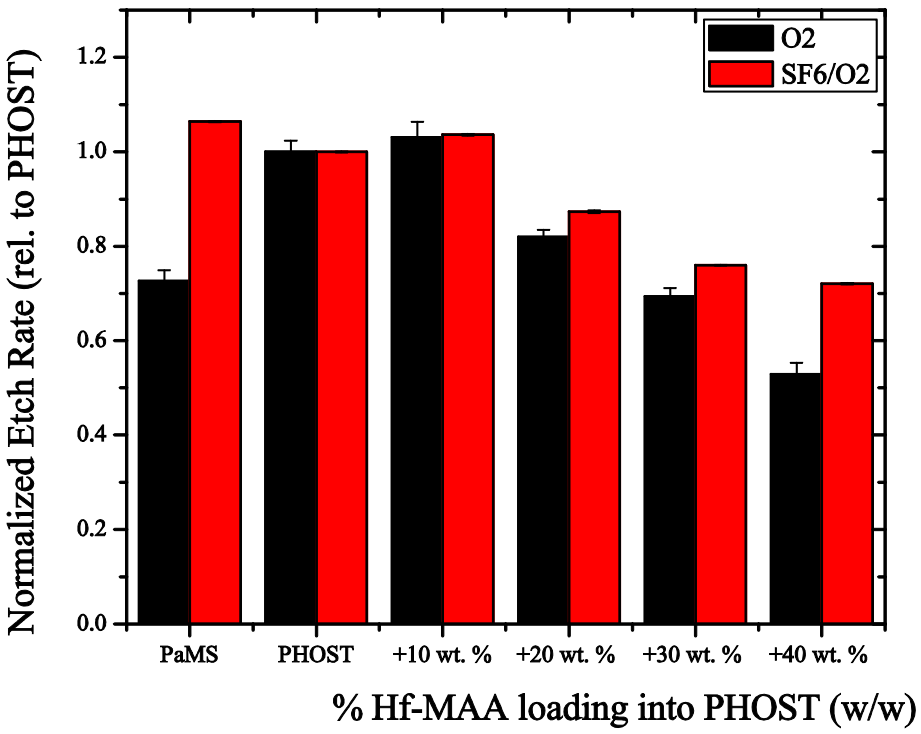


Figure 5.5. $O_2$ and $SF_6/O_2$ plasma etching of each of the respective homopolymers in the PαMS-*b*-PHOST block copolymer

PHOST block. Again, the 10 wt.% loading showed a slight increase in relative etch rate versus that of the PHOST, and then the etch rate decreased upon increasing nanoparticle loading.

### *5.3.6 Patternability of PHOST/Hf-MAA*

The ability to photopattern the PαMS-*b*-PHOST block copolymer must not be compromised by the addition of Hf-MAA nanoparticles. In order to test whether or not this was the case, a set of contrast curves comparing the gel dose of different PHOST/Hf-MAA blends were created. The negative-tone PHOST photoresist is actually a three component system, also containing a small amount of photoacid generating (TPST) and a crosslinking molecule, tetramethoxymethylglycouril (TMMGU). PHOST/ Hf-MAA films were loaded with 2 wt.% TPST and 6 wt. % TMMGU and exposed to increasing doses of ultraviolet radition in order to find the dose required to form a crosslinked gel, which did not dissolve in an aqueous base developing solvent.

A plot of the normalized film thickness versus exposure dose for these films is shown in Figure 5.6(a). The plot shows that the nanoparticle-blended films required about ten times the dose in order to gel, compared to the pure PHOST polymer film. This loss in sensitivity, however, may be caused by the increase of the absorbance of the film from the added nanoparticles. Indeed, we found that the 248 nm absorbance of the films increased by at least a factor of two in the case of the Hf-MAA additions, as measured by a spectrophotometer. This increase in absorbance corresponded to a significant decrease in the transmission of light through the resist film. The UV transmission decreased to about 11% in the case of the 20% Hf-MAA blend, and 7% in the case of the 40% Hf-MAA blend, compared to 75% for the pure PHOST film, as shown in Figure 5.6(b). Taking into account the loss in photon transmission, when the

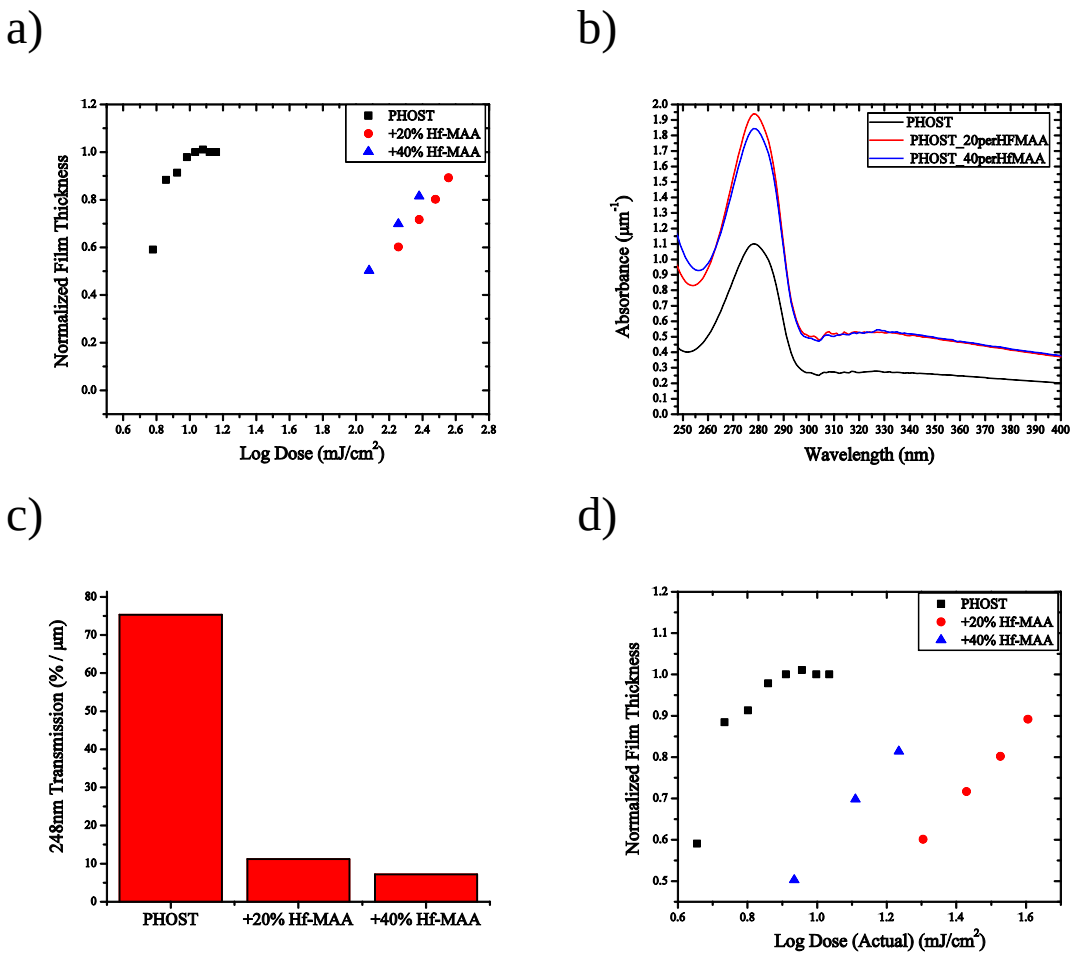


Figure 5.6. a) Contrast curves showing the normalized film thickness versus exposure dose for PHOST and PHOST+Hf-MAA resist films, b) % transmission loss per micron for each film, c) normalized film thickness versus actual dose of photons received.

contrast curve in Figure 5.6(a) is re-plotted based on the actual number of UV photons received by the film, the sensitivity of the Hf-MAA loaded films come closer to that of the neat PHOST film, as displayed in Figure 5.6(c). We found that the remaining discrepancy between PHOST and the PHOST/Hf-MAA contrast curves correlated with the increased $T_g$ in the Hf-MAA blended films. For example, the sensitivity of the 20 wt. % Hf-MAA sample ($T_g$=213 °C) was found to be lower than that of the 40 wt. % Hf-MAA film (211 °C). Therefore, the 115 °C bake performed after UV exposure, which is used to increase TPST diffusion through the film and catalyze the polymer crosslinking reactions with TMMGU, may be insufficient in the Hf-MAA blended films. In other words, the slight increase in $T_g$ for the 20 wt. % Hf-MAA sample may lead to a decreased acid diffusion length, or a decrease in the total amount of catalyzed acid compared to the 40 wt. % sample. By increasing the temperature of the PEB step by an appropriate amount relative to the $T_g$ value of the films, the Hf-MAA loaded PHOST may match the same level of patterning performance as that of a pure PHOST film.

### *5.3.7 PαMS-b-PHOST/Hf-MAA Thin Film Characterization*

For block copolymer lithography applications, the block copolymer must be spin coated as a thin film, and the microdomains processed for long-range order. Block copolymer films of the 27K/11K PαMS-*b*-PHOST sample were blended with 30 wt. % Hf-MAA and spun cast as a thin film from a PGMEA solution to investigate the mobility of the films with Hf-MAA nanoparticle blending.

Solvent annealing was used to impart mobility on the BCP film. BCP films with and without Hf-MAA nanoparticles were placed in a sealed jar saturated with tetrahydrofuran vapor at room temperature. Tetrahydrofuran is a good solvent for both blocks of the block copolymer.[27] The solvent vapor effectively plasticized the film,

which was equivalent to a significant drop in the polymer's $T_g$ and an increase in the mobility of the microdomains at room temperature. The 40 °C increase in the $T_g$ of the Hf-MAA loaded film was expected to lead to a decrease in mobility of the block copolymer microdomains, so the films were left for four days in the solvent-saturated chamber and then dried immediately with a blast of nitrogen to lock in the solvent-annealed morphology. A representative AFM image from a four day sample, and one from the as-cast film are shown in Figure 5.7. The as-cast morphology shows a micellar structure with no evident long-range order, and the solvent-annealed structure showed randomly oriented arrays of lines. Considering that the bulk TEM images of this polymer showed lamellae, a vertical lamellar phase identification was enticing, however, more characterization was necessary to identify the morphology of the block copolymer through the entire depth of the film.

Cross-sectional TEM was used as a complementary characterization technique to identify the morphology more definitively. Using this technique, a profile of the film depth can be seen, again using hafnia nanoparticles as a selective staining agent for the PHOST block. As seen in Figure 5.8, the Hf-MAA nanoparticles appeared as dark dots in the cross-sectional images, which, when considering the lines observed in the top-down AFM, could only signify lying cylinders of PHOST/Hf-MAA. The PαMS block in the BCP is slightly selective to THF vapor, as seen by comparing the Hildebrand solubility parameter of each block to THF. The Hildebrand solubility parameter of THF is 9.1, compared to that of PαMS (9.4) and PHOST (12.0), in units of $(cal/cm^3)^{½}$.[27] Order-order phase transitions such as these are well-known in block copolymer systems, due to an increase in volume fraction caused by the preferential uptake of solvent vapor into one of the blocks.[28] Thus, after four days of THF exposure, the volume fraction of the PαMS has swollen enough to cause a lamellar to cylindrical order-order transition. The cylinders lie in the plane of the substrate due to

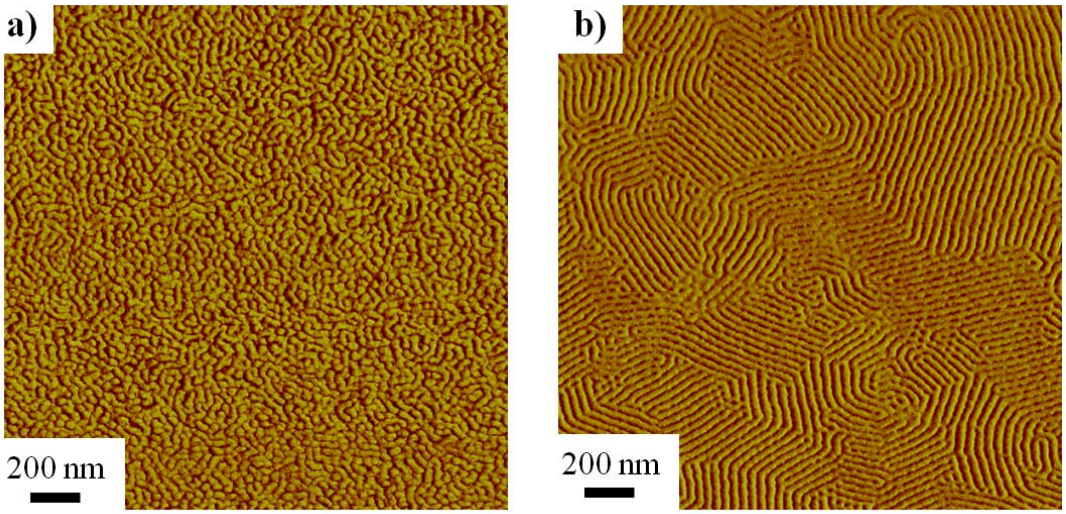


Figure 5.7. Phase AFM images showing (a) the as spun BCP film morphology of PαMS-*b*-PHOST (27K/11K), as well as (b) the same film annealed in THF vapor for four days at room temperature.

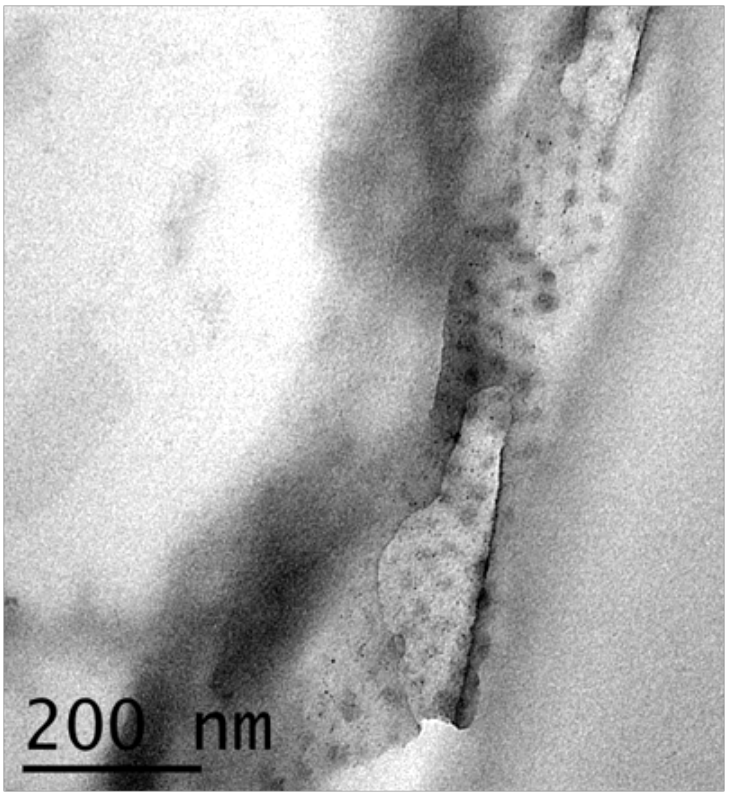


Figure 5.8. Cross-sectional transmission electron microscope image of the THF annealed PαMS-b-PHOST/ 30% Hf-MAA film showing the PHOST/Hf-MAA cylinders lying in the plane of the substrate. The PHOST cylinders appear dark due to embedded Hf-MAA nanoparticles.

the preferential wetting of the PHOST block to the substrate. Neutralization of the polymer/substrate and polymer/vapor interface may be used to orient the microdomains vertically relative to the substrate (Chapter 3).

### *5.3.8 Selective Removal of PαMS Domain*

One of the salient features of the PαMS-*b*-PHOST system is the inclusion of poly(α-methylstyrene) as the minority block, which is well known for its degradability at relatively low temperatures. The reason for this is the low ceiling temperature of PαMS ($T_c$~65 °C), above which the polymer thermodynamically prefers to exist as a monomer. It is theoretically impossible to polymerize the α-methylstyrene monomer at a reaction temperature above its $T_c$.[29] Once the polymer is produced, however, the kinetics of monomer formation are quite slow. Li et al., used a broadband UV radiation source ($\lambda_{peak}$ = 365nm) to produce free radicals within the film that accelerated the kinetics of depolymerization.[17] The authors in this study also used a high vacuum system to remove the monomer produced by the de-polymerization reaction, keeping the monomer concentration low in the film and driving the equilibrium of the reaction towards the production of monomer. Instead of an expensive high vacuum system, we have found that exposure to vacuum ultraviolet radiation in an oxygen-rich environment, followed by a simple soak in ethanol was sufficient to remove the degraded α-methylstyrene oligomers, while the crosslinked PHOST phase remained relatively robust.

PαMS and crosslinked PHOST homopolymer films loaded with and without Hf-MAA were prepared in order to test their degradation rate in a commercial UV/Ozone environment. An 80 °C hotplate temperature was used to bring the temperature of the film above that of the $T_c$ of PαMS to accelerate the depolymerization process. UV/Ozone treatment is well known for its ability to remove

organic molecules from inorganic substrates.[30, 31] The heart of the process is a low-pressure mercury ultraviolet lamp, with peak wavelengths in the vacuum ultraviolet (λ=185.4 nm) and in the deep ultraviolet (λ=253.7nm). The exposure of atmospheric oxygen to vacuum ultraviolet radiation begins the following reaction:

$$\begin{aligned} &O_2 \rightarrow O+O \text{ (Decomposition)} \\ &O + O_2 \rightarrow O_3 \text{ (Synthesis)} \\ &O_3 \rightarrow O^*+O_2 \text{ (Decomposition)} \end{aligned} \qquad \text{(Eq. 5.1)}$$

Atmospheric oxygen molecules are strongly absorbing in the vacuum ultraviolet, which photo-dissociate and then recombine with other oxygen molecules to form ozone, a very active oxidizing agent. In turn, deep ultraviolet radiation is also readily absorbed by the generated ozone molecule, which photo-dissociates to form molecular oxygen and atomic oxygen, the latter of which reacts with the polymer to form free radicals that accelerate the degradation of PαMS above its ceiling temperature. The byproducts for the reaction are carbon dioxide and water vapor, which are exhausted from the chamber in a nitrogen purge following each UV exposure.

Since some previous literature reported an effect of molecular weight on the degradation kinetics of PαMS,[29] we first examined the effect of molecular weight on PαMS degradation. Three thin films of PαMS with different molecular weights were spin coated to form thin films. The molecular weights were selected to match the typical PαMS molecular weights used in the block copolymers that were synthesized for this study. The results are shown in Figure 5.9. The graphs showed the facile degradation of PαMS at a rate of about 10nm/min, but the variation of the degradation rates among the different molecular weights were all within experimental error. Therefore, the results presented no evidence to suggest that the molecular weight of PαMS affected the degradation rate in this experiment. Next, the degradation rate of one representative PαMS sample was compared to that of crosslinked PHOST and

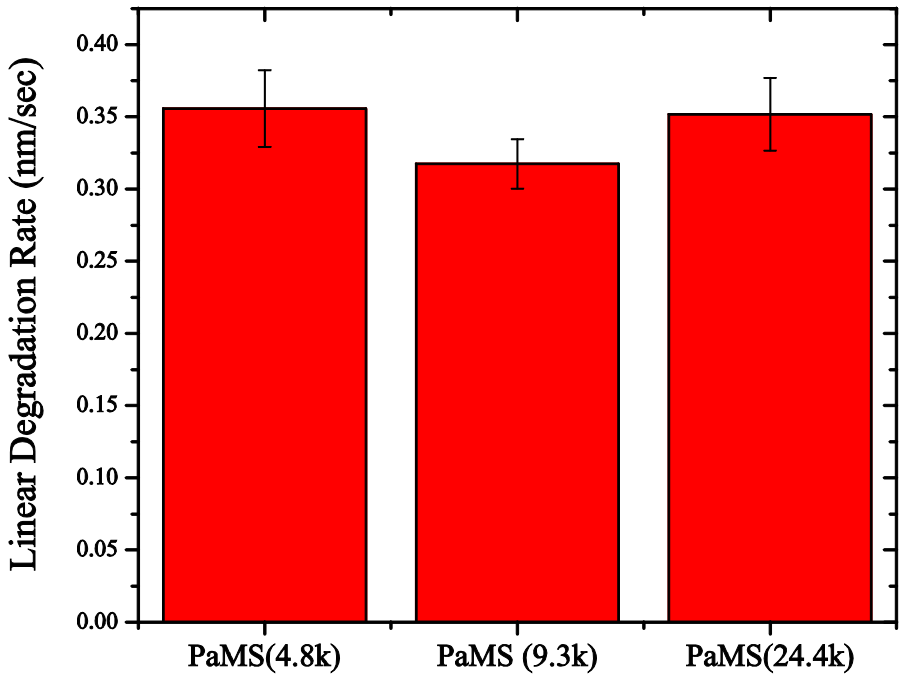


Figure 5.9. Linear degradation rate of poly(α-methylstyrene) of various molecular weights at 80 °C in the presence of oxygen radicals

the same loaded with 40 wt. % Hf-MAA nanoparticles, to simulate the removal of the PαMS from the nanoparticle-loaded PαMS-*b*-PHOST film. A chart comparing the three samples is shown in Figure 5.10. Immediately evident was the significantly lower linear degradation rate of the PHOST sample (0.167 nm/sec) compared to the PαMS sample (0.318 nm/sec). This corresponded to a PαMS removal rate of approximately 1.9:1 relative to that of the crosslinked PHOST sample. We found no significant difference in the degradation rate between the crosslinked PHOST with and without Hf-MAA nanoparticles. A comparison of these results with previously shown plasma etching data (Figure 5.10) demonstrated the power of thermodynamics in the PαMS degradation process. In the latter data set we were only able to achieve a PαMS: (PHOST+40 wt.% Hf-MAA) etch selectivity of 1.37:1, and 1.5:1 using an $SF_6/O_2$ plasma. Although both techniques worked, the data showed that the UV/Ozone method was the most efficient technique to remove the PαMS minor phase. Once the PαMS is efficiently removed, the high plasma etch resistance of the hafnium oxide nanoparticles can be put to good use in order to etch the self-assembled pattern into the silicon substrate with $SF_6/O_2$ plasma.

### *5.4 Conclusion*

The emergence of block copolymer lithography into mainstream semiconductor manufacturing depends on many substantial improvements on existing self-assembly platforms. In this chapter, we demonstrated that a robust, crosslinkable template could be formed by blending PαMS-*b*-PHOST block copolymers with hafnia nanoparticles covered with a methacrylic acid ligand. TEM showed a maximum Hf-MAA loading of up to 40 wt. % (25 vol. %) relative to the PHOST phase before the onset of macrophase separation. SAXS indicated that the block copolymer periodicity expanded by about 7 nm to accommodate the Hf-MAA nanoparticles. The resulting

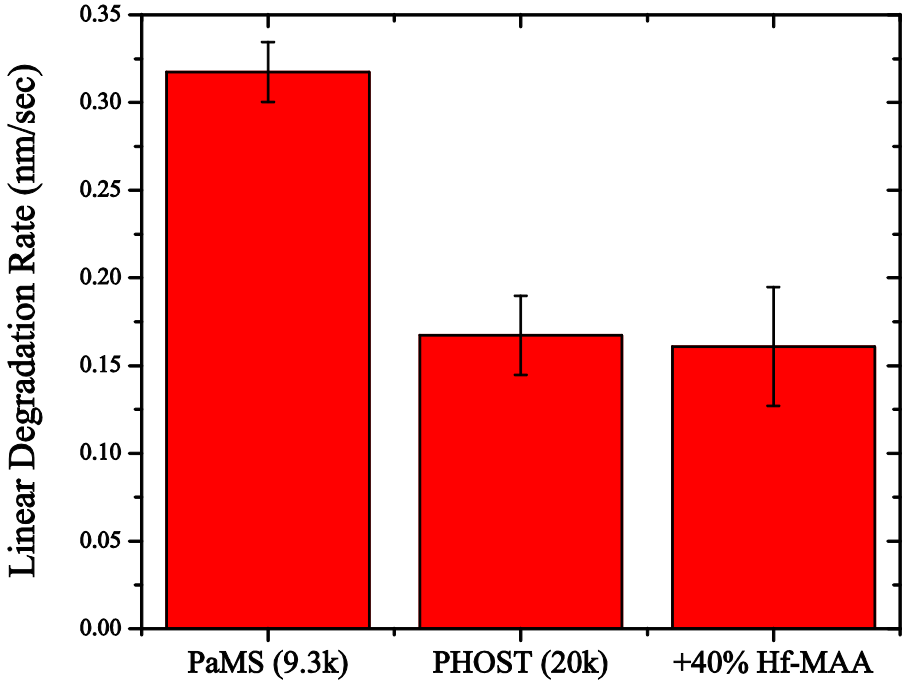


Figure 5.10. Linear degradation rate of PαMS (9,300 g/mol) compared with crosslinked PHOST and crosslinked PHOST loaded with 40% Hf-MAA at 80 °C in the presence of oxygen radicals

blended material showed an $SF_6/O_2$ etch resistance over twenty percent better than pure PHOST. We also demonstrated a new technique for the creation of nanoporosity in block copolymers, by taking advantage of the low ceiling temperature of poly(α-methylstyrene). Continuing work on the chemically amplified block copolymer lithography process will focus on vertical domain alignment of these blended films, followed by pattern transfer of the self-assembled template into semiconductor substrates.

### *5.5 Acknowledgements*

The author would like to acknowledge Mingqi Li and Joan K. Bosworth for the synthesis of the block copolymers used in this study. E.L.S. would also like to thank Suntao Wang for help with the SAXS measurements. Semiconductor Research Corporation, SEMATECH, and Motorola Corp. provided financial support for this work. This work was performed in part at the Cornell NanoScale Facility, a member of the National Nanotechnology Infrastructure Network, which is supported by the National Science Foundation (Grant ECS-0335765). This work made use of various facilities within the Cornell Center for Materials Research (CCMR) with support from the National Science Foundation Materials Research Science and Engineering Centers (MRSEC) program (DMR 0520404).

# APPENDIX

## *5.6 Dimensional Scaling of PαMS-b-PHOST*

Here, we demonstrate the ability to systematically control the critical dimension (CD) of PαMS-*b*-PHOST block copolymers by synthesizing polymers of different molecular weights. Table 5.1 shows the various polymer molecular weights used for this study, as measured by size exclusion chromatography. For a block copolymer photoresist material, it is important to have a continuous network of the negative-tone, crosslinked material in order to completely develop the film after the first lithography step, therefore most of the polymers were synthesized with a majority of PHOST.[32] Aiming for cylindrical PαMS microdomains, block copolymers were synthesized with PαMS wt.% fractions of around 30%. After slowly drying the film from solution and annealing in vacuum above both of the polymers $T_g$, it was possible to observe an equilibrium morphology of the films when they are dried into a bulk, free-standing film. The pieces were then embedded in epoxy, microtomed, and stained with ruthenium tetroxide vapor for contrast using bright field TEM. No observable degradation of the PαMS was observed following the anneal of the block copolymer. As seen from Figure 5.11(a-c), the intercylinder spacing ($L_o$) increased from 15.5 nm for the polymer with a molecular weight of 23,000 g/mol to 53.3nm for the 68,500 g/mol polymer.

Theoretical studies in block copolymer thermodynamics[33] and experimental [34] works have confirmed a power-law relationship between the intercylinder spacing ($L_o$) and the copolymer degree of polymerization, N:

$$L_o \propto N^{\gamma} \qquad \text{(Eq. 5.2)}$$

Table 5.1. The various number-average molecular weights ($M_n$) of the polymers used in this study. * As measured by GPC, ** As measured by bulk TEM analysis

| **PαMS $M_n$* (g/mol)** | **PHOST $M_n$* (g/mol)** | **Total $M_n$ (g/mol)** | **PαMS wt. (%)** | **PHOST wt. (%)** | **d-spacing ($L_o$) (nm) **** | **Morphology **** |
|---|---|---|---|---|---|---|
| **7,000** | 16,000 | 23,000 | 30.4 | 69.6 | 15.5 | Cylinders |
| **27,000** | 11,000 | 38,000 | 71.1 | 28.9 | 30.0 | Lamellae |
| **13,000** | 32,400 | 45,400 | 28.6 | 71.4 | 38.0 | Cylinders |
| **17,000** | 33,000 | 50,000 | 34.0 | 66.0 | 42.5 | Cylinders |
| **24,500** | 44,000 | 68,500 | 35.8 | 64.2 | 53.3 | Cylinders |

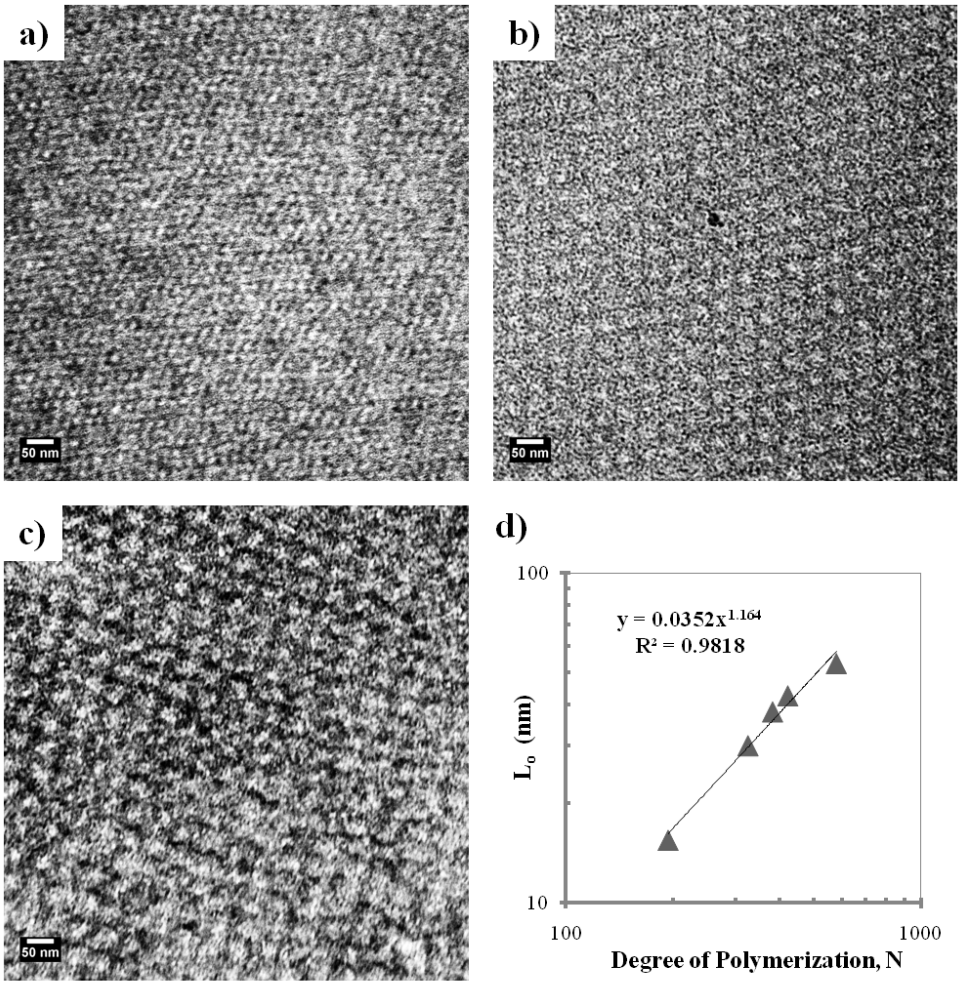


Figure 5.11**.** Bulk TEM micrographs with a fixed square area showing the increase in microdomain period ($L_o$) resulting from the increase in total polymer molecular weight, while keeping the PαMS wt. % at around 30%. PHOST shows as the darker matrix around the lighter PαMS dots, due to chemical staining with ruthenium tetroxide vapor. a) $M_n$= 23,000 g/mol, b) $M_n$= 50,000 g/mol, c) $M_n$= 68,000 g/mol, d) a log-log plot showing the power law scaling relation of PαMS-*b*-PHOST $L_o$ as a function of molecular weight, represented here by the degree of polymerization, N

The scaling exponent $\gamma$ depends strongly upon the degree of incompatibility between the copolymer blocks, usually represented by the Flory-Huggins interaction term, $\chi N$. Theoretical calculation from self-consistent field theory predicts that $\gamma$ ranges from 0.67 in the strong segregation limit ($\chi N > 100$) to 0.99 in the weak segregation limit ($\chi N \sim 10$) for bulk diblock copolymers.[35] Surprisingly, when the $L_o$ values observed for P$\alpha$MS-*b*-PHOST are plotted on a log-log scale versus their respective molecular weight, the scaling exponent equals 1.16 (Figure 5.11(d)).

Despite averaging ten measurements of d-spacing per TEM image, SAXS could have done a better job of measuring the average d-spacing per sample, for the reasons outlined in Section 5.3.2. Assuming the TEM measurements are close to the actual d-spacing values present in the respective systems, the observed deviation from the scaling theory could come from the strong enthalpic hydrogen bonding interactions from the majority PHOST block. It is well known in the literature that polymers with supramolecular interactions such as hydrogen bonds are highly sensitive to external stimuli such as temperature, pressure, or pH. In one example, a block copolymer end-functionalized with hydrogen-bonding groups showed a swelling of the lamellar microphase up to 300% with variation of temperature.[36] As all the polymers used for this study were heated for three days at 200 °C, the data may be skewed by this thermal effect on the degree of incompatibility between the polymer blocks, and will certainly warrant future study.

## REFERENCES


1. Whitesides, G. M.; Grzybowski, B., Self-assembly at all scales. *Science (Washington, DC, United States)* **2002,** *295* (5564), 2418-2421.
2. Bates, F. S.; Fredrickson, G. H., Block copolymers-designer soft materials. *Physics Today* **1999,** *52* (2), 32-38.
3. Park, M.; Harrison, C.; Chaikin, P. M.; Register, R. A.; Adamson, D. H., Block copolymer lithography: periodic arrays of ~1011 holes in 1 square centimeter. *Science (Washington, D. C.)* **1997,** *276* (5317), 1401-1404.
4. Black, C. T.; Guarini, K. W.; Milkove, K. R.; Baker, S. M.; Russell, T. P.; Tuominen, M. T., Integration of self-assembled diblock copolymers for semiconductor capacitor fabrication. *Applied Physics Letters* **2001,** *79* (3), 409-411.
5. Black, C. T., Self-aligned self-assembly of multi-nanowire silicon field effect transistors. *Applied Physics Letters* **2005,** *87*, 163116.
6. IBM Using self assembly to create airgap microprocessors. http://www-03.ibm.com/press/us/en/presskit/21463.wss (accessed October 10).
7. Xu, T.; Hawker, C. J.; Russell, T. P., Interfacial interaction dependence of microdomain orientation in diblock copolymer thin films. *Macromolecules* **2005,** *38*, 2802-2805.
8. Lammertink, R. G. H.; Hempenius, M. A.; Van Den Enk, J. E.; Chan, V. Z. H.; Thomas, E. L.; Vancso, G. J., Nanostructured thin films of organic-organometallic block copolymers. One-step lithography with poly(ferrocenylsilanes) by reactive ion etching. *Advanced Materials* **2000,** *12* (2), 98-103.

9. Simon, Y. C.; Ohm, C.; Zimny, M. J.; Coughlin, E. B., Amphiphilic carborane-containing diblock copolymers. *Macromolecules* **2007,** *40*, 5628-5630.

10. Spatz, J. P.; Chan, V. Z. H.; Mossmer, S.; Kamm, F.-M.; Plettl, A.; Ziemann, P.; Moller, M., A combined top-down/bottom-up approach to the microscopic localization of metallic nanodots. *Advanced Materials (Weinheim, Germany)* **2002,** *14* (24), 1827-1832.

11. Templin, M.; Franck, A.; Du Chesne, A.; Leist, H.; Zhang, Y.; Ulrich, R.; Schadler, V.; Wiesner, U., Organically modified aluminosilicate mesostructures from block copolymer phases. *Science* **1997,** *278*, 1795.

12. Lopes, W. A.; Jaeger, H. M., Hierarchical self-assembly of metal nanostructures on diblock copolymer scaffolds. *Nature* **2001,** *414* (6865), 735-8.

13. Freer, E. M.; Krupp, L. E.; Hinsberg, W. D.; Rice, P. M.; Hedrick, J. L.; Cha, J. N.; Miller, R. D.; Kim, H.-C., Oriented Mesoporous Organosilicate Thin Films. *Nano Letters* **2005,** *5* (10), 2014-2018.

14. Warren, S. C.; Messina, L. C.; Slaughter, L. S.; Kamperman, M.; Zhou, Q.; Gruner, S. M.; DiSalvo, F. J.; Wiesner, U., Ordered mesoporous materials from metal nanoparticle-block copolymer self assembly. *Science* **2008,** *320*, 1748.

15. Jain, A.; Wiesner, U., Silica-type mesostructures from block copolymer phases: formation mechanism and generalization to the dense nanoparticle regime. *Macromolecules* **2004,** *37*, 5665-5670.

16. Kim, P.; Zhang, X.-H.; Domercq, B.; Jones, S. C.; Hotchkiss, P. J.; Marder, S. R.; Kippelen, B.; Perry, J. W., Solution-processible high-permittivity nanocomposite gate insulators for organic field-effect transistors. *Applied Physics Letters* **2008,** *93*, 013302.

17. Li, M.; Douki, K.; Goto, K.; Li, X.; Coenjarts, C.; Smilgies, D. M.; Ober, C. K., Spatially Controlled Fabrication of Nanoporous Block Copolymers. *Chemistry of Materials* **2004,** *16* (20), 3800-3808.

18. Bae, W. J.; Trikeriotis, M.; Sha, J.; Schwartz, E. L.; Rodriguez, R.; Zimmerman, P. A.; Giannelis, E. P.; Ober, C. K., High refractive index and high transparency HfO2 nanocomposites for next generation lithography. *J. Mater. Chem.* **2010,** *20*, 5186-5189.

19. Yeo, B.-S., Chen, Z-H., Sim, W-S., Surface functionalization of Ni (111) with acrylate monolayers. *Langmuir* **2003,** *19*, 2787-2794.

20. Li, D.; Brisson, J., Hydrogen bonds in poly(methyl methacrylate)-poly(4-vinyl phenol) blends. *Polymer* **1998,** *39*, 793-800.

21. Kim, Y.-J.; Ha, S. W.; Jeon, S.-M.; Yoo, D. W.; Chun, S.-H.; Sohn, B.-H.; Lee, J.-K., Fabrication of triacetylcellulose-SiO2 nanocomposites by surface modification of silica nanoparticles. *Langmuir* **2010,** *26* (10), 7555.

22. Al-Kandary, S.; Ali, A. A. M.; Ahmad, Z., Morphology and thermo-mechanical properties of compatibilized polyimide-silica nanocomposites. *J. Appl. Polym. Sci.* **2005,** *98*, 2521-2531.

23. Schwartz, E. L., Christopher K. Ober. Self-assembling block copolymers as photoresists and photoresist additives. M.S. Thesis, Cornell University, Ithaca, NY, 2008.

24. Stoykovich, M. P.; Mueller, M.; Kim, S. O.; Solak, H. H.; Edwards, E. W.; de Pablo, J. J.; Nealey, P. F., Directed assembly of block copolymer blends into nonregular device-oriented structures. *Science (Washington, DC, United States)* **2005,** *308* (5727), 1442-1446.

25. Zhang, D. Y., personal communication.

26. Gokan, H.; Esho, S.; Ohnishi, Y., Dry etch resistance of organic materials. *J. Electrochem. Soc.* **1983,** *130*, 143.

27. Brandrup, J.; Immergut, E. H.; Grulke, E. A., *Polymer Handbook*. 4th ed.; Wiley-Interscience: New York, 1999.

28. Bosworth, J. K.; Ruiz, R.; Paik, M. Y.; Schwartz, E. L.; Huang, J. Q.; Ko, A. W.; Smilgies, D. M.; Black, C. T.; Ober, C. K., Control of Self Assembly of Lithographically-Patternable Block Copolymer Films. *ACS Nano* **2008,** *2* (7), 1396-1402.

29. Cowie, J. M.; Bywater, S. J., *J. Polym. Sci.* **1961,** *54*, 221.

30. Ouyang, M.; Yuan, C.; Muisener, R. J.; Boulares, A.; Koberstein, J. T., Conversion of some siloxane polymers to silicon oxide by UV/Ozone photochemical processes. *Chem. Mater.* **2000,** *12*, 1591.

31. Kim, H.-C.; Wallraff, G.; Kreller, C. R.; Angelos, S.; Lee, V. Y.; Volksen, W.; Miller, R. D., Photopatterned nanoporous media. *Nano Letters* **2004,** *4* (7), 1169.

32. Gabor, A. H.; Lehner, E. A.; Mao, G.; Schneggenburger, L. A.; Ober, C. K., Synthesis and Lithographic Characterization of Block Copolymer Resists Consisting of Both Poly(styrene) Blocks and Hydrosiloxane-Modified Poly(diene) Blocks. *Chemistry of Materials* **1994,** *6* (7), 927-34.

33. Bates, F. S.; Fredrickson, G. H., Block copolymer thermodynamics: theory and experiment. *Annual Review of Physical Chemistry* **1990,** *41*, 525-57.

34. Guarini, K. W.; Black, C. T.; Yeung, S. H. I., Optimization of diblock copolymer thin film self assembly. *Adv. Mater.* **2002,** *14* (18), 1290-1294.

35. Hamley, I. W., *The Physics of Diblock Copolymers*. Oxford University Press: New York, 1998.

36. Huh, J.; Park, H. J.; Kim, K. H.; Kim, K. H.; Park, C.; Jo, W. H., Giant thermal tunability of the lamellar spacing in block-copolymer like supramolecules formed from binary end-functionalized polymer blends. *Adv. Mater.* **2006,** *18*, 624-629.

# CHAPTER SIX:

## SPIN COATING MULTIPLE BLOCK COPOLYMERS PER LAYER USING ORTHOGONAL PROCESSING[*]

[*] Evan L. Schwartz, Wei Min Chan, Joan K. Bosworth, Jin Kyun Lee, John DeFranco, Sandip Tiwari, Christopher K. Ober. *To be submitted.*

### *6.1 Introduction*

As the field of high-resolution patterning progresses towards the sub-20 nm node, alternative techniques are being considered that are not limited by the expensive optics of lithography tools.[1, 2] Of these techniques, the self-assembly of block copolymers stands out as an alternative, "bottom-up" approach to extend lithographic patterning.[3] Block copolymers consist of two polymers connected at one end by a covalent bond. The low entropy of mixing between the two polymers, coupled with the elastic restoring force of the covalent bond, leads to mesoscale (10-100 nm) morphologies such as spheres, cylinders and lamellae that can be controlled by changing the volume fraction of one polymer "block" relative to the other during the synthesis step. The size of the individual microdomains, and their respective domain spacing, can be controlled by changing the molecular weight of the block copolymer. Similar to photoresists, block copolymers can be spin coated from solution to form thin films which can contain an extremely high density of microdomains (~$10^{11}$ per square centimeter).[4] The films can gain long-range order simply by thermal annealing,[5] or the microdomains can be oriented through processing with solvent vapor,[6] electric fields,[7] shear alignment,[8] or by constraining the block copolymers within a lithographically patterned trench.[9] Furthermore, one of the domains of the block copolymer can be selectively removed to create a nanoporous etch mask that can be used to transfer the self-assembled patterns into arbitrary semiconductor substrates, [10] drawing a significant amount of attention from the semiconductor community as a possible route to sub-20 nm periodic patterns for next-generation lithography.[11]

Until now, the block copolymer community has been limited to the use of only one block copolymer per layer due to the damage and intermixing caused by the spin coating of a second polymer solution on top of the first polymer film. The limitation of only one self-assembled block copolymer domain size and pitch is not attractive to the

lithography community, which has grown used to the ability to print patterns of arbitrary shapes and sizes using photolithography. This issue, among others, has been highlighted in a paper discussing the challenges and strategy for future self-assembly goals.[12]

Recently, a new technique has been developed in our group that neatly bypasses the intermixing problem by substituting a semifluorinated photoresist and solvent system in for the hydroxylic solvent-based photoresists traditionally used in lithographic processing.[13-16] The technique allows for spin coating of functional semifluorinated materials on top of hydroxylic-based functional materials (and vice versa) with little to no intermixing between the layers. So called "orthogonal processing" has allowed for the creation of overlaying stacks of functional light-emitting materials with excellent performance and stability.[17] Here we demonstrate an extension of the orthogonal processing concept that allows for the deposition of multiple block copolymers, with different sizes and pitches, adjacent to each other on the same layer. The process, shown in Figure 6.1, uses a combination of additive and subtractive patterning approaches (CASP) which may also be applicable to other functional polymer systems.

### *6.2 Experimental Methods*

#### *6.2.1 Materials*

Hydrofluoroether (HFE) (Novec™) solvents were obtained from 3M Corporation and used as received. Poly($^1$H,$^1$H,$^2$H,$^2$H-perfluorodecyl methacrylate-ran-*tert*-butyl methacrylate) (P(FDMA-*ran*-TBMA), "Ortho 310") photoresist was supplied by Orthogonal Inc. Triphenyl sulfonium triflate (TPST) photoacid generator was obtained from Aldrich and used as received. Tetramethoxymethylglycouril (TMMGU, "Powderlink 1174") was donated by Cytec Industries. All other solvents

were obtained from Aldrich and used as received. PαMS-*b*-PHOST block copolymers ($M_n$=53,000 g/mol, $f_{PαMS}$~34% (**BCP1**) and $M_n$=23,000 g/mol, $f_{PαMS}$~30% (**BCP2**) were synthesized as reported previously. [18] Poly(styrene) with an –OH end group (PS-OH, $M_n$=10,000 g/mol, PDI= 1.07) was obtained from Polymer Source (Dorval, CA) and used as received. Single-polished <100> Silicon wafers containing a ~2 nm native oxide layer were obtained from WRS (Spring City, PA).

### *6.2.2 Film Preparation*

Silicon wafers cleaned with oxygen plasma were coated with a 1 wt. % solution of PS-OH in methyl isobutyl ketone and annealed for 12 hours at 140 °C under vacuum. A dehydration reaction between the –OH groups of the polymer and the Si-OH groups on the cleaned silica wafers covalently bound PS-OH brushes to the silica surface. Excess polymer was washed off by soaking in toluene for 30 minutes and the wafer was blown dry with a stream of dry nitrogen. PαMS-*b*-PHOST was dissolved in propylene glycol methyl ether acetate (PGMEA), and the film thickness was controlled by varying the solution concentration and spin speed. **BCP1** was mixed with 2 wt. % TPST photoacid generator and 4 wt. % TMMGU crosslinker relative to the weight of the polymer. **BCP1** was spin coated on top of the grafted PS-OH brush and solvent annealed, as described previously.[19]

The solvent annealing was performed in a 1L glass dessicator with 5 mL of either tetrahydrofuran (~8 hr) or acetone (~5 hr) solvent placed in a small petri dish cover at the bottom of the chamber. Vacuum grease was applied liberally underneath the glass lid to ensure a good seal and the formation of a saturated solvent vapor inside the chamber. After solvent annealing, the block copolymer was flood exposed to 254

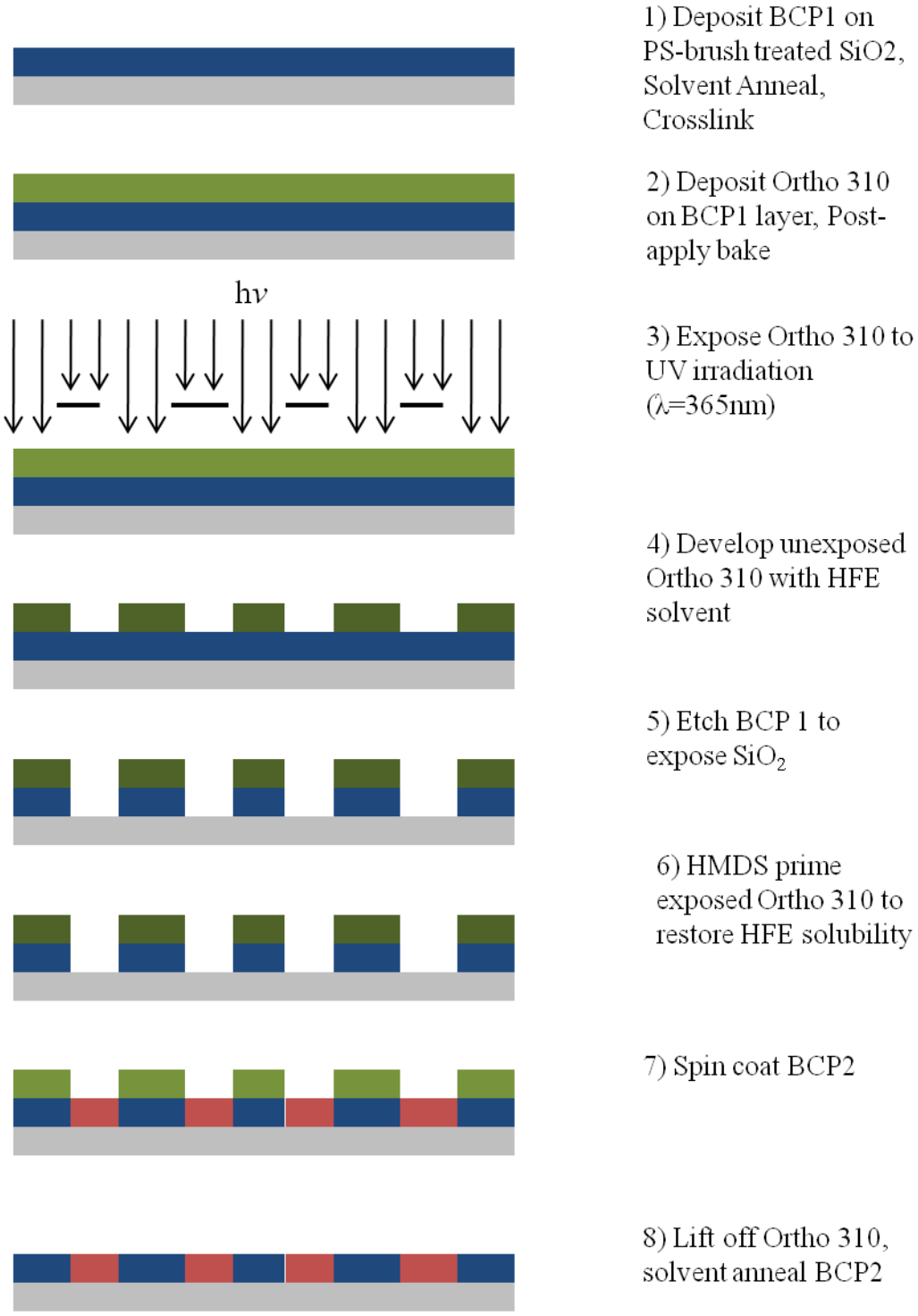


Figure 6.1. Schematic of CASP process flow

nm UV irradiation (Dose=360 mJ/cm$^2$) and baked for 60 seconds at 115 °C to accelerate the acid catalyzed crosslinking reaction. For the second block copolymer deposition, no crosslinking was necessary after the solvent anneal.

### *6.2.3 Deposition and Patterning of the Orthogonal Photoresist*

Ortho 310 photoresist was spin coated on top of the crosslinked block copolymer film (thickness ~650 nm) and exposed to 365nm UV radiation using a GCA Autostep 200 DSW i-line Wafer Stepper (Dose = 18.7 mJ/cm$^2$). After exposure, the films were baked for 60 seconds at 75 °C, and then developed in HFE 7300 for approximately 30 seconds. Oxygen plasma etching was performed using a Plasmatherm 72 (50 sccm $O_2$, 60 mTorr, 100 W) to etch through BCP1 while also etching about half of the thickness of the Ortho 310. HMDS priming treatment of the exposed Ortho 310 pattern was performed in a Yield Engineering Systems (YES-LPIII) vacuum oven.

### *6.2.4 Characterization Methods*

Scanning probe microscopy was performed using a Veeco Dimension 3100 operated in tapping mode. Olympus cantilevers were used (Spring constant = 42 N/m, radius <=10nm) and Nanoscope imaging software was used for the analysis. Water contact angle measurements were executed using a VCA Optima contact angle measurement system.

## *6.3 Results and Discussion*

In the past, the sub-field of patternable block copolymers may not have been properly motivated by industrial applications.[20] However, since then new technology

has emerged that makes clear the need for more spatial control over the location of nanoporous templates.[21,22] The work of Li et al. took a significant step in this direction by proving that the incorporation of a negative-tone photoresist as the matrix phase of a block copolymer could make it lithographically patternable.[18] Using this approach, the un-crosslinked block copolymer could be simply washed away in a developing solvent. To pattern an additional block copolymer in another region of the wafer, however, the crosslinked resist will swell upon exposure to the spin coating solvent, potentially changing or damaging the delicate block copolymer morphology. The orthogonal patterning approach proposed here neatly sidesteps this problem by protecting the top of the first crosslinked block copolymer with a non-interacting fluorinated photoresist, which can be cleanly removed after deposition of the second block copolymer.

### *6.3.1 Deposition of Orthogonal Fluorinated Photoresist*

In order to ensure the non-interaction of the block copolymer in the hydrofluoroether (HFE) processing solvent, we soaked a solvent-annealed block copolymer film (**BCP1**) in a bath of one of the stronger hydrofluoroether solvents, HFE 7600, and examined the morphology before and after solvent exposure. Figure 6.2(a) and (b) shows that the parallel-oriented cylindrical morphology remained unharmed after exposure to HFE 7600 before and after solvent exposure, respectively.

To begin the orthogonal processing of two block copolymers on the same layer, the first block copolymer (**BCP1**, $L_o$=48 nm) is spin coated on top of a polystyrene brush. The polystyrene brush was used to preferentially attract the PαMS domain for the creation of parallel-oriented cylinders, as well as ease the mobility of the polymer during the solvent annealing step through a reduction in substrate pinning.[23]

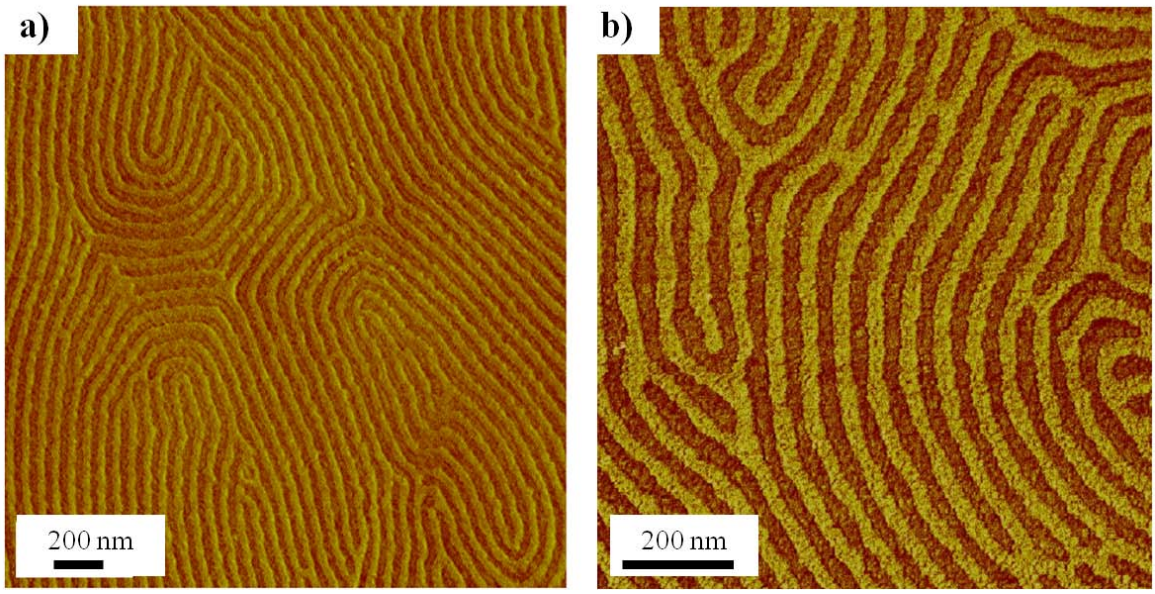


Figure 6.2. PαMS-*b*-PHOST "BCP1" annealed in THF vapor for 8 hours a) before exposure to HFE 7600, and b) after soaking in HFE 7600 for several minutes

Afterwards, the polymer was photocrosslinked using a flood exposure to 254nm radiation to prevent lift-off in future deposition steps.

### *6.3.2 Subtractive Patterning of BCP1*

For the first patterning step, a thick layer of a semifluorinated polymeric photoresist P(FDMA-*ran*-TBMA) was dissolved in HFE 7600, spin coated as a thick (~650 nm) film and lithographically patterned using 365-nm irradiation. The ultraviolet radiation triggered the release of acid from a photoacid generating molecule blended into the resist. The acid deprotected the *tert*-butyl groups on the PTBMA component of the photoresist, transforming the polymer into the HFE-phobic poly(methacrylic acid) (PMAA), as shown in Figure 6.3. We found that the resist could be patterned with a lower dose if a stronger developing solvent was used, which made the polymer easier to lift off later in the process flow.

The unexposed Ortho 310 was then washed away to open up windows for the subsequent oxygen plasma etching of **BCP1**, via a subtractive patterning approach. The relative etch rates of both the Ortho 310 (4-5 nm/sec) and **BCP1** (1.5 nm/sec) were taken into account to make sure that a sufficient amount of Ortho 310 remained to protect the underlying **BCP1** during the deposition of **BCP2**. In our process, approximately 360 nm of Ortho 310 remained after the etching process was complete, and windows of silica were exposed in preparation for the spin coating of **BCP2** .

### *6.3.3 Restoring HFE Solubility to P(FDMA-ran-MAA)*

We found that an organosilane (hexamethyldisilazane, HMDS) vapor priming treatment was required before the application of **BCP2**, for two reasons. First, Hwang et al. showed that the hydroxyl groups of PMAA from the exposed Ortho 310 must be capped to restore HFE solubility for subsequent lift-off.[13] The HMDS vapor diffused into the exposed resist

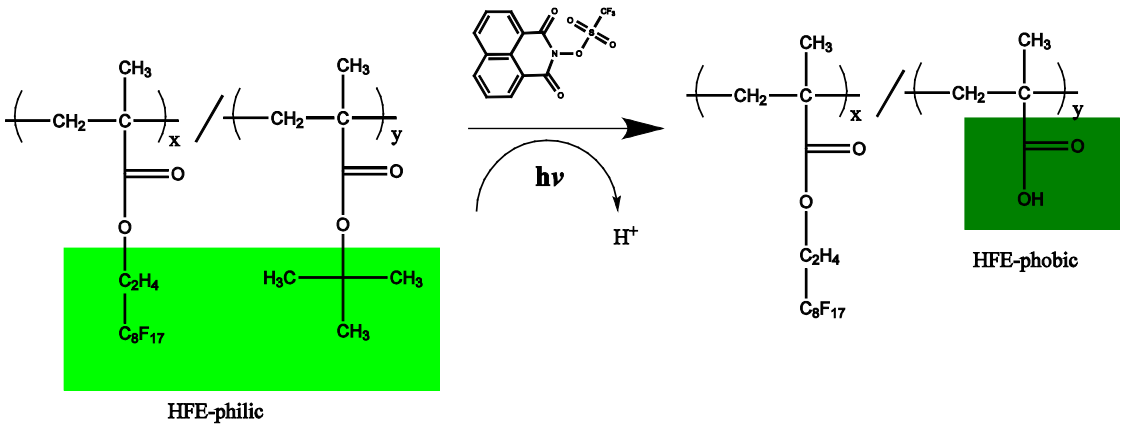


Figure 6.3. Schematic of the lithographic patterning of P(FDMA-*ran*-TBMA)

and efficiently capped most –OH groups with the more HFE-philic methylated silica moiety, as shown in Figure 6.4. Second, the capping of the polar –OH groups on PMAA with HMDS created a more hydrophobic polymer surface that resisted the adhesion of **BCP2** during spin coating. We found that if **BCP2** adhered well to the surface of the Ortho 310 it became much harder to lift off afterward in the HFE stripping bath. The water contact angles of the resist before and after HMDS treatment were investigated. The HMDS-capped resist showed a water contact angle approximately 4° higher, as shown in Figure 6.4(b) and (c), indicating a slightly lower surface energy than the neat P(FDMA-*ran*-MAA). We found that the vapor primed resist removed cleanly and left behind smooth underlying films. The film thickness after stripping was equal to 124 nm, equivalent to the film thickness of **BCP1**. Therefore, we can be reasonably certain that the HMDS has restored full HFE solubility to the fluorinated photoresist and allowed for a complete removal of the resist from the block copolymer film.

### *6.3.4 Additive Patterning of BCP2*

The HMDS vapor also reacts with the silanol groups on the exposed silica surface, which makes the surface more hydrophobic, but not hydrophobic enough to block the adhesion of the second block copolymer to adhere to the wafer. The PGMEA solution for the **BCP2** ($L_o$ = 23nm) was puddled on top of the HMDS-primed silica surface and the Ortho 310 resist and spin coated. At this step, we found that if **BCP1** was not crosslinked before being covered by Ortho 310, partial lift-off of the **BCP1**/Ortho 310 film stack would occur. This caused major distortion of the patterns, as shown in Figure 6.5(a), compared to the film stack from crosslinked **BCP1** in Figure 6.5(b). The only interaction of the crosslinked BCP1 and the PGMEA solvent

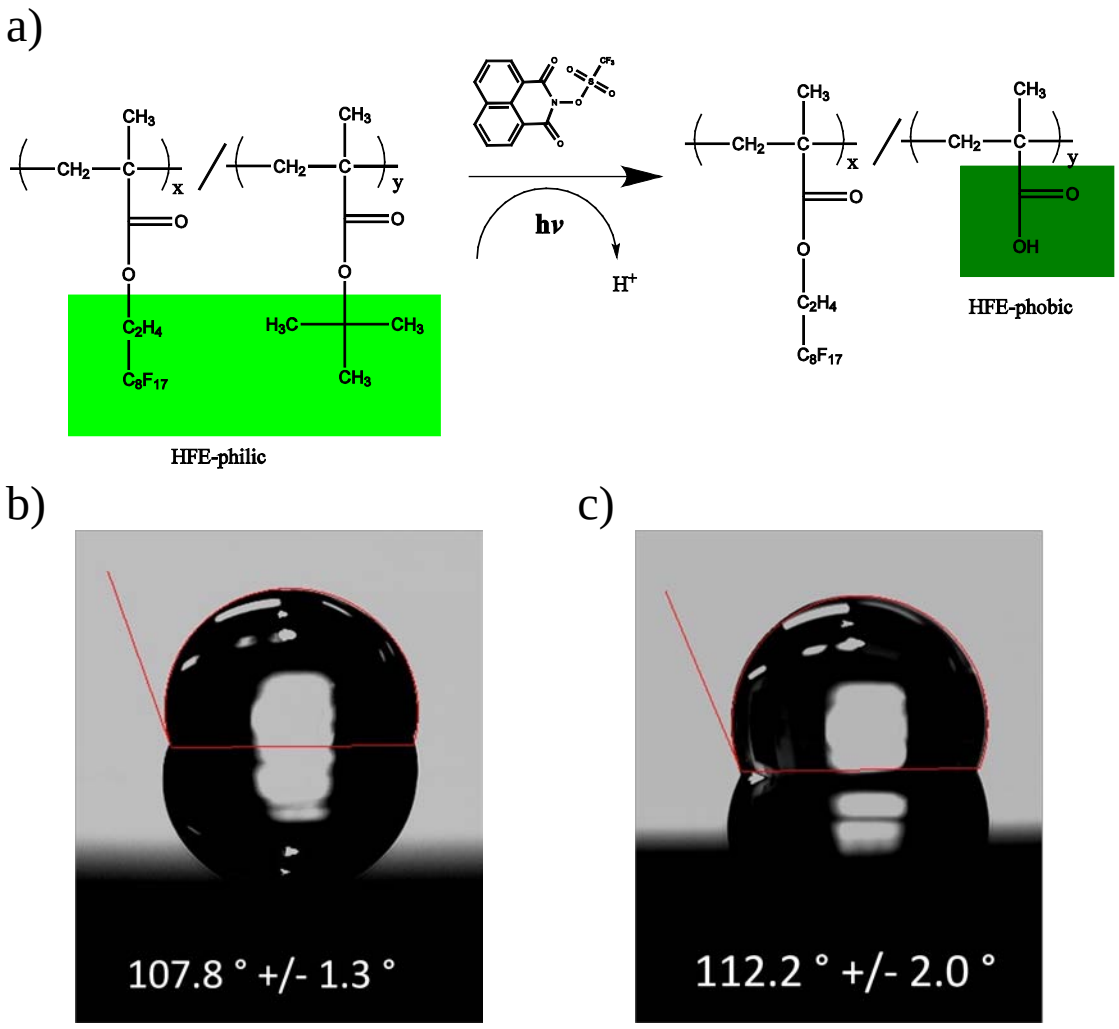


Figure 6.4. a) Chemical reaction of P(FDMA-*ran*-MAA) with HMDS restores its ability to dissolve in HFE solvents, b) water contact angle of P(FDMA-*ran*-MAA) , and c) P(FDMA-*ran*-MAA) capped with HMDS deposited using the vapor priming method.

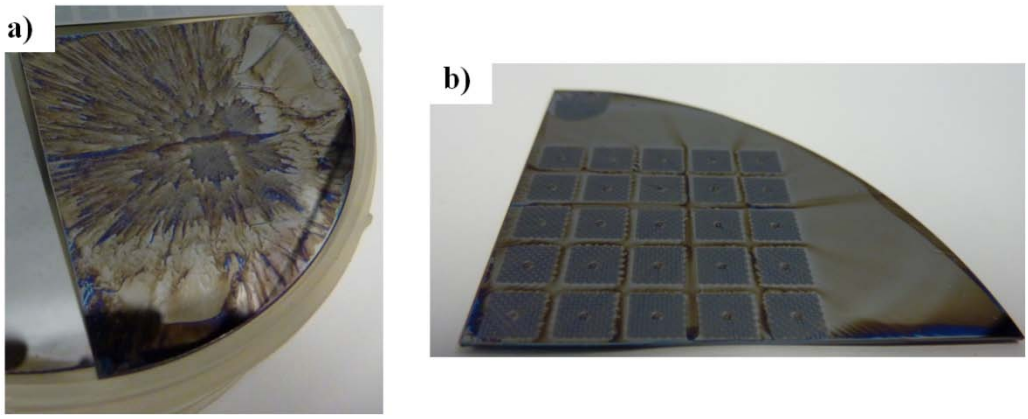


Figure 6.5. Comparison of the integrity of the patterned filmstack after spin coating **BCP2** with a) uncrosslinked **BCP1**, and b) crosslinked **BCP1**

occurred at the cross-section of each BCP1/Ortho 310 film stack, which should not cause any significant swelling of the microdomains. No post-apply bake was performed on the BCP2 film after spin coating. Then, the wafer was soaked in HFE7600 to remove the Ortho 310, which exposed the underlying BCP1. We observed some difficulty in getting the Ortho 310 to remove completely, due to a small amount of **BCP2** film covering its surface and blocking HFE solvent entry into the resist. After ten minutes of exposure to HFE 7600, some pieces of the Ortho 310 were still left clinging to the underlying polymer. These could be removed by sonicating the wafer in HFE7600 for three minutes, leaving behind squares of **BCP1** surrounded by a matrix of **BCP2**, as shown in Figure 6.6. The composite film could then be solvent annealed to gain long-range ordering in the uncrosslinked **BCP2** region.

Atomic force microscopy was used to analyze the respective block copolymer morphologies located in each region of the wafer. Each block copolymer was deliberately spin coated at a different thickness to delineate the separate block copolymer films more clearly using the optical microscope attached to the AFM. Region 1 in Figure 6.6 shows the wafer area coated by **BCP1** ($L_o$=48 nm), whereas region 2 shows the area coated by **BCP2** ($L_o$= 23 nm). The AFM image of **BCP1** clearly showed the cylindrical morphology and domain spacing we expected, so we can be sure that no significant amount of residue was left over from the Ortho 310 coating. To the best of the author's knowledge, this is the first time two different polymer films have been spin coated adjacent to each other on the same layer without any damage or intermixing.

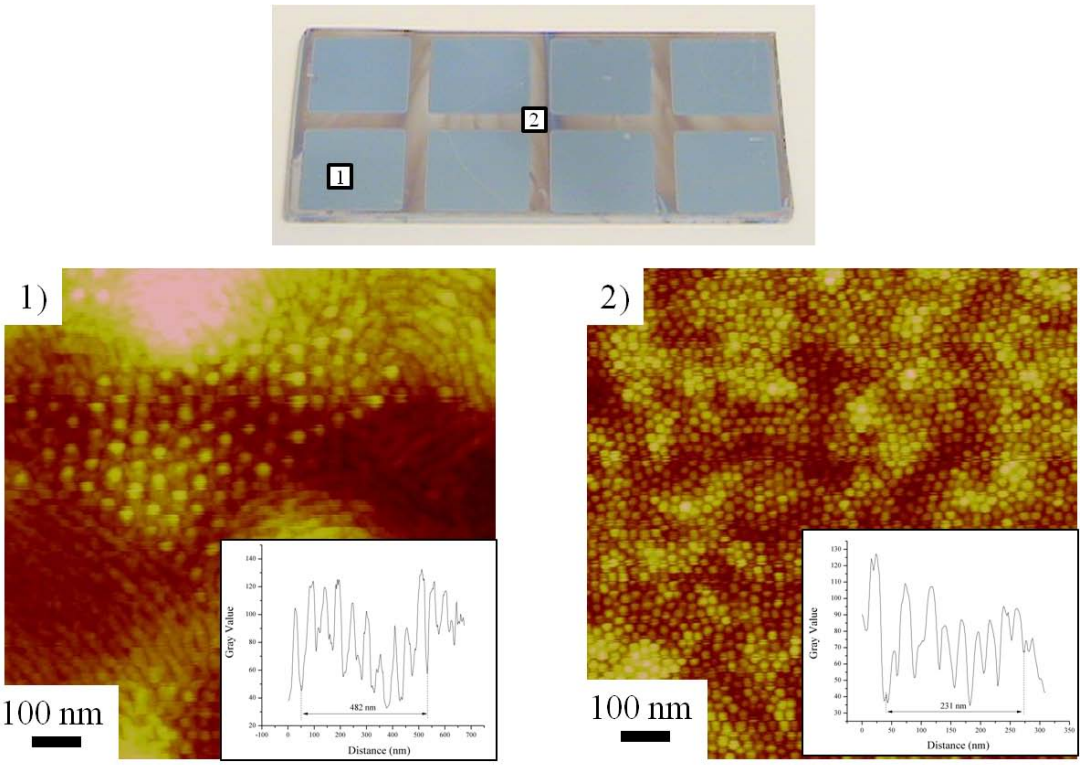


Figure 6.6. Wafer after final patterning step, showing two block copolymers spin coated on the same layer of the wafer. Boxes labeled (1) and (2) show representative phase AFM images taken in that area showing the morphology of the two respective block copolymers. $L_o$ (1) ~ 48 nm, $L_o$ (2) ~ 23 nm. The scale bar shown in both images is equal to 100 nm.

### *6.4 Conclusion*

A novel process was introduced which allowed for the orthogonal processing of thin polymer films in a combined additive and subtractive patterning (CASP) approach. As a proof of principle for this concept, two block copolymers with different self-assembled domain sizes and pitches were deposited adjacent to one another on the same layer of a silicon wafer surface. It was shown that the first polymer must be crosslinked to avoid lift-off during the spin coating of the second polymer, which is a unique ability of the PαMS-*b*-PHOST block copolymer used in this study. The CASP approach is designed to minimize swelling of the crosslinked resist due to solvent exposure. This approach could be extended to the deposition of multiple functional polymers on the same layer for many other applications in electronics, biology or beyond.[24]

### *6.5 Acknowledgements*

E. L. S. would like to thank the Semiconductor Research Corporation (SRC), International SEMATECH and Motorola Corp. for financial support. W.M.C acknowledges the financial support of the Air Force Office for Scientific Research. This work was performed in part at the Cornell NanoScale Facility, a member of the National Nanotechnology Infrastructure Network, which is supported by the National Science Foundation (Grant ECS-0335765). The authors also acknowledge the use of facilities at Cornell University Nanobiotechnology Center (NBTC).

## REFERENCES


1. Rothemund, P. W. K., Folding DNA to create nanoscale shapes and patterns. *Nature* **2006,** *440*, 297-302.
2. Wu, B.; Kumar, A., Extreme ultraviolet lithography: A review. *J. Vac. Sci. Tech. B* **2007,** *25*, 1743.
3. Bates, F. S.; Fredrickson, G. H., Block copolymers-designer soft materials. *Physics Today* **1999,** *52* (2), 32-38.
4. Park, M.; Harrison, C.; Chaikin, P. M.; Register, R. A.; Adamson, D. H., Block copolymer lithography: periodic arrays of ~1011 holes in 1 square centimeter. *Science (Washington, D. C.)* **1997,** *276* (5317), 1401-1404.
5. Harrison, C.; Adamson, D. H.; Cheng, Z.; Sebastian, J. M.; Sethuraman, S.; Huse, D. A.; Register, R. A.; Chaikin, P. M., Mechanisms of ordering in striped patterns of diblock copolymers. *Science (Washington, D. C.)* **2000,** *290* (5496), 1558-1561.
6. Kim, S. H.; Misner, M. J.; Xu, T.; Kimura, M.; Russell, T. P., Highly oriented and ordered arrays from block copolymers via solvent evaporation. *Advanced Materials (Weinheim, Germany)* **2004,** *16* (3), 226-231.
7. Morkved, T. L.; Lu, M.; Urbas, A. M.; Ehrichs, E. E.; Jaeger, H. M.; Mansky, P.; Russell, T. P., Local control of microdomain orientation in diblock copolymer thin films with electric fields. *Science (Washington, D. C.)* **1996,** *273* (5277), 931-933.
8. Angelescu, D. E.; Waller, J. H.; Adamson, D. H.; Deshpande, P.; Chou, S. Y.; Register, R. A.; Chaikin, P. M., Macroscopic orientation of block copolymer cylinders in single-layer films by shearing. *Advanced Materials (Weinheim, Germany)* **2004,** *16* (19), 1736-1740.

9. Sundrani, D.; Darling, S. B.; Sibener, S. J., Guiding Polymers to Perfection: Macroscopic Alignment of Nanoscale Domains. *Nano Letters* **2004,** *4* (2), 273-276.

10. Park, M.; Chaikin, P. M.; Register, R. A.; Adamson, D. H., Large area dense nanoscale patterning of arbitrary surfaces. *Applied Physics Letters* **2001,** *79* (2), 257-259.

11. Kim, H.-C.; Park, S.-M.; Hinsberg, W. D., Block copolymer based nanostructures: materials, processes, and applications to electronics. *Chem. Rev.* **2010,** *110*, 146-177.

12. Herr, D. J. C., Challenges in directed self-assembly. *Future Fab International* **2007,** *22*, 69-71.

13. Hwang, H. S.; Zakhidov, A. A.; Lee, J.-K.; Andre, X.; DeFranco, J. A.; Fong, H. H.; Holmes, A. B.; Malliaras, G. G.; Ober, C. K., Dry photolithographic patterning process for organic electronics using supercritical carbon dioxide as a solvent. *J. Mater. Chem.* **2008,** *18*, 3087-3090.

14. Lee, J.-K.; Chatzichristidi, M.; Zakhidov, A. A.; Taylor, P. G.; DeFranco, J. A.; Hwang, H. S.; Fong, H. H.; Holmes, A. B.; Malliaras, G. G.; Ober, C. K., Acid-sensitive semiperfluoroalkyl resorcinarene: an imaging material for organic electronics. *J. Am. Chem. Soc.* **2008,** *130*, 11564-11565.

15. Lee, J.-K.; Fong, H. H.; Zakhidov, A. A.; McCluskey, G. E.; Taylor, P. G.; Santiago-Berrios, M.; Abruna, H. D.; Holmes, A. B.; Malliaras, G. G.; Ober, C. K., Semiperfluoroalkyl polyfluorenes for orthogonal processing in fluorous solvents. *Macromolecules* **2010,** *43*, 1195-1198.

16. Taylor, P. G.; Lee, J.-K.; Zakhidov, A. A.; Chatzichristidi, M.; Fong, H. H.; DeFranco, J. A.; Malliaras, G. G.; Ober, C. K., Orthogonal patterning of

PEDOT:PSS for organic electronics using hydrofluoroether solvents. *Adv. Mater.* **2009,** *21*, 2314-2317.

17. Zakhidov, A. A.; Lee, J.-K.; Fong, H. H.; DeFranco, J. A.; Chatzichristidi, M.; Taylor, P. G.; Ober, C. K.; Malliaras, G. G., Hydrofluoroethers as orthogonal solvents for the chemical processing of organic electronic materials. *Adv. Mater.* **2008,** *20*, 3481-3484.
18. Li, M.; Douki, K.; Goto, K.; Li, X.; Coenjarts, C.; Smilgies, D. M.; Ober, C. K., Spatially Controlled Fabrication of Nanoporous Block Copolymers. *Chemistry of Materials* **2004,** *16* (20), 3800-3808.
19. Bosworth, J. K.; Ruiz, R.; Paik, M. Y.; Schwartz, E. L.; Huang, J. Q.; Ko, A. W.; Smilgies, D. M.; Black, C. T.; Ober, C. K., Control of Self Assembly of Lithographically-Patternable Block Copolymer Films. *ACS Nano* **2008,** *2* (7), 1396-1402.
20. Li, M.; Coenjarts, C. A.; Ober, C. K., Patternable block copolymers. *Advances in Polymer Science* **2005,** *190* (Block Copolymers II), 183-226.
21. Shinada, T.; Okamoto, S.; Kobayashi, T.; Ohdomari, I., Enhancing semiconductor performance using ordered dopant arrays. *Nature* **2005,** *437*, 1128-1131.
22. IBM Using self assembly to create airgap microprocessors. http://www-03.ibm.com/press/us/en/presskit/21463.wss (accessed October 10).
23. Harrison, C.; Chaikin, P. M.; Huse, D. A.; Register, R. A.; Adamson, D. H.; Daniel, A.; Huang, E.; Mansky, P.; Russell, T. P.; Hawker, C. J.; Egolf, D. A.; Melnikov, I. V.; Bodenschatz, E., Reducing Substrate Pinning of Block Copolymer Microdomains with a Buffer Layer of Polymer Brushes. *Macromolecules* **2000,** *33* (3), 857-865.

24. Menard, E.; Meitl, M. A.; Sun, Y.; Park, J.-U.; Shir, D. J.-L.; Nam, Y.-S.; Jeon, S.; Rogers, J. A., Micro- and nanopatterning techniques for organic electronic and optoelectronic systems. *Chem. Rev.* **2007,** *107,* 1117-1160.